

Dissertation in Astronomy

submitted to the

Combined Faculties of the Natural Sciences and Mathematics

of the Ruperto-Carola-University of Heidelberg, Germany

for the degree of

Doctor of Natural Sciences

put forward by

María Jesús Jiménez-Donaire, M.Sc.

born in Badajoz, Spain

Oral examination: December 1, 2017

Dense Gas and Interstellar Medium in Nearby Galaxies

*The interplay between dense gas and the galactic
environment*

MARÍA JESÚS JIMÉNEZ DONAIRE

Referees:

Dr. Frank Bigiel

Prof. Dr. Hans-Walter Rix

ABSTRACT

Galaxies act like engines converting gas into stars, which in turn produce the matter around us, laying the foundations of life. Studying the composition of this interstellar gas informs our understanding of how star formation proceeds, while also providing insight into the structure and evolution of our own Galaxy and the Universe. Research has found a strong connection between star formation and the molecular gas within galaxies.

However, the most easily accessed molecular observables, such as carbon monoxide (CO) emission, only probe low-density gas in extragalactic systems, allowing us to scratch the surface of the star-forming structures. Molecules which trace denser gas, such as hydrogen cyanide (HCN), are more challenging to observe but probe the immediate sites of star formation. In this thesis I analyze data from the first survey mapping the entire star forming disk of a sample of nearby galaxies in a suite of dense gas tracers (EMPIRE), to understand the interplay between dense gas and a wide range of galactic environments, distinct from the Milky Way. By studying the content of this dense gas in nearby galaxies I find surprising results: systematic variations of the dense gas fraction and its efficiency to form stars within and among galaxies. While more dense gas is located in regions of high interstellar pressure, this dense gas is less efficient to form stars.

To characterize the dense gas, I also explore how changes in the optical depth can affect the effective gas densities where the dense gas tracers emit, a new measurement in the disks normal star-forming galaxies. To better understand the bulk, lower-density molecular gas out of which the dense gas eventually forms, I also analyze CO line ratios to constrain carbon isotope abundances. I find the abundance to vary systematically within galaxy disks, likely due to strong fractionation effects. The results obtained in this thesis support a model where star formation depends strongly on host galaxy and the local galactic environment in the disk.

ZUSAMMENFASSUNG

Galaxien sind wie Maschinen die Gas in Sterne umwandeln, welche wiederum die Materie herstellen, die uns umgibt, und bilden so die Grundlagen für die Entstehung von Leben. Informationen über die Zusammensetzung dieses interstellaren Gases helfen uns dabei zu verstehen, wie Sternentstehung abläuft, und geben uns Einblicke in die Struktur und Entwicklung unserer eigenen Galaxie und des Universums. Bisherige Forschungsergebnisse zeigen einen starken Zusammenhang zwischen Sternentstehung und molekularem Gas in Galaxien.

Mit Hilfe der am einfachsten zu beobachtenden Moleküle wie Kohlenstoffmonoxid (CO) lässt sich allerdings nur Gas niedriger Dichte in extragalaktischen Systemen aufspüren. Somit ist es nicht möglich, in das Innere von Sternentstehungsgebieten zu sehen. Moleküle, mit denen dichteres Gas ausgespürt werden kann, wie z.B. Cyanwasserstoff (HCN), sind deutlich schwieriger zu beobachten aber ermöglichen einen Blick auf die tatsächlichen Stätten der Sternentstehung. In dieser Doktorarbeit analysiere ich Daten der ersten systematischen Kartierung solcher Moleküllinien der gesamten stellaren Scheiben in einer Auswahl naher Galaxien durch, um das Zusammenspiel zwischen dichtem Gas unter verschiedenen galaktischen, von der Milchstraße verschiedenen, Umgebungsbedingungen zu verstehen. Bei der Untersuchung des dichten Gases in nahen Galaxien zeigen sich interessante Ergebnisse: Sowohl innerhalb einer Galaxie als auch beim Vergleich verschiedener Galaxien gibt es systematische Variationen im Anteil Gases hoher Dichte im interstellaren Gas und in der Effizienz, mit der dieses Gas in Sterne umgewandelt wird. Dichtes Gas befindet sich eher in Gebieten mit hohem interstellarem Druck, ist aber zunehmend weniger effizient bei der Sternentstehung.

Um das dichte Gas zu charakterisieren, untersuchen ich auch wie die Opazität der Moleküllinien die effektiven Gasdichten beeinflussen können, bei denen diese Moleküllinien emittieren. In normalen Scheibengalaxien ist dies eine völlig neue Analyse. Um auch das Gas niedrigerer Dichte, aus dem sich letztlich das Gas hoher Dichte bildet, besser zu charakterisieren, analysiere ich auch die Verhältnisse von CO Linien um die Häufigkeiten von Kohlenstoffisotopen einschränken zu können. Es zeigt sich dass diese Häufigkeiten systematisch innerhalb von Galaxien variieren, vermutlich durch den Effekt der Fraktionierung. Die Ergebnisse dieser Arbeit untermauern ein Model, in dem Sternentstehung stark von Galaxie und der lokalen galaktischen Umgebung in der Scheibe abhängt.

*Para mis padres
y mi hermano*

Caminante, son tus huellas
el camino y nada más;
caminante, no hay camino,
se hace camino al andar.
Al andar se hace el camino,
y al volver la vista atrás
se ve la senda que nunca
se ha de volver a pisar.
Caminante no hay camino
sino estelas en la mar.

Proverbios y cantares XXIX, Campos de Castilla (1912)

Antonio Machado

TABLE OF CONTENTS

	Page
List of Tables	xi
List of Figures	xiii
1 Introduction	1
1.1 The Interstellar Medium	4
1.2 Structure and components of the ISM	4
1.2.1 Neutral atomic gas	5
1.2.2 Ionized gas	6
1.2.3 Molecular gas	7
1.2.4 Additional components of the ISM	10
1.3 Properties of Molecular Clouds	12
1.3.1 Larson’s relations for molecular clouds	14
1.3.2 Measuring molecular clouds mass	15
1.3.3 The need for high critical density tracers	17
1.4 Observed Star Formation Relations	17
1.4.1 Global Star Formation Law	18
1.4.2 Spatially resolved Star Formation Law	19
1.4.3 The Milky Way perspective	21
1.4.4 The Dense Gas regime	24
2 The EMPIRE Dense Gas Galaxy Survey	29
2.1 Survey parameters	29
2.1.1 The EMPIRE sample	29
2.2 The IRAM-30m telescope	30
2.2.1 The EMIR receiver	32
2.2.2 Observing strategy	33

TABLE OF CONTENTS

2.2.3	EMPIRE dense gas observations	36
2.2.4	New $^{12}\text{CO}(1-0)$ observations	37
2.3	Data reduction & processing	38
2.3.1	Spectral line calibration	38
2.3.2	Baseline fitting	39
2.3.3	Pathological data	40
2.3.4	Constructing data cubes	40
3	Dense gas and star formation in nearby galaxies	45
3.1	Ancillary data	46
3.1.1	Estimating physical parameters	47
3.1.2	Spectral stacking technique	51
3.2	Results	53
3.2.1	Distribution of dense gas emission	53
3.2.2	Radial profiles	54
3.2.3	Molecular line ratios	60
3.2.4	Scaling relations	62
3.2.5	Dense gas fraction and $\text{SFE}_{\text{dense}}$: what drives the observed variations?	64
3.2.6	Global environmental trends	68
3.2.7	Are variations in the $\text{SFE}_{\text{dense}}$ real?	77
3.3	Discussion	82
3.3.1	Interpreting line ratios	82
3.3.2	Zooming into the galaxy centers	84
3.3.3	The role of pressure	87
3.3.4	Does HCN always trace the same density?	89
3.4	Summary and conclusions	91
4	Optical Depth Estimates and Effective Critical Densities of Dense Gas Tracers	93
4.1	Abstract	94
4.2	Introduction	94
4.3	Observations and data reduction	95
4.3.1	IRAM 30m Observations of NGC 5194	95
4.3.2	ALMA observations of NGC 3351, NGC 3627, NGC 4254, NGC 4321 and NGC 253	96

4.4	Methodology	96
4.5	Results	98
4.5.1	Line Ratios	99
4.5.2	Line Widths	107
4.6	Discussion	108
4.6.1	Carbon Isotope Abundance Ratio	109
4.6.2	Optical Depth in the Simple Case	110
4.6.3	Non-LTE Effects and Variable Beam Filling Factors	113
4.6.4	Implications for Dense Gas Tracers	115
4.7	Summary and conclusions	116
5	The ^{13}CO-to-C^{18}O ratio across galaxy disks	119
5.1	Abstract	120
5.2	Introduction	120
5.3	Observations	121
5.4	Results	123
5.5	Discussion	128
5.5.1	Variations in the Molecular Abundances	128
5.5.2	Changes in the Optical Depth	130
5.6	Conclusions	131
6	Summary and Outlook	133
6.1	Summary of results	133
6.2	Outlook	135
A	Appendix A	139
B	Appendix B	149
	Bibliography	161

LIST OF TABLES

TABLE	Page
1.1 Phases of the Interstellar Medium.	5
2.1 The EMPIRE galaxy sample.	31
2.2 Spectral lines covered with EMPIRE	39
2.3 Observing parameters	42
3.1 Dense gas ratios	62
3.2 Dense gas fractions fitting parameters	79
3.3 SFE fitting parameters	80
4.1 Galaxy sample for optical depth determination	97
4.2 Spectral line parameters	101
4.3 Line ratios in galaxy centers	102
4.4 Line ratios in the literature	105
4.5 Carbon isotope ratios	110
4.6 Derived optical depths and effective critical densities	113
4.7 Optical depths and effective critical densities for different beam filling factors	115
5.1 The ^{13}CO -to- C^{18}O ratio	124

LIST OF FIGURES

FIGURE	Page
1.1 Large-scale Star Formation	3
1.2 Molecular cloud structure	13
1.3 Star formation law at sub-kpc scales.	22
1.4 Galactic and extragalactic comparison of star formation relations.	25
1.5 Global dense gas scaling relation.	27
1.6 Dense gas scaling relation	28
2.1 The IRAM 30-m telescope.	32
2.2 The EMPIRE EMIR/FTS setup.	34
2.3 EMIR/FTS setup for ^{12}CO (1-0)	35
2.4 On-the-fly mapping strategy.	37
2.5 EMPIRE line calibrators	43
3.1 Example of stacked vs. averaged spectrum	52
3.2 EMPIRE HCN and CO moment maps	55
3.3 Radial profiles	61
3.4 Typical line ratios in EMPIRE	62
3.5 Dense gas star formation relation	65
3.6 Star formation efficiency of dense gas in EMPIRE and literature	66
3.7 Dense gas fraction vs. stellar surface density	71
3.8 Dense gas fraction vs. molecular gas fraction	72
3.9 Dense gas fraction vs. hydrostatic pressure	73
3.10 Star formation efficiency vs. stellar surface density	74
3.11 Star formation efficiency vs. molecular gas fraction	75
3.12 Star formation efficiency vs. hydrostatic pressure	76
3.13 Global environmental trends	78
3.14 EMPIRE galaxy centers and the CMZ	85

LIST OF FIGURES

3.15	Dense gas emission with changing pressure	88
3.16	Expected line ratios due density and opacity changes	90
4.1	Integrated intensity maps	100
4.2	Stacked central ^{13}CO , HCN, and HCO^+ spectra	103
4.3	Stacked central H^{13}CN and H^{13}CO^+ spectra	104
4.4	Literature and measured line ratios	107
4.5	Stacked spectra in the disk of NGC 3627 and NGC 5194	109
5.1	Stacked ^{12}CO (2-1), ^{13}CO (1-0) and C^{18}O (1-0) spectra	122
5.2	$^{13}\text{CO}/\text{C}^{18}\text{O}$ vs. galactic radii	126
5.3	$^{13}\text{CO}/\text{C}^{18}\text{O}$ vs. SFR	127
5.4	ALMA profiles	128
5.5	Optical depth check	129
6.1	$\text{CO}(2-1)$ emission in M51, seen with the SMA	138
A.1	Individual radial stacks	140
B.1	Montecarlo test for the EMPIRE dataset	150

INTRODUCTION

Stars are our guiding light to the understanding of the Cosmos. When we look at the magnificent night sky, their light shines out of the darkness in the Universe, and make us wonder where we are and how we got here. They make us want to understand how planets, stars and galaxies are formed. They play a crucial role in the evolution cycle of galaxies from a chemical, morphological and dynamical point of view (van Dishoeck & Blake, 1998; Tielens, 2010). Stars are responsible for the production of all heavy elements¹ up to iron, such as carbon, nitrogen or oxygen; by consuming hydrogen and helium in fusion processes in their cores. At the end of their lives, stars eject these elements into the interstellar medium (ISM) through various processes (e.g. supernovae explosions), which will give rise to a new generations of stars, enriched with heavier elements.

We know that stars form out of the coldest and densest regions in molecular clouds (e.g., Lada & Lada, 2003; Tielens, 2010; Draine, 2011; André et al., 2014). However, the chain of events that leads to star formation is a multi-scale process that involves a continuous gas flow and the interplay of a large range of physical processes, including: self-gravity, turbulence, hydrodynamics, outflows, radiation and magnetic fields (see review by Mac Low & Klessen, 2004). A representation of the very basic steps of the global-scale star formation process is illustrated in Figure 1.1, which involves many orders of magnitude in densities and spatial sizes. Firstly, gas is accreted from satellite objects or the intergalactic medium (Mpc) onto galactic disks up, where it can cool down

¹in Astronomy, also referred to as metals

and form a neutral phase (kpc). In this neutral phase we can find hydrogen in an atomic state (HI) but, as gas cools down contraction gets more important, allowing for denser cloud structures to form (from $n \sim 10 \text{ cm}^{-3}$ to $n \sim 100 \text{ cm}^{-3}$) where gas is mostly molecular (H_2). This transition typically takes place where total gas surface densities are around $\Sigma_{\text{gas}} \approx 12 M_{\odot}$ (Wong & Blitz, 2002; Blitz & Rosolowsky, 2004) and the midplane pressure is about $P/k = 10^4 - 10^5 \text{ K cm}^{-3}$ (Blitz & Rosolowsky, 2006).

Turbulence is a relevant phenomenon which involves a cascade of kinetic energy from large to small scales; from entire molecular clouds down to the formation of cores (Larson, 1981; Ballesteros-Paredes et al., 1999; Mac Low & Klessen, 2004). At these scales ($\sim 10 - 0.1 \text{ pc}$, $n \sim 10^3 - 10^4 \text{ cm}^{-3}$), turbulence becomes dynamically important helping gravity to trigger local collapse, and hierarchical formation of denser substructures within globally, gravitationally stable molecular clouds occurs (e.g., Klessen et al., 2000; Heitsch et al., 2001; Vázquez-Semadeni et al., 2005). As these regions contract, the individual clumps collapse to form stars in dense clusters or cores ($n > 10^4 \text{ cm}^{-3}$ and $\sim 0.1 \text{ pc}$), which may as well merge while collapsing and contain multiple protostars. These newly-born stars play a key role in the subsequent evolution of the parent molecular cloud (feedback), as they can ionize, photodissociate, and disperse the gas.

Over the past decades, major observational efforts to characterize these steps have resulted in multi-wavelength surveys of external galaxies and in Milky Way clouds. These have started to provide statistically significant samples of tracers that can probe the very distinct physical processes, which constitutes a major step forward to obtain a complete observational picture of the large-scale star formation process. In the extragalactic context, detailed observations of individual star-forming regions ($\leq 1 \text{ pc}$) are not possible; instead most of our knowledge on extragalactic star formation comes from the integration of several star-forming regions or entire galaxies. In that direction, extragalactic surveys such as THINGS (Walter et al., 2008) and HERACLES (Leroy et al., 2009) have provided the first systematic measurements on the neutral atomic hydrogen and molecular gas phases, respectively, by using the hydrogen 21 cm line and the emission of ^{12}CO (2-1). Nevertheless, probing the exact regions of gas from which stars form remains an extremely challenging but necessary task.

The observations presented in this work focus on the interface regions between molecular clouds and denser substructures that lead to star formation, as illustrated in the lower right region of Figure 1.1. How the formation of dense, immediately star-forming gas depends on physical conditions within the low-density, bulk molecular gas

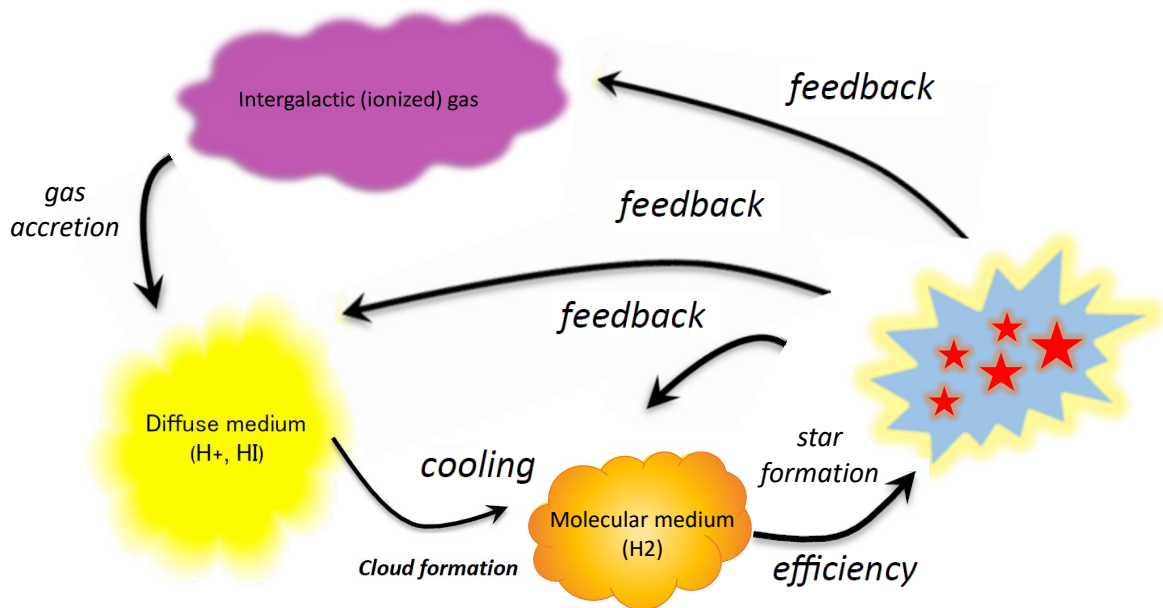


FIGURE 1.1. Illustrative sketch representing the main steps for large-scale star formation. Star formation is a multi-scale process that involves the accretion of diffuse atomic gas onto the galaxy from the ionized intergalactic medium, the formation of molecular clouds and dense substructures and the birth of stars within them. These newly born stars will exert feedback in all phases of the ISM.

and how this regulates the process of star formation, are completely open issues in the context of galactic-scale star formation. Moreover, *how do local physical conditions set by galactic environment influence the efficiency ($\text{SFR}/M_{\text{H}_2}$) at which stars form?*

In this thesis we provide systematic observations of molecules that can trace this dense, immediately star-forming gas, such as HCN and HCO^+ across the disks of nearby galaxies. The goal of this work is to place the most comprehensive observational constraints on how the dense gas fraction, and the efficiency with which this gas forms stars, depend on local physical conditions across a wide range of galactic environments. In this project we work with multiple lines tracing the dense gas and molecular gas phases, including isotopologues, which are important to constrain those environmental conditions (including abundances, optical depths and densities). In combination with our current detailed knowledge of the various properties in these galaxies and in the Milky Way (e.g. star formation rates, molecular gas content, metallicity gradients), we

aim to improve our interpretation of the observed discrepancies between Galactic and extragalactic scaling relations, for a better understanding of the interplay between ISM and star formation across a variety of environments and physical scales.

1.1 The Interstellar Medium

The interstellar medium is one of the most exciting and important components of galaxies: it constitutes *everything* that occupies the space between stars, the dominant sources of energy. During the lifetime of a galaxy there is a constant exchange of matter and energy: the ISM is gradually converted into stars and these will eventually replenish the ISM through stellar winds and supernovae explosions. The interstellar matter is a mixed of solids and gas, and it accounts for $\sim 10 - 15\%$ of the total mass of the Milky Way disk, concentrated mostly near the Galactic plane, along the spiral arms. The solid phase (dust) is characterized by grains with a distinctive size peaked at about $0.1\mu\text{m}$. The interstellar gas contains mostly hydrogen (70.4% of mass), which can be found in a neutral (H I), molecular (H_2) or ionized (H II) state. In addition, a 28.1% of the mass is of helium and a small amount (1.5% of the total mass) of heavy elements such as carbon, oxygen, and nitrogen.

A key aspect of the ISM is that the physical conditions (e.g., densities and temperatures) in interstellar space are very heterogeneous, especially at small scales. Most of the interstellar mass can be found in discrete cold clouds, which occupy a very small fraction of the interstellar volume. Density, temperature and pressure can change over many orders of magnitude between ISM phases due to mass and energy flows. Despite its intrinsic complexity, several classification schemes have attempted to describe the different ISM phases, characterized by temperatures and densities which are set by the balance between cooling and heating mechanisms. We focus on the following: hot and warm ionized gas, warm and cold neutral atomic gas, and a molecular phase. However, it should always be kept in mind that the observations we present in this thesis target large regions (200 pc-1.5 kpc) within the galactic disks, where we unresolve the transition between phases.

1.2 Structure and components of the ISM

The interstellar medium presents many different structures that cover all scale lengths, from smaller than 1 pc to larger than 1 kpc (see Table 1.1). The characteristic ra-

1.2. STRUCTURE AND COMPONENTS OF THE ISM

ISM Phase	Density (cm^{-3})	Temperature (K)	Mass ($10^9 M_{\odot}$)	f_0 (%)	Observed by
WNM	0.5	8000	2.8	30	HI 21 cm line emission, absorption, optical & UV absorption lines
CNM	50	80	2.2	1	HI 21 cm line emission, absorption, optical & UV absorption lines
WIM	0.1	8000	1.0	25	Optical line emission, thermal radio continuum
HIM	0.003	10^6	–	~ 50	UV & X-ray emission, radio synchrotron emission
Molecular clouds	$> 10^2$	10	1.3	0.05	CO line emission and dust FIR emission

TABLE 1.1. Phases of the Interstellar Medium. Table adapted from [Tielens \(2005\)](#) and [Draine \(2011\)](#).

diation is emitted over broad range of the electromagnetic spectrum, which is why multi-wavelength observations are absolutely necessary to characterize the different ISM phases. In the following subsections, we describe the various phases of the ISM where these structures can be found ([Mihalas & Binney, 1981](#); [Kulkarni & Heiles, 1988](#)), making a particular emphasis on the molecular gas phase.

1.2.1 Neutral atomic gas

Neutral atomic hydrogen is extensively distributed across galaxies' ISM, for example around the Milky Way it extends out to at ~ 30 kpc from the Galactic center ([Diplas & Savage, 1991](#)). Particle collisions do not occur very often under normal interstellar conditions, which is why most neutral hydrogen atoms are in their energy ground state and HI is not observable in the optical range. Nevertheless, it is possible to observe HI via its hyperfine 21 cm line transition. In a neutral hydrogen atom, the electron's spin can change its orientation -parallel or anti parallel- with respect to the proton spin (also known as spin-flip transition), giving rise to an emission line that is observable at 1420 MHz.

The main heating mechanism of atomic gas is UV radiation from stars, and cosmic rays; the cooling of this neutral regions is mainly due to line emission of forbidden lines such as [O I] $63 \mu\text{m}$ and [C II] $158 \mu\text{m}$. This neutral phase can be subdivided according to their temperature:

- **Warm Neutral Medium (WNM)**: provides the bulk of neutral atomic hydrogen and it is easily detected in HI line emission. This warm intercloud gas is diffuse, has typical low densities ($n_{\text{H}} \sim 0.5 \text{ cm}^{-3}$) and warm temperatures $\sim 8000 \text{ K}$.
- **Cold Neutral Medium (CNM)**: mostly traced by HI in absorption, shows a structure which is more organized in denser clumps, in comparison to the WNM phase, and it occupies a minor volume filling fraction of the ISM. The typical volume densities in this phase are of the order of 10 cm^{-3} and the temperatures are $\sim 70 \text{ K}$. This cold phase is not easily detectable in emission, therefore it is commonly studied in absorption against background continuum sources or in self-absorption against bright background HI emission.

Since the groundbreaking first HI detection by [Ewen & Purcell \(1951\)](#), the 21 cm line has been extensively used to probe the structure and kinematics in the Milky Way and other galaxies. The use of the 21 cm line has several advantages: does not suffer from extinction by interstellar dust (unlike optical or UV radiation), its Doppler shift provides information about the velocity of the emitting gas, and in addition it is optically thin under most conditions encountered in normal disk galaxies. It is therefore relatively easy to convert the observable line intensities (T_0) and widths (Δv) into HI column densities via

$$(1.1) \quad \left[\frac{N(\text{HI})}{\text{cm}^{-2}} \right] = 1.8224 \times 10^{18} \left[\frac{T_0}{\text{K}} \right] \left[\frac{\Delta v}{\text{km s}^{-1}} \right].$$

1.2.2 Ionized gas

Ionized gas comprises the hottest regions of the ISM, with observed temperatures within the range $\sim 10^4 - 10^7 \text{ K}$. Two main components can be defined:

- **Warm Ionized Medium (WIM)**: refers to gaseous regions that have been photoionized by UV photons from hot stars. While the extended, low-density regions are known as WIM, the ionized gas can also be denser if it is constituted by material from nearby clouds (HII regions). The WIM constitutes most of the mass of the ionized gas ($10^9 M_{\odot}$) in the Milky Way ([Tielens, 2005](#)) and has a characteristic low density of ($\sim 0.1 \text{ cm}^{-3}$) and typical temperatures of $\sim 8000 \text{ K}$. It can be observed through optical and UV absorption lines against background sources, or through recombination lines in emission.

- **Hot Ionized Medium (HIM):** or coronal gas, these are shock-heated regions produced by supernova explosions, where hydrogen ionized by collisions with electrons. The characteristic temperatures are extremely high ($10^5 - 10^7$ K) and the densities are low ($\sim 10^{-3} \text{ cm}^{-3}$), filling approximately half of the volume of the galactic disk (Draine, 2011). This gas phase cools via both a Bremsstrahlung continuum and line electronic transitions in the far-UV and X-ray wavelength regions. Some slightly less energetic regions are revealed by absorption lines such as O VI, C IV and NV (e.g., Jenkins & Meloy, 1974; Sembach & Savage, 1992).

1.2.3 Molecular gas

Molecular gas (H_2) is found in the coldest ($\sim 10 - 20$ K) and densest ($n \geq 10^2 - 10^3$ and up to 10^8 cm^{-3}) phase of the ISM. It is predominantly structured in cold dense giant molecular clouds (GMCs), mostly gravitationally bound. On average, it contains as much mass as the atomic phase for star-forming galaxies and it is the main component in mass in most of the inner regions of spirals (Young & Scoville, 1991). While ion-molecule reactions can generally explain the abundance of most of the observed molecules in the ISM, the most abundant one (H_2) needs to be formed in high densities through 3-body reactions, on the surface of dust grains. When molecular hydrogen forms, the energy excess is absorbed by the dust grains, and is later employed in taking the molecule back to the gaseous phase. Dust not only acts as a catalizer of these reactions, but it also shields H_2 from UV radiation. The dominant heating mechanism for most of the molecular hydrogen are cosmic rays, whereas cooling is mainly driven by the rotational transitions of the CO molecule (Tielens, 2005). Denser regions also show cooling from other molecules such as H_2O and O_2 .

Molecular emission can be classified in three types of transitions: electronic, vibrational and rotational transitions. The characteristic low temperatures of molecular clouds ($\sim 10 - 20$ K) however, only allow for rotational transitions of molecules to take place in this phase. Rotational transitions are caused by the change in angular momentum in a molecule, which for a diatomic molecule is given by

$$(1.2) \quad E_J = \frac{\hbar^2}{2\mu R_0^2} J(J+1),$$

where \hbar is the reduced Planck constant, μ is the reduced mass, R_0 is the equilibrium distance and J is the quantum rotational number. H_2 is a homo-nuclear diatomic molecule

and as a result, is a very poor emitter of radiation by rotational transitions² because there is no change in its dipolar moment. Only in very hot regions which are affected by shocks it is possible to directly observe emission due to vibrational transitions of H₂; however these conditions are not representative of the general state of the bulk molecular gas found in the ISM. Thus, there is a need to find other molecules which, although far less abundant, can trace the H₂ content. In that regard, the ¹²CO molecule has been essential to study the distribution and physical conditions of the molecular gas in our Galaxy. Some of the characteristics that make it an ideal tracer are:

- It is the most abundant molecule after H₂ ([CO/H₂] ~ 10⁻⁴).
- It is a resistant molecule, with a photodissociation energy of about 11.2 eV.
- It is easily observed through its rotational transitions in the sub-mm regimes.
- Its dipole moment is small, which makes rotational transitions easily thermalized for the typical densities found in molecular clouds. Its critical density is $n_{\text{crit}} \sim 5 \times 10^2 \text{cm}^{-3}$.
- ¹²CO has isotopologues with observable transitions with significantly lower optical depth (e.g. ¹³CO and C¹⁸O). These isotopologues are extremely useful to study physical parameters of the clouds, and in particular to quantify column densities (see Section 1.3.2).

Because of its high abundance, and the low energies needed to excite the ¹²CO rotational transitions, the cooling of molecular gas at low densities ($n \sim 10^2 \text{cm}^{-3}$) is dominated by the ¹²CO rotational emission lines. However, as we describe in Section 1.3, much higher densities can be found in substructures within molecular cloud complexes. At densities of $n \sim 10^3 \text{cm}^{-3}$, carbon monoxide isotopologues such as ¹³CO and C¹⁸O start contributing to the cooling. In some cases, the emission coming from these two molecules can be comparable to that of ¹²CO because the latter is optically thick. At even higher densities ($n \geq 10^3 \text{cm}^{-3}$) the importance of cooling by the CO isotopologues diminishes, and other molecules with higher critical densities, such as HCN, are needed to trace the densest regions inside molecular clouds.

An additional challenge when using tracers of H₂ is that some conversion factor is needed in order to translate observed integrated CO intensities to H₂ column densities.

²There is only a very weak contribution from the non-dipolar terms.

We relate the molecular gas column density and mass to the ^{12}CO (1-0) emission line via

$$(1.3) \quad N_{\text{H}_2} [\text{cm}^{-2}] = X_{\text{CO}} I_{\text{CO}} [\text{K km s}^{-1}]$$

$$(1.4) \quad M_{\text{H}_2} [M_{\odot}] = \alpha_{\text{CO}} I_{\text{CO}} [\text{K km s}^{-1} \text{pc}^2]$$

In the local Galaxy environment, a canonical $X_{\text{CO}} = 2 \times 10^{20} \text{ cm}^2 (\text{K km s}^{-1})^{-1}$ was derived (e.g., [Solomon et al., 1987](#); [Strong & Mattox, 1996](#)), which in turn implies $\alpha_{\text{CO}} = 4.36 M_{\odot} (\text{K km s}^{-1} \text{pc}^2)^{-1}$ ³. The values calculated in the disks of nearby, star-forming galaxies agree with the Galactic value, with variations of about an order of magnitude ([Bolatto et al., 2013b](#); [Sandstrom et al., 2013](#)). However X_{CO} is expected to depend on the molecular cloud properties, such as density, temperature, turbulence or metallicity (e.g., [Wolfire et al., 2010](#); [Shetty et al., 2011](#)). As a result, the X_{CO} factor is sensitive to the radiative processes and gas chemistry and, therefore, can vary across individual galaxies and from galaxy to galaxy (e.g., [Downes & Solomon, 1998](#); [Papadopoulos et al., 2012](#); [Sandstrom et al., 2013](#)). In particular, there are some circumstances where the proportionality between the CO luminosity and molecular mass does not hold:

- Low-metallicity systems. In regions with low metallicity ($Z < 0.5 Z_{\odot}$, [Bolatto et al., 2013b](#)) the dust-to-gas ratio is lower and CO cannot shield as effectively. As a result, a larger fraction of gas within molecular clouds is not associated with the CO emitting region, which becomes smaller and pushed inside the cloud. Since the total amount of H_2 does not change because it can self-shield, but the CO emission decreases, larger X_{CO} factors are found in metal-poor environments such as the Magellanic Clouds ([Mizuno et al., 2001](#); [Fukui et al., 2008](#)).
- Gas motions not related to self-gravity. One of the key assumptions to use the CO-to- H_2 proportionality is that the velocity dispersion of the gas is a reflection of its self-gravity. Some types of galaxies such as starbursts and (U)LIRGs are very rich in gas, and they can maintain a diffuse phase of intercloud molecular medium that is good at emitting in CO. However this medium not only experiences its own gravitational effects, but also the combined effect from the gas, stellar and dark matter potential well. Velocity dispersions are found to be significantly larger, but it does not arise from a larger H_2 repository, which gives rise to lower X_{CO} factors (e.g., [Downes & Solomon, 1998](#); [Papadopoulos et al., 2012](#)).

³This value already includes a 36% contribution from helium to the mass according to its cosmological abundance.

Lower X_{CO} factors have also been derived in the centers of some normal, star-forming galaxies such as the Milky Way. In these environments a combination of effects may take place: their temperatures are usually higher, which makes CO emission brighter for a fixed amount of total molecular gas; and their observed velocity dispersions are large. This occurs because galaxy centers contain large amounts of molecular gas, therefore some of it can originate in a more diffuse phase, and also suffer a larger effect from the stellar gravitational potential (Bolatto, 2015).

1.2.4 Additional components of the ISM

So far we have focused on the main physical properties of the gaseous phases of the ISM. However, it is also important to comment on the presence of other components for a general description of the ISM: interstellar dust, cosmic rays and magnetic fields.

1.2.4.1 Dust

Interstellar dust grains are solid particles with a characteristic size of $\sim 0.1 \mu\text{m}$, mainly composed of dielectric and refractory materials (Draine, 2003). Its main observational effects are the extinction of stellar light, reddening and interstellar polarization. In our Galaxy the typical dust-to-gas mass ratio is about 1%, which means it comprises roughly 0.1% of the total baryonic mass. Even though its content may seem insignificant, it absorbs about 30-50% of the starlight and then re-radiates in the far infrared as dust continuum emission. Dust grains are a key element for molecular chemistry in the ISM. They reduce the UV stellar radiation, preventing molecular photodissociation. They also constitute the formation sites for molecules, and are the main channel for the H_2 formed in the ISM. It further controls the temperature of the ISM: because of its importance for forming molecular hydrogen and its pre requisite for chemistry, dust is very important for gas cooling; and dust itself is a main coolant of the ISM. In addition, it also provides a heating mechanism through the photoelectric effect in dust grains (Draine, 2003; Tielens, 2005, and references therein).

The existence and physical properties of dust grains can be inferred from extinction curves, which can be built by comparing spectra of pairs of stars of the same spectral type, one being obscured by dust. It is possible to obtain information about the dust components by analyzing different wavelength domains: while molecular bands from polycyclic aromatic hydrocarbons (PAHs) contribute to most of the emission at shorter

wavelengths ($\sim 10\mu\text{m}$), longer infrared wavelengths ($\gtrsim 20\mu\text{m}$) are dominated by the thermal continuum emission from cold dust grains.

Observationally, dust grain formation occurs in the atmospheres of Red Giant stars and Planetary Nebula envelopes and Novae. On the other hand, dust destruction occurs when the grains collide with high-velocity ions produced in warmer phases of the ISM; this process is known as sputtering and is typically a result of supernova shocks. Modeling the formation/destruction of interstellar dust grains is an active topic: currently models predict that grains in the Milky Way should be destroyed by SNe ($\sim 10^8$ yr, [Seab, 1987](#)) much faster than they are produced by stellar ejecta ($\sim 10^9$ yr, [Tielens et al., 1994](#)).

1.2.4.2 Cosmic rays

Cosmic rays are high energy particles, mostly protons at all energies, but also electrons and ions. They are a crucial component in the ISM since they are a source of ionization and heating of the gas, therefore they can initiate and affect the chemistry of the ISM.

The interactions of cosmic rays with the other ISM components can be analyzed according to their kinetic energy, which comes mainly from supernovae explosions (about 10% of the ejecta energy). High-energy (1-10 GeV) cosmic-ray protons interact with the interstellar gas giving rise to gamma rays with energies $\gtrsim 50$ MeV. These gamma rays can be observed and used to trace back the distribution of cosmic rays in the Galaxy. Low-energy cosmic rays ($\lesssim 100$ MeV) are more important as a heating source of the ISM via ionizing collisions, therefore determining the cosmic ray ionization rate is of fundamental importance.

Their flux, however, has proven to be difficult to directly determine by observations because it needs to be corrected by solar wind effects, which can be rather uncertain ([Webber & Yushak, 1983](#)). This rate can also vary among galaxies: in the Milky Way it is estimated to be about $\sim 10^{-17} \text{ s}^{-1}$. This is a mean value, however there are physical mechanisms that can drive higher values such as the compression of magnetic fields in dense star-forming clouds (up to 10^{-14} s^{-1} , [Pellegrini et al., 2007, 2009](#)), yielding CO equilibrium temperatures of ~ 100 K. Large scale variations in diffuse gas also exists ($\sim 10^{-12} \text{ s}^{-1}$, [Padoan & Scalo, 2005; Bayet et al., 2011](#)). These variations introduce potential systematic uncertainties in the determination of the X_{CO} conversion factor, and therefore in the molecular gas mass.

1.2.4.3 Magnetic fields

Magnetic fields are a major energy and pressure agent in the interstellar medium of galaxies. Not only may they affect the gas flow in spiral arms, bars and in galaxy halos; they play a central role in the onset of star formation by removing angular momentum from the protostellar cloud during collapse. In addition, they also control the density and distribution of cosmic rays.

Galactic magnetic fields can be observed in several ways: 1) in the optical range, due to polarization by interstellar dust; 2) polarized infrared emission by aligned dust grains; 3) Zeeman splitting of radio spectral lines; and 4) synchrotron emission emitted by cosmic rays. This last technique can also be used to observed distant galaxies. In the Milky Way, magnetic fields are about $2 - 8 \mu\text{G}$, and its intensity depends on the ISM density as $B \sim n^\alpha$, with $\alpha \sim 1/3 - 2/3$. They contribute significantly to the total pressure, balancing the ISM against gravity. In particular, the magnetic field strength can reach values of $B \simeq 30 \mu\text{G}$ at $n \simeq 10^4 \text{cm}^{-3}$.

1.3 Properties of Molecular Clouds

Among the five gaseous phases of the ISM described in Section 1.2, stars form out of the coldest and densest one: the molecular gas. As molecular gas gets formed out of neutral atomic phase, its density increases and gravity is the dominant force helping the contraction. The organization of this gas results in more massive and roughly self-gravitating objects known as Giant Molecular Clouds (GMCs, [Sanders et al., 1985](#)), which are typically distributed around the mid-plane of galaxies. The boundaries chosen to delimit molecular clouds are typically defined by using a threshold of low-J CO emission, or alternatively, a level of extinction due to background stars. Increasing resolution has continued to reveal increasing complex substructure within molecular clouds (e.g., [Allers et al., 2005](#); [André et al., 2010](#); [Molinari et al., 2010](#); [Pety et al., 2017](#)), as we illustrate in Figure 1.2.

A GMC complex is well detected in ^{12}CO and shows characteristic masses of $\sim 10^4 - 10^6 M_\odot$ and sizes of about tens of parsecs ([Blitz, 1993](#)). Its environment is dense ($n \sim 50 - 500 \text{cm}^{-3}$) and cold ($T \sim 10 \text{K}$) enough so that denser substructures can form and collapse in a hierarchical way. Therefore GMCs can contain various regions where star formation can occur. These overdense regions within molecular clouds are also known as star-forming *clumps*: they are self-gravitating objects which concentrate most of the

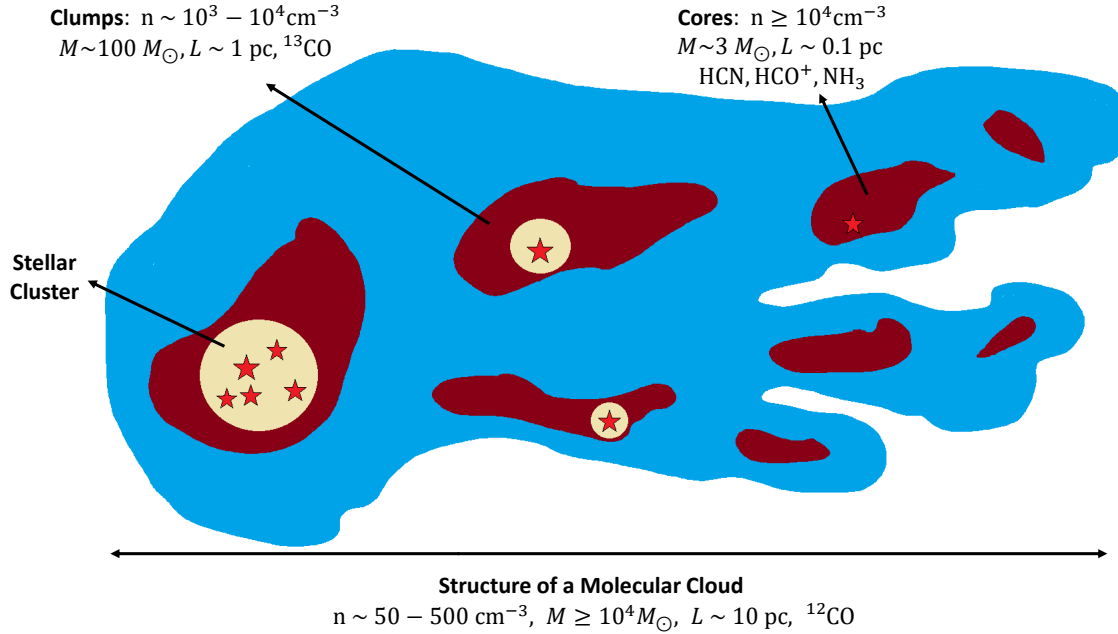


FIGURE 1.2. Qualitative picture of a molecular cloud’s substructure as inferred from the different tracers used to probe the distinct density regimes where star formation takes place.

mass of the cloud (Bertoldi & McKee, 1992). Their typical densities are of the order of 10^3 cm^{-3} and linear size scales of $\sim 1 \text{ pc}$.

High resolution surveys within nearby Galactic clouds have revealed a highly structured filamentary morphology in both $^{12}\text{CO}(1-0)$ and $^{13}\text{CO}(1-0)$ (Taurus, Goldsmith et al., 2008) and in thermal dust emission (Aquila and Polaris, André et al., 2010; Molinari et al., 2010). Along the filaments, compact and small ($\sim 0.1 \text{ pc}$) structures defined as *cores* were found at very high densities ($n \geq 10^4 - 10^5 \text{ cm}^{-3}$), where single stars can form (prestellar cores). Cores which do not show evidence of star formation are also called starless cores.

Molecular clouds are surrounded by atomic regions known as photodissociation or photon-dominated regions (PDRs, Hollenbach & Tielens, 1997). The energy balance and chemical processes occurring in PDRs are driven by far-UV photons coming mainly from the interstellar radiation field (ISRF) or nearby, very hot stars. As these photons penetrate and dissociate the molecules in different layers of the PDRs, they create a

stratified chemical structure around the GMCs. The most external layer is characterized by the presence of ionized hydrogen (H^+) and singly ionized carbon (C^+) formed after the recombination of C^{++} with electrons. As we get into deeper layers, the H^+ recombines into HI and can eventually form H_2 (at $N_H \sim 10^{21} \text{ cm}^{-2}$) in the innermost region. In a similar way, C^+ can recombine into atomic carbon at $N_H \sim 2 \times 10^{21} \text{ cm}^{-2}$. Larger depths ($N_H \sim 4 - 5 \times 10^{21} \text{ cm}^{-2}$) are required for CO to form (van Dishoeck & Black, 1988), and this difference with respect to the lower column densities needed to form molecular hydrogen directly implies that some fraction of H_2 is not traced by CO observations. Therefore there is a layer where hydrogen is molecular but carbon is still in atomic form, which is hard to observe and has been referred to as CO-dark gas (Grenier et al., 2005).

1.3.1 Larson's relations for molecular clouds

Studying the physical properties of individual molecular clouds can further improve our knowledge about the star formation process itself. Larson (1981) was the first to analyze a comprehensive collection of local molecular clouds and complexes, ranging several orders of magnitude in size scales. He gathered observations of various molecules including CO, H_2CO and NH_3 , and characterized the following relationships:

- **Velocity dispersion - cloud size.** Larson found a power-law relation between the 3D internal velocity dispersion σ and the size of the emitting regions (L), $\sigma \propto L^{0.38}$, typical of turbulent velocity distributions. More recent work found power-law indexes of ~ 0.5 instead (Solomon et al., 1987), suggesting high compressible, supersonic turbulent motions in larger regions.
- **Velocity dispersion - cloud mass.** The second scaling law observed by Larson linked the internal velocity dispersion of clouds with their masses as $\sigma \propto 0.42 M^{0.20}$. He calculated the ratio between the kinetic and potential energy for the clouds and found that $2GM/(\sigma^2 L) \sim 1$, the expected value for clouds in virial equilibrium. He therefore concluded that most clouds were gravitationally bound and their collapse is not simply as radial free fall but supported by turbulent motions.
- **Density - cloud size.** Larson noted an anti-correlation between cloud's mean volume density and its size: $\langle n(H_2) \rangle \propto 3400 L^{-1.1}$. This last relation implies that the column density is nearly independent of cloud size (Solomon et al., 1987) and $\Sigma_{H_2} = 150 M_{\odot} \text{ pc}^{-2}$.

Large observational efforts have allowed to observe molecular clouds in other tracers and in different galactic environments. Recent studies have shown that not only the observed GMC's surface densities are not constant in our Milky Way ($\sim 10 - 200 M_{\odot} \text{pc}^{-2}$, Heyer et al., 2009) but they differ from galaxy to galaxy (Hughes et al., 2013) and vary with the dynamical environment within the same galaxy (M51, Colombo et al., 2014). New improved capabilities of observing sites such as ALMA (Atacama Large Millimeter/submillimeter Array), NOEMA (NOthern Extended Millimeter Array), GBT (Green Bank Telescope) and SMA (Sub-Millimeter Array) allow for efficient mapping of 10 – 40 pc clouds in nearby galaxies which will bring deeper insight into the physical properties of molecular clouds.

1.3.2 Measuring molecular clouds mass

As explained in Section 1.2.3, we cannot directly measure the emission from molecular hydrogen; instead we need to observe the emission from another molecular species that accounts for the mass of the molecular cloud. Generally, the molecular cloud mass is inferred from the ^{12}CO (1-0) rotational transition.

The rotational levels of ^{12}CO (and of any molecular species) can be populated through collisions with other molecules. The most common collisional partner is H_2 , but it is also possible to have collisions with H atoms and electrons. One of the main reasons why the ^{12}CO (1-0) transition is chosen to probe the molecular gas content is because of its characteristic *critical density*, n_{crit} :

$$(1.5) \quad n_{\text{crit}} = \frac{A_{ij}}{\Sigma C_{ij}},$$

where A_{ij} is the Einstein coefficient for spontaneous emission and C_{ij} is the collisional rate coefficient. The critical density describes a regime where the density of the collisional partner balances the spontaneous de-excitation. Therefore, when the gas densities are larger than the critical density, the level populations are thermalized and follow the Boltzmann distribution for a given gas kinetic temperature, recovering the local thermodynamic equilibrium (LTE). The critical density for ^{12}CO (1-0) in the optically thin limit is $\sim 5 \times 10^3 \text{cm}^{-3}$, which makes it a good tracer for the typical densities found in GMCs.

In order to get a H_2 column density estimation using ^{12}CO as a tracer, a conversion factor is needed (see Equation 1.3). The theory of conversion factors is complex, making it difficult to disentangle many physical processes in the emission of CO. Several methods

have been used to estimate its value in the Galaxy and in extragalactic sources, for a complete review we refer the reader to the work by [Bolatto et al. \(2013b\)](#). Nevertheless ^{12}CO is generally optically thick (e.g., [McKee & Ostriker, 2007](#)), therefore its brightness temperature provides an estimate of the surface temperature, but not the column density of the gas. In the Milky Way, where individual GMCs can be observed, the extension of the ^{12}CO (1-0) emission is related to the size of the cloud which encompasses the molecular mass. In that case, it is possible to estimate the mass of a molecular cloud with the virial theorem: in virialized clouds twice the internal kinetic energy equals the gravitational potential energy. For external galaxies, this argument is not directly applicable without, but we can use the scaled ^{12}CO emission assuming that it is proportional to the number of clouds in the beam, and that we are looking at Milky Way-like clouds.

When available, simultaneous observations of two carbon monoxide isotopologues -such as ^{12}CO and ^{13}CO - can also be used to estimate molecular cloud masses. In addition to LTE condition, the basic assumptions that go into the method are:

- Both isotopologues originate from the same volume, therefore they can be described using the same excitation temperature T_{ex} and similar beam filling factors.
- One isotopologue is optically thick ($\tau_{12} \gg 1$), and the other is optically thin ($\tau_{13} \ll 1$).
- The emission lines coming from the two different isotopologues have similar line profiles.

In particular for the carbon monoxide the optical depth of ^{13}CO and its column density are:

$$(1.6) \quad \tau_{13} = \ln \left(1 - \frac{I_{13}}{I_{12}} \right),$$

$$(1.7) \quad N_{13} = \frac{3 \times 10^{14}}{1 - \exp(-5.29/T_{\text{ex}})} \frac{\tau_{13}}{1 - \exp(-\tau_{13})} I_{12},$$

where I is the integrated CO line intensity (in K km/s). Because ^{13}CO remains optically thin in GMCs (except for the high-density cores, [McKee & Ostriker, 2007](#)), it is possible to obtain $N(\text{H}_2)$ by assuming a fixed H_2 -to- ^{13}CO abundance ratio. In general, the method can be applied to any pair of isotopologues and we refer the reader to Chapter 4 for more details. We derive optical depths for the general case following [Wilson et al. \(2012b\)](#), and we investigate the effect of having different beam filling factors for the pair of molecules considered.

1.3.3 The need for high critical density tracers

Molecular species with higher critical densities than that of the ^{12}CO are needed to probe the densest environments, such as clumps or cores within individual molecular clouds, where stars form. Species such as HCN, HCO^+ or CS have typical critical densities of about $10^4 - 10^6 \text{ cm}^{-3}$, and constitute, in principle, better tracers for the dense, cold fraction of the ISM. Over the past decades we have seen a large progress in (sub)millimetric, single dish and interferometric facilities, and extragalactic observations of these faint molecules are also possible. In particular this thesis work presents the first systematic sample of resolved maps of a suite of high critical density tracers in nearby galaxy disks: the EMPIRE survey (Chapters 2 and 3).

Nevertheless, these molecules are also optically thick in molecular clouds, and therefore will suffer from the same problems as the ^{12}CO when estimating column densities. In addition to that, their effective critical densities are in fact affected by their optical depth (e.g., [Shirley, 2015](#)) and therefore estimating the amount of gas which is being probed is a topic of debate. A major part of this thesis will be dedicated to the study of isotopologues of dense gas tracers (e.g., H^{13}CN , H^{13}CO^+ and HN^{13}C) and how assumptions such as on the beam filling factors or excitation temperatures can affect the interpretation of the density which is traced by these molecules (Chapter 4). A final part of this work will be devoted to study the carbon isotopic ratio in external galaxies and its variations across nearby galaxy disks (Chapter 5). This quantity remains poorly constrained but is of key importance to the determination of column densities; therefore we thoroughly discuss the physical and chemical processes contributing to its variations.

1.4 Observed Star Formation Relations

Stars constitute a large amount of the total mass of a galaxy, therefore star formation and evolution are key drivers of galactic and cosmic evolution. However, a general theory of the star formation process remains poorly constrained because of the many scales (from Mpc to astronomical units) and physical processes (e.g., turbulence, gravity, feedback, ISM dynamics, chemistry) involved.

In this attempt, we are forced to take a more phenomenological approach and make empirical prescriptions of the star formation rate in external galaxies and in our own Milky Way. In that regard, the molecular phase of the ISM is key to understand the onset and evolution of the star formation process in galaxies, as described in Sections

1.2 and 1.3. The following questions remain fundamental in astrophysical research: (1) *How does the gas turn into stars?* (2) *How does the gas content of galaxies change with cosmic time?* (3) *How are the building blocks for star formation affected by the galaxy environment?* Currently, molecular astrophysics represents one of our best tools to study how observations of molecules correlate with the physical state of molecular clouds, and how this relates to their ability to form stars. Although the $^{12}\text{CO}(1-0)$ emission line has been extensively used to map the molecular ISM in external galaxies and trace H_2 mass (e.g., [Wada & Tomisaka, 2005](#); [Narayanan et al., 2012](#)), over the past decade we have seen significant advances in instrumentation in the sub(mm) regime. Single-dish telescopes equipped with broad band heterodyne receivers and the high sensitivity of high resolution sub-millimeter and millimeter arrays have allowed to detect up to 60 different molecular species in external galaxies⁴. These are currently helping us understand the different chemical scenarios and physical conditions in the gas of nearby galaxies.

In the following, we present a summary of the current observational picture of the star formation relations and their implications from a theoretical perspective.

1.4.1 Global Star Formation Law

Quantifying rigorously the main processes that lead to the formation of stars, from the contraction and fragmentation of molecular clouds, can only be done (up to a certain level of detail) in our Galaxy. Observations of such detail are now starting to become possible in extragalactic sources (see Section 6.2); before that, it was only possible to obtain information about entire star-forming regions or sometimes, in whole, averaged galaxies. At these large scales, most of our knowledge of star formation consists of some sort of scaling relation between the total mass of the gas that is thought to be forming stars and the rate to which this gas is converted in stars.

In order to quantify this in a galactic context, theory and observations have focused on the idea that there must be a relation between the gas density and the rate at which it can form stars. This idea was first introduced by [Schmidt \(1959\)](#), who studied how atomic gas and stars were distributed in the solar neighborhood and suggested that the rate of star formation was proportional to the square of the gas density. Later on, the work presented by [Kennicutt \(1989\)](#) and [Kennicutt \(1998\)](#) on integrated galaxies supported this idea: he targeted a sample of 61 nearby normal spirals and 36 infrared-selected

⁴<http://www.astro.uni-koeln.de/cdms/molecules>

starburst galaxies and found a tight relation between the disk-averaged gas surface density (Σ_{gas}) and the averaged star-formation rate (SFR) surface density (Σ_{SFR}) in the form:

$$(1.8) \quad \Sigma_{\text{SFR}} \propto \Sigma_{\text{gas}}^N,$$

where N is the power law index and $\Sigma_{\text{gas}} = \Sigma_{\text{HI}} + \Sigma_{\text{H}_2}$. This SFR-gas relation is what we currently know as the "Kennicutt-Schmidt law". The individual measurements of Σ_{gas} (as traced by HI and CO observations) and Σ_{SFR} (obtained from H_α luminosities, corrected for extinction) were fitted to a power-law with $N = 1.40 \pm 0.15$. Before that, many other studies also targeted Local Group galaxies (e.g., M31 and SMC, [Hartwick, 1971](#); [Sanduleak, 1969](#)) and derived $N_{\text{M31}} = 3.50 \pm 0.12$ and $N_{\text{SMC}} = 1.84 \pm 0.14$. Similar studies to [Kennicutt \(1989\)](#) and [Kennicutt \(1998\)](#), targeting observations of disk-averaged galaxies have also estimated the SFR with various tracers such as UV, radio continuum and FIR emission, and also found power-laws with $N = 0.9 - 1.7$ ([Buat et al., 1989](#); [Buat, 1992](#); [Deharveng et al., 1994](#)).

The nature of the observed non-linear relation between the SFR and gas surface densities implies that the efficiency with which gas can form stars, $\text{SFE} \equiv \Sigma_{\text{SFR}}/\Sigma_{\text{gas}}$, or the total gas depletion time, $\tau_{\text{dep}} \equiv \Sigma_{\text{gas}}/\Sigma_{\text{SFR}}$, is not constant but stars form more efficiently in high average gas surface density systems. The relation is expressed in terms of surface densities integrated along the line of sight, which is what most observations of extragalactic systems can provide, but the most fundamental relation should exist between volume densities of gas and SFR.

1.4.2 Spatially resolved Star Formation Law

After the formulation of the Kennicutt-Schmidt relation, many observational studies started using high-resolution CO maps in order to explore what physical parameters could drive this relation within galaxy environments. Azimuthally-averaged SFR and gas (e.g., [Martin & Kennicutt, 2001](#); [Wong & Blitz, 2002](#); [Boissier et al., 2003](#); [Schuster et al., 2007](#)) and point-by-point measurements (e.g., [Kuno et al., 1995](#); [Zhang et al., 2001](#); [Heyer et al., 2004](#)) in individual galaxies allowed to obtain the first results of a "resolved star formation law". These studies further agreed with a Kennicutt-Schmidt law, and derived a power-law index ranging $N = 1.2 - 2.1$. As particular examples, [Wong & Blitz \(2002\)](#) studied the relation between the SFR, derived from H_α data, and the total gas mass from HI and CO in a sample of 7 CO bright galaxies, and found that Σ_{SFR} correlated much

more strongly with Σ_{H_2} than with Σ_{HI} . In a similar way, [Schuster et al. \(2007\)](#) studied the same relation in M51 by combining HI maps with new ^{12}CO (2-1) and derived SFR from radio-continuum at 20 cm wavelength. They found a strong correlation between Σ_{SFR} and Σ_{gas} but only a weak correlation with Σ_{H_2} .

The large variation found for the power-law indices in the literature, $N \approx 1-3$, made it unsure if a unique, "global" star formation law could hold among and within galaxy disks or, on the other hand, if the power-law index N could depend strongly on the methodology employed to measure gas masses and SFRs or even on the spatial resolution. Moreover, it was unclear how the SFR should correlate with the different gas components -HI, H_2 or the total gas.

One of the most important limitations when comparing these studies is the different prescriptions used to determine star formation rates and the corrections for dust extinction. Studying external galaxies in a consistent way was indispensable and large multi-wavelength surveys represented a major step forward in that regard. The SINGS survey (*Spitzer* Infrared Nearby Galaxies Survey, [Kennicutt et al., 2003](#)) mapped 75 nearby galaxies and provided IR imaging between 3.6-160 μm and 5-40 μm resolved spectroscopy. Building up on these efforts, the Key Insights on Nearby Galaxies: a Far-Infrared Survey with Herschel (KINGFISH, [Kennicutt et al., 2011](#)) used *Herschel* to produced complete maps at 70, 100, 160, 250, 350, and 500 μm for 61 nearby galaxies. GALEX NGS (Galaxy Evolution Explorer Nearby Galaxy Survey, [Gil de Paz et al., 2007](#)), obtained UV maps of more than 1000 galaxies, overlapping with SINGS. In combination with H_α ground-based observations, it was possible to trace obscured and unobscured star formation ([Calzetti et al., 2005](#); [Leroy et al., 2008, 2013](#); [Calzetti et al., 2007](#)). Following up on this work, the VLA (Very Large Array) large program THINGS (The HI Nearby Galaxy Survey, [Walter et al., 2008](#)) mapped 34 galaxies belonging to the previous surveys in the 21 cm line with high angular ($\sim 6''$) and velocity ($\sim 5 \text{ km s}^{-1}$) resolution and sensitivity. Later on, the IRAM (Institut de Radioastronomie Millimétrique) large program HERACLES (Heterodyne Receiver Array CO Line Extragalactic Survey, [Leroy et al., 2009](#)) mapped 48 galaxies in the CO 2-1 line.

For the first time it was possible to use a matched set of sensitive, high spatial resolution datasets that allowed to study regions with specific physical conditions in a large sample of nearby galaxies. [Bigiel et al. \(2008\)](#) combined the HI data from THINGS with the first CO HERACLES data to study the relationship between Σ_{gas} and the SFR, at a linear resolution of 750 pc. They studied 7 nearby ($d < 12 \text{ Mpc}$), H_2 -dominated, spiral

galaxies and found a strong non-linear correlation between Σ_{SFR} and $\Sigma_{\text{HI}} + \Sigma_{\text{H}_2}$ with $N = 1.4 - 3.1$, whereas an index ranging $N = 1.0 - 1.4$ was found when using molecular gas surface density only. Recently, many other studies have also measured the star formation rates and gas content of galaxies at resolved scales up to ~ 0.2 kpc, finding similar power law indices of $\sim 0.8 - 1.6$ (e.g., [Thilker et al., 2007](#); [Braun et al., 2009](#); [Blanc et al., 2009](#); [Verley et al., 2010](#)) when using molecular gas.

To illustrate this, Figure 1.3 taken from [Bigiel et al. \(2008\)](#), shows the star formation law obtained from resolved measurements. Two regimes can be easily identified: one where the ISM is HI dominated (low gas columns), and a second one where it is H₂ dominated (high gas columns, roughly linear correlation) and stars form at a constant efficiency $\Sigma_{\text{SFR}}/\Sigma_{\text{H}_2}$ ([Leroy et al., 2008](#); [Schruba et al., 2011](#)). The separation between them coincides with the atomic-molecular phase transition at $\Sigma_{\text{HI}} \sim 10 M_{\odot} \text{pc}^{-2}$.

Starburst galaxies are an interesting regime. They contain much more molecular gas ($10^2 - 10^4 M_{\odot} \text{pc}^{-2}$) and show larger Σ_{SFR} up to $\sim 1000 M_{\odot} \text{yr}^{-1} \text{kpc}^{-2}$ than normal nearby galaxies, which would result into a fast depletion of the gas⁵ and starburst galaxies would constitute a transient phenomena. Recent work by [Daddi et al. \(2010\)](#) and [Genzel et al. \(2010\)](#) suggest that this interpretation depends on the chosen conversion factor X_{CO} . Lower X_{CO} factors for starbursts galaxies (see Section 1.2.3) would keep the same slope in the Kennicutt-Schmidt relation, but the galaxies would be systematically offset suggesting an independent starbursts relation with enhanced SFEs.

1.4.3 The Milky Way perspective

The Milky Way offers an interesting perspective to study scaling relations. In contrast with extragalactic studies where measurements of star formation rates and total gas content are limited to scales of hundreds of parsecs or more, observations in our Galaxy can be compared directly to the individual molecular clouds and dense clumps where star formation takes place. However, only recently we have started to study scaling relations and SFR indicators in the context of the Milky Way, thanks to the on-going large-scale surveys of molecular clouds.

Spitzer imaging of nearby molecular clouds has made possible the determination of SFR by counting individual young stellar objects (YSOs), a method that accounts for low-mass star formation, invisible to most tracers used to derive SFR in extragalactic sources

⁵ ~ 100 Myr, in comparison with the typical ~ 2 Gyr found for normal galaxies ([Leroy et al., 2013](#)).

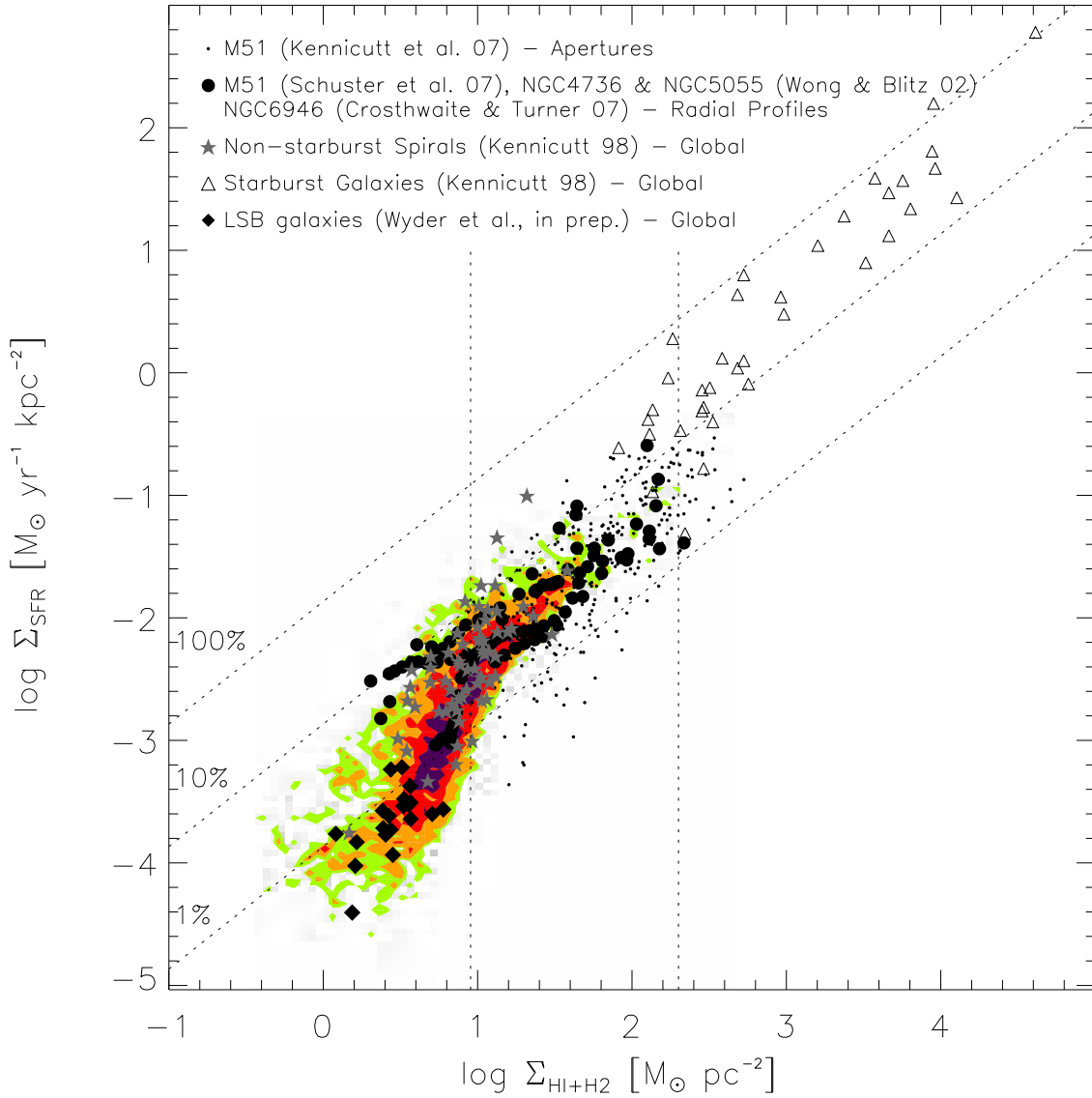


FIGURE 1.3. Figure taken from Bigiel et al. (2008), showing the relation between star formation rate and total gas (atomic and molecular) surface densities for various datasets. Coloured regions show measurements from subregions of the SINGS galaxies, together with individual apertures corresponding to M51 (small black dots, Kennicutt et al., 2007). The radial profiles from M51 (Schuster et al., 2007), NGC 4736 and NGC 5055 (Wong & Blitz, 2002), and NGC 6946 (Crosthwaite & Turner, 2007) are shown as black filled circles. The disk-averaged measurements from Kennicutt (1998) are overplotted as gray stars for the 61 normal spiral galaxies, and as open triangles for the 36 starburst galaxies. The data from Wyder et al. (2009) (filled diamonds) show global measurements from 20 low-surface-brightness galaxies.

(e.g., H_α , UV, FIR). With the idea that the Milky Way results could help us understanding the observed relations in nearby galaxies described above, several studies have analyzed the SFR-gas scaling relations in Galactic clouds and dense clumps. Using extinction maps from the *Spitzer* cores to disks survey (c2d, [Evans et al., 2003](#)) to derive mean surface densities of nearby clouds, [Evans et al. \(2009\)](#) found that they lay much further above the relations derived by [Kennicutt \(1998\)](#) and [Bigiel et al. \(2008\)](#). Extending this dataset with clouds contained in the Gould’s Belt (GB) Legacy project ([Spezzi et al., 2011](#); [Peterson et al., 2011](#)) and a set of ~ 50 dense Galactic clumps from [Wu et al. \(2010\)](#), [Heiderman et al. \(2010\)](#) extrapolated this study to smaller scales by selecting only Class I and flat spectral energy distribution YSOs, still connected to their birthplace. Their main results can be summarized in Fig. 1.4, where the data corresponding to Galactic clouds, YSOs and dense clumps are shown in comparison to the extragalactic relations. They find evidence for a threshold of star formation, $\Sigma_{\text{th}} = 129 \pm 14 M_\odot \text{pc}^{-2}$, above which the SFR-gas scaling relation is linear, but far above the extragalactic ones. Below Σ_{th} the surface density of SFR increases rapidly with increasing surface density of gas.

Moreover, in an independent approach, [Lada et al. \(2010\)](#) also used the YSO counting method to determine SFRs in a sample of nearby clouds. Similarly to [Heiderman et al. \(2010\)](#), they found that the SFR per cloud mass linearly scales with the cloud mass above a surface density contour $\Sigma_{\text{th}} = 116 \pm 28 M_\odot \text{pc}^{-2}$. These and other studies (e.g., [Onishi et al., 1998](#); [André et al., 2010](#)) have shown that Σ_{SFR} correlates strongly with gas above a threshold of $\Sigma_{\text{th}} \sim 125 M_\odot \text{pc}^{-2}$, which also coincides with reasonable surface levels of star-forming clumps. The slopes found for the observed relations in the Galactic studies are very similar to those found in extragalactic, however the SFRs computed for Galactic regions are much higher. This offset may be due to the fact that extragalactic studies cannot directly measure the same scales as in Galactic star-forming regions, and use tracers as CO to identify the molecular gas. Even in spatially resolved studies, any beam will also contain a fraction of molecular gas that is not directly forming stars, but is instead diffuse. This can easily increase the total CO emission that is identified as star-forming gas.

As a conclusion, the process of star formation must be localized in the high surface density regions of molecular clouds. In that regard, we need observations of dense gas tracers such as HCN in nearby galaxies, that can directly probe the star-forming gas outside our Milky Way, where we would expect to see similar relations to those found for local clumps. In Section 1.4.4 we see that there seems to be a unique relation between SFR and the dense gas mass traced by HCN that extends across all scales and SFR

regimes.

1.4.4 The Dense Gas regime

The cold, dense regions where star formation takes place are better traced by molecules with higher dipole moments such as HCN or HCO⁺, since they are collisionally excited into emission at higher densities. The pioneer work by [Gao & Solomon \(2004\)](#), followed by many recent studies using dense gas tracers (e.g., [Graciá-Carpio et al., 2006, 2008](#); [García-Burillo et al., 2012](#)), have highlighted the super linear relation observed between the total SFR, as traced by the total infrared emission, and the luminosity of high critical density lines (e.g. HCN). This study targeted entire galaxies or integrated bright galaxy centers across a large range of galaxy types from normal spirals to (ultra)luminous infrared galaxies ($L_{\text{TIR}} \geq 10^{11}L_{\odot}$, hereafter (U)LIRGs). In the Milky Way, [Wu et al. \(2005\)](#) extended this IR-to-HCN correlation down to individual star-forming molecular clouds and dense cores. In addition, the work by [Lada et al. \(2012\)](#) analyzed nearby molecular clouds and measured SFRs by counting young stellar objects (YSOs) in gas above a threshold surface density. They find the same correlation cited above and attribute the observed scatter to different dense gas fractions within molecular gas.

The combined results obtained for the Milky Way and extragalactic sources, as summarized in Figure 1.6 by [Bigiel et al. \(2016\)](#), suggest that the global SFR is driven by the amount of dense gas in both individual molecular clouds and entire galaxies. In that regard, understanding how gas properties, first and foremost density, are related to average cloud properties across galaxy disks is fundamental. Multi-line spectroscopy has become an extremely useful tool to investigate the density of gas across galaxies: a suite of lines with a range of density sensitivities and the ratios among these lines (e.g., HCN-to-CO) allow us to trace changing distributions of gas densities. Systematic observations of normal galaxy disks constitute an excellent laboratory to probe different environmental galactic conditions (e.g. densities gradients, pressure, gravitational potential, radiation fields) and can provide deep insight into the star formation process.

Until very recently, however, resolving high-critical density tracers in large sets of individual regions in nearby galaxies remained extremely challenging, given the weakness of their emission lines, typically ~ 30 times fainter than the CO (1-0) emission line (e.g., [Usero et al., 2015](#); [Bigiel et al., 2016](#)). There is recent evidence that the relationship between high critical density lines, CO emission, and star formation is complex and remains poorly understood. In a study which targeted whole bright galaxies,

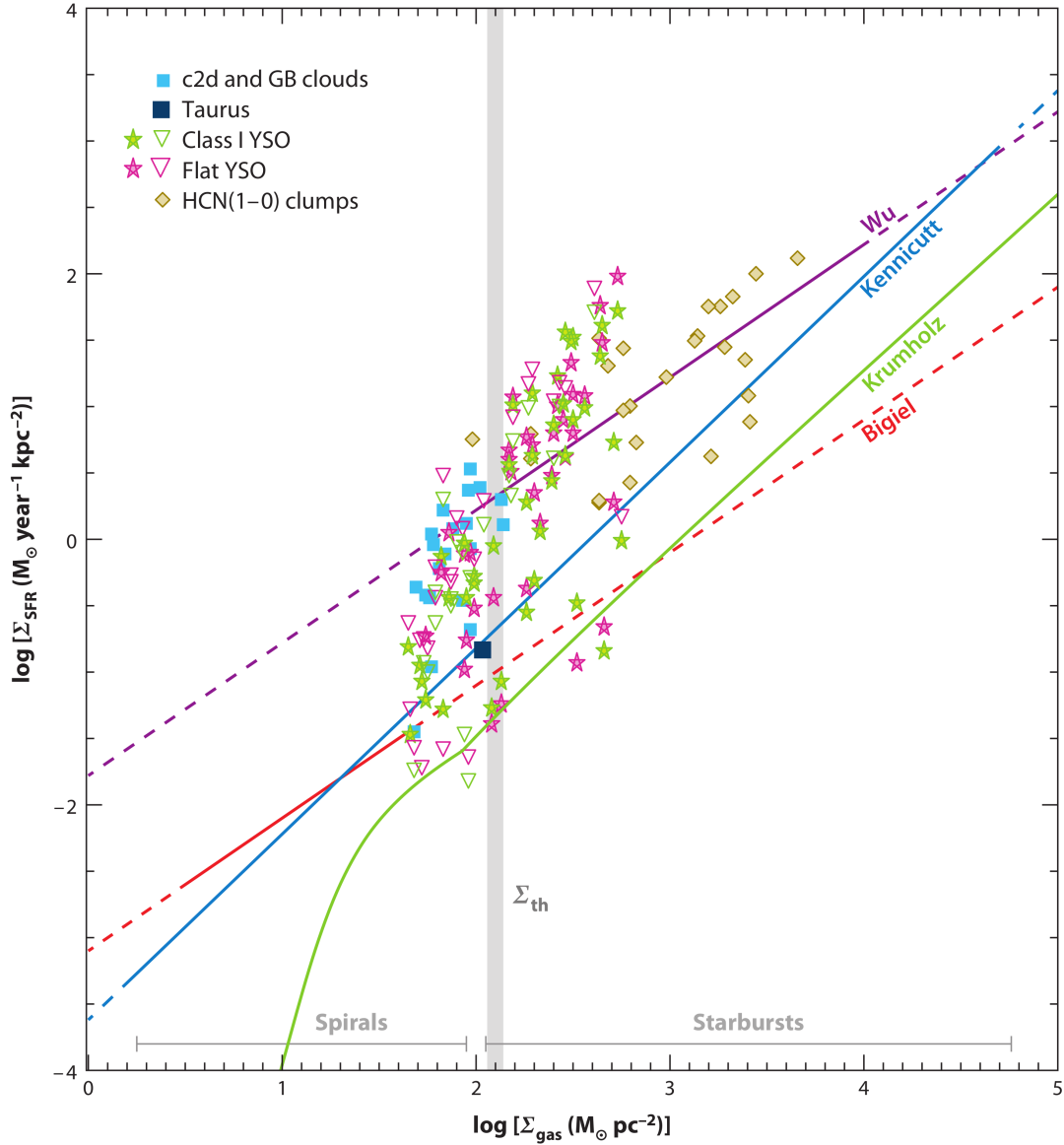


FIGURE 1.4. Figure taken from [Kennicutt & Evans \(2012\)](#) and adopted from [Heiderman et al. \(2010\)](#). The extragalactic observed scaling relations for total molecular gas ([Kennicutt \(1998\)](#), blue line; [Bigiel et al. \(2008\)](#), red line), and dense molecular gas ([Wu et al., 2005](#), purple) are shown together with the predicted total gas star formation law ([Krumholz et al., 2009](#), light green) in comparison with the Galactic total c2d and GB clouds (cyan squares), YSOs (green and magenta stars) and massive clumps (dark yellow diamonds).

[García-Burillo et al. \(2012\)](#) showed that there is a variation in the SFE_{dense} between starburst and normal spiral galaxies. Furthermore, the individual pointings from [Usero et al. \(2015\)](#) across 30 different galaxy disks, and the dense gas mapping of M51 ([Chen et al., 2015](#); [Bigiel et al., 2016](#)) show that the dense gas fractions and the efficiency of dense gas vary systematically across galaxy disks.

These results, together with observations of lower SFE in the CMZ of the Galaxy (e.g., [Longmore et al., 2013](#)) suggest that there may be an environment-dependent efficiency of star formation in dense gas, contradicting theories which argue for a universal gas density threshold for star formation. Other environmental variables (pressure, stellar surface density, shear, etc.) can play an important role, therefore observations of different dense gas tracers across entire disks of normal, star-forming galaxies have the potential to solve these issues.

However, caution must be taken when working with tracers of dense gas. The intensity of the HCN (1-0) emission line is only an approximation to the dense gas content and the definition of "dense cores" is not precise. Dense gas tracers may allow to detect gas above a higher density threshold, but they suffer from the same caveats as the CO molecule, regarding physical conditions. They are optically thick at low total column densities and they are even more sensitive to photodissociation processes, and so more dependent on metallicity (e.g., [Rosolowsky et al., 2011](#)). Furthermore, there is evidence that the observed correlation may not simply be because star formation occurs in the denser gas, but also because HCN emission can be enhanced by high X-ray radiation and IR pumping ([Aalto et al., 2007](#)). Cosmic rays can also free electrons, increasing the formation rates of many molecular species including HCN, and significantly altering its relative abundance to CO and H₂ ([Pellegrini et al., 2009](#)).

The first results and data products of the EMPIRE Nearby Galaxy Dense Gas Survey are presented in this thesis. Chapter 3 describes how these environmental quantities measurements systematically relate to the dense gas content of a galaxy and the efficiency with which it forms stars on kpc scales. This work also presents a detailed study of the emission coming from high density tracers. The understanding of the relationship between star formation rates and dense gas depends strongly on the conditions under which dense gas tracers' emission peaks. Dense gas emission does not exclusively come from gas above some threshold density, that is a too simple picture; in reality, the emissivity of a molecule depends on several factors such as the line critical density, its optical depth, temperature and abundance. Chapter 4 addresses the topic of how optical depth effects can modify the effective critical density of the employed molecules. At the same

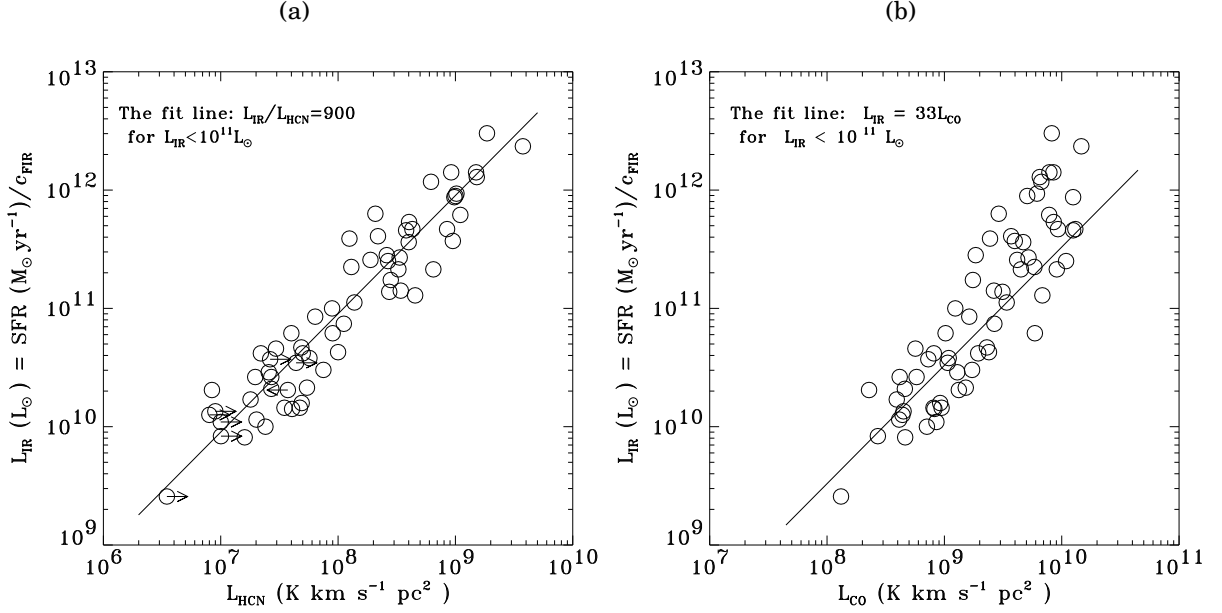


FIGURE 1.5. The correlation between IR and HCN 1-0 (a) and CO 1-0 (b) luminosity of 65 normal-disk galaxies and starbursts, taken from [Gao & Solomon \(2004\)](#). The solid line represents a linear fit of slope unity, indicating that the star formation efficiency per unit dense gas mass is roughly constant.

time, the optical depth of the dense gas lines we utilize -HCN, HCO⁺ and HNC- depends largely on the molecule filling factor and the carbon abundance ratio [¹²C/¹³C], which is large unconstrained in extragalactic systems. In that regard, Chapter 5 describes how carbon isotopologues can be employed to gauge their relative abundance due to chemistry or stellar nucleosynthesis effects.

In summary, the efforts presented in this thesis aim to answer the following questions: **(1) How do dense gas fractions and star formation efficiency of dense gas depend on galactic environment?** **(2) In which way do optical depths and abundance variations affect our interpretation of the observed dense gas?**

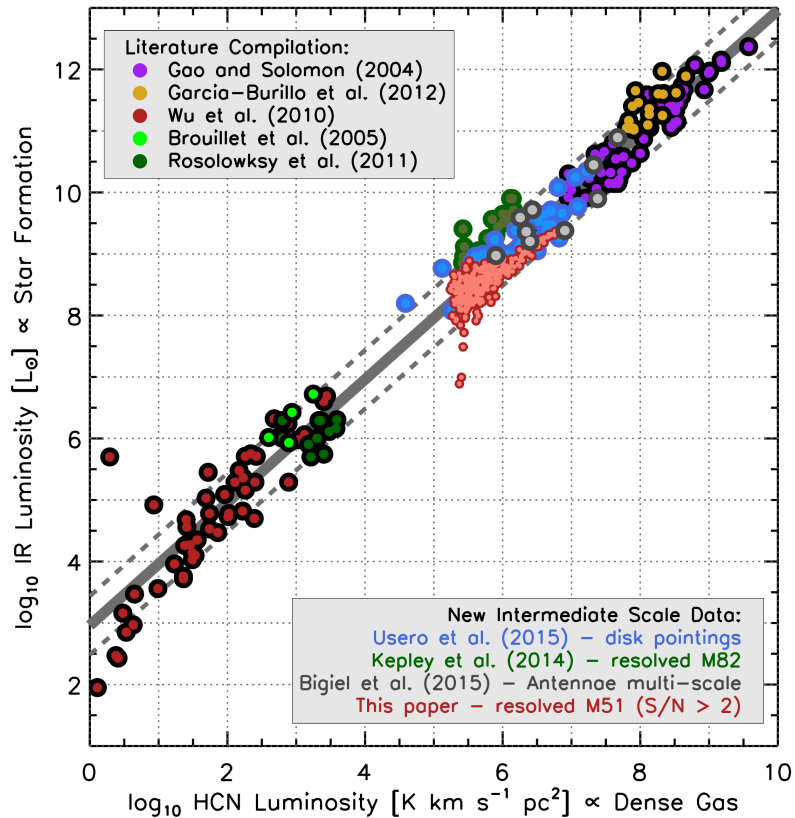


FIGURE 1.6. Figure taken from [Bigiel et al. \(2016\)](#), showing the IR luminosity as a proxy for the recent SFR as a function of the HCN luminosity, a proxy for the dense gas content. The plot shows the striking correlation between different dense gas structures, ranging from Milky Way cores to entire starburst galaxies. Recent studies targeting resolved observations of dense gas in extragalactic systems are starting to populate the regions (\sim kpc size) corresponding to large parts of galaxies.

THE EMPIRE DENSE GAS GALAXY SURVEY

This chapter presents a detailed description of the data provided by the EMPIRE survey of dense gas in nearby galaxies. The following dataset constitute the cornerstones for the analysis and results presented in this thesis, therefore this chapter emphasizes the observation procedure, data reduction and final data processing.

2.1 Survey parameters

The EMIR Multi-Line Probe of the ISM Regulating Galaxy Evolution (EMPIRE) is a large survey carried at the IRAM¹ 30-m, single-dish telescope, consisting of more than 500h of observing time. The survey was conceived to use the EMIR heterodyne receiver in order to provide full emission maps of high-density tracers such as HCN, HCO⁺ and HNC along with optically thin carbon monoxide isotopologues such as ¹³CO and C¹⁸O in the $J = 1 - 0$ transition across the disks of nine nearby galaxies to probe the physical conditions of the cold, dense star-forming gas.

2.1.1 The EMPIRE sample

The EMPIRE sample consists of well-resolved galaxies that are nearby ($d \sim 10$ Mpc), face on ($i \leq 60^\circ$) and bright enough to yield good maps of dense gas tracers. Since our main goal is to link between the physical conditions of the molecular gas to star

¹<http://www.iram-institute.org/>

formation, the 9 targets chosen for this survey (listed in Table 2.1) span a broad range of physical properties, morphological and dynamical features. The sample also covers a wide range of star formation rates ($\sim 3 - 20 \times 10^{-3} M_{\odot} \text{yr}^{-1} \text{kpc}^{-2}$, see Table 2.1). While NGC 628 and NGC 3184 show strong spiral arms, the sample also contains strong barred galaxies (NGC 2903, NGC 3627), flocculent sources (NGC 5055, NGC 6946), strong nuclear bursts (NGC 2903, NGC 4321, NGC 6946) and interacting galaxies (NGC 3627, NGC 4254, NGC 4321). These targets are all spiral galaxies drawn from the HERA CO-Line Extragalactic Survey (HERACLES, Leroy et al., 2009), which are furthermore among the best-studied local galaxies: all have existing CO (1-0) data from the BIMA SONG survey (Helfer et al., 2003), the Nobeyama Atlas (Kuno et al., 2007), and CARMA STING (Rahman et al., 2011); CO (3-2) mapping from the JCMT Nearby Galaxy Legacy Survey (NGLS, Wilson et al., 2012a); IR maps ($3.6 - 500 \mu\text{m}$) from the *Spitzer* Infrared Galaxies Survey (SINGS, Kennicutt et al., 2003), the Local Volume Legacy Survey (LVL, Dale et al., 2009) and *Herschel* (KINGFISH, Kennicutt et al., 2011), H_{α} (Kennicutt et al., 2008), GALEX UV (NGS, Gil de Paz et al., 2007), and VLA HI mapping (THINGS, Walter et al., 2008). Some of them, especially NGC 6946, present a large molecular-bright area, which is greatly beneficial to study trends with high fidelity within a galaxy disk.

This selection is therefore an excellent sample to study the dense gas emission as a function of environment across entire galaxy disks. Moreover, the observations of this large survey constitute more than ~ 600 independent lines of sight across the sample, a major improvement of more than an order of magnitude over any previous observations.

2.2 The IRAM-30m telescope

The key goal of the EMPIRE survey is to map and resolve tracers of high density molecular gas, which are directly connected to the coldest and densest structures of the ISM, in nearby galaxies; and therefore provide a deep insight into the understanding of how gas from galaxy's reservoirs can be converted into stars. In order to do that, HCN, HCO^+ and HNC are the main molecular lines selected to trace dense gas regions in nearby galaxies, the main reason being because they are the most abundant high-critical density tracers in the ISM². The frequency of the $J = 1 - 0$ emission line of these molecules is 88.63 GHz, 89.19 GHz and 90.66 GHz, respectively, and therefore they lay at $\sim 3 \text{mm}$ on the so called *radio* window.

²Their intensity is about 30 times fainter than that of the ^{12}CO

Galaxy	RA(2000.0) hh mm ss.s	DEC(2000.0) dd mm ss.s	i ($^{\circ}$)	PA ($^{\circ}$)	r_{25} ($^{\circ}$)	D (Mpc)	V_{sys} km s $^{-1}$	Metal. $12 + \log(\text{O}/\text{H})$	Morphology	$\langle \Sigma_{\text{SFR}} \rangle$ $10^{-3} M_{\odot} \text{yr}^{-1} \text{kpc}^{-2}$
(1)	(2)	(3)	(4)	(5)	(6)	(7)	(8)	(9)	(10)	(11)
NGC 628	01:36:41.8	15:47:00	7	20	4.9	7.2	659.1	8.35	SAC	4.0
NGC 2903	09:32:10.1	21:30:03	65	204	5.9	8.7	556.6	8.68	SABbc	5.7
NGC 3184	10:18:17.0	41:25:28	16	179	3.7	12.0	593.3	8.51	SABcd	2.8
NGC 3627	11:20:15.0	12:59:30	62	173	5.1	9.4	717.3	8.34	SABb	7.7
NGC 4254	12:18:50.0	14:24:59	32	55	2.5	14.4	2407.0	8.45	SAC	18
NGC 4321	12:22:55.0	15:49:19	30	153	3.0	14.3	1571.0	8.50	SABbc	9.0
NGC 5055	13:15:49.2	42:01:45	59	102	5.9	8.2	499.3	8.40	SAbc	4.1
NGC 5194	13:29:52.7	47:11:43	20	172	3.9	7.6	456.2	8.55	Sbc	20
NGC 6946	20:34:52.2	60:09:14	33	243	5.7	6.8	42.4	8.40	SABcd	21

TABLE 2.1. **Notes.** – Galaxy names (1), adopted centers (2-3) and morphological types (10) are taken as listed in NED, the NASA Extragalactic Database. The orientation parameters: inclinations (4), position angles (5) and radius of the B -band 25th magnitude isophote (6) are taken from the compilation of Leroy et al. (2012). Distances (7) adopted from a compilation by Kennicutt et al. (2011). Systemic velocities (8) are taken from Walter et al. (2008). Globally averaged metallicities (9) from Moustakas et al. (2010), except for NGC 2903 (Engelbracht et al., 2008). Average star formation rate surface density inside $0.75r_{25}$, adopted from Leroy et al. (2013).

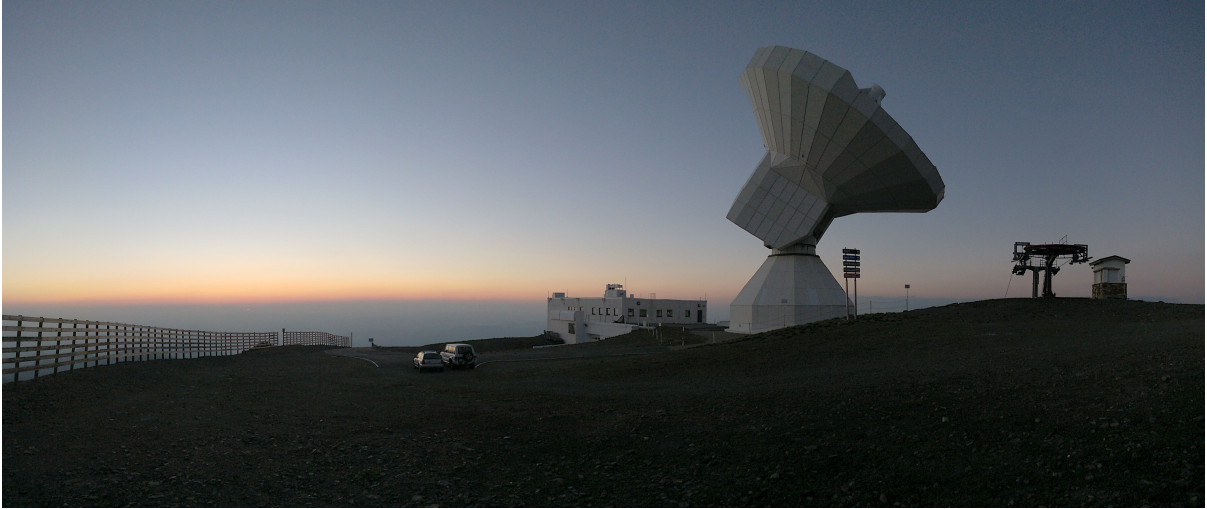


FIGURE 2.1. The IRAM 30-m single dish telescope, located in Sierra Nevada, Granada, Spain. Picture taken by M. Jiménez-Donaire during sunset in July, 2017.

Building on the previous HERACLES CO (2-1) observations, the IRAM-30m telescope (Figure 2.1) is the ideal radio telescope to carry the observations of the EMPIRE survey, because of its ability to provide well calibrated, high-quality maps of dense, cold molecular gas tracers. This radio telescope is located at an elevation of 2850 meters on Pico Veleta, in Sierra Nevada, Spain. Built from 1980 to 1984, it is a single dish parabolic antenna and one of today’s largest and most sensitive radio telescopes observing in the millimeter wavelength regime. The telescope is also equipped with a series of heterodyne receivers and continuum cameras that operate at 3, 2, 1, and 0.9 mm.

The resolution achieved using EMIR at the 30-m telescope corresponds to 1–2 kpc for the proposed sample of nearby galaxies (~ 10 Mpc). Hence, it is ideal to study systematic variations in the dense gas fraction and star formation efficiency among and within galaxies. While it averages over the detailed evolution of individual star forming regions, it allows us to extract the impact of local conditions on the time-average star formation process (e.g., [Schruba et al., 2010](#))

2.2.1 The EMIR receiver

The two most used receivers in radio astronomy are heterodyne receivers and bolometric receivers. The first ones, convert the frequency of the incoming signal from the sky (ν_{sky}) down to a lower frequency by mixing it with a reference signal generated at

the local oscillator of the system ν_{LO} . The result is an intermediate frequency signal $\nu_{\text{IF}} = \nu_{\text{sky}} - \nu_{\text{LO}}$ which can easily be amplified, sampled and sent to the spectrometers for further processing. On the other hand, bolometers simply have a resistance which is sensitive to the temperature changes due to the incoming photons from the signals. They can only record signal intensities over a range of wavelengths, therefore are only used for photometric studies. EMIR (Eight MIXer Receiver; [Carter et al., 2012](#)) is a spectral heterodyne receiver that operates in the 3, 2, 1.3 and 0.9 mm atmospheric windows, designated as E090, E150, E230, and E330, respectively. EMIR can be tuned in the broad frequency range 73 – 350 GHz. The different bands have two orthogonal linear polarization channels and are equipped with dual sideband mixers, offering 8 GHz of instantaneous bandwidth per sideband and per polarization.

For the EMPIRE survey, the EMIR receiver was set to operate in the E090 window, with the local oscillator frequency set as ~ 89.3 GHz as shown in Figure 2.2. Its flexibility allows us to obtain dual polarization observations of the dense gas tracers HCN(1-0), HCO+(1-0), and HNC(1-0) and the optically thin 1-0 lines of ^{13}CO and C^{18}O . Given that our sensitivities are driven by the bright dense gas tracers HCN, HCO^+ and HNC, a suite of slightly fainter dense gas and shock tracers such as $\text{C}_2\text{H}(1-0)$, $\text{N}_2\text{H}^+(1-0)$ and $\text{HNCO}(4-3)$ is also included in the bandpass. This setup provides a fantastic characterization of physical conditions within the molecular gas. The EMPIRE pilot program targeted the nearby galaxy NGC 5194 (M51, the so called Whirlpool Galaxy), and used a slightly different E090 configuration where the local oscillator frequency was set as ~ 88.7 GHz. This configuration allowed to capture the optically thinner isotopologues from the main dense gas tracers, H^{13}CN , H^{13}CO^+ and HN^{13}C , leaving C^{18}O unobserved for this galaxy.

Backends. The signal processing is carried by the spectral line backends connected to the EMIR E090 band. For the EMPIRE survey we employed the Fast Fourier Transform Spectrometer (FTS), consisting on a series 24 modules working at either wide (~ 200 kHz) or fine (~ 50 kHz) resolution. We used the FTS default configuration in wide mode, which yields a bandwidth of 15.6 GHz per polarization with a spectral resolution of 195 kHz, corresponding to ~ 0.5 km s $^{-1}$ for the E090 band.

2.2.2 Observing strategy

The line radiation that is normally received in radio and (sub)mm observations from the targeted source is only a small fraction of the total signal, which is commonly

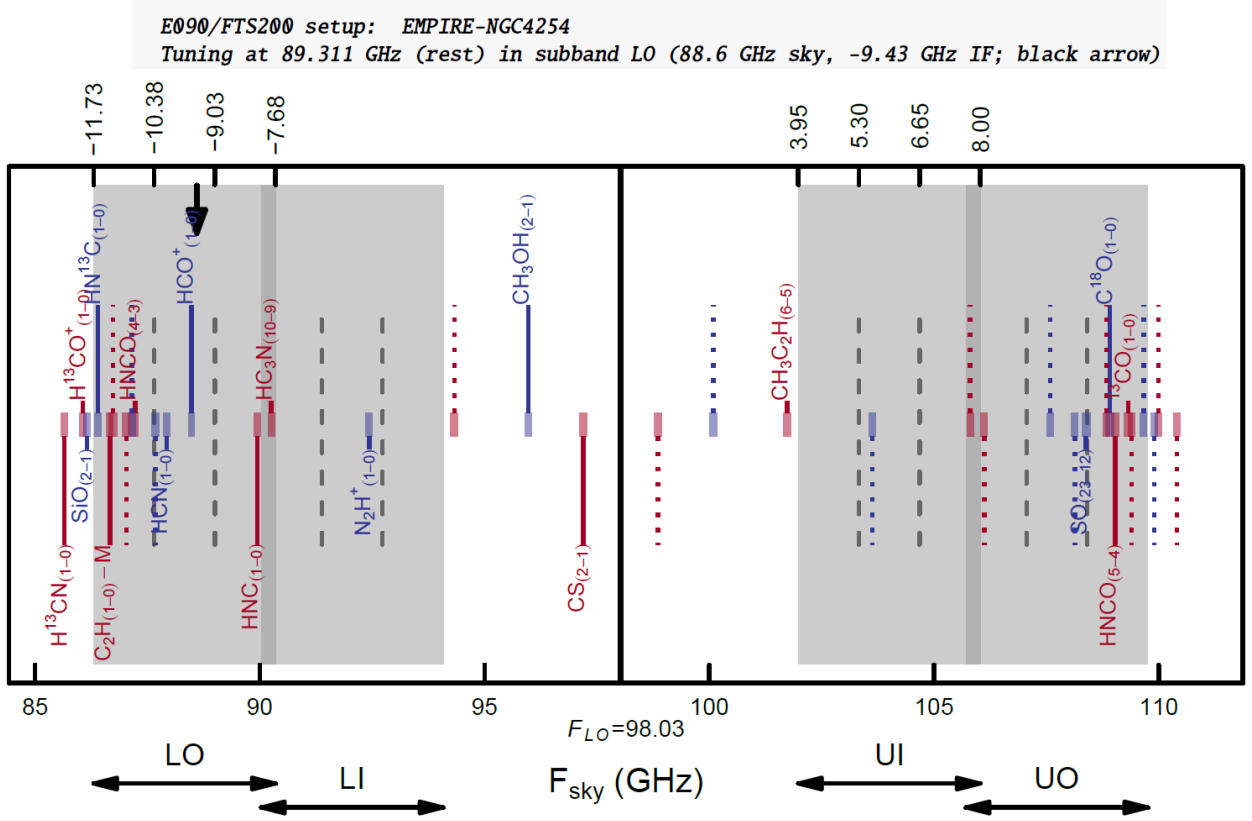


FIGURE 2.2. EMPIRE dense gas observations setup with major lines indicated. Observations simultaneously target the dense gas tracers HCN(1-0), HCO+(1-0), and HNC(1-0) as well as the (comparatively) optically thin molecular column tracers ^{13}CO and C^{18}O .

contaminated by other emitters, e.g., the ground, the atmosphere emission or the system noise. The total signal measured by the antenna, which includes the difference noise sources and the measured output is known as *system temperature*

$$(2.1) \quad T_{\text{sys}} = T_{\text{A}} + T_{\text{atm}} + T_{\text{scat}} + T_{\text{rec}} + T_{\text{cmb}},$$

where T_{A} is the *antenna temperature*, closely related to the source brightness T_{b} . The additional signal terms are the temperature of the atmosphere, T_{atm} ; the contribution from the receivers, T_{rec} ; the scattered emission from the ground into the beam path, T_{scat} and the temperature of the Cosmic Microwave Background.

A commonly used strategy to obtain the signal containing the line radiation consists of comparing the total power received when observing the source of interest (the *on*

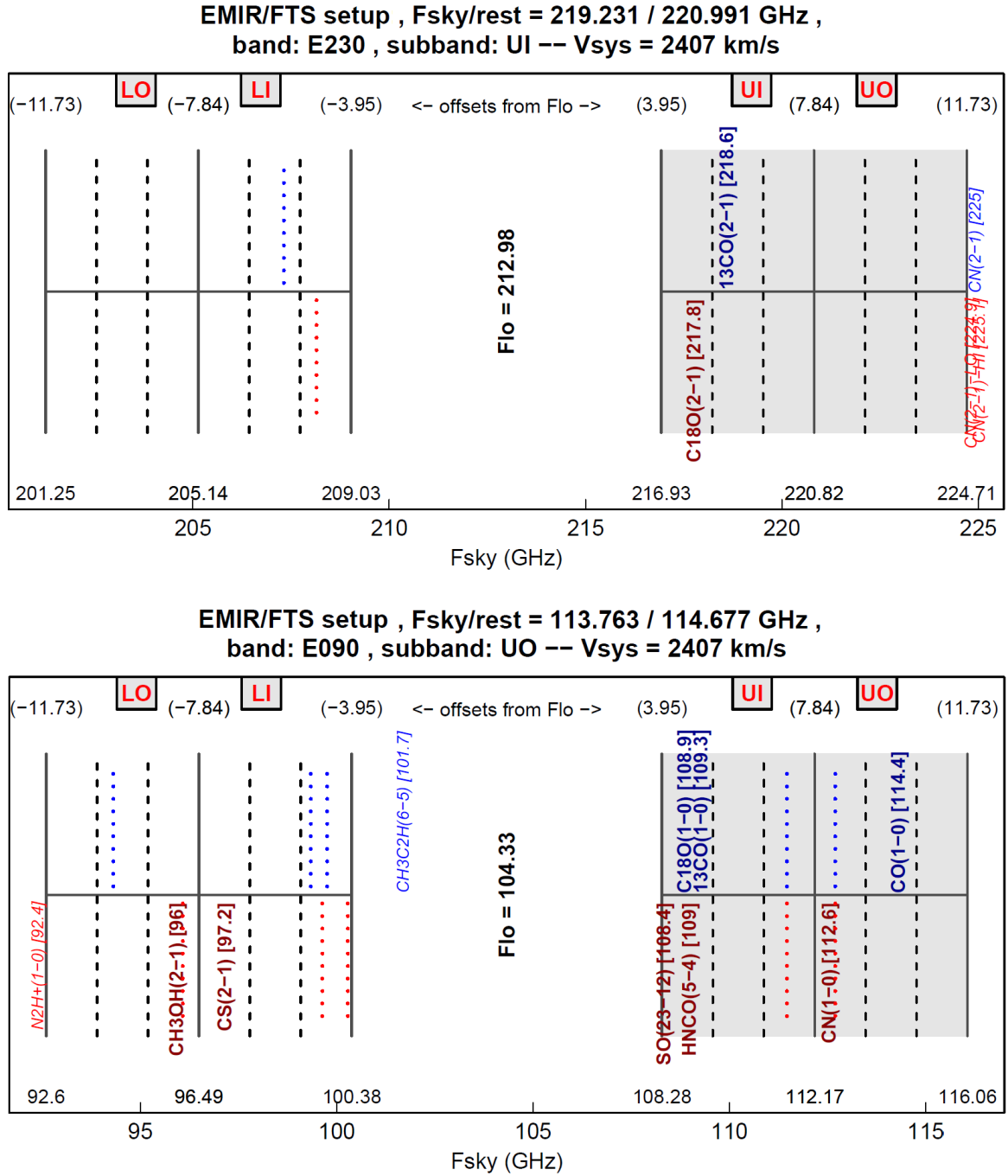


FIGURE 2.3. EMPIRE ^{12}CO (1-0) observations setups with major lines indicated. The upper sub-bands for E090 and E230 were simultaneously used to target the molecular gas tracer ^{12}CO (1-0) and the isotopologues ^{13}CO and C^{18}O in the 1-0 and 2-1 transitions.

position) and a nearby region of the sky without sources (the *off* position). This sequence of observations is known as *position switching* and, after subtraction of the signals in both positions, one can obtain the antenna temperature of the source. One important advantage of this method is that contaminating features in the spectra such as baseline ripples are less likely to appear. Broadband emission from sky, ground and continuum sources are similar, which makes these features to cancel more easily.

The observing strategy of the EMPIRE survey is slightly different, since the goal is to map large areas and the heterodyne instruments only contain one pixel. Large-scale maps are obtained by performing on-the-fly (OTF) mapping, i.e., moving the EMIR receiver over the source and scanning a strip of the sky. During each scan, we integrate and record the observed spectra in many different positions, repeating measurements at the *off* positions between scans. We map the entire galaxies by setting the scan legs parallel to each other, and then repeat these procedure in the orthogonal direction, creating a grid of spectra as illustrated in Figure 2.4. Even though each individual spectrum along the scan leg has a low signal-to-noise ratio (S/N), averaging the observed grids allows to obtain final images with great accuracy and high S/N.

2.2.3 EMPIRE dense gas observations

Most of the observations for the EMPIRE survey were carried out from December 2014 through December 2016 in 16 consecutive runs. NGC 5194 (M51) was observed in July and August 2012, as a previous pilot program for EMPIRE (Bigiel et al., 2016).

We mapped the disks of the galaxies using the on-the-fly (OTF) mapping mode, as described in Section 2.2.2. We scanned across the targeted disks at a speed of 8" per second, in order to obtain Nyquist sampled maps. The size of the fields were chosen to encompass the area where $^{12}\text{CO}(2-1)$ emission is detected in the HERACLES maps. The observed dates for the individual galaxies, the covered fields and scanning modes are shown in Table 2.3. At the beginning of each observing session focusing of the telescope was performed on planets or bright quasars and then repeated the process every ~ 3 hours, including sunset and sunrise. The telescope pointing was corrected every 1 – 1.5 hours using a point-like source close to the target galaxy. Chopper wheel calibrations were performed every ~ 15 minutes employing standard hot/cold-load absorber measurements; these are used to perform the first basic calibration and to convert the data to antenna temperature scale, as described in Section 2.3.1. Line calibrators were observed as part

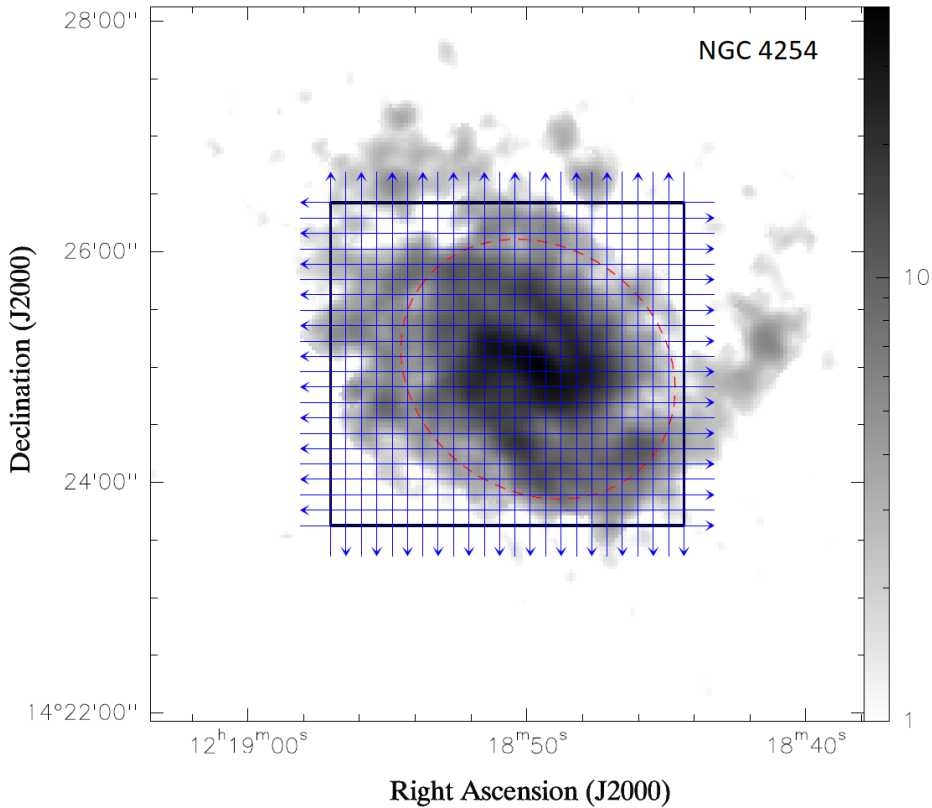


FIGURE 2.4. On-the-fly mapping strategy for NGC 4254. The gray scale map shows the ^{12}CO (2-1) integrated intensity map in units of K km s^{-1} from HERACLES. Arrows indicate the length and orientation of individual scan legs which fully sample the area of interest. The red ellipse shows the $0.5 r_{25}$ radius of the galaxy.

of EMPIRE once a day during the observing runs, and they varied by $\sim 3 - 8\%$ between observations (see Figure 2.5).

2.2.4 New ^{12}CO (1-0) observations

A key goal of EMPIRE is to measure dense gas fraction variations and relate these to local ISM conditions. As described in Section 1.3.2, the ratio of high critical density ($> 10^5 \text{ cm}^{-3}$) tracers like HCN (1-0), to tracers of total molecular material ($> 10^2 \text{ cm}^{-3}$) such as CO (1-0), is sensitive to gas density changes. Thus, e.g., HCN/CO is one of our best observational diagnostics of the dense gas fraction and so central to understand the physics of what drives gas density in galaxies. Therefore having high-quality CO (1-0) data is essential to all aspects. In that regard, EMPIRE was initially designed to rest on top of the best available CO maps: HERACLES (Leroy et al., 2009), BIMA-SONG (Helfer

et al., 2003), and the Nobeyama Atlas (Kuno et al., 2007). However, these data data have uncertain pointing and calibration, small field of view and high root-mean-square (rms) noise (0.13 K, compared to that of HERACLES of 25 mK).

In order to be uniform in our data set, we proposed to obtain new, well calibrated, high-quality maps of the CO ground transition transition using EMIR on the IRAM 30-m. We measured the distribution of the cold molecular gas across the disks of eight³ nearby star forming galaxies from the IRAM 30m large program EMPIRE, distributed in three different projects 061-15, 059-16 (PI Jiménez-Donaire). Our maps sample a similar area mapped by HERACLES in ^{12}CO (2-1) emission to guarantee that we cover a significant fraction of the optical disk and we observe the galaxy with uniform criteria, reducing and analyzing all the data using well-defined, uniform procedures. The upper 8 GHz sub-band of EMIR was set at 3mm to cover the ^{12}CO (1-0) line and the isotopologues ^{13}CO (1-0) and C^{18}O (1-0). Under good atmospheric conditions we center the remaining 8 GHz bandwidth at 212.98GHz, and so we used the 1.3 mm band, in order to capture (2-1) transition lines of ^{13}CO and C^{18}O (see Figure 2.3).

We determine our target sensitivity based on the existing ^{12}CO (1-0) maps for 2 galaxies in EMPIRE and by scaling the respective HERACLES ^{12}CO (2-1) maps for our target galaxies (assuming an average line ratio of 0.7) to achieve high signal-to-noise detections across the disks while keeping the time request modest. Thus, we aim at a noise rms of 25-30 mK (T_A) in 5.2 km s^{-1} channels (see Table 2.3 for more details about the observations). The observing procedure used was the PSW on-the-fly observing mode described in Section 2.2.2, successfully adopted for the previous EMPIRE observations.

2.3 Data reduction & processing

2.3.1 Spectral line calibration

The spectral line calibration was carried out using the the Multichannel Imaging and Calibration Software for Receiver Arrays (MIRA)⁴, which is part of the Grenoble Image and Line Data Analysis Software (GILDAS)⁵ package. The calibration procedure performed at the IRAM 30-m telescope is also called the *chopper wheel* method, and it uses sky observations (the *on* and *off* positions) as well as internal hot and cold loads, to set

³NGC 5055 was already mapped in project D15-12 (PI Cormier) and NGC 5194 was available in the ^{12}CO (1-0) transition from the PAWS survey (Schinnerer et al., 2013).

⁴www.iram.fr/IRAMFR/GILDAS/doc/html/mira-html/mira.html

⁵www.iram.fr/IRAMFR/GILDAS

Species	ν_{rest} (GHz)	E_{up}^a (K)	n_c (cm^{-3})	Beam size (")
$\text{H}^{13}\text{CN} 1-0^b$	86.34	4.14	9.7×10^6	34.24
$\text{H}^{13}\text{CO}^+ 1-0^b$	86.75	4.16	6.7×10^5	34.08
$\text{HN}^{13}\text{C} 1-0^b$	87.09	4.18	1.2×10^6	33.95
$\text{HCN} 1-0$	88.63	4.25	2×10^5	33.36
$\text{HCO}^+ 1-0$	89.19	4.28	3×10^4	33.15
$\text{HNC} 1-0$	90.66	4.35	1×10^5	32.61
$\text{C}^{18}\text{O} 1-0^c$	109.78	5.27	4×10^2	26.83
$^{13}\text{CO} 1-0$	110.20	5.29	4×10^2	26.93
$^{12}\text{CO} 1-0$	115.27	5.53	4×10^2	25.65

TABLE 2.2. Main spectral lines covered by our EMIR setups and used in this thesis.

Notes: ^a The critical densities (n_c) at 20 K and energies of the upper level were extracted from the Leiden LAMDA database, [van der Tak et al. \(2007\)](#). ^b Only available for NGC 5194. ^c Not available for NGC 5194.

an absolute temperature scale. The main concept is that the difference of counts between the source and the *off* positions is related to the difference of counts between the hot load and blank sky:

$$(2.2) \quad T_A^* = T_{\text{cal}} \frac{C_{\text{on}} - C_{\text{off}}}{C_{\text{hot}} - C_{\text{off}}},$$

where T_{cal} is a calibration factor determined separately, and T_A^* is the *corrected antenna temperature*: the brightness temperature of an equivalent source filling the entire 2π steradians of the forward beam pattern. These data are then written out for line extraction using the Continuum and Line Analysis Single-dish Software (CLASS)⁶ package, which is also part of GILDAS. The following steps in the reduction process -baseline fitting, identification and rejection of pathological data and data cube construction- were carried out using our *in-house* pipeline in IDL.

2.3.2 Baseline fitting

After the calibration procedure, the observed spectra can show different features that need to be adjusted before constructing the final dataset. In a first step, we flag the data in order to find spikes (individual channels which show an extremely high emission, compared to the background) in the data or platforming effects (large emission offsets

⁶<http://www.iram.fr/IRAMFR/GILDAS/doc/html/class-html/class.html>

from well defined channel ranges) which could be obscured after a baseline fitting process.

Individual spectra can still show non-linear variations over the bandpass most likely due to atmospheric and receiver instabilities. Given the large amounts of data from the survey, it is necessary to deal with baseline fits in an automated way. To this end, we used the mean velocity of the CO (2-1) emission line from HERACLES in order to define regions in the spectra where the high-density tracers such as HCN are likely to appear. This is true if we assume that the bulk molecular medium, H₂ (traced by CO), is well mixed with the denser medium traced by HCN. The method employed defines a window which is centered on the mean CO (2-1) velocity and its size varies depending on the galaxy, ranging between 50-300 km s⁻¹. After that, we define two additional windows adjacent to the central one and with the same width, which we use to fit a second order polynomial baseline. This fit is later subtracted from the entire spectrum.

2.3.3 Pathological data

Pathological data which are still remaining after our fitting procedure can introduce artifacts into the final data cubes, therefore they should be removed in a systematic way. For the EMPIRE survey we reject spectra with rms (calculated after subtracting the baselines) uncertainties above 3 times the theoretical temperature noise. This theoretical noise is computed with the radiometer equation, which describes how the uncertainty in measuring a noise temperature (the system temperature in our case) decreases as the square-root of the number of independent samples averaged together:

$$(2.3) \quad \sigma_T = \frac{T_{\text{sys}}}{\sqrt{N}} = \frac{T_{\text{sys}}}{\sqrt{\Delta\nu t}},$$

where N is the number of independent data points, $\Delta\nu$ is the observed bandwidth and t is the integration time. The observed signal is statistically independent over an interval of time $1/(2\Delta\nu)$, therefore $N = t/(1/(2\Delta\nu)) = 2t\Delta\nu$. On the other hand, the fluctuations in a given measurement of the system temperature are $\sqrt{2} T_{\text{sys}}$.

2.3.4 Constructing data cubes

Finally, the data from each spectral line were projected onto grids of 4" pixel size and 4 km s⁻¹ channel width. The data is additionally convolved with a Gaussian kernel with a full width of $\sim 2/3$ the FWHM 30m beam size. We employed forward (F_{eff}) and

beam efficiencies (B_{eff}) available from the IRAM documentation⁷ in order to convert the temperature scales, T_{A}^* , to main beam temperature (T_{mb}). As for the 2013 campaign, the typical F_{eff} values at 88.6 and 115.3 GHz are 0.95 and 0.94, respectively; for B_{eff} the typical values are 0.81 and 0.78. T_{A}^* is connected to T_{A} by the forward beam efficiency:

$$(2.4) \quad F_{\text{eff}} T_{\text{A}}^* = T_{\text{A}} e^{\tau_{\nu}},$$

where τ_{ν} is the optical depth, to correct for the atmospheric attenuation at frequency ν . We can obtain the brightness temperature that accounts only for the emission inside the main beam (T_{mb}), by multiplying by the ratio of the forward and main beam efficiency:

$$(2.5) \quad T_{\text{mb}} = \frac{F_{\text{eff}}}{B_{\text{eff}}} T_{\text{A}}^*.$$

The true brightness temperature of the source would be best represented by a temperature scale that depends on the size of the source. When extended sources completely fill the beam size ($\theta_s \sim \text{FWHM}_{\text{mb}}$), T_{mb} is a good approximate of the source brightness temperature T_{b} . For very extended sources which are larger than the beam size, the beam efficiency can vary with the size of the source and $T_{\text{mb}} > T_{\text{b}} > T_{\text{A}}^*$. For the remainder of the text, we work in units of T_{mb} .

⁷<http://www.iram.es/IRAMES/mainWiki/Iram30mEfficiencies>

Galaxy	Scanned Field ($''$)	Dates Observed	Mapping time (h)	RMS (mK)
EMPIRE dense gas observations				
NGC 628	4.0×4.0	17, 20, 21 Jun 2015; 16-21 Sep 2015; 1, 15-16, 21-22 Oct 2015	44	2.4
NGC 2903	2.0×3.5	6-7 Apr 2016; 3-7 May 2016; 30 Nov - 5 Dec 2016	19	2.0
NGC 3184	3.0×3.0	4 May 2016; 31 May - 6 Jun 2016; 20-25 Jul 2016	24	1.9
NGC 3627	2.5×4.0	5-10 Nov 2015; 30 Nov - 5 Dec 2016	30	2.4
NGC 4254	3.0×3.0	3-9 Mar 2015; 22-26 Apr 2015	27	1.5
NGC 4321	4.0×2.5	8-12 May 2015; 4 Nov 2015; 8-12 Jan 2016	30	1.8
NGC 5055	6.0×3.0	13-17 Aug 2015; 7-10 Jan 2016; 31 May - 6 Jun 2016; 20-25 Jul 2016	38	2.3
NGC 5194	4.2×5.7	31 Jul - 6 Aug 2012	75	2.8
NGC 6946	4.5×6.5	3-8 Dec 2014; 22-26 Apr 2015; 17-22 Jun 2015; 12-17 Aug 2015	52	2.3
CO (1-0) complementary observations				
NGC 628	8.0×8.0	4-9 Aug 2016; 19-21 Oct 2016	18	16.3
NGC 2903	4.0×7.0	8-9 Sep 2016	4	22.5
NGC 3184	6.0×5.5	9-12 Sep 2016	8	17.3
NGC 3627	5.0×2.5	13-15 Sep 2015; 10-11 Sep 2016	6	16.2
NGC 4254	7.0×7.0	24-25 May 2015	8	20.2
NGC 4321	6.0×6.5	7-8 Aug 2016; 30-31 Oct 2016	12	13.1
NGC 6946	10.5×9.5	3-8 Aug 2016; 31 Oct 2016	13	23.5

TABLE 2.3. EMPIRE dense gas and complementary CO (1-0) observing dates, field sizes and mapping times. Typical RMS (T_A^*) values are given for the HCN (1-0) and CO (1-0) data cubes per galaxy, computed in 4 km s $^{-1}$ velocity channels.

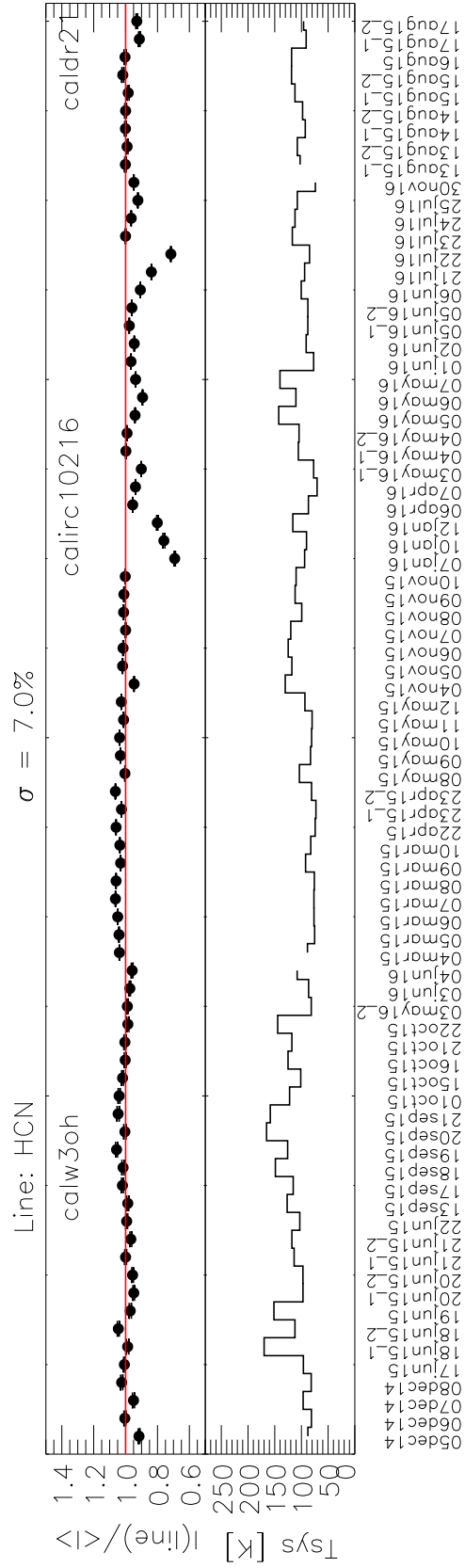


FIGURE 2.5. HCN integrated intensity for each day and line calibrator, divided by the mean of all measured intensities (top panel). During the EMPIRE observing runs, three different line calibrators were used: W3(OH), IRC 10216 and DR21(OH). The bottom panel shows the standard deviation from the mean intensity. The variations seen over the course of the observations are of the order of 7%.

DENSE GAS AND STAR FORMATION IN NEARBY GALAXIES

The EMPIRE Dense Gas Survey of Nearby Galaxy Disks
 M. J. Jiménez-Donaire, F. Bigiel, A. Leroy, D. Cormier, A. Usero,
 M. Gallagher, A. Bolatto, G. Dumas, S. García-Burillo, A. Hughes,
 C. Kramer, A. Kepley, J. Pety, K. Sandstrom, E. Schinnerer, A. Schruba,
 K. Schuster, F. Walter, L. Zschaechner; in preparation.

The results presented in this chapter are extracted from our ongoing EMPIRE Survey paper: *The EMPIRE dense gas survey of nearby galaxies* (M. Jiménez-Donaire et al., in prep.). Given that the introduction and data acquisition and reduction sections from the original paper are already contained in Chapters 1 and 2, we omit them in this chapter and provide an abridged version, to avoid repetition.

As a general overview, in this chapter of the thesis we employ the complete set of EMPIRE observations described in Chapter 2. Particularly, we utilize the brightest data products: HCN (1-0), HCO⁺ (1-0), HNC (1-0) and ¹²CO (1-0) high quality maps for the entire galaxy sample at a typical resolution of $\sim 1 - 2$ kpc. We explore the key HCN-to-CO and IR-to-HCN ratios, our observational tracers of dense gas fractions (f_{dense}) and dense gas efficiency ($\text{SFE}_{\text{dense}}$). Recent studies have found evidence for variation in the $\text{SFE}_{\text{dense}}$ (García-Burillo et al., 2012; Usero et al., 2015; Bigiel et al., 2016) in the disks of external galaxies. These results are at odds with a whole class star formation models based on Milky Way studies (e.g., Heiderman et al., 2010; Lada et al., 2010, 2012), which

argue for a constant star formation efficiency above a certain gas density threshold. Our goal is to investigate whether these variations are real and common to the very different environments characteristic of the EMPIRE galaxy sample. To further understand these variations, we relate them to local ISM conditions, such as stellar surface densities, molecular gas fraction regions and dynamical equilibrium pressure.

This chapter is structured as follows: Section 3.1 presents a summary of the archival data employed to compute physical quantities out of direct observables (Section 3.1.1). Section 3.1.2 describes the basic principle of our stacking techniques to recover the low signal-to-noise lines of sight. The results are presented in Section 5.4: we study the spatial distribution of the dense gas emission in Sections 3.2.1-3.2.3. In Section 3.2.4 we compare our dataset to the star formation scaling relations obtained from previous Milky Way studies and unresolved observations of galaxies. We investigate systematic variations of the star formation efficiencies and the dense gas fractions in Sections 3.2.5 and 3.2.6. Section 3.3 offers a thorough discussion: we overview possible interpretations for the observed line ratios in our galaxy disks in Section 3.3.1, and we compare the observed trends in f_{dense} and $\text{SFE}_{\text{dense}}$ with recent results in the CMZ of the Milky Way. We discuss the different factors that could alter the observed trends such as hydrostatic pressure, interstellar radiation fields in Section 3.3.3, and the implications of having sub-thermally excited and optically thick dense gas emission lines (3.3.4).

3.1 Ancillary data

The EMPIRE galaxy sample contains some of the best-studied nearby galaxies, as described in Section 2.1.1. They all have existing data across the electromagnetic spectrum that characterizes the ISM properties across their disks. In combination with our dense molecular gas observations from EMPIRE, we make use of the following data, and we refer the reader to Section 1.4.2 for more detailed information about these surveys:

1. We use the new complementary CO (1-0) IRAM 30m observations to trace the bulk molecular content coming from similar size regions in the EMPIRE galaxy targets. These observations are part of the EMPIRE survey, and are detailed in Section 2.2.4. The molecular gas intensities are converted into molecular gas masses using a fiducial conversion factor, α_{CO} as described in Section 3.1.1.
2. The atomic gas content is traced using the HI line emission from the The HI Nearby Galaxy Survey (THINGS).

3. We employ broadband IR photometry in the $3.6 - 500 \mu\text{m}$, from the Spitzer Infrared Galaxies Survey (SINGS) and the Key Insights on Nearby Galaxies: a Far-Infrared Survey with *Herschel* (KINGFISH). This broadband IR emission is then used to compute the total or bolometric infrared emission following Galametz et al. (2013), which will be later converted into star formation surface densities (Σ_{SFR}) as we describe in Section 3.1.1. In addition, the Spitzer $3.6 \mu\text{m}$ maps (Dale et al., 2009) are used to account for the stellar emission and to compute stellar surface densities (Σ_*) in galaxy disks.

3.1.1 Estimating physical parameters

Physical parameters that are needed for this work have to be inferred from the observed emission in both infrared and sub(mm) regimes. Although major effort is being put into converting observables into physical quantities, those conversions still bear large uncertainties (e.g., Sandstrom et al., 2013; Usero et al., 2015; Leroy et al., 2017a). In addition, the different physical quantities we are interested in - e.g. Σ_{dense} , Σ_{H_2} , Σ_{SFR} - have been derived following Usero et al. (2015), in order to keep the physical parameters as close as the observed intensities as possible.

Molecular gas surface density. We estimate the mass surface density of molecular gas using the new CO(1-0) line emission observed with the IRAM 30m telescope and PAWS to trace the molecular hydrogen (H_2) content. The molecular surface density can be derived as:

$$(3.1) \quad \Sigma_{\text{mol}} = \alpha_{\text{CO}} I_{\text{CO}} \cos(i),$$

where α_{CO} is the CO-to-molecular mass conversion factor. We assume this value to be Galaxy-like throughout the sample ($\alpha_{\text{CO}} = 4.4 M_{\odot} \text{pc}^{-2} (\text{K km s}^{-1})^{-1}$, i.e. including helium), and it is often applied as a default to Solar metallicity massive galaxies (see Bolatto et al., 2013b). However this value is expected to depend on the molecular cloud properties, such as density, temperature, turbulence, metallicity and even cosmic ray rate (e.g., Wolfire et al., 2010; Shetty et al., 2011). As a result, it is sensitive to radiative processes and gas chemistry and can vary from galaxy to galaxy and across individual galaxies (e.g., Downes & Solomon, 1998; Papadopoulos et al., 2012; Sandstrom et al., 2013). The values calculated in the disks of nearby, normal disk galaxies agree with the Galactic value, with variations of about an order of magnitude (Bolatto et al., 2013b;

[Sandstrom et al., 2013](#)). This, of course, can translate into an additional, large source or uncertainty in the molecular and dense gas masses.

Dense gas surface density. As for the molecular gas surface densities, one can also define a conversion factor (α_{HCN}) to calculate the mass surface density of dense molecular gas, Σ_{dense} , from the HCN (1-0) integrated intensity:

$$(3.2) \quad \Sigma_{\text{dense}} = \alpha_{\text{HCN}} I_{\text{HCN}} \cos(i).$$

This density corresponds directly to the dense, star-forming substructures within clouds. [Gao & Solomon \(2004\)](#) proposed $\alpha_{\text{HCN}} = 10 M_{\odot} \text{ pc}^{-2} (\text{K km s}^{-1})^{-1}$ as a typical for the disks of normal, star-forming galaxies. However, as described for α_{CO} many physical and chemical processes can influence this value (e.g., [Shimajiri et al., 2017](#)).

Atomic gas surface density. We calculate the atomic gas mass surface density, Σ_{HI} , from the 21 cm line integrated intensity maps obtained by The H I Nearby Galaxy Survey (THINGS, [Walter et al., 2008](#)), via:

$$(3.3) \quad \frac{\Sigma_{\text{HI}}}{M_{\odot} \text{ pc}^{-2}} = 0.020 \frac{I_{21 \text{ cm}}}{\text{K km s}^{-1}} \cos(i).$$

This conversion accounts for inclination and includes a factor of 1.36 to reflect the presence of helium.

Stellar surface density. We derive the stellar surface density, Σ_{*} , from the Spitzer 3.6 μm maps ([Dale et al., 2009](#)), since the emission from old stellar photospheres is responsible for most of the emission seen in the Infrared Array Camera (IRAC) 3.6 μm band. We convert these values from each kpc-size element into luminosities with our adopted distances, and apply a fixed a fixed 3.6 μm mass-to-light ratio. The stellar surface density:

$$(3.4) \quad \frac{\Sigma_{*}}{M_{\odot} \text{ pc}^{-2}} = 280 \frac{I_{3.6}}{\text{MJy sr}^{-1}} \cos(i)$$

which is, however, uncertain by $\sim 50\%$ due to contamination from young stars and very hot dust and PAH features. Another important uncertainty factor is the the mass-to-light ratio ([Zibetti et al., 2009](#); [Meidt et al., 2014](#)).

Total infrared intensity and Star Formation Rate. We use the total infrared (TIR) surface brightness as a proxy for the local surface density of star formation. To estimate this, we combine $\lambda = 70, 160,$ and $250\mu\text{m}$ maps from *Herschel*. We convolve these to match the $33''$ beam of our line data (Aniano et al., 2011), calculate the TIR surface brightness following Galametz et al. (2013), and then convert to star formation rate surface density using the prescription of Murphy et al. (2011). NGC 2903 lacks *Herschel* data, therefore we use Spitzer $24\mu\text{m}$ (from LVL, Dale et al., 2009) and IRAS $70\mu\text{m}$ to estimate the IR surface brightness.

In a study of the $^{13}\text{CO}(1-0)$ emission among the EMPIRE galaxies, D. Cormier et al. (in prep.) estimates the surface densities of star formation rates with the TIR maps from Galametz et al. (2013) for all galaxies with available KINGFISH data. They find that the differences between using the TIR maps and the generic prescriptions are of the order of 10% when combining the MIPS, PACS and SPIRE bands, and about 20% when only using the MIPS bands.

Hydrostatic pressure of the ISM. The gravitational force of a galaxy at any point in disk is the sum of contributions from the ISM and stars, both old and young. The external pressure on a given cloud with massive stars, in a galaxy is set by the combined effects of the hydrostatic pressure (P_h) in the galaxy disk and the radiation from stars (P_{rad}). In order to prevent the immediate collapse of molecular clouds, cloud densities must increase in response to different gravitation potentials until a quasi-hydrostatic equilibrium is achieved. The cloud pressure, which is mainly a combination of gas, turbulent and magnetic pressures (Pellegrini et al., 2007), responds to the external hydrostatic potential and feedback so that, in quasi-hydrostatic equilibrium:

$$(3.5) \quad P_{\text{cloud}} = P_{\text{gas}} + P_{\text{turb}} + P_{\text{mag}} = P_h + P_{\text{rad}}.$$

The resolution of the EMPIRE observations does not allow to resolve individual cloud structure, but averages the emission in $\sim\text{kpc}$ size regions. Furthermore, we do not have an estimation of the radiation pressure from stellar feedback, which can be orders of magnitude higher than the hydrostatic pressure but only on sub-cloud scales. Therefore, for the remainder of the chapter we consider that the cloud pressure is mainly driven by the external hydrostatic pressure (P_h).

This hydrostatic pressure, needed to support galactic disks is directly proportional to the gas volume density. Therefore it is not only the critical quantity that sets the ability of the ISM to form molecular hydrogen (Elmegreen, 1989; Elmegreen & Parravano, 1994),

but it should also be the key parameter describing the role of the gas at any particular density, for a given density distribution (e.g., [Helfer & Blitz, 1997](#); [Usero et al., 2015](#)). In this work we investigate how the dense gas content and its efficiency in forming stars can relate with hydrostatic pressure. Following [Elmegreen \(1989\)](#), [Wong & Blitz \(2002\)](#) and [Blitz & Rosolowsky \(2006\)](#), the hydrostatic pressure needed to balance the gravity on the gas in the disk can be expressed as:

$$(3.6) \quad P_h = \frac{\pi}{2} G \Sigma_{\text{gas}} \left(\Sigma_{\text{gas}} + \frac{\sigma_g}{\sigma_{*,z}} \Sigma_* \right),$$

where Σ_{gas} is the total atomic and molecular surface densities, σ_g is the velocity dispersion of the gas and $\sigma_{*,z}$ is the stellar velocity dispersion. While the first term in the equation expresses the gas self-gravity, the second one reflects the weight of the gas in the stellar potential well. Since direct measurements of $\sigma_{*,z}$ in nearby galaxy disks are very rare, several assumptions need to be made in order to give an estimation. Following [Leroy et al. \(2008\)](#), we assume:

1. The galaxies scale height (h_*) is constant with radius, as typically observed for edge-on disk sources (e.g., [van der Kruit, 1988](#); [Kregel et al., 2002](#)). The stellar surface density and the midplane stellar volume density are related via h_* as $\Sigma_* \approx 4\rho_* h_*$ ([van der Kruit, 1988](#)).
2. We can relate h_* to the observed stellar scale length by the flattening ratio measured by [Kregel et al. \(2002\)](#) as $l_*/h_* = 7.3 \pm 2.2$.
3. We assume hydrostatic equilibrium (the galaxy disks are isothermal in the z direction):

$$(3.7) \quad h_* = \frac{1}{2} \sqrt{\frac{\sigma_{*,z}^2}{2\pi G \rho_*}}.$$

Or, expressing $\sigma_{*,z}$ in terms of Σ_* , which we can measure directly:

$$(3.8) \quad \sigma_{*,z} = \sqrt{\frac{2\pi G l_*}{7.3} \Sigma_*}.$$

4. We finally connect the radial and vertical velocity dispersions by $\sigma_{*,z} = 0.6\sigma_{*,r}$, a reasonable value for most late-type galaxies ([Shapiro et al., 2003](#)).

We adopt $\sigma_g \approx 15 \text{ km s}^{-1}$, a value observed to be appropriate for large scales and high surface density regions of galaxy disks (e.g., [Tamburro et al., 2009](#); [Caldú-Primo](#)

et al., 2013; Mogotsi et al., 2016). We expect this pressure estimation to be a good representation of the time-averaged hydrostatic pressure needed to balance the galaxy disk against its own self-gravity and the stellar gravitational potential well.

3.1.2 Spectral stacking technique

The molecular emission of the high density tracers tends to be weak for individual lines of sight. With EMPIRE we map the emission from the entire galaxy disks and, as a consequence, a significant fraction of the diffuse medium ($10 - 100 \text{ cm}^{-3}$) fills the beam, where the dense gas tracers are hard to detect. We tackle this issue by using spectral shifting and stacking to improve the signal-to-noise ratio (SNR) of the fainter dense gas tracers (Schruba et al., 2011; Caldú-Primo et al., 2013; Jiménez-Donaire et al., 2017a). The resulting radial profiles are shown in Figure 3.3 for each target, and the data presented is stacked in bins of galactocentric radius. The selected bin size is $30''$ wide, comparable to the angular resolution of our data, which corresponds to $\sim 1 - 2 \text{ kpc}$ for our sample.

We use the $^{12}\text{CO}(1-0)$ emission to estimate the local mean velocity of the molecular gas. This value is then used as a reference for spectral shifting, since the line of sight velocities can vary significantly with position due to the galaxy rotation. The velocity axis of all our spectral lines is shifted to a common velocity of 0 km s^{-1} . In the stacking analysis, the molecular emission from a tracer from different lines of sight is averaged to produce higher signal-to-noise spectrum. Figure 3.1 shows the mean averaged HCN(1-0) emission coming from the arm region¹ of NGC 5194 in two different ways to describe the result of this approach. While the left panel shows simply averaged spectra as they were observed, the right panel shows the result of shifting the spectra utilizing the CO mean velocity associated for each line of sight and then average. The fact that the signal appears at the expected velocity reinforces that is not due to any baseline features but real HCN emission.

The stacked HCN measurements have the potential to reflect an astronomical signal in the velocities and line of sights with a weak emission. In Figure A.1 we provide an example of the resulting HCN spectral stacks (blue lines) in radial bins of $30''$ for every EMPIRE galaxy. We also give upper limits to the emission in those cases where the stacking analysis does not yield a spectral line (marked as red spectra). In all these cases,

¹The different regions within galaxies are defined using $^{12}\text{CO}(1-0)$ intensity contours. See Cormier, D., Bigiel, F., Jiménez-Donaire, M., et al. (in prep.), for more details.

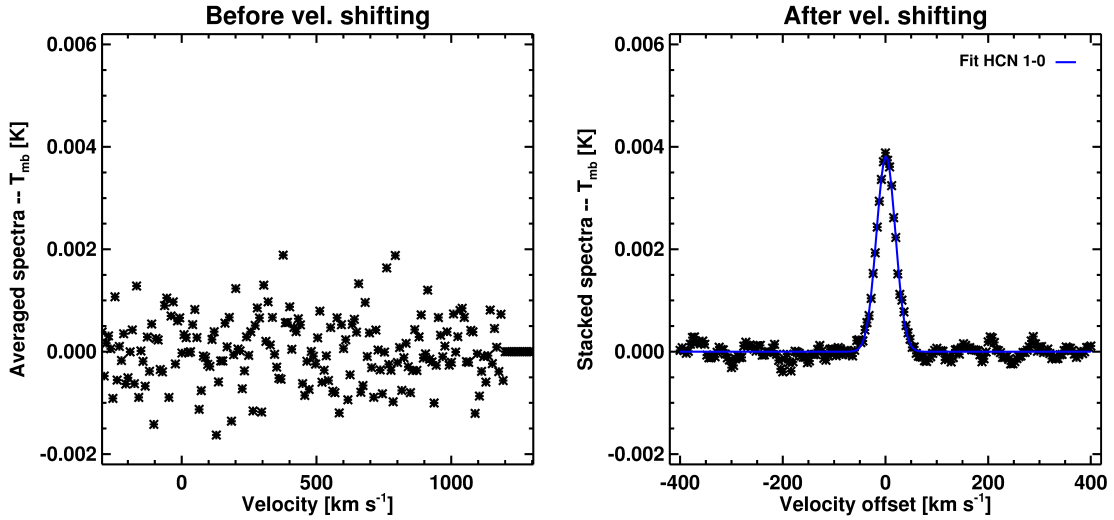


FIGURE 3.1. Averaging vs. stacking HCN (1-0) spectra corresponding to individual lines-of-sight within the arms of NGC 5194. While the left panel shows a simple average of all spectra, on the right panel we recover lost HCN emission when averaging after shifting the different spectra to the local mean ^{12}CO (1-0) velocity.

we also provide the stacked ^{12}CO (1-0) emission (black line) divided by a factor of 20, for comparison.

We fit the stacked spectrum of each line with a single Gaussian profile, which allows us to measure the spectral line parameters. To perform the fit, we center a 100 km s^{-1} window on the peak of emission and use the MPFIT function in IDL. Some galaxy centers exhibit very broad emission lines with a saturated and optically thick profile due to unresolved gas motions that coincide with central bars or molecular rings. In those cases a Gaussian is not a good description for the line profile and we fit a double-horn profile instead. The free parameters we calculate from the fit are the line center velocity, the peak intensity, and the velocity dispersion. We compute the uncertainties on the integrated intensity from the width of the profile and the rms value of the noise, measured from the signal-free part of the spectrum. We also compute upper limits to the integrated intensities when the peak intensity of the stacked spectrum is below 3σ . These limits are derived integrating over a Gaussian line profile with a peak set to the 3σ rms value of the noise, and a width set to the typical FWHM found for high SNR in (e.g., 75 km s^{-1} for HCN, [Jiménez-Donaire et al., 2017a](#), see Chapter 4 for more details).

3.2 Results

3.2.1 Distribution of dense gas emission

Figure 3.2 shows the HCN (1-0) integrated intensity maps for the nine targets of the EMPIRE survey. Contours of the ^{12}CO (1-0) emission are over plotted on the HCN maps for comparison, and its emission is typically 30-70 times brighter, on average. When creating the dense gas moment maps, we use the central velocities and the line widths of the complementary ^{12}CO (1-0) data. These quantities are used as an initial guess for the fit of the lines, using a single Gaussian. The centers of galaxies are often very broad and not Gaussian, thus for these cases we directly integrate the emission over a window defined as $\sim 3 \times \text{FWHM}$ of the ^{12}CO (1-0) line. We also generate uncertainty maps, where we compute the error in each pixel as the standard deviation in the line-free parts of each spectrum, multiplied by the square root of the number of channels inside the FWHM given by the Gaussian fit (or the defined window in case of broad, saturated centers).

The HCN integrated intensity peaks at the centers of each target and it varies in a range of ~ 2 -7 depending on the galaxy. We find the maximum peak values towards the center of NGC 6946, where the HCN integrated intensity is $6.96 \pm 0.02 \text{ K km s}^{-1}$, while the weakest central emission is found to be $0.30 \pm 0.02 \text{ K km s}^{-1}$ in NGC 3184. In general, the HCN zeroth moment maps reproduce very well the large-scale structure traced by CO and $70 \mu\text{m}$ emission. In some galaxies, like NGC 628 and NGC 3184, the dense gas emission is simply very faint, therefore the data is quite noisy despite the large observing times employed. In those cases, this is reflected in the large uncertainties presented in the data, and most of the information can only be extracted by employing stacking. Because of this, we have been careful with the uncertainty determination and also explored the possible influence of the noise in the data on our results (see Section 3.2.7). In addition, some spectra in NGC 5055 also exhibits a remaining platforming effect at the edges of EMIR corresponding to a $\sim V_{\text{sys}} + 650 \text{ km s}^{-1}$ due to the overlap of the FTS sub-bands, which are discarded for this study. We are currently employing refined masking and signal identification techniques to improve the current dataset especially for the faintest galaxies. Many of our measurements are obtained from stacking spectra which, given the faintness of such measurements, is often the only option to derive high SNR measurements over the entire galaxy disks.

The molecular structure seen for the rest of the sources appears to be very well recovered by the HCN emission, which also allows to identify very clearly strong features

such as spiral arms (NGC 5055, NGC 5194 and NGC 6946) and central bars (NGC 2903 and NGC 3627). Some targets also show a slight deviation from the bright HCN and CO centers. For example, in the following cases: NGC 5194, the HCN emission peaks 21" SW to the maximum CO emission; in NGC 4254, the HCN observed emission peaks 25" SW to the CO center, and the HCN central emission for NGC 3627 is located 6" north from the CO central emission. Two of these sources, NGC 3627 and NGC 4254 also have higher spatial resolution (5" vs. 33") maps from ALMA, shown in M. Gallagher et al. (subm.) and [Jiménez-Donaire et al. \(2017a\)](#). We compare the offset calculated from the EMPIRE images, with the ALMA HCN (1-0) and ^{13}CO (1-0). The offset between the HCN and the ^{13}CO emission found for NGC 3627 is only 0.6", whereas the offset found for NGC 4254 is 7". Therefore most of the differences we find are due to the lower resolution of our EMPIRE data.

3.2.2 Radial profiles

In Figure 3.3 we show the resulting radial profiles from applying the stacking techniques to the main dense gas tracers, HCN, HCO^+ and HNC, together with the ^{12}CO and ^{13}CO radial profiles for comparison. Our targets present a very similar behavior on large scales despite their vastly different morphologies: the stacked intensities of the different tracers (^{12}CO , ^{13}CO , HCN, HCO^+ and HNC) decrease steadily as a function of radius. As a general trend, the emission coming from the dense gas tracers decreases more rapidly than that of lower density gas tracers ^{12}CO and ^{13}CO .

The figure also shows that our stacking technique recovers well the signal from the lowest SNR regions, detecting HCN out to $\sim 9 - 11$ kpc, HCO^+ out to $\sim 7 - 10$ kpc, and HNC out to $\sim 4 - 6$ kpc. We observe the brightest emission coming from high density tracers in NGC 6946, where the averaged HCN emission peaks at $3.2 \pm 0.1 \text{ K km s}^{-1}$, HCO^+ peaks at $2.8 \pm 0.1 \text{ K km s}^{-1}$ and HNC at $1.1 \pm 0.2 \text{ K km s}^{-1}$. It is important to note that these values correspond to averaged intensities over the central 30", and therefore the inner \sim kpc region. NGC 5194 and NGC 4321 also show bright emission ($2.8 \pm 0.1 \text{ K km s}^{-1}$ and $1.7 \pm 0.1 \text{ K km s}^{-1}$ vs. $1.1 \pm 0.2 \text{ K km s}^{-1}$ on average) for dense gas tracers in their centers. These galaxies also show very rich molecular emission and present strong spiral structures.

Among the three main dense gas emission lines, HCN is generally the strongest one, with typical ^{12}CO -to-HCN ratios that range between 30-70 (see Table 3.1 for an overview of the line ratios found), depending on the target and region under consideration. We

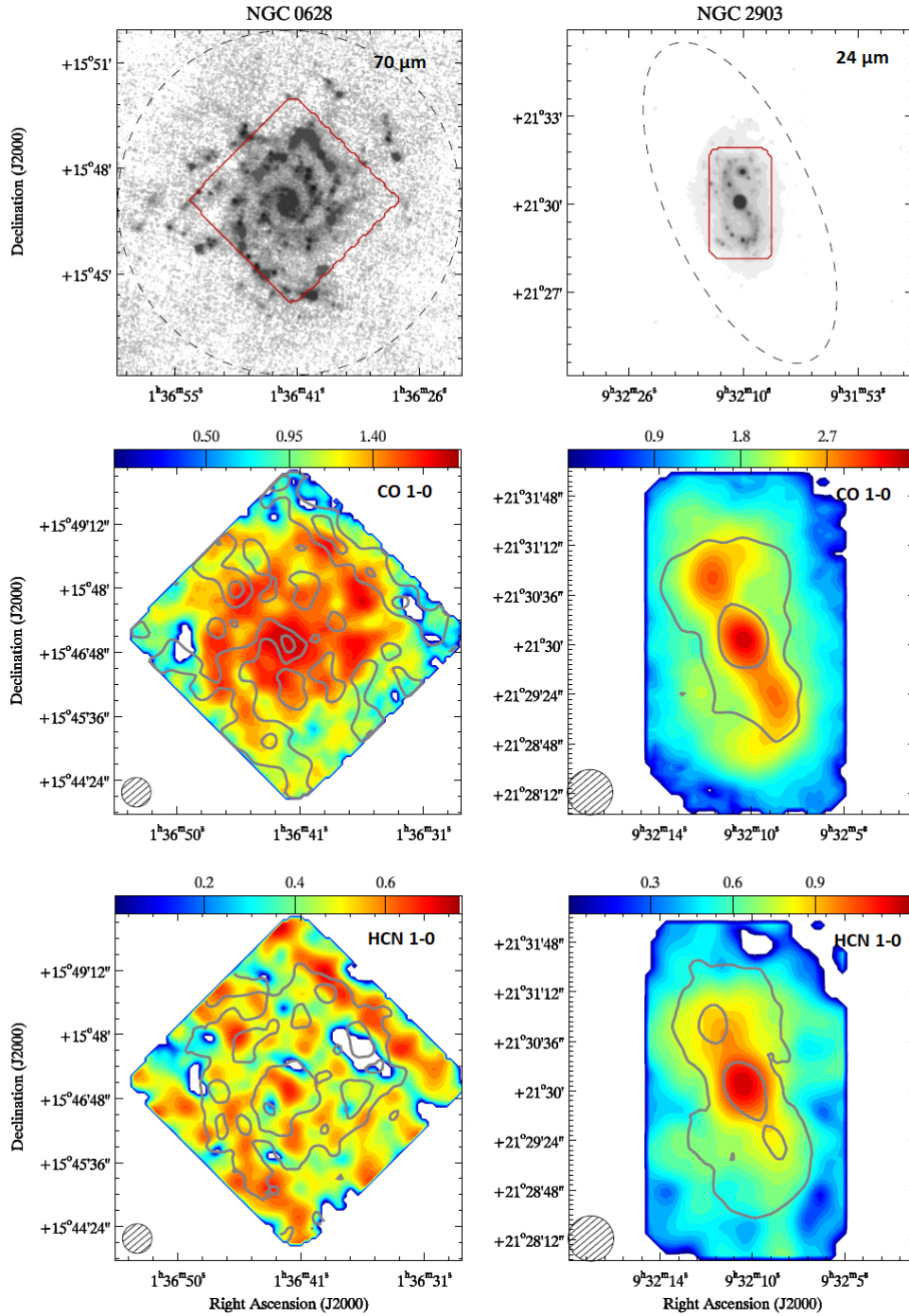


FIGURE 3.2. Top: *Herschel* $70\ \mu\text{m}$ map (*Spitzer* $24\ \mu\text{m}$ map in the case of NGC 2903). The dashed ellipse shows the r_{25} radius, and the IRAM coverage is shown in red. We show the ^{12}CO (1-0) and HCN (1-0) zeroth moment maps in the middle and bottom panels, respectively. The original beam size of $\sim 26''$ and $\sim 33''$ (30-m at 115.3 GHz and 88.6 GHz, respectively) is indicated on the bottom left corner. ^{12}CO contours are shown on the HCN (1-0) maps, scaled by values of 1.5 and 3 for NGC 628, and 2 and 6 for NGC 2903. HCN (1-0) contours are also shown on the ^{12}CO maps. The maps are shown in square root scale and colorbars are in units of $\text{sqrt}(\text{K km s}^{-1})$.

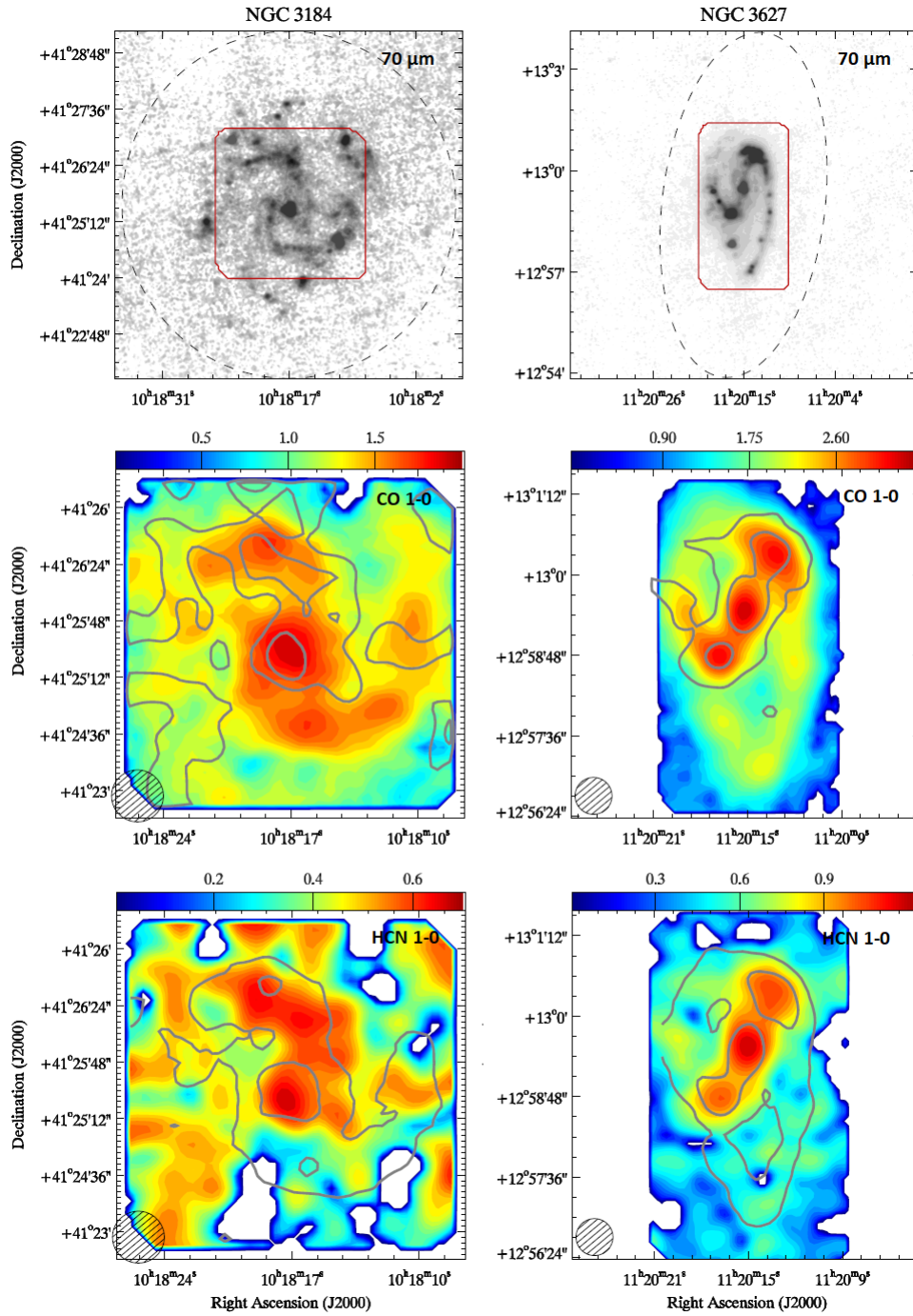


Figure 3.2: continued. The ^{12}CO contours shown on the HCN (1-0) maps are scaled by values of 1.5 and 3 for NGC 3184, 2 and 6 for NGC 3627.

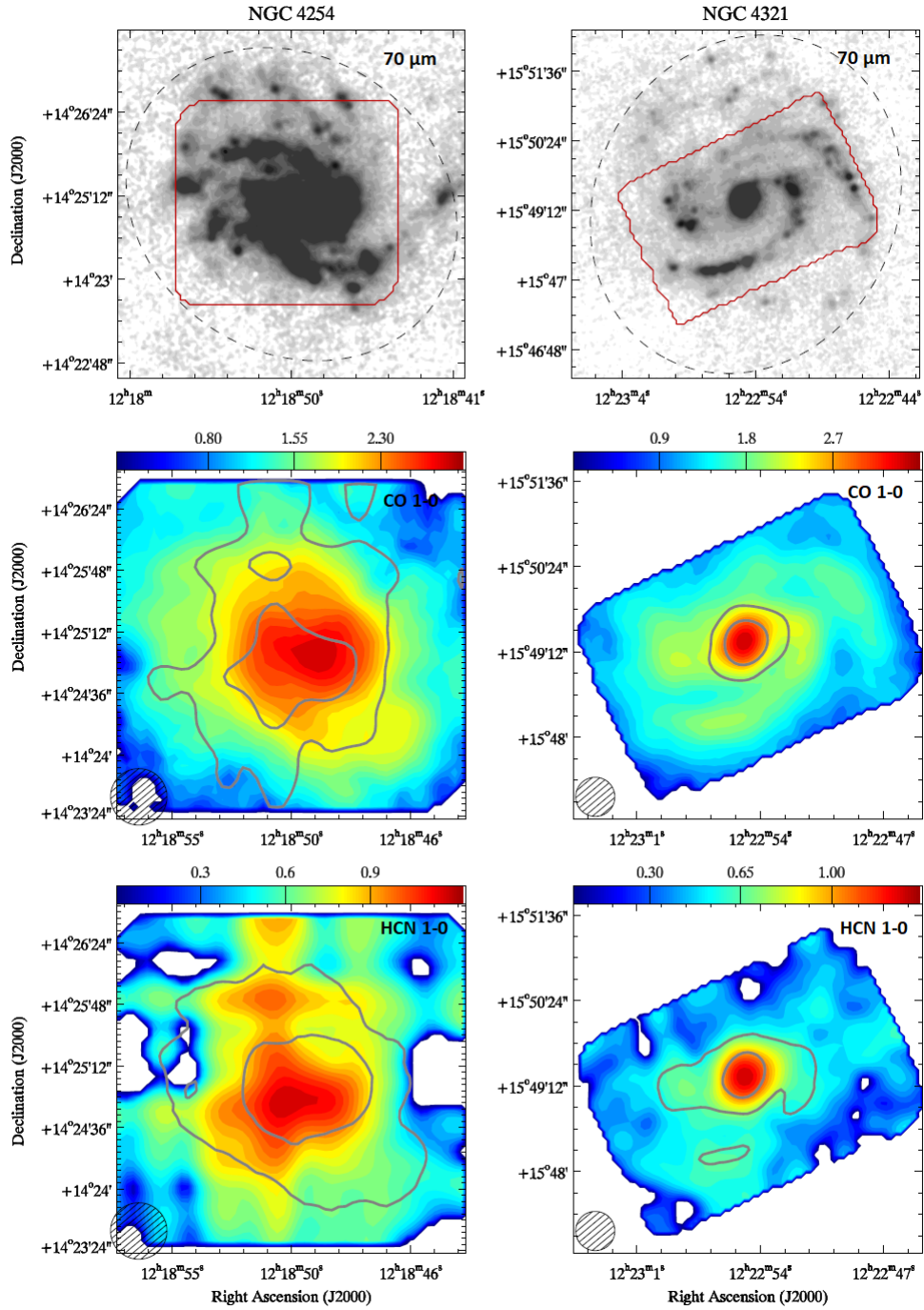


Figure 3.2: continued. ^{12}CO contours shown on the HCN (1-0) maps are scaled by values of 2 and 6 for NGC 4254 and NGC 4321.

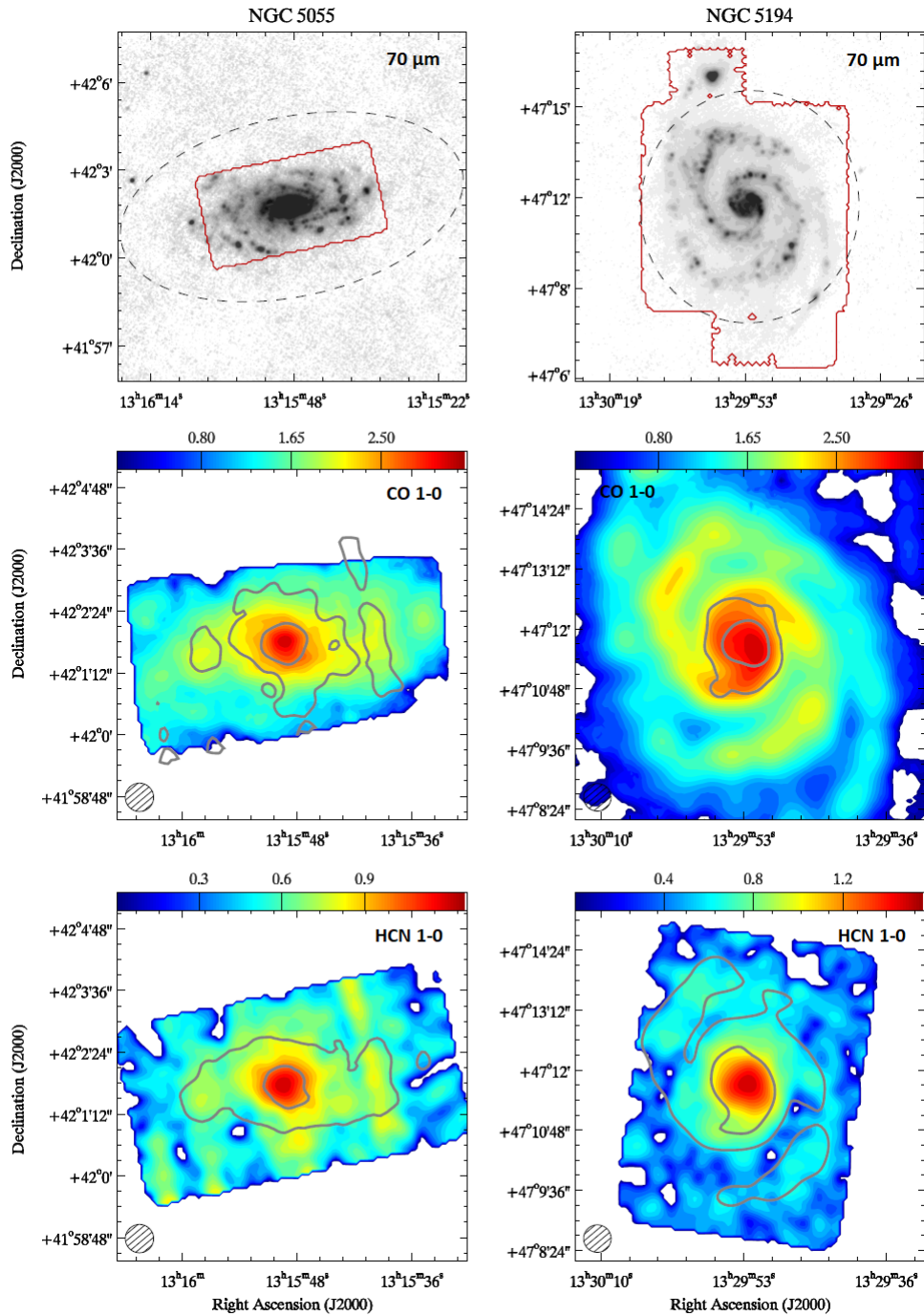


Figure 3.2: continued. ^{12}CO contours shown on the HCN (1-0) maps are scaled by values of 2 and 6 for NGC 5055 and NGC 5194.

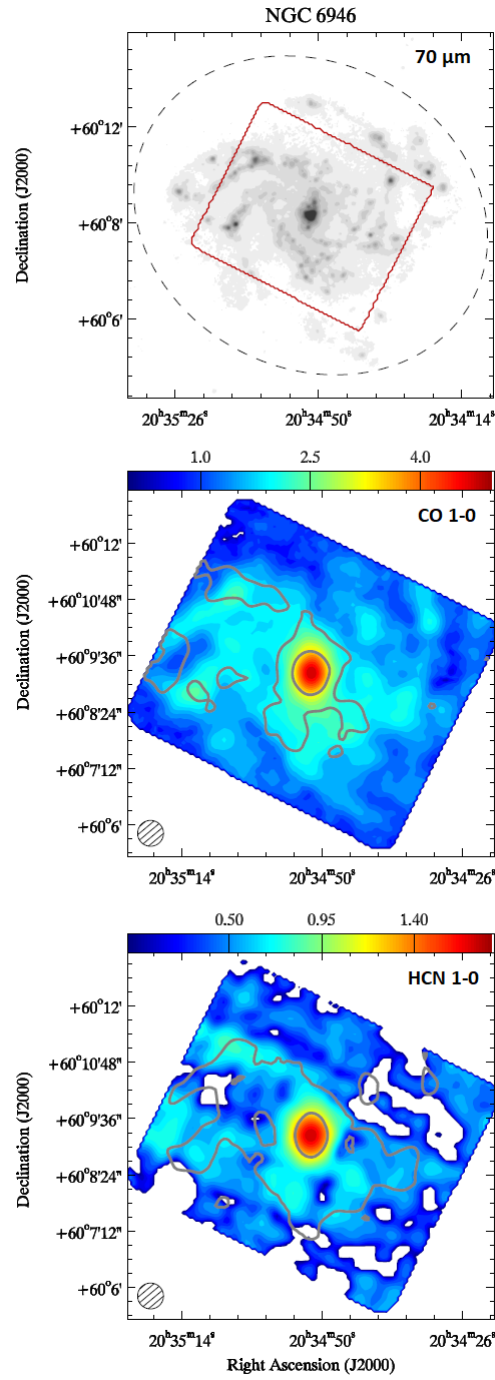


Figure 3.2: continued. The ^{12}CO contours shown on the HCN (1-0) maps are scaled by values 3 and 20 for NGC 6946.

note that HCN and HCO⁺ present almost coincident profiles in NGC 3627, NGC 4254, NGC 4321, NGC 5194 and NGC 6946, where they are only significantly different from each other in the galaxy centers and at large radii. This is also seen in detail in the high resolution data shown in M. Gallagher et al. (subm.), where they are practically identical in the inner ~ 4 kpc.

3.2.3 Molecular line ratios

Line intensity ratios between the dense gas tracers employed in this work -HON, HCO⁺ and HNC- and the bulk molecular tracer CO, depend on the gas physical conditions and chemistry. The HCN/CO and HCO⁺/CO ratios are commonly used to study the relative fraction of dense gas in galaxies. On the other hand, line ratios among the high critical density tracers constitute a good diagnostics of the dense component of the ISM. In the past years a lot of effort has been dedicated to understanding these species, especially thanks to the much improved sensitivity of mm telescopes. Most observations can be found towards nearby starbursts and LIRGs (e.g., [Henkel et al., 1991](#); [Kohno et al., 2001](#); [Aalto et al., 2002](#); [Baan et al., 2008](#); [Aladro et al., 2011](#); [Meier & Turner, 2012](#); [Meier et al., 2014](#)), galactic nuclei (e.g., [Nguyen et al., 1992](#); [Helfer & Blitz, 1997](#); [Chin et al., 1997](#); [Curran et al., 2000](#)) and a few galactic disks (e.g., [Kohno et al., 1996](#); [Braine et al., 1997](#); [Brouillet et al., 2005](#)).

Here we explore the observed changes in the cited line ratios across our nearby galaxy sample. However, detailed analysis of the physics driving these line ratios will be presented in forthcoming studies (e.g., Usero et al. in preparation). Figure 3.4 displays the typical ratios tracing dense gas fractions (HCN/CO, HCO⁺/CO and HNC/CO) stacked across selected regions of our sample of nearby galaxies: centers (circles), spiral arms (triangles) and interarm regions (squares). The average values for each region are shown in Table 3.1: while HCN/CO and HCO⁺/CO are of the order of 3% in the galaxy centers and about 2% in the arm and interarm regions, HNC/CO is $\sim 1\%$ in all zones. It is particularly interesting that our central measurements are scattered in all ratios (up to $\sim 5-4\%$ for HCN/CO and HCO⁺/CO) when comparing to our arm/interarm values. A more detailed comparison between these ratios and the typical dense gas fractions found in the literature is given in Sections 3.2.5 and 3.3.1.

As for the line ratios among high density tracers, we find average HCO⁺/HCN values of ~ 0.8 and HNC/HCN values of ~ 0.4 across the disks of our targets. These mean values show little variation ($\sim 10\%$) except for two targets, NGC 4254 and NGC 6946, where

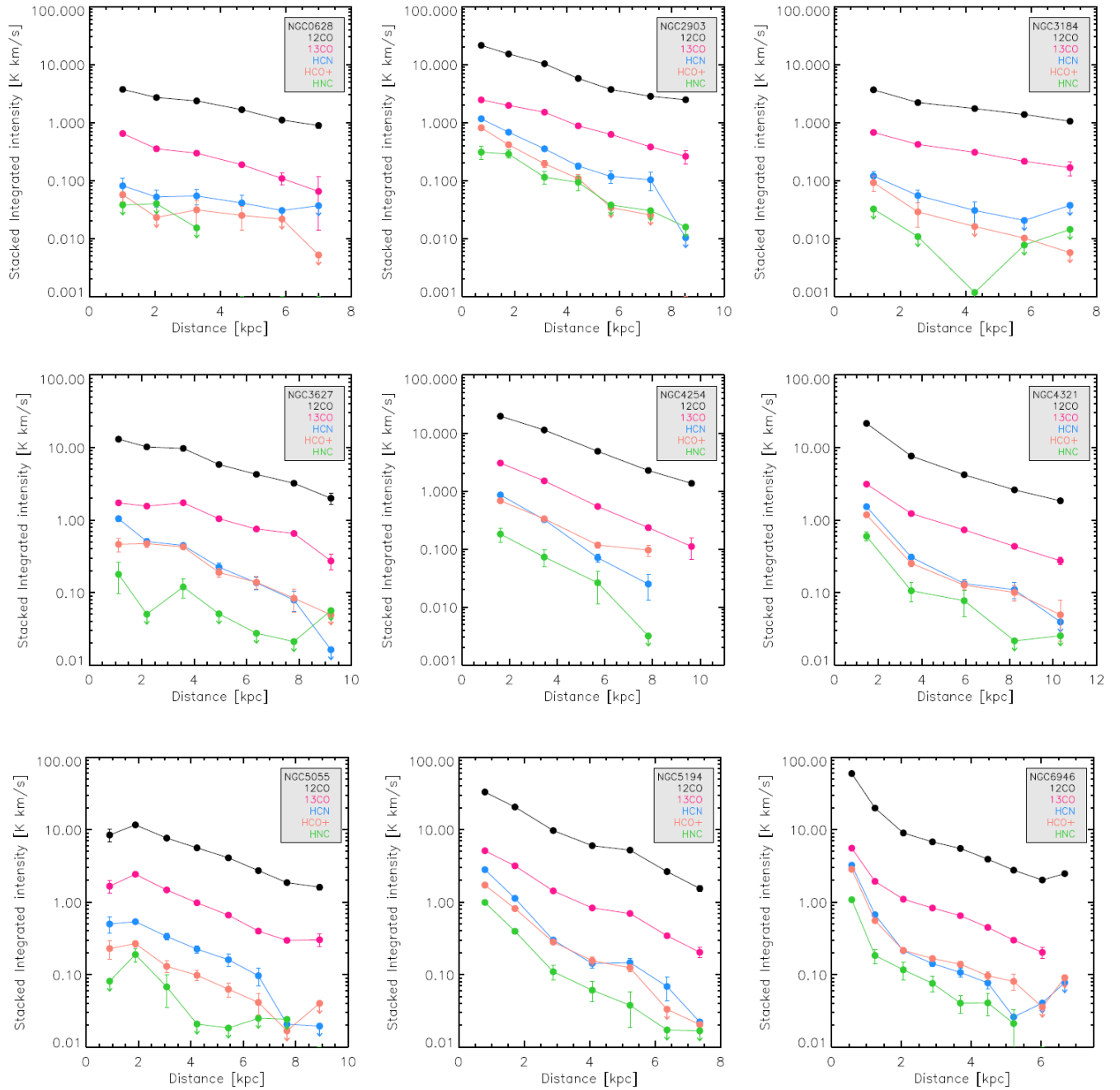


FIGURE 3.3. Stacked HCN, HCO⁺ and HNC integrated intensity in 30'' size radial bins. The stacks span the entire galaxy disks, out to $\sim 8 - 10$ kpc, depending on the target. Points show secure detections and arrows show 3σ upper limits in those regions where the molecule emission is not detected.

Ratio	Center	Arms	Interarm
HCN/CO	0.032 ± 0.002	0.020 ± 0.002	0.020 ± 0.008
HCO ⁺ /CO	0.026 ± 0.002	0.016 ± 0.002	0.016 ± 0.005
HNC/CO	0.013 ± 0.002	0.007 ± 0.003	0.009 ± 0.002
HCO ⁺ /HCN	0.8 ± 0.1	0.8 ± 0.2	0.8 ± 0.6
HNC/HCN	0.4 ± 0.1	0.4 ± 0.1	0.5 ± 0.4

TABLE 3.1. Average dense gas line ratios (excluding upper limits) found in the centers, arms and interarm regions of the EMPIRE nearby spiral galaxies.

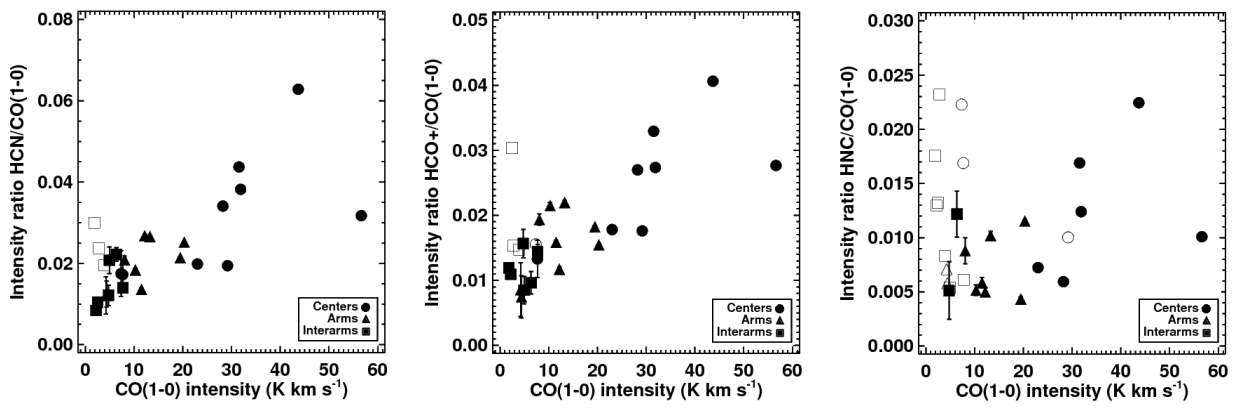


FIGURE 3.4. Dense gas to molecular gas typical line ratios found in the centers (circles), arms (triangles) and interarm (squares) regions of the EMPIRE nearby galaxy targets. Upper limits to the respective emission lines are represented by empty symbols.

the HCO⁺-to-HCN ratio reaches values up to ~ 1.2 in the spiral arms and ~ 1.5 -3 in the interarm regions. These values are quite large in comparison to those found in their central regions (~ 0.8 -0.9), and are similar to those found in low metallicity systems such as M31 (1.2, [Brouillet et al., 2005](#)), M33 (1.1-2.5, [Buchbender et al., 2013](#); [Braine et al., 2017](#)) or the Magellanic Clouds (1.8-3, [Chin et al., 1997, 1998a](#)). We consider possible scenarios to explain the resulting line ratios in Section 3.3.1.

3.2.4 Scaling relations

Based on the tight relation observed by [Gao & Solomon \(2004\)](#) between the SFR and the dense gas mass, which extends from the higher luminosities found in galaxies to the lower luminosities found in Galactic clumps, a universal star formation efficiency in

dense gas was hypothesized. Our main goal is to understand the context-dependent role of dense gas and disentangle whether these observed scaling relations are universal or, on the contrary, whether they can break down at certain scales (e.g., [Chen et al., 2015](#); [Kruijssen et al., 2014](#)).

IR vs. HCN luminosities In Figure 3.5 we study the IR luminosity, an indicator of the star-formation rate, as a function of the HCN luminosity tracing the dense gas content. We compare the definite (3σ) HCN detections from EMPIRE, displayed as pink triangles on the plot, with all the available HCN observations covering every possible environment: from Galactic cores ([Wu et al., 2010](#); [Stephens et al., 2016](#)), giant molecular clouds (GMCs) in the SMC, LMC and other low- Z galaxies ([Chin et al., 1997, 1998a](#); [Braine et al., 2017](#)), giant molecular associations in nearby galaxies ([Brouillet et al., 2005](#); [Buchbender et al., 2013](#); [Chen et al., 2017](#)), resolved nearby galaxy disks ([Kepley et al., 2014](#); [Bigiel et al., 2015](#); [Chen et al., 2015](#), and this work), and whole galaxies and centers ([Gao & Solomon, 2004](#); [Gao et al., 2007](#); [Krips et al., 2008](#); [Graciá-Carpio et al., 2008](#); [Juneau et al., 2009](#); [García-Burillo et al., 2012](#); [Privon et al., 2015](#)). The collected data from the literature constitutes 225 data points for the resolved cores and GMCs in the Milky Way and other nearby galaxies; about 194 data points correspond to observations of entire galaxies or bright centers; and 415 data points (only taking into account secure detections for EMPIRE) are available from resolved ($\sim 0.3 - 2$ kpc) galaxy disks. At a resolution of ~ 1 kpc, the new EMPIRE data populates the intermediate regime corresponding to large parts of galaxy disks, between GMAs and GMCs in external galaxies, and observations of entire galaxies. In addition, we include our globally average data for each individual galaxy (filled gray circles), which display a similar dispersion to that seen in the observations of entire galaxies. The compiled literature data shown in Figure 3.5 follows the same relationship found by [Gao & Solomon \(2004\)](#) between IR and HCN for starbursts and whole galaxies, and extend across almost ten orders of magnitude with a scatter of a factor of two. The EMPIRE data (and the resolved data from [Chen et al., 2015](#), for M51) bridges the gap in scale between the resolved cores (~ 0.5 pc), and the integrated emission from whole galaxies.

SFE_{dense} vs. HCN luminosity Such a relationship - the observed constant $L_{\text{IR-to-}}L_{\text{HCN}}$ ratio- has motivated the idea that star formation in dense gas is a universal process, where the dense gas fraction is directly related to the star formation efficiency of molecular gas (e.g., [Gao & Solomon, 2004](#); [Lada et al., 2010](#)). Figure 3.6 displays the

$L_{\text{IR-to-}}L_{\text{HCN}}$ ratio, which traces the SFR per unit dense gas, showing a linear relation within ~ 10 orders of magnitude. This figure shows more clearly that there is significant scatter that extends over ~ 2 orders of magnitude in the observed ratio. While IR emission appears to correlate well with HCN luminosity in individual regions ($\sim \text{kpc}$) and in global galaxies, a unique spatially resolved SFR-HCN relation does not exist to explain the large variations we find: on kpc scales we find that IR-HCN shows clear sub-linear relationships. The observed IR-to-HCN ratios are quite different from region to region, which indicates an environment-dependent efficiency of star formation in dense gas. In other words: there is no linear one-to-one relation between the HCN luminosity and the expected $\text{SFE}_{\text{dense}}$. Figures 3.5 and 3.6 also include the data for the central molecular zone (CMZ) in our Galaxy (inner $\sim 500 \text{ pc}$ [Jones et al., 2012](#)) and the ALMA data (M. Gallagher et al. *subm.*) corresponding to the inner centers (500 pc) of four nearby galaxies (NGC 3351, NGC 3627, NGC 4254 and NGC 4321) in filled yellow circles. These data are consistent with the observed linear relation within the observed scatter, although some data points reflect a much lower $\text{SFE}_{\text{dense}}$ for a given amount of HCN luminosity than the rest of the intermediate-scale EMPIRE data points.

3.2.5 Dense gas fraction and $\text{SFE}_{\text{dense}}$: what drives the observed variations?

In this Section we explore the dependence of the fraction of dense gas and its efficiency to form stars for each individual galaxy disk. For that, we focus on the brightest of the dense gas tracers, the HCN (1-0) emission line, and we look at every individual line of sight where we have measured HCN in each disk. In Figures 3.7-3.10 and 3.8-3.12 in the appendix, we plot the basic line ratios we want to analyze: HCN-to-CO as a proxy for the dense gas fraction, and TIR-to-HCN as a proxy for the $\text{SFE}_{\text{dense}}$. These quantities are shown as a function of several parameters which have the potential to drive the observed variations of the HCN-to-CO and IR-to-HCN ratios: stellar surface density (Σ_*), molecular fractions (Σ_{mol}) and hydrostatic pressure.

Dense gas fraction. Figures 3.7, 3.8 and 3.9 show the variation of the amount of dense gas, traced by the HCN-to-CO ratio, with respect to three different physical parameters: stellar surface density, molecular-to-atomic gas fraction and hydrostatic pressure. The main detections in these figures indicate that the measured dense gas fractions show little variation among individual targets ($\sim 8\%$), while dense gas fractions in selected

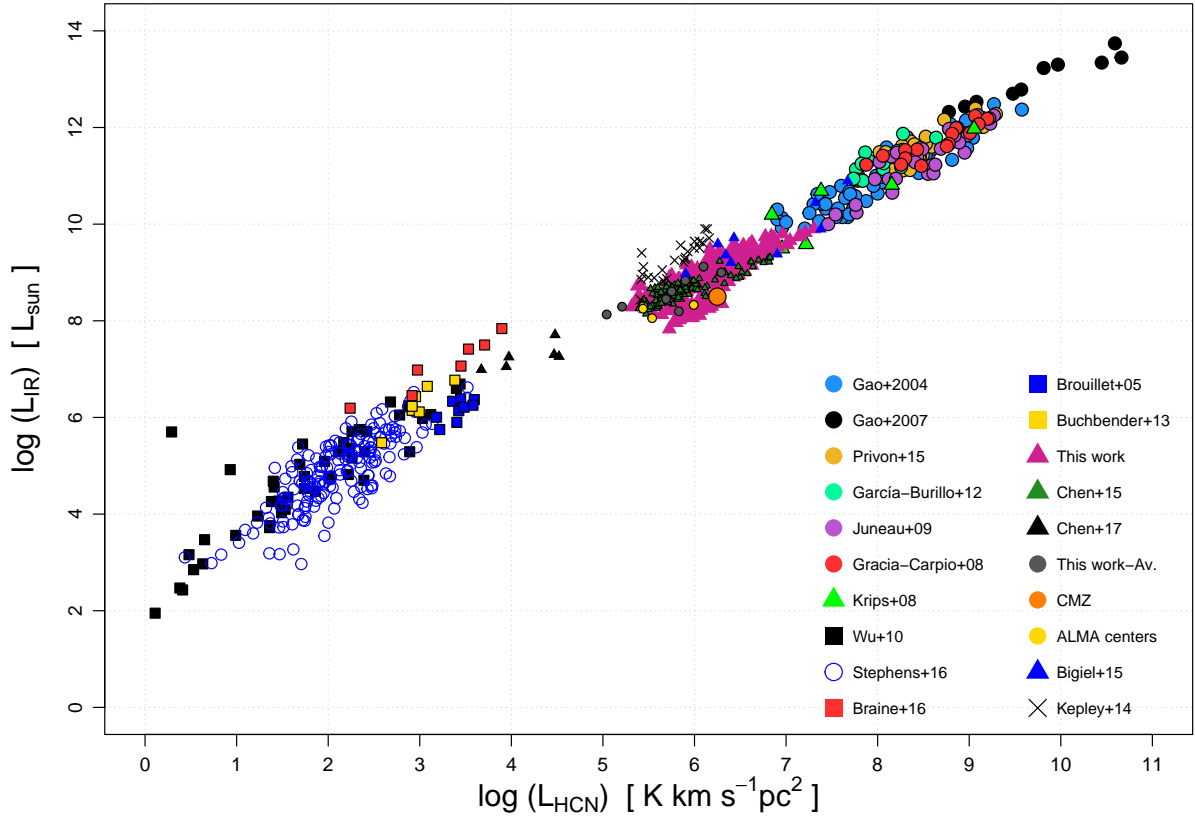


FIGURE 3.5. Luminosity-luminosity correlation between L_{IR} , as a tracer for star formation rate (SFR) and L_{HCN} , tracing dense gas mass. Our literature compilation includes all the available HCN observations ranging from Galactic clumps and cores (Wu et al., 2010; Stephens et al., 2016), giant molecular clouds (GMCs) in the SMC, LMC and other low- Z galaxies (Chin et al., 1997, 1998a; Braine et al., 2017), giant molecular associations in nearby galaxies (Brouillet et al., 2005; Buchbender et al., 2013; Chen et al., 2017), resolved nearby galaxy disks (Kepley et al., 2014; Bigiel et al., 2015; Chen et al., 2015, Gallagher et al. subm., and this work), and whole galaxies and centers (Gao & Solomon, 2004; Gao et al., 2007; Krips et al., 2008; Graciá-Carpio et al., 2008; Juneau et al., 2009; García-Burillo et al., 2012; Privo et al., 2015).

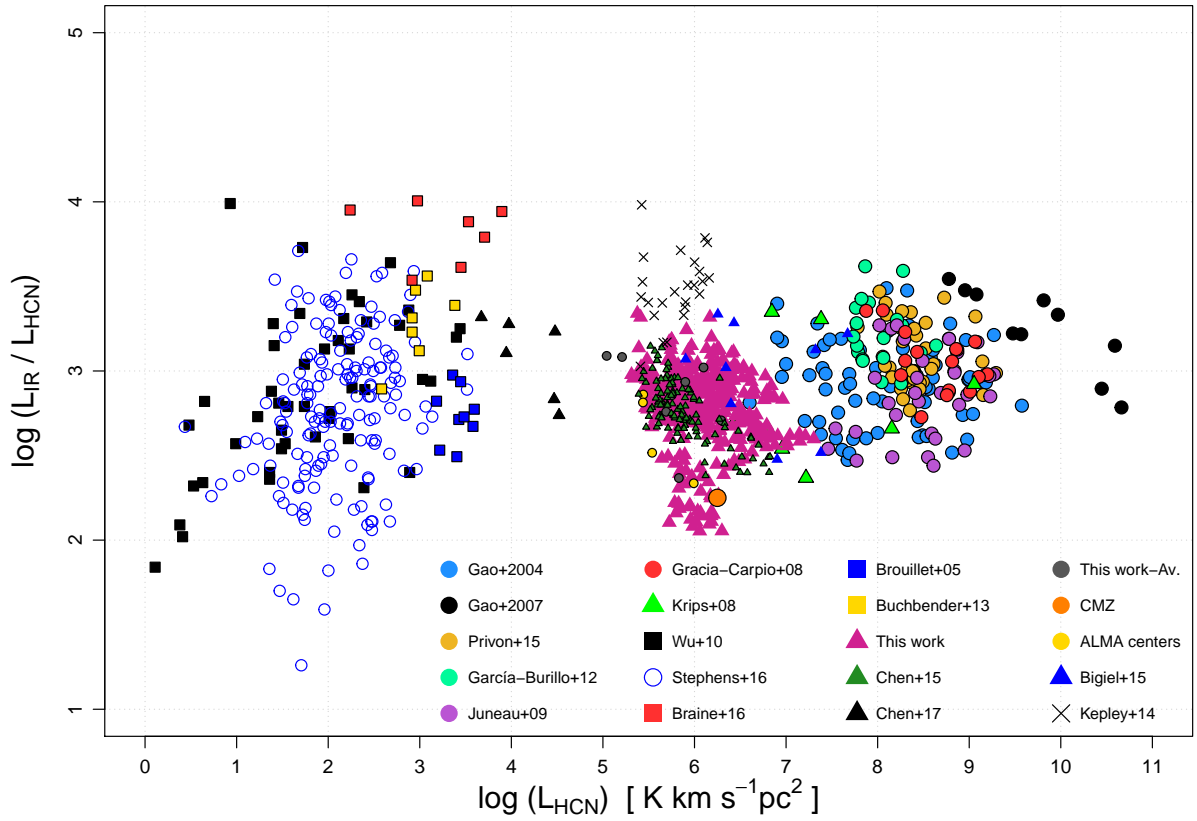


FIGURE 3.6. Variation of star formation efficiency of dense gas (as traced by $L_{\text{IR}}/L_{\text{HCN}}$) with the amount of dense gas observed (L_{HCN}). Our literature compilation is the same as described in Figure 3.5.

targets vary systematically across the disks. For a comparison with previous literature results, we adopt the fiducial conversion factors described in Section 3.1.1 and derive $f_{\text{dense}} = \Sigma_{\text{dense}}/\Sigma_{\text{mol}}$ values of ($\sim 0.3 - 30\%$). The range of dense gas fractions probed vary with galaxies, and the mean values in each galaxy disk range between 3.0% and 5.3%, therefore we consider a median value of $f_{\text{dense}} = 4\%$ as an indication. This value is in good agreement with the recent high resolution study of nearby galaxies presented by M. Gallagher et al. (subm.), who also find a median value of 4% for the inner kpc of four nearby galaxy disks. We find, however, lower f_{dense} values than [Usero et al. \(2015\)](#) and [Gao & Solomon \(2004\)](#) (median values of 8% and 12%), most likely attributed to the very different regions probed. The EMPIRE and ALMA can resolve wider areas (0.3 – 2kpc) in normal galaxy disks, recovering lower dense gas fractions.

In particular Figures 3.7, 3.8 and 3.9 show that the dense gas fraction across galaxy disks increases with increasing stellar surface density, molecular gas fractions and hydrostatic pressure. These results agree with previous observations (e.g., [Chen et al., 2015](#); [Usero et al., 2015](#); [Bigiel et al., 2016](#)): more dense gas is observed at lower galactocentric radii, where the molecular gas content traced by CO is higher, the stellar potential well is larger and there are higher interstellar pressures. We define bins of about 1 dex in stellar surface density, molecular-to-atomic gas fraction and hydrostatic pressure, and stack the emission of CO and HCN in those regions to compute the dense gas ratio. For each parameter, the resulting trends are over-plotted on these panels as blue points, showing that the trends are evident in the binned relation. In each figure, we include the HCN error bars from the stacks, which results from the propagation of the statistical $1 - \sigma$ uncertainties in the HCN data. These trends which confirm the dependence of the dense gas fraction on the environmental factor analyzed and help guiding the reader's eye.

Star formation efficiency of dense gas. The ratio of IR to HCN emission ($\text{SFE}_{\text{dense}}$, shown in Figures 3.10, 3.11 and 3.12) is directly related to the dense gas star formation efficiency. In contrast to the observed trends in the dense gas fractions, $\text{SFE}_{\text{dense}}$ generally decreases towards regions of high stellar surface density, high molecular fractions and high pressure environments. Figures 3.10, 3.11 and 3.12 also show the resulting stacked spectra over the same binned regions as in Figures 3.7, 3.8 and 3.9, which recover emission from the low signal-to-noise regions and highlight in blue the decreasing trends of $\text{SFE}_{\text{dense}}$ towards the centers of galaxies. Most galaxies show a systematic decrease in the IR-to-HCN intensity ratio of about one order of magnitude, from low pressure

regions to active galaxy centers. In other words: in regions where there is more dense gas, this gas appears to be strikingly less efficient at forming stars. It is also interesting to note that, whereas most galaxies show this gradually decreasing behavior towards their centers, the two galaxies with strong barred morphologies -NGC 2903 and NGC 3627- exhibit a quite flat $\text{SFE}_{\text{dense}}$ profile, but their centers behave quite differently: while $\text{SFE}_{\text{dense}}$ appears to also decrease abruptly for NGC 3627, it increases in the center of NGC 2903. We will further discuss in Section 3.3.3 how the galactic morphology and environment can drive the observed trends.

These results are in good agreement with previous observations of dense gas in nearby galaxy disks (see [Chen et al., 2015](#); [Usero et al., 2015](#); [Bigiel et al., 2016](#), M. Gallagher et al. *subm.*), and show that the physical conditions responsible for the dust/molecular emission in the ISM change systematically across galaxy disks. While the observed ratios, HCN-to-CO (\propto dense gas fraction) and IR-to-HCN ($\propto \text{SFE}_{\text{dense}}$), could directly drive variations in f_{dense} and $\text{SFE}_{\text{dense}}$ within galaxy disks; physical conditions in the ISM of these galaxy disks could also change systematically in such a way that, for example, the HCN conversion factor α_{HCN} , cancels the trends we observe ([Usero et al., 2015](#); [Shimajiri et al., 2017](#)).

3.2.6 Global environmental trends

We explore the global dependence of f_{dense} and $\text{SFE}_{\text{dense}}$ with environmental factors in galaxy disks, and the possible interpretations in more detail in Figure 3.13. Each panel row displays the stacked data points for all galaxies, reflecting the observed trends of f_{dense} (left) and $\text{SFE}_{\text{dense}}$ (right) with respect to the environmental parameters. Globally, the EMPIRE targets probe many orders of magnitude in stellar surface densities, molecular fractions and hydrodynamic pressure within their disks.

In order to quantify the observed trends between dense gas fractions, star formation efficiencies of dense gas, and the set of variables analyzed, we use simple linear fits from a total-least square minimization, employing the IDL procedures LINFIT. The minimization was performed in the log-log space and excluding upper-limits. Tables 3.2 and 3.3 provide the computed coefficients of the fits of f_{dense} and $\text{SFE}_{\text{dense}}$, respectively, for every galaxy and each physical parameter. The uncertainties on the coefficients are also given from the fit and they correspond to a 1σ level. In spite of not including our non detections for the fits, we can check that these values are compatible with the solutions provided by the least square minimization procedure, ensuring that their

exclusion does not bias our results. Tables 3.2 and 3.3 also include the Spearman’s rank correlation coefficient for every set of variables. This value is calculated using the IDL procedure `R CORRELATE` and provides a measurement of the strength of the relations in a non-parametric way, without taking non-detections into account. In our case, we consider that correlations are strong when the rank correlation coefficient is larger than 0.65.

As seen in each individual galaxy disk (Figures 3.7, 3.8 and 3.9), the observed dense gas fractions, traced by the HCN-to-CO ratio, systematically increase towards large values of stellar surface densities (Σ_* up to $10^3 - 10^4 M_\odot \text{pc}^{-2}$), high molecular-to-atomic gas fractions ($f_{\text{mol}} \sim 10$) and high pressure in the disk ($P_{\text{h}}/k \sim 10^6 - 10^7 \text{K cm}^{-3}$) for every galaxy. The main differences we find are related to differences in the abscissa axis, and so corresponding to the environmental variables. While all the sources show a common range in stellar surface densities, there are large offsets in the molecular fractions and ISM pressures probed in their disks. Nevertheless, the sense of the relations is very similar for every source. A slightly different picture is seen in the behavior of the $\text{SFE}_{\text{dense}}$, where some galaxies also show a somewhat flatter profile, whereas most of them show a declining IR-to-HCN ratio with any of the analyzed quantities, and similar slopes.

Dependence on Σ_* and molecular fractions. The variety of ISM parameters to explore is extremely large (e.g., shear and gravitational instabilities, dust abundance, radiation field, total gas surface density), however in this chapter we focus on a set of 3 variables (stellar surface densities, molecular gas fractions, and dynamical pressure) to study possible systematic variations in the dense gas fractions and the efficiency of dense gas. In particular, Σ_* and $f_{\text{mol}} = \Sigma_{\text{mol}}/\Sigma_{\text{atom}}$ are simple, independent quantities that allow us to quantify possible trends in a very straightforward way. Also, the HCN (1-0) observations in our galaxy sample span a range of ~ 1.8 dex in stellar surface density and ~ 3.0 dex in molecular-to-atomic gas ratio, reflecting a large range of environmental conditions within the selected sources. The systematic increase in the HCN-to-CO ratio we see towards large values of Σ_* and f_{mol} agree with our expectation of finding more dense gas in regions where the mean density is higher (as indicated by f_{mol}) and where the stellar potential well can facilitate the accumulation of more and denser gas (as indicated by higher values of Σ_*).

As for the efficiency with which dense gas can form stars, $\text{SFE}_{\text{dense}}$, most galaxies show the opposite trend with Σ_* and f_{mol} : dense gas is less efficient at forming stars in regions with higher stellar surface densities and molecular-to-atomic gas fractions,

therefore regions with higher average gas density. Nevertheless, two galaxies show different trends: NGC 628 and NGC 2903. While the case of NGC 628 shows a much flatter profile for $\text{SFE}_{\text{dense}}$, this is most likely due to a poor recovery of the line emission from the non-detections. The number of high SNR lines of sight is very limited in this galaxy and the uncertainties on the stacked profiles is much higher, therefore it is difficult to conclude on a significant correlation. NGC 2903 displays a flat $\text{SFE}_{\text{dense}}$ profile in its outer disk, but the central kpc of this galaxy shows a much higher efficiency than the rest of the points, as opposed to what we see in the rest of EMPIRE targets, and also contrary to previous observations of the Galactic center which show a much lower efficiency in the CMZ (e.g., Jones et al., 2012; Longmore et al., 2013; Barnes et al., 2017). Since NGC 2903 is the only galaxy of our sample which has not been part of SINGS or KINGFISH and therefore has no *Herschel* observations, we obtained the TIR by empirical conversion of the $24\mu\text{m}$ photometry. We explored the same trends by computing TIR for the rest of the targets only using the $24\mu\text{m}$, finding no significant changes in the observed trends when estimating TIR with the conversions of Murphy et al. (2011). Therefore, some other physical reason must be causing the increase in the dense gas efficiency.

The Spearman’s rank correlation coefficients provided in Tables 3.2 and 3.3 show tight correlations between f_{dense} and $\text{SFE}_{\text{dense}}$ and Σ_* and f_{mol} . The fitting results indicate that the relations are somewhat steeper (globally) in both quantities with f_{mol} rather than with Σ_* , and the coefficients are in good agreement on average with the results found by Usero et al. (2015), Bigiel et al. (2016) (using this same dataset for M51) and ALMA high spatial resolution data from M. Gallagher et al. (subm.).

Environmental dependence with pressure. The large variations we find in the dense gas fractions (of about one order of magnitude) within galaxy disks suggest that physical conditions in the overall molecular gas are very distinct among galaxy disks. The fact that dense gas appears to correlate with the molecular-to-atomic gas fraction and stellar surface density in these disks is indicative of the presence of some other physical quantity driving the formation of dense gas. In particular, the presence of larger amounts of dense gas in the inner regions of galaxies suggests that the internal pressure there is much higher than in the galactic disks. These two quantities (Σ_* and f_{mol}) are intrinsically connected by the ambient pressure, which plays a key role regulating the dynamics of the midplane gas governed by hydrostatic equilibrium. Several authors have hypothesized that the molecular and dense gas fraction in a galaxy disk are determined by the mean hydrostatic pressure (e.g., Spergel & Blitz, 1992; Elmegreen, 1993; Helfer &

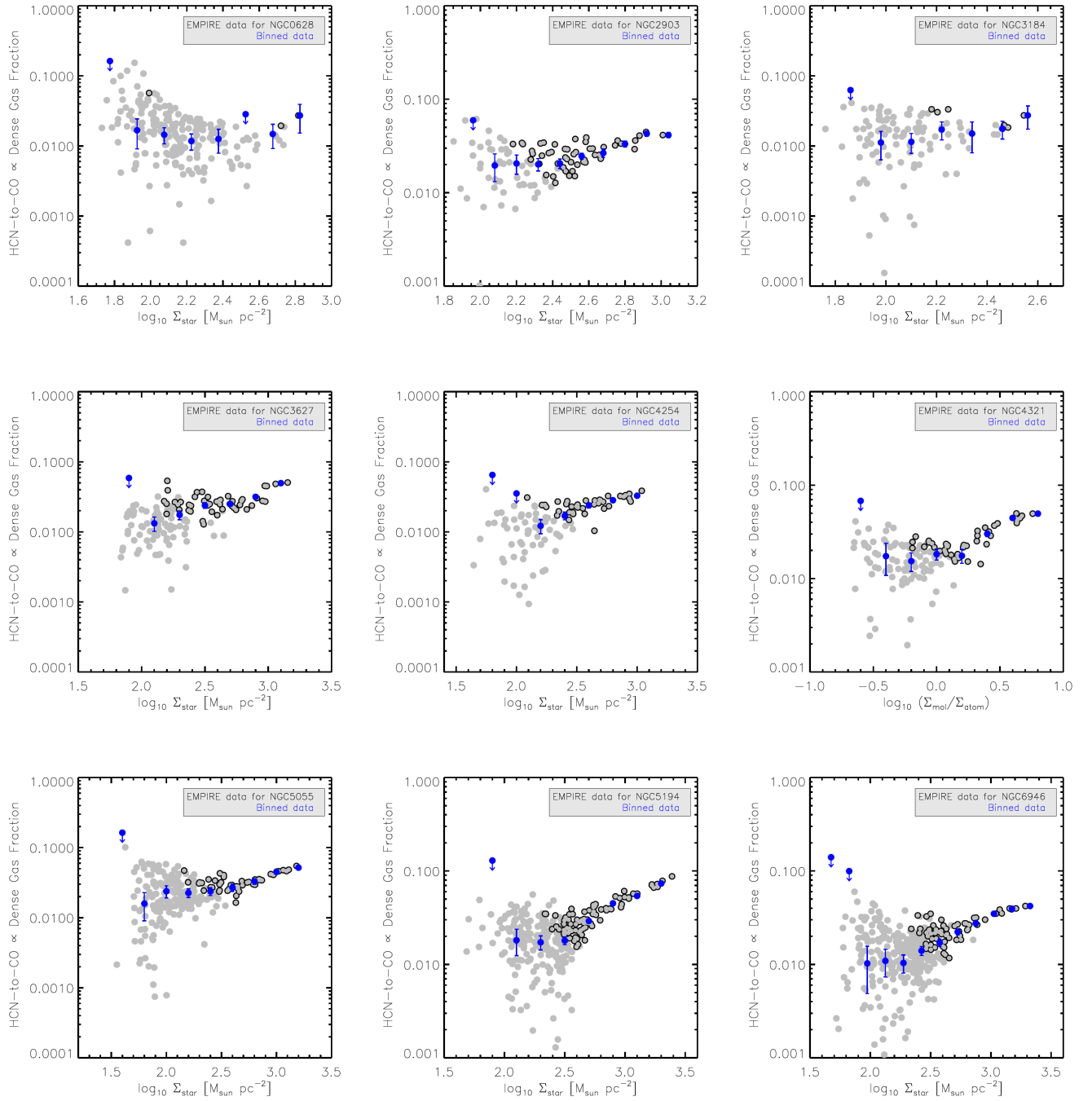


FIGURE 3.7. HCN-to-CO ratio, tracing the dense gas fraction, as a function of local stellar surface density, Σ_* . Each data point represents a \sim kpc size measurement per line of sight. Grey points with black outlines show regions where HCN is detected at $S/N > 3$, whereas light grey points without outline show points with lower S/N . Blue points show the stacked HCN data, which recovers signal in low S/N regions; downward arrows give a lower limit to the ratio in those regions where HCN is not detected. The dense gas fraction in all galaxy disks appears to be lower at high stellar surface densities.

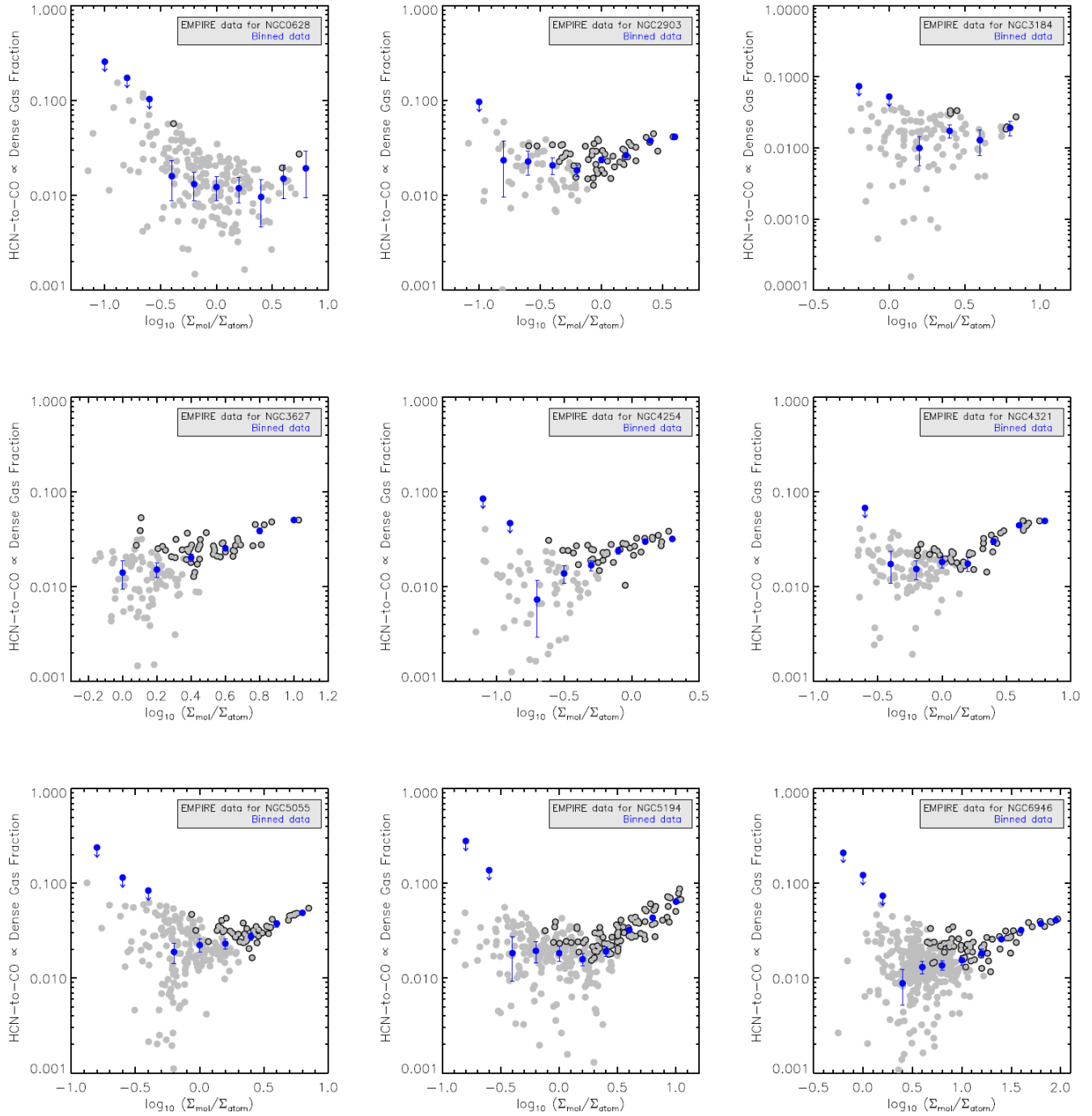


FIGURE 3.8. HCN-to-CO ratio, tracing the dense gas fraction, as a function of the molecular-to-atomic gas ratio, f_{mol} . The description of each data point is the same as in Figures 3.7 and 3.10. The dense gas fraction in all galaxy disks appears to decrease for lower values of molecular-to-atomic gas ratio.

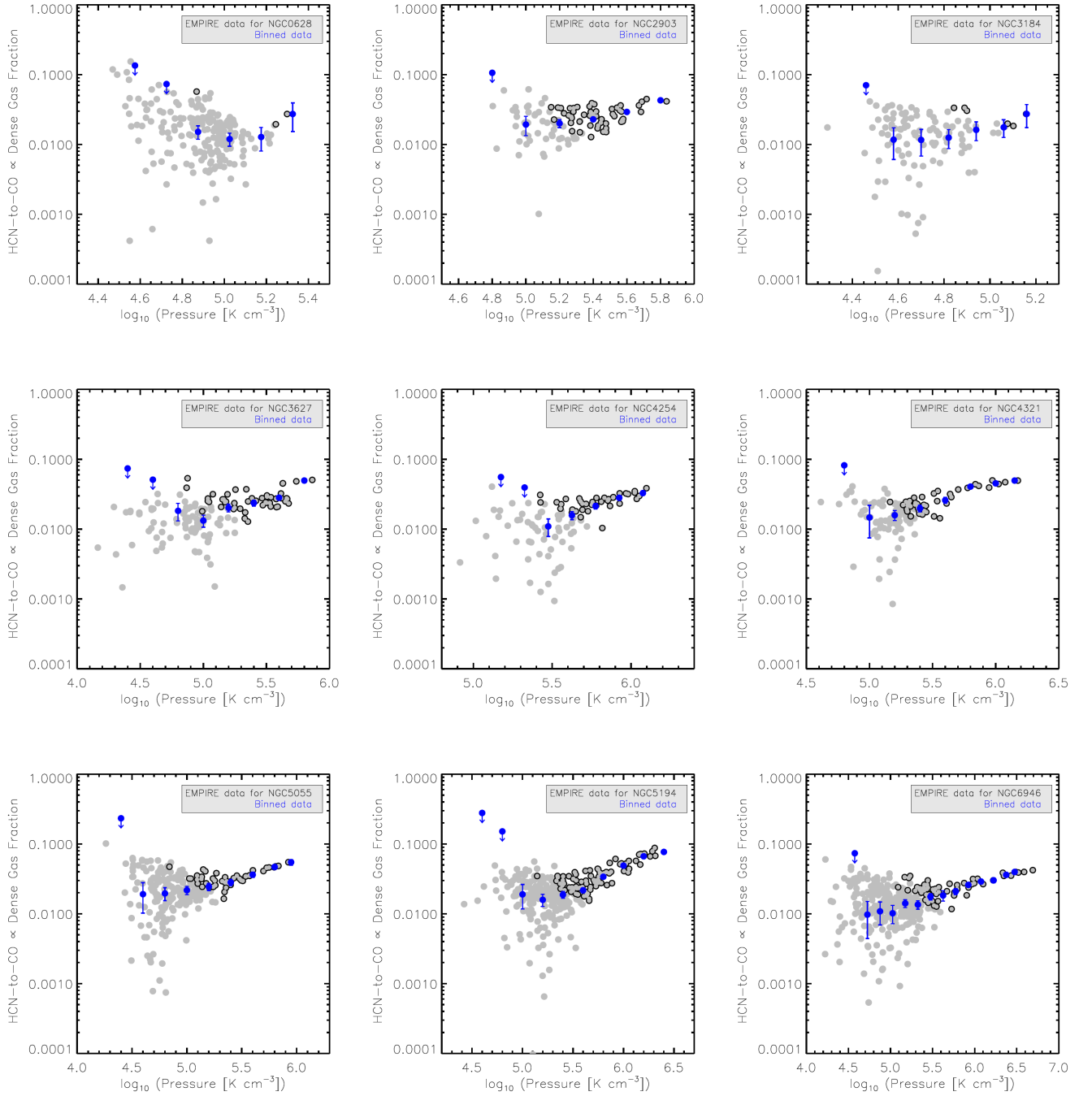


FIGURE 3.9. HCN-to-CO ratio, tracing the dense gas fraction, as a function of the external hydrostatic pressure, P_{ext} . The description of each data point is the same as in Figures 3.7 and 3.10. The dense gas fraction in all galaxy disks appears to increase for higher ISM pressures.

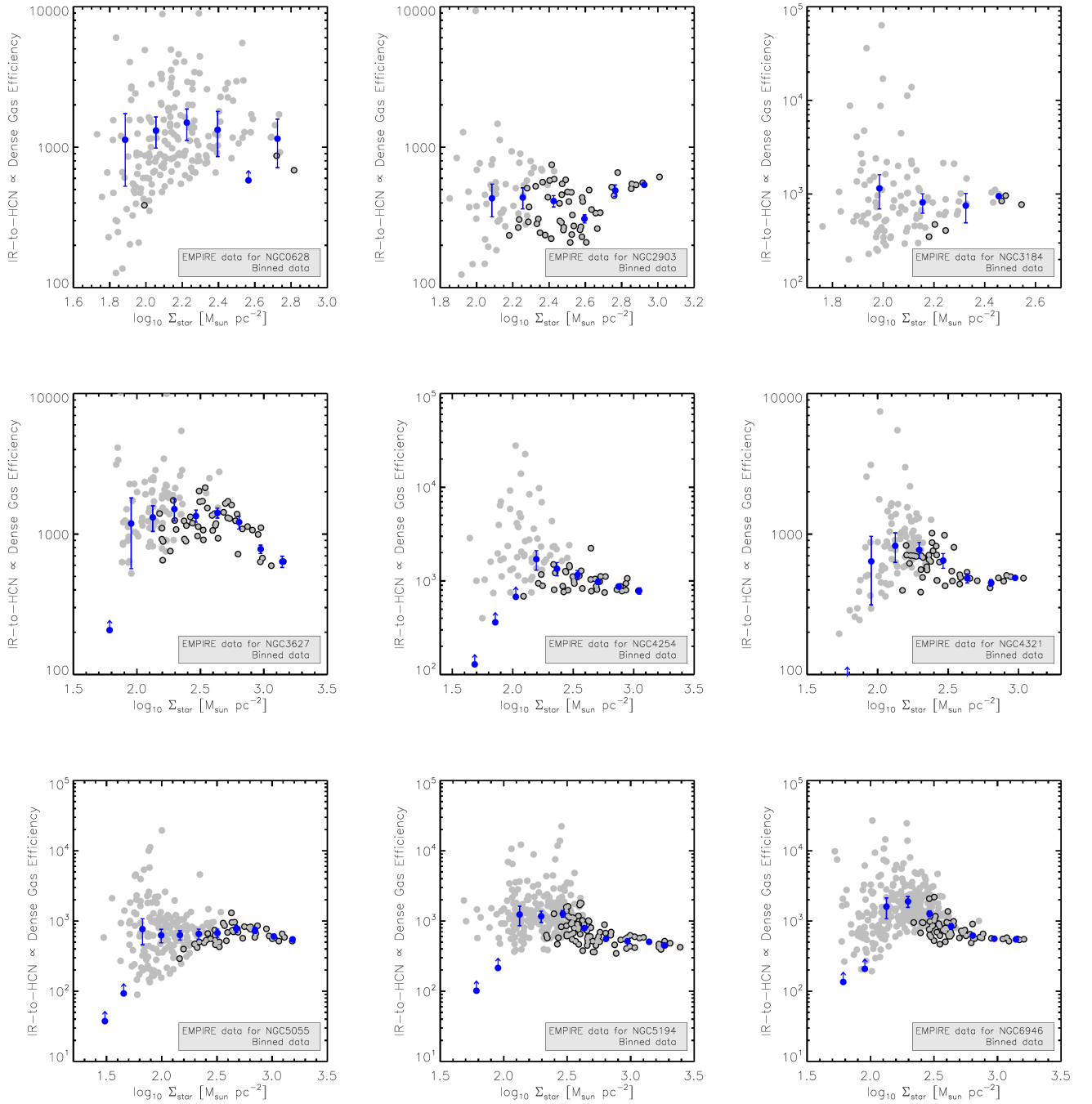


FIGURE 3.10. IR-to-HCN ratio, tracing the efficiency of dense gas, as a function of local stellar surface density, Σ_* . The description of each data point is the same as in Figure 3.7. The dense gas efficiency to form stars appears to increase with higher values stellar surface densities.

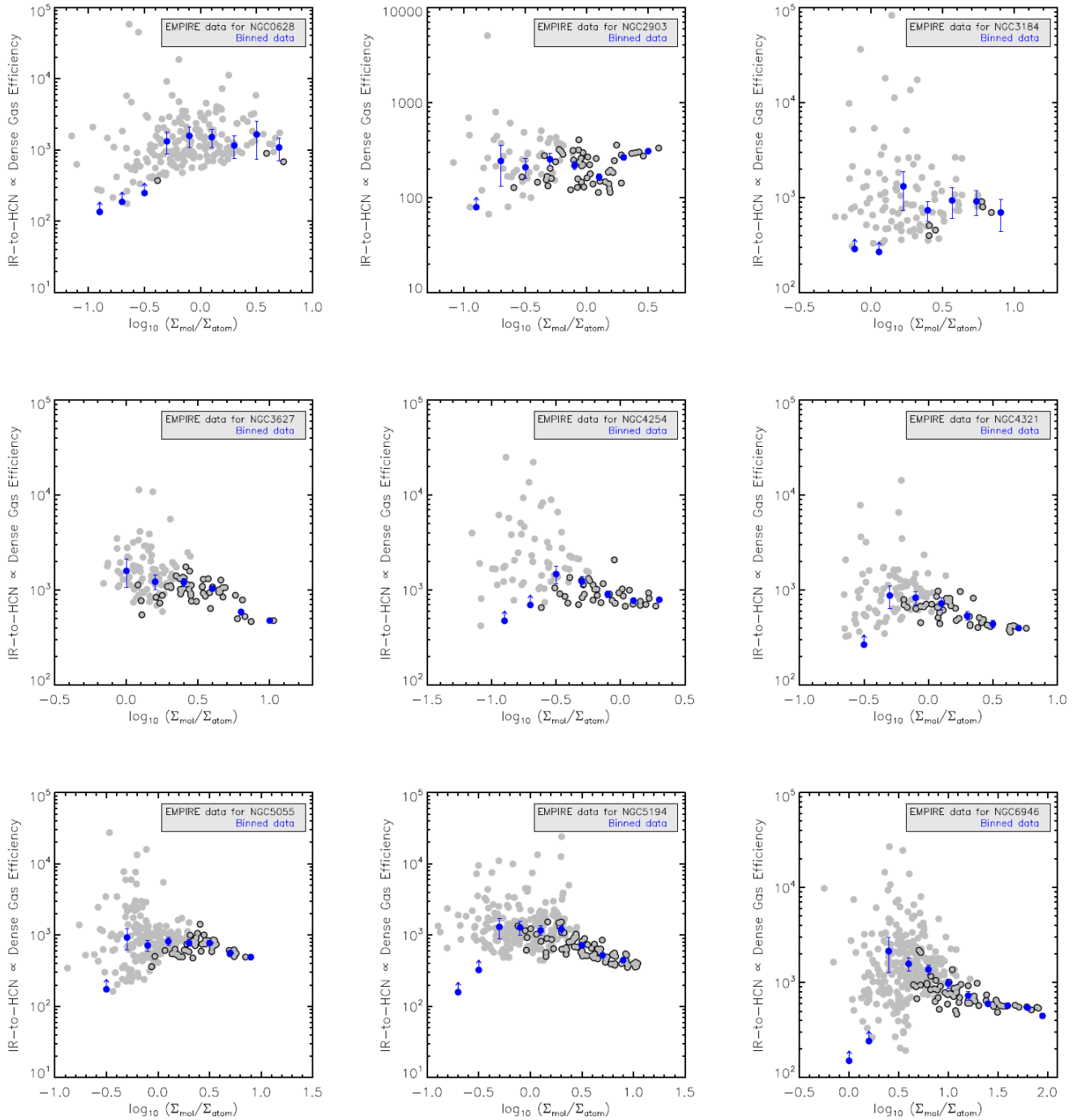


FIGURE 3.11. IR-to-HCN ratio, tracing the efficiency of dense gas, as a function of the molecular-to-atomic gas ratio, f_{mol} . The description of each data point is the same as in Figures 3.7 and 3.10. The dense gas efficiency fraction appears to decrease for higher values of the molecular-to-atomic gas ratio.

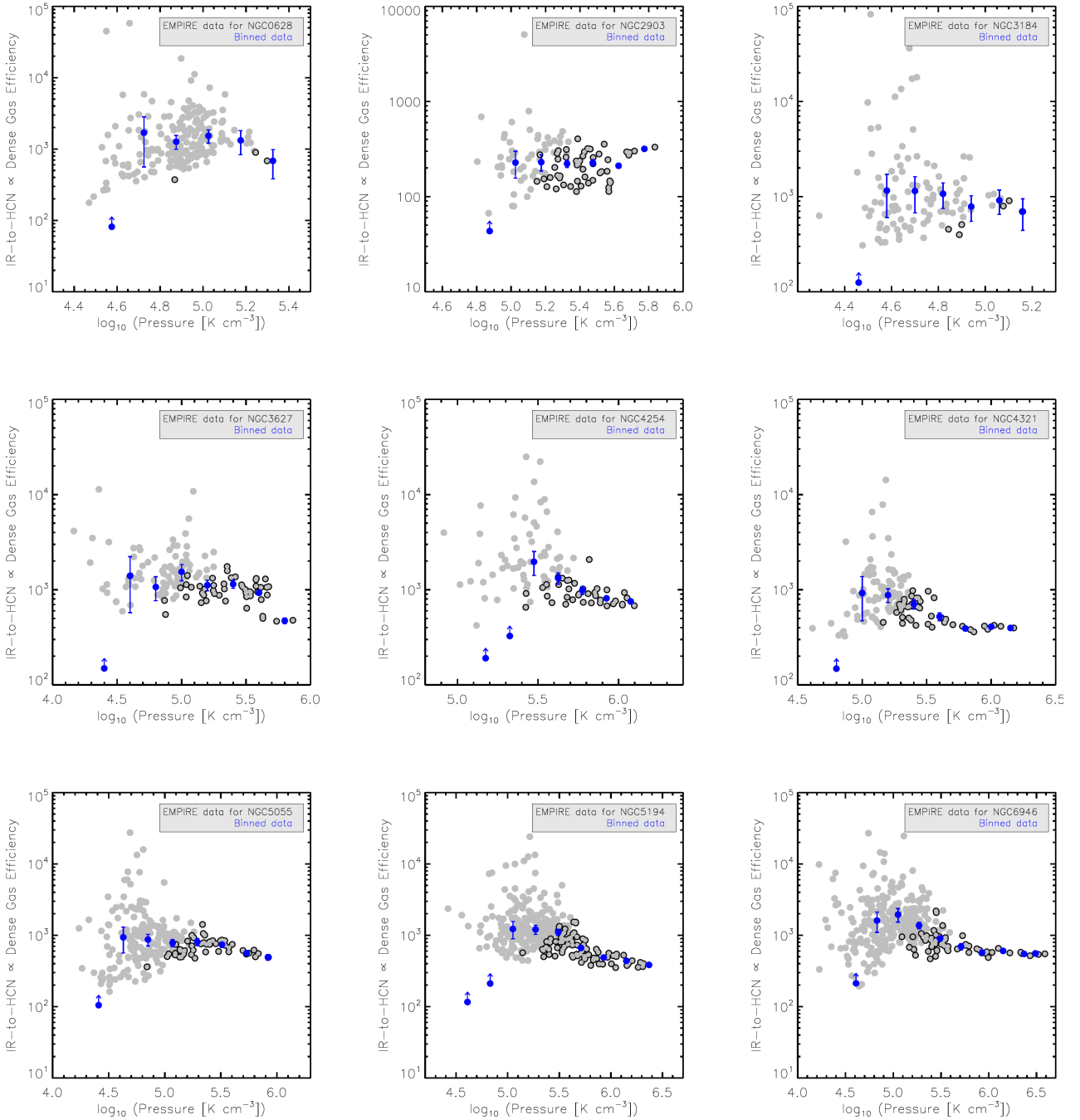


FIGURE 3.12. IR-to-HCN ratio, tracing the efficiency of dense gas, as a function of the external hydrostatic pressure, P_{ext} . The description of each data point is the same as in Figures 3.7 and 3.10. The dense gas efficiency appears to decrease for higher values of the ISM pressure.

Blitz, 1997), which simultaneously should control the rate of star formation, enabling us to make prescriptions based on the external pressure for star formation on global scales (Blitz & Rosolowsky, 2004). Some of the most recent studies of dense gas in nearby galaxies (Usero et al., 2015; Bigiel et al., 2016, M. Gallagher et al. subm.) have highlighted the idea of a context dependent role for star formation where the ambient pressure sets the average density of a star-forming cloud. Moreover, these clouds constitute over densities where stars form, causing that the emission of dense gas tracers will come from different mean densities, depending on the local environment. In this study we explore the role of the dynamical equilibrium pressure by analyzing the very different morphologies probed by the full EMPIRE survey galaxies.

The hydrostatic pressure is computed as described in Section 3.1.1, and its main contributions are self-gravity of the gas in the galaxy disk and the gas weight which is following the gravitational potential due to the presence of stars. The individual galaxy plots of Figure 3.9 and the bottom left panel of Figure 3.13 shows that the dense gas fractions of every galaxy relate tightly with the external pressure. This is further supported by the Spearman’s rank correlation coefficients provided in Table 3.2, much larger than 0.65 for all galaxies except for NGC 628, where the detected HCN emission is very limited. In addition, the observed ambient pressures (in K cm^{-3}) vary over almost 2.5 dex, probing very distinct galaxy environments within the different galaxy disks.

On the contrary, the efficiency of dense gas to form stars appears to be much lower in regions of high hydrostatic pressure, as seen in Figure 3.12. The fit results also indicate a strong anti-correlation for all sources but NGC 2903, whose $\text{SFE}_{\text{dense}}$ profile appears flat with the exception of the inner-most region, as seen in the previous analysis of Σ_* and f_{mol} . These results are in good agreement with the recent trends reported by M. Gallagher et al. (subm.) for the inner regions of 4 nearby galaxies overlapping EMPIRE at high resolution, and also with the recent predictions by Meidt (2016).

3.2.7 Are variations in the $\text{SFE}_{\text{dense}}$ real?

Our main results for star formation efficiencies in the different galaxy disks we analyzed suggest a variation in the SFE with respect to several environmental parameters, somehow interconnected (radius, stellar surface densities, molecular-to-atomic gas fractions

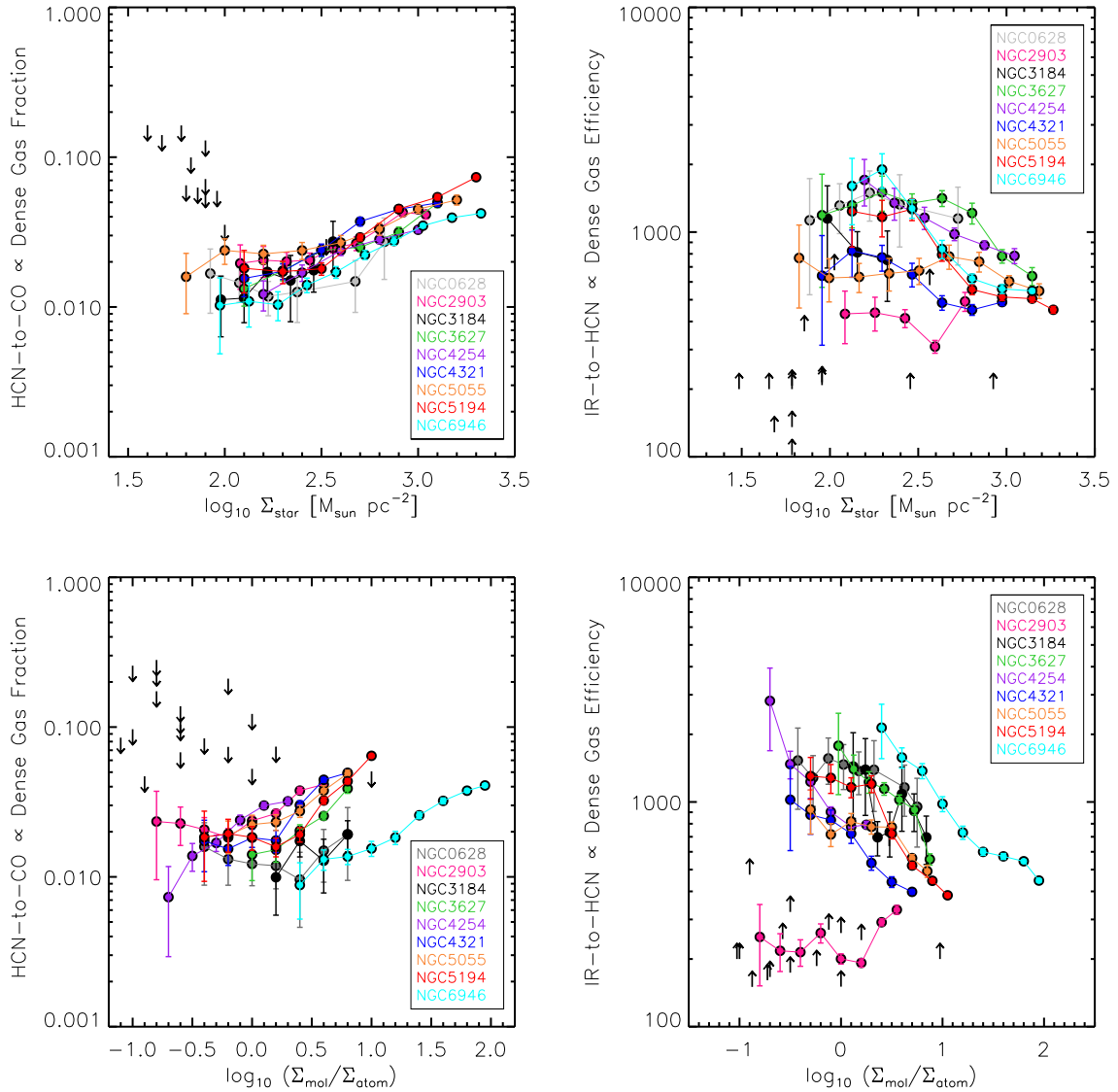


FIGURE 3.13. Dense gas fraction (left) and star formation efficiency of dense gas (right) versus stellar surface densities (top) and molecular gas fraction (bottom). Individual circles show the stacked measurements with respect to each environmental parameter, as shown in blue in Figures 3.7-3.10 and 3.8-3.12. Arrows show upper (lower) 3σ limits for the dense gas fractions (star formation efficiencies).

Parameters:	HCN/CO vs.		Σ_*
Galaxy	<i>A</i>	<i>B</i>	Rank correlation
NGC 628	-2.3±0.5	0.2±0.2	0.3
NGC 2903	-2.9±0.2	0.5±0.1	0.96
NGC 3184	-3.1±0.7	0.6±0.3	0.94
NGC 3627	-3.0±0.2	0.5±0.1	1.00
NGC 4254	-2.8±0.2	0.4±0.1	1.00
NGC 4321	-2.9±0.1	0.5±0.1	1.00
NGC 5055	-2.5±0.1	0.37±0.05	0.93
NGC 5194	-3.3±0.1	0.65±0.03	0.89
NGC 6946	-3.0±0.1	0.50±0.03	0.98
$\Sigma_{\text{mol}}/\Sigma_{\text{atom}}$			
NGC 628	-1.8±0.1	0.1±0.2	0.1
NGC 2903	-1.61±0.02	0.34±0.05	0.76
NGC 3184	-1.9±0.2	0.3±0.3	0.8
NGC 3627	-2.0±0.1	0.7±0.1	1.00
NGC 4254	-1.59±0.02	0.4±0.1	1.00
NGC 4321	-1.72±0.03	0.6±0.1	0.93
NGC 5055	-1.71±0.04	0.5±0.1	1.00
NGC 5194	-1.88±0.03	0.68±0.03	0.71
NGC 6946	-2.17±0.04	0.41±0.02	1.00
Pressure			
NGC 628	-3±2	0.3±0.4	0.4
NGC 2903	-4.8±0.4	0.6±0.1	1.00
NGC 3184	-5±2	0.6±0.3	0.94
NGC 3627	-4.8±0.4	0.6±0.1	0.94
NGC 4254	-5.6±0.6	0.7±0.1	1.00
NGC 4321	-4.4±0.3	0.51±0.05	1.00
NGC 5055	-3.8±0.3	0.43±0.05	1.00
NGC 5194	-5.1±0.2	0.17±0.04	0.93
NGC 6946	-3.8±0.1	0.37±0.03	0.94

TABLE 3.2. Rank correlation coefficients and fit parameters of the dense gas fractions (HCN/CO) versus different quantities: Σ_* , molecular fraction and pressure. Fit of the form $y = 10^A x^B$.

Parameters:	IR/HCN vs.		Σ_*
Galaxy	A	B	Rank correlation
NGC 628	3.2 ± 0.6	-0.04 ± 0.3	0.30
NGC 2903	2.6 ± 0.3	0.01 ± 0.12	0.10
NGC 3184	4.0 ± 1.5	-0.5 ± 0.6	-1.00
NGC 3627	4.2 ± 0.2	-0.4 ± 0.1	-0.50
NGC 4254	4.0 ± 0.2	-0.4 ± 0.1	-1.00
NGC 4321	3.3 ± 0.2	-0.2 ± 0.1	-0.70
NGC 5055	3.0 ± 0.1	-0.08 ± 0.04	-0.40
NGC 5194	3.9 ± 0.1	-0.37 ± 0.03	-0.93
NGC 6946	4.0 ± 0.1	-0.41 ± 0.04	-0.96
$\Sigma_{\text{mol}}/\Sigma_{\text{atom}}$			
NGC 628	3.1 ± 0.1	-0.1 ± 0.2	-0.69
NGC 2903	2.33 ± 0.02	0.26 ± 0.05	0.31
NGC 3184	3.0 ± 0.2	-0.1 ± 0.3	-0.68
NGC 3627	3.29 ± 0.05	-0.54 ± 0.09	-1.00
NGC 4254	2.95 ± 0.01	-0.33 ± 0.07	-0.94
NGC 4321	2.86 ± 0.03	-0.37 ± 0.05	-1.00
NGC 5055	2.94 ± 0.04	-0.26 ± 0.06	-0.78
NGC 5194	3.09 ± 0.03	-0.48 ± 0.03	-0.98
NGC 6946	3.31 ± 0.04	-0.33 ± 0.02	-1.00
Pressure			
NGC 628	5 ± 2	-0.4 ± 0.4	-0.70
NGC 2903	0.8 ± 0.4	0.3 ± 0.1	0.00
NGC 3184	5 ± 2	-0.4 ± 0.3	-0.94
NGC 3627	5.9 ± 0.4	-0.5 ± 0.1	-0.72
NGC 4254	5.9 ± 0.6	-0.5 ± 0.1	-1.00
NGC 4321	4.4 ± 0.3	-0.29 ± 0.05	-0.89
NGC 5055	4.2 ± 0.3	-0.25 ± 0.05	-0.96
NGC 5194	5.0 ± 0.2	-0.39 ± 0.02	-1.00
NGC 6946	4.3 ± 0.2	-0.24 ± 0.02	-0.95

TABLE 3.3. Rank correlation coefficients and fit parameters of the star formation efficiencies (IR/HCN) versus different quantities: Σ_* , molecular fraction and pressure. Fit of the form $y = 10^A x^B$.

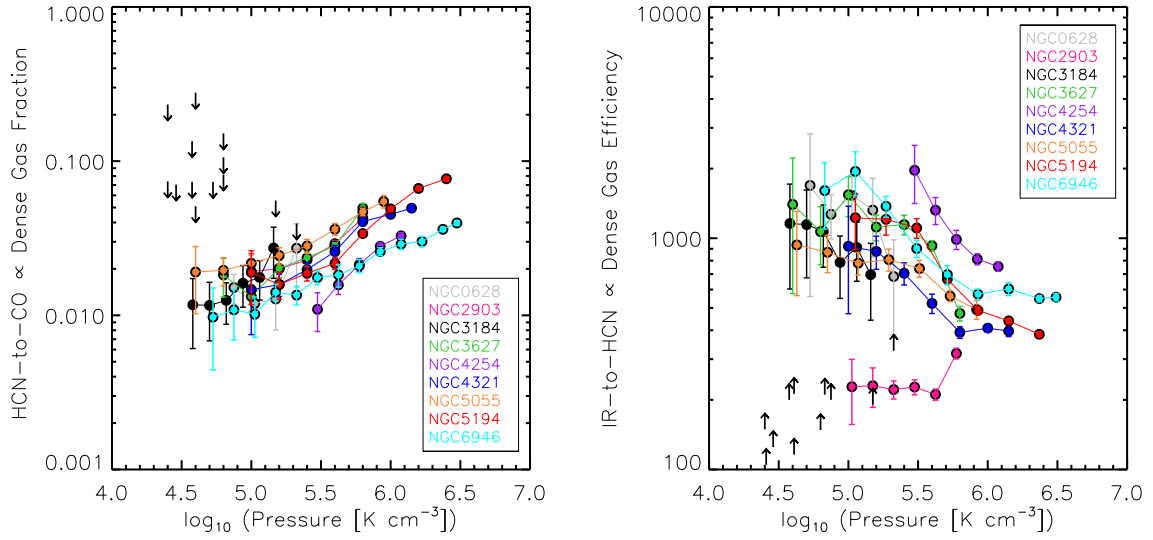


Figure 3.13: continued. Dense gas fraction (left) and star formation efficiency of dense gas (right) versus hydrostatic pressure.

and hydrostatic pressure, Figures 3.7 to 3.12). Before we continue to interpret the physical mechanism behind the line ratio variations, we assess whether they could be driven by the large noise in the HCN data. We build a simple Montecarlo test that includes the uncertainties on the data which can be significant. The basic premise of this model is that the underlying true ratios:

$$(3.9) \quad \frac{\text{IR}}{\text{HCN}} \propto C,$$

are constant, C . We compute random values that will be added to our HCN emission measurements as randomly generated values within the range of actually observed HCN uncertainties in our data. After that, we compute new, *synthetic* ratios as:

$$(3.10) \quad \frac{\text{IR}}{\text{HCN}} = \frac{C \times \text{IR} + \Delta(\text{HCN})}{\text{IR}}.$$

As seen above, we perturb the HCN observations with some random value, which is realistic within our observations to check if the observed scatter in Figures 3.7 to 3.12 can be explained. We perform 100000 realizations of the experiment and we compute the mean IR-to-HCN ratio obtained among them, as well as the standard deviation from the mean. We also repeat the experiment for a range of possible values of C , which is initially determined from the positions in the galaxy disks where we have high SNR measurements of HCN.

Figure B.1 in the Appendix B shows the simple Montecarlo test for the EMPIRE dataset. It displays the HCN-to-IR ratio as a function of the IR emission computed in every individual sampling point for every particular galaxy. The EMPIRE original observations are shown as dark blue points, whereas the light blue points reflect the mean value of a constant HCN/IR model from 100000 realizations. In those models, as described above, the HCN value includes a random, realistic perturbation within the range of the observed uncertainties. The various panels show the different cases obtained depending on the constant chosen for the model, which is initially inferred from our high SNR measurements in the galaxy. The error bars are the (1σ) standard deviations from the modeled points in 100000 realizations. Every panel of Figure B.1, for all galaxies, shows that there are variations in the HCN-to-IR ratio for both high and low IR values, and the amplitude of these variations cannot be explained by our Montecarlo test. Therefore there are real and systematic variations beyond what we can expect from the noise; there must be physical and chemical processes responsible for the even larger scatter at low IR values.

3.3 Discussion

3.3.1 Interpreting line ratios

Line intensity ratios can provide useful information about the gas physical and chemical conditions. We study different lines that span several orders of magnitude in critical densities (see Table 2.2). While lines with high critical densities such as HCN(1-0) are efficiently excited in high density gas, mostly located at the central parts of our targets; lines with low critical densities such as $^{12}\text{CO}(1-0)$ can be excited in more diffuse gas, therefore its emission can be more extended, having a higher beam filling factor.

One of the main concerns when comparing line ratios from single dish observations is the lack of spatial information. Therefore, can HCN/CO be a good tracer for the dense gas fraction? We have shown that the HCN-to-CO ratio strongly correlates with the stellar surface density (Σ_*) and the molecular gas fraction ($f_{\text{mol}} \propto \text{CO}/\text{HI}$), and the same occurs to other tracers of dense gas (HCO^+ and HNC). Figure 3.4 also shows the typical dense gas fractions measured over different regions in the nearby galaxy population that correlate with the CO 1-0 emission: high HCN/CO, HCO^+ /CO and HNC/CO values are found in regions with high surface brightness of CO. Given the large differences in critical densities for these molecules, the trends seen in HCN/CO, HCO^+ /CO and

HNC/CO are indicative of a changing density in the media.

Dense gas line ratios such as HCO^+/HCN and HNC/HCN are also interesting because they are not only sensitive to gas density, but also to chemical processes such as ionization due to cosmic rays, and can be used to distinguish X-ray-dominated regions (XDRs) from UV-ionized or photodissociation regions (PDRs). Thus, they are useful to probe distinct dense molecular environments. Our measured HCO^+/HCN line ratios are close to unity, with a mean value of 0.8. The HNC-to-HCN line ratio is generally lower, with a mean value 0.4 in the galaxy centers and slightly increases towards the outskirts of galaxies. These values are compatible with observations in the CMZ and Galactic GMCs (e.g., [Jones et al., 2012](#)), nearby galaxies (such as M51, NGC 253 and NGC 6946 [Chen et al., 2015](#); [Meier et al., 2015, 2014](#)), and a number of LIRGs ([Loenen et al., 2008](#)).

Several scenarios can explain the line ratios we report in this chapter. The centers of galaxies are regions where we expect to find higher densities and high kinetic temperatures. The HCO^+/HCN line ratio is more sensitive to density changes, given that the critical density for HCO^+ is about one order of magnitude lower than HCN, therefore we would expect to find low HCO^+/HCN ratios in the centers in comparison to the outer regions. In addition, HCO^+ is a molecular ion and would tend to recombine faster with electrons at higher densities (e.g., [Papadopoulos et al., 2007](#)), and therefore its abundance would decrease. The HNC/HCN is more sensitive to the radiation field and therefore, kinetic temperature: HNC is easily converted into HCN in those regions where the gas is hotter ([Schilke et al., 1992](#)).

Most of our regions show HCO^+/HCN less, but close to unity, and change little over the galaxy disks. This is indicative of HCN and HCO^+ being optically thick as observed in [Jiménez-Donaire et al. \(2017a\)](#), and slightly subthermal in the galaxies nuclei ([Knudsen et al., 2007](#); [Meier et al., 2015](#)). In high density gas, HCO^+/HCN slightly lower than one can be reproduced in UV-dominated regions (PDRs), with gas densities $n > 10^5 \text{ cm}^{-3}$. However it is also possible that similar values are obtained if the gas we trace is low-density $n < 10^5 \text{ cm}^{-3}$ in XDRs for H_2 column densities lower than 10^{22} cm^{-2} ([Meijerink et al., 2007](#)). In a study of HCN, HCO^+ and HNC line ratios, [Loenen et al. \(2008\)](#) classify these ratios for a sample of LIRGs and differentiate the two excitation regimes dominated by XDRs or PDRs. In their study, almost all the sources lie in the PDR regime, and so do our values. Therefore we consider the XDR dominated emission unlikely in the scales we probe with EMPIRE.

Only two galaxies, NGC 4254 and NGC 6946, show larger HCO^+ -to-HCN ratio values

(~ 1.2 - 3) in their arm/interarm regions than in their centers. These values are also typically found in high density ($n > 10^5 \text{ cm}^{-3}$) XDRs for H_2 column densities larger than 10^{23} cm^{-2} (Meijerink et al., 2007) due to the high ionization degree in these regions. In addition, metallicity gradients within galaxy disks could be responsible for some of the variations in the HCO^+ -to-HCN ratios. Low N/O abundance ratios have been found in low-metallicity galaxies (e.g., Nishimura et al., 2015, 2016) as a consequence of the small amount of nitrogen produced by massive stars (Vincenzo et al., 2016). As a result, the high HCO^+ -to-HCN ratios can be explained as a reduction of nitrogen-bearing molecules like HCN or HNC.

All these interpretations assume that line ratios are directly related to relative abundances, which is not always the case when the emission lines under consideration have different excitation properties and are optically thick, as it occurs with HCO^+ and HCN, for example. A simple and logical explanation for the low HCO^+ in comparison to HCN is that the critical density for HCO^+ is about an order of magnitude lower, and therefore has a larger beam filling factor. The HCO^+/HCN line ratio would tend to be larger in lower density regions, as observed for the interarm areas in NGC 4254 and NGC 6946.

3.3.2 Zooming into the galaxy centers

The picture where a universal relationship connects the star formation rate and dense molecular gas content in a galaxy disk is still under active debate. Our results clearly contradict this particular scenario, and also the recent studies of dense gas emission in nearby galaxies (e.g., Usero et al., 2015; Chen et al., 2015): $\text{SFE}_{\text{dense}}$ systematically drops towards the centers of galaxy disks, for almost all targets in our sample. This appears to be the general behaviour with respect to any physical quantity we want to study. What regulates the dense gas content in the galaxy disk and drives the low star formation efficiencies?

In our own Milky Way there is observational evidence that the SFR in the inner ~ 500 pc of the Galactic center, the central molecular zone (CMZ) is strongly suppressed, and is therefore significantly lower than what is predicted by the Schmidt-Kennicutt relation (Longmore et al., 2013). The CMZ contains a large concentration of molecular gas and about 80% of the total dense gas in the Galaxy (Morris & Serabyn, 1996). It constitutes a site of recent star formation (Yusef-Zadeh et al., 2009) and shows a very rich chemistry with detected complex molecules (e.g., Requena-Torres et al., 2008), shock

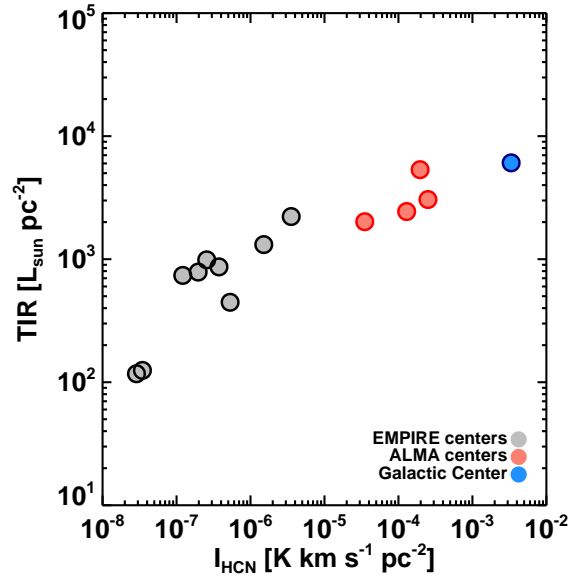


FIGURE 3.14. HCN surface brightness emission as a function of the TIR emission averaged over the beam size corresponding to the different observations. In grey circles we display the centers of the galaxies observed in the EMPIRE survey (inner ~ 1 kpc), and we compare them with higher resolution measurements of four nearby galaxy centers observed with ALMA (inner ~ 500 pc, M. Gallagher et al., *subm.*) shown as red circles. We include recent observations for the CMZ of our Galactic center in HCN (Jones et al., 2012) and TIR (Barnes et al., 2017) for a comparison with a well-known, studied extreme environment.

tracers (SiO, Martín-Pintado et al., 1997) and dense gas tracers such as HCN (Jackson et al., 1996). Its extreme properties -e.g., large average densities, pressure, temperature, interstellar radiation field, high velocity dispersions- are comparable to those seen in extragalactic centers (Kruijssen & Longmore, 2013).

The extreme environments of galaxy centers are challenging the current star formation theories, and therefore it is important to understand the physical processes regulating the SFR in those regions. Most likely, it is not only one parameter causing this underproduction of stars, but rather a combination of physical processes. Recent studies have provided possible explanations for the low SFR in particular in the CMZ of the Galactic center:

- The SFE could appear to be much lower in the CMZ if there are systematic errors when converting observables to gas masses and SFRs. In a recent study, Barnes et al. (2017) compared different SFR diagnostics: integrated light measurements

and counts of young stellar objects (YSOs), and found that the SFRs agree within a factor of two.

- There is some physical mechanism making the CMZ very inefficient during a long time-scale. It could be possible that the large internal velocity dispersions could disrupt the compact star-forming regions before they can collapse and form stars (Longmore et al., 2013). Another possibility is that a high turbulence level can suppress $\text{SFE}_{\text{dense}}$ efficiently. This has been tested in simulations of CMZ-like molecular clouds (Bertram et al., 2015), but the predicted SFR is not as low as the observed values. These simulations, however, lack important drivers of turbulence such as stellar winds, supernova feedback and strong magnetic fields. Magnetic fields have been observed to be ~ 1000 times stronger in the Galactic center than in the solar neighborhood, which could lower the SFR by slowing down the collapse of dense cores (Pillai et al., 2015). In addition, it is not yet clear what would be the effect of considering only solenoidal velocity modes, which could strongly suppress the SFE (Federrath et al., 2010; Federrath, 2015).
- The last hypothesized possibility is that the low SFR in the CMZ is due to an episodic cycle of gas inflow (Kruijssen et al., 2014). In that case, the dense gas would build up due to spiral instabilities until it becomes gravitationally unstable, giving rise to an intense episode of star formation. After that, turbulent motions are driven by feedback from the newly formed stars, which increases the virial ratio of the gas and stars formation is suppressed. Several authors have studied this possibilities with distinct models (e.g., Emsellem et al., 2015; Krumholz & Kruijssen, 2015; Suzuki et al., 2015; Torrey et al., 2017), predicting similar trends in star formation activity.

In an attempt to bring insight to the extremely low production of stars seen in the CMZ (e.g., Taylor et al., 1993; Longmore et al., 2013), we compare the centers of EMPIRE galaxies with the much better studied CMZ of our Galactic center. Figure 3.14 shows the HCN surface brightness emission as a function of the total IR emission averaged by the beam size, for the EMPIRE galaxy centers (inner most pointing corresponding to about 1 kpc size in diameter) plotted as gray circles. As a comparison, the CMZ region of the Milky Way is displayed as a blue circle on the plot, corresponding to a linear size of ~ 500 pc, and the data are extracted from Jones et al. (2012) and Barnes et al. (2017). In addition, we include the integrated HCN emission coming from the inner ~ 500 pc of

four nearby galaxies: NGC 3351, NGC 3627, NGC 4254 and NGC 4321. These are higher resolution ALMA data presented in M. Gallagher et al. (subm.), and can directly probe similar conditions to those seen in the CMZ.

Figure 3.14 shows that the amount of dense gas emission we trace per unit area is also tightly correlated with the averaged TIR emission in the region, suggesting a strong similarity between galaxy centers. We note, however, that whereas the CMZ and ALMA high resolution data may be tracing similar and comparable environments, it is possible that the EMPIRE observations could contain large regions within the beam which are empty, since the HCN emission is very compact compared to the beam size. The CMZ appears to contain a larger amount of HCN but also TIR, so it is as inefficient as other nearby galaxy disks. Within the observed uncertainties, it may also occur that the CMZ exhibits a similar TIR emission as the extragalactic sources (as observed by ALMA), and therefore it would appear to be a much more inefficient case. However, this is currently difficult to disentangle. The uncertainties in the TIR emission for the CMZ are estimated to be about 20% due to the background diffuse Galactic contribution (Barnes et al., 2017) and the HCN emission could be contaminated by the presence of other sources in the line of sight, as opposed to our EMPIRE and ALMA face-on observations.

In any case, the results presented in Figures 3.5 and 3.14 show that the CMZ of our Galactic Center is very similar to other galactic centers: its star formation activity correlates with the presence of dense gas (HCN) related to the bulk molecular gas (CO). The specific reason for the particularly low star formation efficiencies in the CMZ (large velocity fields, turbulence or episodic states) is still under debate, but it could be a common feature to all galactic centers and not only limited to the Galactic center.

3.3.3 The role of pressure

The main results in this chapter provide evidence for an environmental dependence of dense gas fractions and star formation efficiency of the dense gas. These results are in good agreement with the observations previously presented by Chen et al. (2015) and Bigiel et al. (2016) in M51, and Usero et al. (2015) in disk pointings of ~ 30 nearby galaxies. We have observed large concentrations of dense gas in the centers of 9 different nearby galaxies (see Figures 3.3 and 3.13) regardless of their morphology, however the apparent rate of star formation per unit dense gas decreases in those regions. This picture is surprisingly similar to that observed in our Milky Way center.

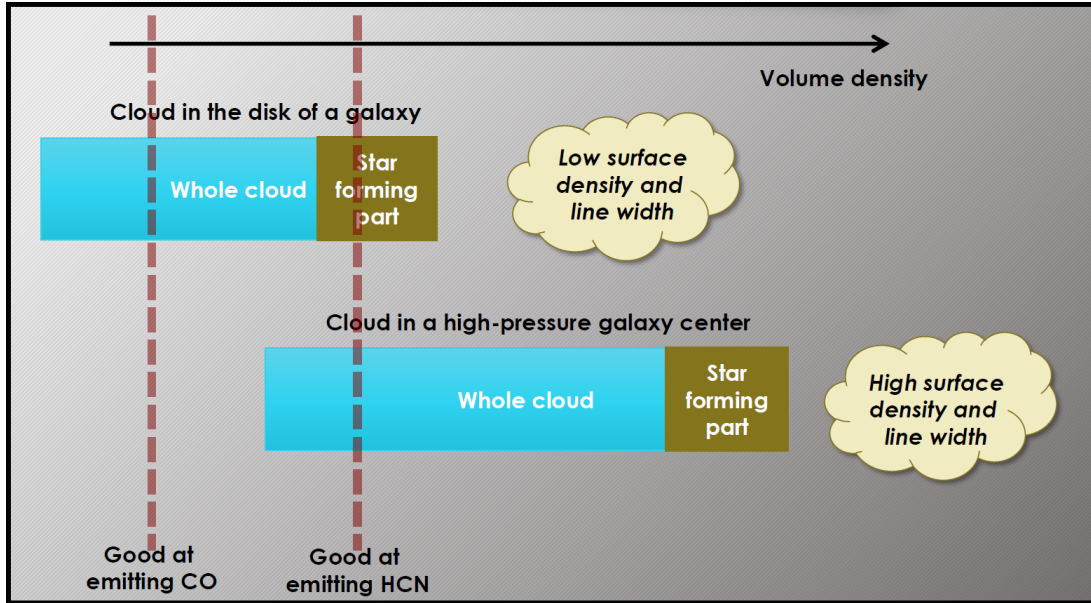


FIGURE 3.15. Qualitative picture explaining the role of pressure. Adapted from A. Leroy.

A logical scenario to understand the inner concentrations of dense gas is that a lot of material is transported towards the inner parts of galaxies, driven by the presence of a central galactic bar (e.g., [Krumholz & Kruijssen, 2015](#)). Our galaxy sample also contains non-barred, spiral galaxies such as NGC 628, NGC 4254, NGC 5055 and NGC 5194. These galaxies (except for NGC 628, most likely due to the limited number of HCN detections) show the same behaviour: an increase of dense gas per unit molecular gas of about one order of magnitude in the centers. This therefore supports the idea that not only the presence of a bar can funnel gas towards galactic centers, but also the inner regions of spiral arms ([Meidt et al., 2013](#); [Querejeta et al., 2016a](#)).

We do not only see that f_{dense} is correlated with Σ_* , an indicator of stellar gravitational potential, and f_{mol} a good tracer of density (e.g., M. Gallagher et al., *subm.*); in addition the rate of star formation per unit dense gas $\text{SFE}_{\text{dense}}$ shows a tight anti-correlation with these physical quantities. These two independent parameters are related via a more general indicator of density in galaxy disks, hydrostatic pressure P_h . f_{dense} increases with P_h : gas is in average denser where the gravitational potential is larger. $\text{SFE}_{\text{dense}}$ decreases with P_h : that central dense gas becomes more inefficient at forming stars where the ISM pressure is higher. This behavior suggests that for molecular clouds to constitute over-pressured or over-density regions with respect to the ambient pressure and subsequently form stars, their mean density must vary with the surface density of

the galactic disk.

This idea of a context-dependent role of density for star formation has been already suggested by M. Gallagher et al., *subm.*, and discussed in recent studies (e.g., [Usero et al., 2015](#); [Bigiel et al., 2016](#); [Leroy et al., 2017a](#)) and constitutes a compatible, although not unique, interpretation for the EMPIRE results. Figure 3.15 presents a qualitative picture to explain this interpretation. As volume density increases towards the centers of galactic disks, the internal pressure and mean density of the molecular clouds in a high density region also needs to shift towards higher values in order to actually constitute over-density structures. The further collapsing material in molecular clouds (which will eventually lead to star formation), follows a log-normal distribution of densities (e.g., [Kainulainen et al., 2009](#)) which is shifted towards higher densities as the internal pressure of clouds increases (and so inner in the disk). If our dense gas tracers always trace the same densities (which may be a too naive assumption, see Section 3.3.4), the emission coming from these molecules in low-density environments (top clouds shown in Figure 3.15) would still trace over-density regions corresponding to structures where star formation takes place. However, if molecular clouds are surrounded by a high density medium such as gas in central galactic regions, our high density tracers emission will no longer peak in regions where pressure and density are the highest (where star formation would occur). Instead, they will trace better the bulk of the molecular gas within clouds (bottom cloud case in Figure 3.15). This would translate into a lower apparent star formation efficiency of dense gas.

3.3.4 Does HCN always trace the same density?

When we use the HCN emission as a dense gas tracer, our main assumption is that this molecule requires much higher gas densities to get excited than other molecular gas tracers (such as CO), because its critical density $n_{\text{crit}} = \frac{A_{ul}}{\gamma_{ul}}$ is higher. HCN should therefore be a much better tracer of the dense gas supply. This is true for gas densities above the critical density of HCN, $\sim 10^6 \text{ cm}^{-3}$, when the de-excitation process is dominated by collisions and the kinetic temperature of the gas sets the level population. However the critical density of a particular transition is a crude approximation to determine the actual density of the gas. Molecular species, and in particular HCN, can also emit when the gas density is much lower than their critical density via radiative excitation and posterior de-excitation. This is particularly important when interpreting ratios such as $\text{SFR}/\text{HCN} \propto \text{SFE}$, since the initial assumption of HCN always tracing dense gas may be

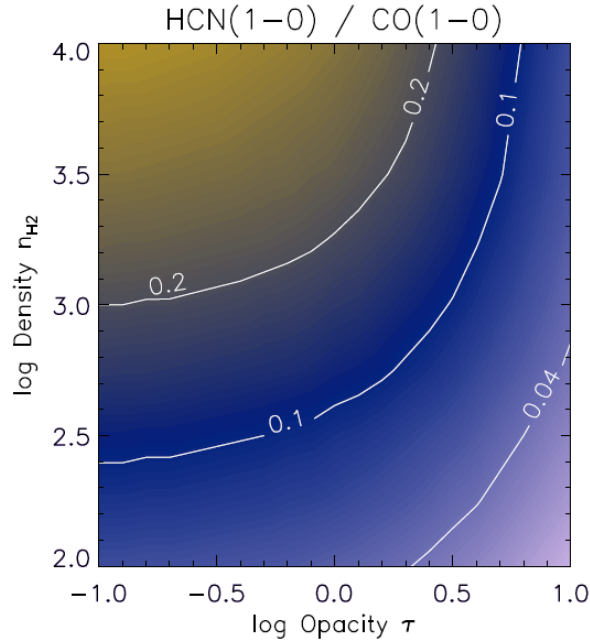


FIGURE 3.16. Expected HCN-to-CO line ratio shown as a contour map, and plotted as a function of the gas mean density n_{H_2} , for a lognormal+tail distribution and $T_{\text{kin}} = 25$ K (data from Leroy et al., 2017a). The ratio is also plotted as a function of HCN optical depth τ , which can reproduce similar line ratios as varying the mean density.

incorrect.

Radiative excitation can play an important role when trying to capture the densest regions which will eventually form stars, since the HCN emission can be significantly affected by sub-thermal emission of large amounts of low-density gas along the observed lines-of-sight. There is observational evidence that this subthermal emission constitutes a significant contribution to the dense gas luminosity of entire galaxies (e.g., Papadopoulos et al., 2007; Aravena et al., 2014), especially in those cases where the surveyed areas are much larger than the compact regions occupied by dense gas clumps (Stephens et al., 2016). Observations of another dense gas tracer, CS(2-1) by McQuinn et al. (2002) in the Galactic Plane, support this scenario, and revealed that about 65% of the total intensity is dominated by subthermal emission.

Other factors, not related to the star formation process, can also become important for the HCN excitation. Active galactic nuclei (AGN) can emit strong infrared ($14\mu\text{m}$) continuum emission that can vibrationally excite HCN, whose emission has been recently detected (e.g., Sakamoto et al., 2010; Aalto et al., 2015; Costagliola et al., 2015; Imanishi et al., 2016). Not only this IR-pumped emission would enhanced the HCN molecular

emission, it would also contribute to the computed TIR, therefore it would not be a good proxy to account for star formation rates. However, we do not expect this effect to be important in our nearby-galaxies study since only a few of them are known to host an AGN in their centers (NGC 3627 and NGC 5194, which would also not be resolved at the resolution we are working ($\sim 1 - 2$ kpc)).

Another important factor to consider is the impact of the optical depth on the critical densities of tracers. Our most basic measurements are directly observable line ratios like HCN-to-CO, and its variations reflect a changing density in the gas. Recent work modeling the emission from sub-beam density distribution (Leroy et al., 2017b), as it is the case for the EMPIRE survey measurements, are based on line ratio variations which assume fixed optical depths and are affected by relative abundance variations. The emission coming from common dense gas tracers is often found to be optically thick (Jiménez-Donaire et al., 2017a), which leads to line trapping effects that allow the lines to be excited at lower densities (Shirley, 2015). In addition, variations in the optical depth can also produce line ratio variations similar to those from density changes (Figure 3.16), a direct translation of line ratios into density variations is currently uncertain. Knowing the optical depth of these lines is essential to determine the actual density that these lines probe and thus to estimate the gas mass encompassed in the ISM.

3.4 Summary and conclusions

In this Chapter, we present the key dense gas tracers from the EMPIRE survey (HCN, HCO⁺, HNC) and bulk molecular gas (¹³CO). We investigate how the dense gas fraction, and the efficiency with which this gas forms stars, depend on environmental conditions. The main results are summarized below and will be published in M. Jiménez-Donaire (in prep.).

1. We detected bright dense gas emission as traced by the HCN (1-0), HCO⁺ (1-0) and HNC (1-0) across the entire galaxy sample. We employed stacking techniques to recover the emission from low signal-to-noise regions, which allowed us to detect HCN out to $\sim 9 - 11$ kpc for HCN, $\sim 7 - 10$ kpc for HCO⁺, and HNC out to $\sim 4 - 6$ kpc. In general, the HCN integrated intensity maps reproduce very well the large-scale structure traced by CO and 70 μ m emission.
2. We studied molecular line ratios of the dense gas tracers related to the total amount of molecular gas, as traced by CO emission. We found average values for HCN/CO

and HCO^+/CO to be of the order of 3% in galaxy centers and 2% in the arm and inter-arm regions; whereas HNC/CO is $\sim 1\%$ everywhere. The ratios among dense gas tracers show mean values of $\text{HCO}^+/\text{HCN} \sim 0.8$ and HNC/HCN values of ~ 0.4 across the disks of our sources. Our results are indicative of optically thick and slightly sub-thermal emission, compatible with photon-dominated regions with high density gas ($n > 10^5 \text{ cm}^{-3}$). NGC 4254 and NGC 6946 show large HCO^+/HCN values of about 1.2 in spiral arms and $\sim 1.5 - 3$ in their inter-arm regions, which could be associated to a lower-density medium and/or a decreasing metallicity in those sources.

3. The key HCN-to-CO ratio, tracing the dense gas fraction, systematically increases towards galaxy centers and correlates with the apparent surface density of stars, the molecular-to-atomic gas fractions, and the hydrodynamical equilibrium pressure P_h needed to support the gas in the mid-plane of the galaxy, supporting [Helfer & Blitz \(1997\)](#) in their suggestion of a link between the ISM pressure and the dense gas fractions.
4. The IR-to-HCN ratio (our observational tracer of $\text{SFE}_{\text{dense}}$) systematically anti-correlates with the stellar surface densities, the molecular-to-atomic gas fractions, and the hydrodynamical equilibrium pressure. As a result, the inner regions of nearby galaxies, characterized by high surface densities and deep potential wells caused by the presence of large amounts of gas and stars, show much higher dense gas fractions, but these seem much more inefficient at forming stars.
5. We find that the amplitude of the observed variations is larger than what is expected from the HCN noise, assuming an underlying constant IR-to-HCN ratio. The variations in $\text{SFE}_{\text{dense}}$ are physical, and provide additional support for a context-dependent role of density in the star formation process.

OPTICAL DEPTH ESTIMATES AND EFFECTIVE CRITICAL DENSITIES OF DENSE GAS TRACERS

*Optical depth estimates and effective critical densities of dense gas tracers
in the inner parts of nearby galaxy discs*

*M. Jiménez-Donaire, F. Bigiel, A. Leroy, D. Cormier,
M. Gallagher, A. Usero, A. Bolatto, D. Colombo,
S. García-Burillo, A. Hughes, C. Kramer, M. Krumholz,
D. Meier, E. Murphy, J. Pety, E. Rosolowsky,
E. Schinnerer, A. Schrubba, N. Tomicic, L. Zschaechner,
2017, MNRAS, 466, 49.*

The results presented in Chapter 3 revealed systematic variations in the dense gas fractions and the efficiency of dense gas to form stars. These measurements are based on line ratios (e.g., HCN/CO), which are sensitive to gas density. However, optical depth changes are known to produce line ratio variations similar to those due to density changes (Leroy et al., 2017b). In this Chapter, we address how the optical depth of the dense gas tracers may affect the effective critical densities they are sensitive to. The content presented in this Chapter has been originally published as: *Optical depth estimates and effective critical densities of dense gas tracers in the inner parts of nearby galaxy discs* (Jiménez-Donaire et al., 2017, MNRAS, 466, 49). In order to avoid overlap with the previous Chapters, the following Sections present an abridged form of the original publication and we refer to the appropriate Sections when necessary.

4.1 Abstract

High critical density molecular lines like HCN (1-0) or HCO⁺ (1-0) represent our best tool to study currently star-forming, dense molecular gas at extragalactic distances. The optical depth of these lines is a key ingredient to estimate the effective density required to excite emission. However, constraints on this quantity are even scarcer in the literature than measurements of the high density tracers themselves. Here, we combine new observations of HCN, HCO⁺ and HNC (1-0) and their optically thin isotopologues H¹³CN, H¹³CO⁺ and HN¹³C (1-0) to measure isotopologue line ratios. We use IRAM 30-m observations from the large program EMPIRE and new ALMA observations, which together target 6 nearby star-forming galaxies. Using spectral stacking techniques, we calculate or place strong upper limits on the HCN/H¹³CN, HCO⁺/H¹³CO⁺ and HNC/HN¹³C line ratios in the inner parts of these galaxies. Under simple assumptions, we use these to estimate the optical depths of HCN (1-0) and HCO⁺ (1-0) to be $\tau \sim 2-11$ in the active, inner regions of our targets. The critical densities are consequently lowered to values between $5-20 \times 10^5$, $1-3 \times 10^5$ and 9×10^4 cm⁻³ for HCN, HCO⁺ and HNC, respectively. We study the impact of having different beam-filling factors, η , on these estimates and find that the effective critical densities decrease by a factor of $\frac{\eta_{12}}{\eta_{13}} \tau_{12}$. A comparison to existing work in NGC 5194 and NGC 253 shows HCN/H¹³CN and HCO⁺/H¹³CO⁺ ratios in agreement with our measurements within the uncertainties. The same is true for studies in other environments such as the Galactic Center or nuclear regions of active galactic nucleus dominated nearby galaxies.

4.2 Introduction

The immediately star-forming structures ($\sim 0.1 - 1$ pc, $n_{\text{H}_2} > 10^4$ cm⁻³) remain too small to resolve in external galaxies. In particular, they are most easily studied using lines that preferentially select the dense, star-forming material. The low-J transitions HCN, HCO⁺, and HNC are among the brightest of these high critical density lines and can now be studied in other galaxies. Emission of common dense gas tracers like H¹²CN, H¹²CO⁺ and HN¹²C is often found to be optically thick. This leads to line trapping effects that allow the lines to be excited at lower densities than one would naively assume; at high optical depth, the critical density scales linearly with the inverse of the opacity for any optically thick line. That is, the density of gas traced by dense gas tracers depends on their optical depth. As a result, knowing the optical depth of lines like HCN (1-0) and

HCO⁺ (1-0) is essential to estimating the masses and density structure of the dense interstellar medium (ISM).

A good observational way to test the opacity of dense gas tracers is to combine observations of the main dense gas tracing lines with those of their rarer isotopologues, e.g., those that include ¹³C instead of ¹²C. These lines, e.g., H¹³CN and H¹³CO⁺, are usually optically thin because the molecules are less abundant by the isotopic ratio. Combined with few simplifying assumptions, the ratio of, e.g., H¹³CN (1–0) to H¹²CN (1–0) offers the prospect to test the opacity of dense gas tracers and so to help quantify the density to which these lines are sensitive.

The obstacle to such measurements is the faintness of emission from dense gas tracer isotopologues. As a result, these have been detected only within few very nearby galaxies (Henkel et al., 1998; Chin et al., 1998b; Wang et al., 2004; Aladro et al., 2013). In this chapter, we rely on two main data sets: whole disk mapping of NGC 5194 (EMPIRE, see Section 2.2.3) and ALMA observations of four nearby star-forming galaxies: NGC 3351, NGC 3627, NGC 4254, NGC 4321 presented in detail by Gallagher, et al. (subm.). We supplement these with observations of the nuclear starburst in NGC 253 (Bolatto et al., 2013a), see Section 4.3.2. All of these observations targeted both dense gas tracers and optically thin isotopologues. The properties of each target can be found in Table 4.1

The chapter is structured as follows. We describe the data in Section 4.3. We present the methods used to analyze the spectra in Section 4.4 and the main results are shown in Section 4.5, and are discussed in Section 4.6. Finally, we summarize our main conclusions in Section 4.7. Throughout the chapter, we will refer to the ¹²C isotopologues without special notation, e.g. HCN, etc., and mention explicitly if we refer to their isotopologues composed of other carbon isotopes.

4.3 Observations and data reduction

4.3.1 IRAM 30m Observations of NGC 5194

NGC 5194 or M51 is a nearby spiral galaxy (SAbc) at a distance of 7.6 Mpc (Ciardullo et al., 2002). It was mapped with the IRAM 30-m telescope at Pico Veleta over the course of 75 hours spread across seven runs during July and August 2012. We refer the reader to Chapter 2 for a detailed description of the data acquisition (see Section 2.2.3) and data reduction (see Section 2.3).

4.3.2 ALMA observations of NGC 3351, NGC 3627, NGC 4254, NGC 4321 and NGC 253

We also study four galaxies, NGC 3351, NGC 3627, NGC 4254 and NGC 4321 were observed during ALMA Cycle 3 campaign (Gallagher et al. *subm.*). These observations covered the molecular lines listed in Table 2.2 except for HN^{13}C and ^{12}CO . The data were processed using the ALMA pipeline and the CASA software (McMullin et al., 2007), with details presented in Gallagher et al. (*subm.*). After calibration, the data were continuum subtracted and then imaged into separate data cubes for each line. We reached a sensitivity value of $\text{RMS}(T_{\text{mb}}) = 1.5 \text{ mK}$. A mild $u - v$ taper was applied to increase surface brightness sensitivity and then the data were convolved to have a 5" circular beam ($\sim 300 \text{ pc}$) and 10 km s^{-1} wide channels.

We supplement these new observations with data for the nearby starburst galaxy NGC 253. These data, obtained as part of ALMA Cycle 0 campaign, were originally presented by Meier et al. (2015) and Leroy et al. (2015). Like the new data above, these cover HCN and HCO^+ , H^{13}CN , and H^{13}CO^+ . The average beam size is $\sim 4''$ ($\sim 70 \text{ pc}$) over a field of view of approximately $1'.5$ ($\sim 1.5 \text{ kpc}$). A summary of our data sets is given in Table 2.2 and Table 4.1.

4.4 Methodology

Our main goal is to detect emission from the faint isotopologues, H^{13}CN , H^{13}CO^+ and HN^{13}C and compute the line ratios $\text{HCN}/\text{H}^{13}\text{CN}$, $\text{HCO}^+/\text{H}^{13}\text{CO}^+$ and $\text{HNC}/\text{HN}^{13}\text{C}$. The emission from these molecules is faint for individual lines of sight. To overcome this, we use spectral stacking. Because the line of sight velocity varies with the position in each galaxy due to rotation, we first re-grid velocity axis of each spectrum in order to set the local mean velocity of the bulk molecular medium to zero km/s . We then co-add the emission from many different lines of sight to produce an average, higher signal-to-noise spectrum. This procedure resembles the one described by Schrubba et al. (2011) and Caldú-Primo et al. (2013). We use the ^{13}CO emission to estimate the local mean velocity of the molecular gas that we use as a reference for the stacking. In NGC 5194, we use the ^{13}CO map from PAWS (Schinnerer et al., 2013; Pety et al., 2013). For the ALMA data, we use ^{13}CO maps also observed by ALMA in a separate tuning.

We stack spectra in several different ways: the inner parts of the galactic disks, the entire disks of the galaxies, and in regions of high (> 4) signal-to-noise HCN emission.

Source	RA (2000.0)	DEC (2000.0)	i ($^{\circ}$)	PA ($^{\circ}$)	r_{25} ($'$)	D (Mpc)	Morphology	Σ_{SFR} ($M_{\odot} \text{ yr}^{-1} \text{ kpc}^{-2}$)	Inner aperture (kpc)	Telescope
NGC 253	00:47:33.1	-25:17:19.7	76	55	13.5	3.5	SABc	14^a	0.17	ALMA
NGC 3351	10:43:57.7	11:42:13.0	11.2	73	3.6	4.2	SBb	$5.2 \times 10^{-3}{}^b$	0.20	ALMA
NGC 3627	11:20:15.0	12:59:30.0	62	173	5.1	9.4	SABb	$7.7 \times 10^{-3}{}^b$	0.45	ALMA
NGC 4254	12:18:50.0	14:24:59.0	32	55	2.5	14.4	SAC	$18 \times 10^{-3}{}^b$	0.70	ALMA
NGC 4321	12:22:55.0	15:49:19.0	30	153	3.0	14.3	SABbc	$9.0 \times 10^{-3}{}^b$	0.69	ALMA
NGC 5194	13:29:52.7	47:11:42.9	20	172	3.9	7.6	Sbc	$20 \times 10^{-3}{}^b$	1.84	IRAM-30m

TABLE 4.1. Properties of the galaxy sample. **Notes.** – ^a Leroy et al. (2015), taking SFR $\sim 1 M_{\odot} \text{ yr}^{-1}$ within r_{50} ; ^b Leroy et al. (2013), average SFR surface density inside $0.75r_{25}$.

In the following, however, we focus on the former, as this approach yields the highest signal-to-noise in the stacked spectra. We defined the active “inner region” of our targets by specifying a circular aperture with fixed angular size for the ALMA galaxies and different size for the M51 30m data. This leads to modestly varying physical aperture size from galaxy to galaxy. The size of the aperture for each galaxy is indicated in Figure 4.1 and noted in Table 4.1. Specifically, for the ALMA galaxies we stack spectra inside a central 10" radius aperture. For M51 we picked a larger aperture of 50" in radius due to the lower resolution of the observations.

In order to measure spectral line parameters, we fit the stacked spectrum of each line with a single Gaussian. To perform the fit we use the MPFIT function in IDL. The free parameters we calculate from the fit are the line center velocity, the peak intensity, and the velocity dispersion. We obtain the integrated HCN, H¹³CN, HCO⁺ and H¹³CO⁺ line intensities by integrating the fitted profile. We compute the uncertainties on the integrated intensity from the width of the profile and the rms noise measured from the signal-free part of the spectrum. If the peak intensity of the stacked spectrum is below 3σ , then we compute an upper limit to the integrated intensity. We take the limit to the integrated intensity to be the flux of a Gaussian profile with the FWHM of the corresponding ¹²C line and a peak three times the noise level for the ¹³C profile. This assumes that the ¹²C and ¹³C lines are well mixed, and, although the limit is formally stronger than 3σ , this approach matches what one would identify as an upper limit by eye.

4.5 Results

Our targets, listed in Table 4.1, are all massive, star-forming, nearby disk galaxies. These are among the closest and hence best-studied star-forming galaxies. Our goal is to measure the ratios among dense gas tracers and their (presumably) optically thin ¹³C isotopologues. Figure 4.1 shows the distribution of ¹³CO (1-0) and HCN (1-0) emission from each targets. We use the ¹³CO emission, shown in color, to indicate the distribution of the total molecular gas reservoir. It also serves as the reference for our spectral stacking. Bright ¹³CO emission is widespread across our targets, and we see it at good signal to noise everywhere that we see HCN. Red contours show the location of significant HCN (1-0) emission, tracing higher density gas. Although detected at lower significance than the ¹³CO, HCN is also widespread across our targets. In both lines and all galaxies,

the brightest emission comes from the central regions of the target (the NGC 253 data cover only the center), with emission which extends along the spiral arms.

Although we detect dense gas tracers over large areas in each target, in most of our targets only the inner, bright regions yield useful stacked constraints on the isotopologue line ratios. We experimented with also stacking over the disks of our targets, but the emission of the ^{12}C lines over this region already has only modest signal-to-noise. Stacking over the extended disks of galaxies typically yielded upper limits that barely constrained the ^{13}C lines to be fainter than the ^{12}C lines and so offered little constraint on the optical depth. Thus, we concentrate mainly on the bright inner regions for the remainder of this chapter. As Figure 4.1 shows, these are bright in ^{13}CO , HCN, and HCO^+ . Here we detect the ^{13}C lines in some cases and in all cases place limits comparable to typical $^{12}\text{CO}/^{13}\text{CO}$ ratios in nearby galaxies (though see discussion below).

Figures 4.2 and 4.3 show the stacked spectra for ^{13}CO , the HCN, HCO^+ , HNC lines, and their ^{13}C isotopologues for the bright, inner region of each target galaxy. Table 4.2 lists the line parameters derived from a Gaussian fit. Table 4.3 reports key ratios derived from comparing these fitted parameters. Figure 4.2 shows that we detect ^{13}CO , HCN, HCO^+ , and (in NGC 5194) HNC at very high significance over these active regions. The ordering of intensity is the same across all systems, with the intensity of $^{13}\text{CO} > \text{HCN} > \text{HCO}^+$. In NGC 5194, where we also measure HNC, this line is the weakest of the four.

Figure 4.3 shows the stacked spectra for the ^{13}C isotopologues of the dense gas tracers. Here, scaled versions of the ^{12}C lines appear for reference. The ^{13}C isotopologues of the dense gas tracers are all far fainter than the ^{12}C lines. We do securely detect H^{13}CN in NGC 3351, NGC 3627, and NGC 253. In the other targets, we place firm upper limits on the intensity of these lines. We detect H^{13}CO^+ only in NGC 253, placing limits in the other systems.

4.5.1 Line Ratios

Table 4.3 reports the line ratios averaged over the active regions, which are the main objective of our investigations. We measure $\text{HCN}/\text{H}^{13}\text{CN}$ ratios of 24, 7, and 14 in NGC 3351, NGC 3627 and NGC 253, respectively; we constrain the ratio to be $\gtrsim 6$, 24, and 15 in the other systems. For $\text{HCO}^+/\text{H}^{13}\text{CO}^+$, we constrain the ratio to be $\gtrsim 20$, 8, 8, 18, and 9; we measure a ratio of 16 in NGC 253. This compares to $^{12}\text{CO}/^{13}\text{CO}$ ratios of ~ 6 – 10 commonly measured in the disks of galaxies, including the Milky Way and M51. The $^{12}\text{C}/^{13}\text{C}$ ratios for the dense gas tracers are significantly higher than those for CO

CHAPTER 4. OPTICAL DEPTH ESTIMATES AND EFFECTIVE CRITICAL DENSITIES OF DENSE GAS TRACERS

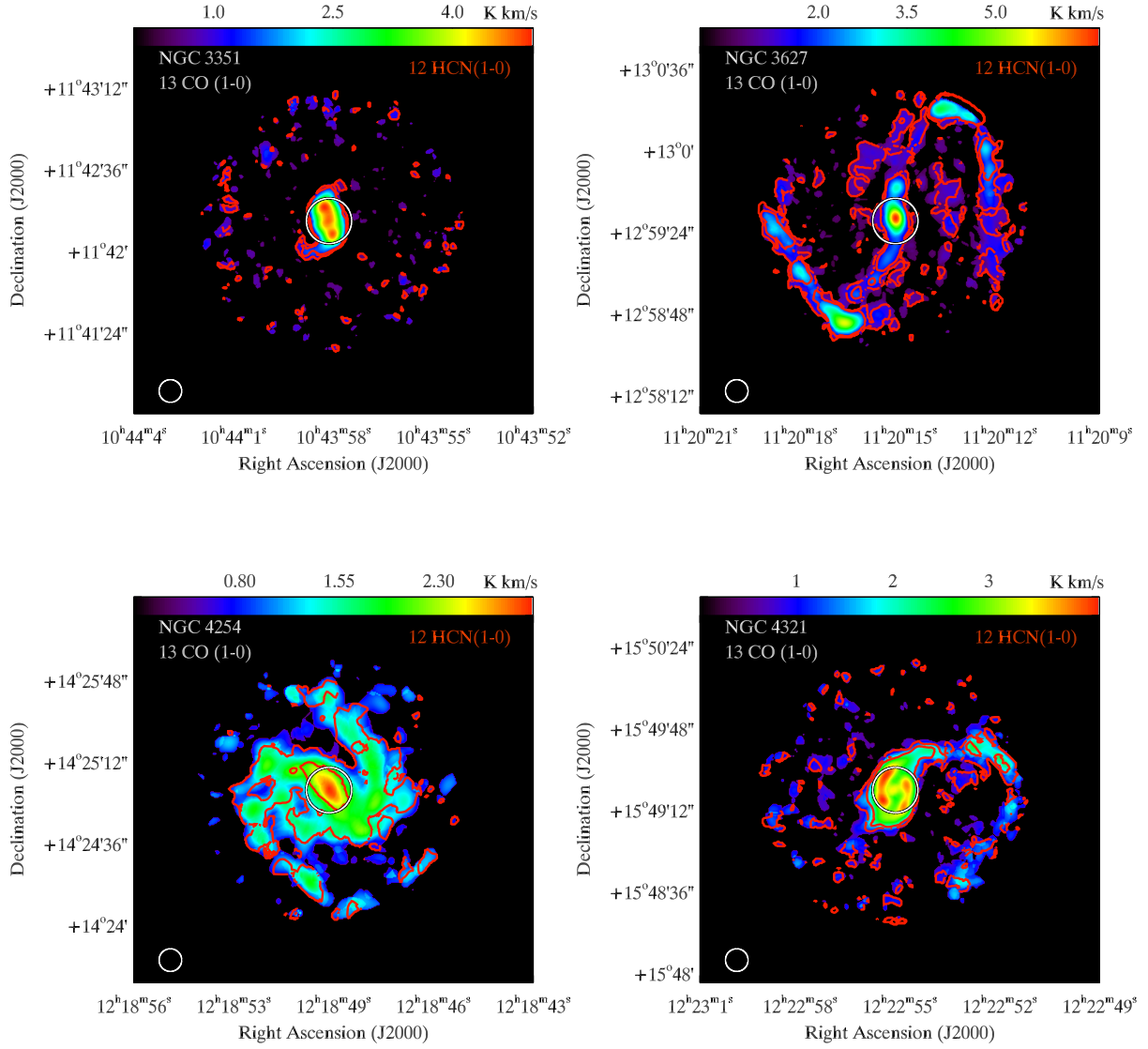


FIGURE 4.1. $^{13}\text{CO}(1-0)$ integrated intensity maps for our target galaxies. The red contours show HCN (1-0) intensity levels between 3 and 40σ for NGC 5194, between 8 and 25σ in NGC 3351, NGC 3627, NGC 4254 and NGC 4321; and between 30σ and 60σ for NGC 253. The white circle in the inner part of each target shows the selected region for each galaxy to stack the spectra, see details in Section 4.5.

Galaxy	Molecule	Integrated intensity (K km s ⁻¹)	Line width (km s ⁻¹)	Peak ×10 ⁻² (K)	rms (mK)
NGC 3351	¹³ CO	12.0±0.1	62±10	19.4±0.4	1.1
	HCN	8.4±0.1	67±11	11.8±0.6	1.5
	H ¹³ CN	0.4±0.1	59±10	0.7±0.1	0.9
	HCO ⁺	5.0±0.1	64±11	7.4±0.2	1.4
	H ¹³ CO ⁺	<0.3	–	<0.4	1.3
NGC 3627	¹³ CO	7.4±0.1	121±14	6.8±0.4	1.0
	HCN	5.1±0.1	129±14	4.5±0.1	0.8
	H ¹³ CN	0.7±0.1	170±17	0.4±0.1	1.0
	HCO ⁺	4.9±0.1	128±14	3.5±0.1	1.0
	H ¹³ CO ⁺	<0.4	–	<0.5	1.4
NGC 4254	¹³ CO	8.5±0.2	44±9	18.1±0.4	2.3
	HCN	2.9±0.2	48±9	5.5±0.2	3.3
	H ¹³ CN	<0.5	–	<1.3	4.0
	HCO ⁺	2.0±0.1	44±9	3.8±0.1	1.8
	H ¹³ CO ⁺	<0.3	–	<1.0	1.9
NGC 4321	¹³ CO	10.7±0.1	55±10	19.3±0.4	1.1
	HCN	6.9±0.1	69±11	9.7±0.2	1.4
	H ¹³ CN	<0.3	–	<1.0	1.6
	HCO ⁺	4.6±0.1	63±11	6.8±0.2	1.4
	H ¹³ CO ⁺	<0.3	–	<1.0	1.3
NGC 5194	¹³ CO	4.6±0.1	71±6	6.4±0.2	0.9
	HCN	2.2±0.1	76±8	2.7±0.1	0.6
	H ¹³ CN	< 0.2	–	<0.2	0.7
	HCO ⁺	1.4±0.1	78±10	1.6±0.3	0.6
	H ¹³ CO ⁺	< 0.2	–	<0.2	0.7
	HNC	0.8±0.1	77±8	1.1±0.2	0.8
	HN ¹³ C	< 0.2	–	<0.2	0.9
NGC 253	¹³ CO	312±9	25±6	1250±40	4.0
	HCN	32±2	22±4	120±4	9.0
	H ¹³ CN	1.9±0.4	19±5	9.0±0.3	5.6
	HCO ⁺	29±3	21±5	109±4	9.2
	H ¹³ CO ⁺	1.2±0.4	18±4	6.1±0.2	8.0

TABLE 4.2. Spectral line parameters for the galaxies derived from the stacked spectra in Figures 4.2 and 4.3.

CHAPTER 4. OPTICAL DEPTH ESTIMATES AND EFFECTIVE CRITICAL DENSITIES OF DENSE GAS TRACERS

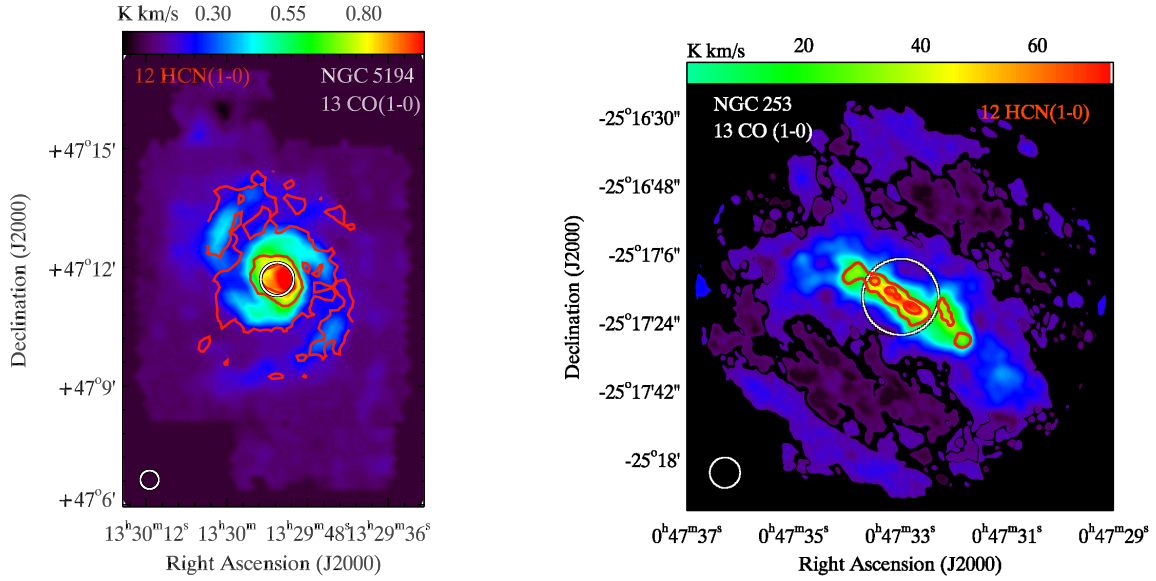


Figure 4.1: continued.

Galaxy	NGC 3351	NGC 3627	NGC 4254	NGC 4321	NGC 5194	NGC 253
HCN/H ¹³ CN	21±3	7±1	>6	>23	>11	17±1
HCO ⁺ /H ¹³ CO ⁺	>17	>12	>7	>15	>7	24±2
HNC/HN ¹³ C	–	–	–	–	>4	–
HCN/HCO ⁺	1.7±0.1	1.0±0.1	1.5±0.1	1.5±0.1	1.6±0.1	1.1±0.1
¹³ CO/HCN	1.4±0.2	1.5±0.1	3.0±0.3	1.6±0.2	2.1±0.1	10±1

Table 4.3: Computed line ratios for the galaxies.

in our targets. Possible explanations are: lower optical depth in the dense gas tracers, isotopic abundance variations in the active parts of galaxies, or different filling factors for the ¹²C and ¹³C lines. We will discuss this further in Section 4.6

How do our measured ratios compare to previous measurements? Table 4.4 summarizes literature measurements of isotopologue line ratios from the Milky Way and nearby galaxies, including two that overlap our targets (NGC 253 and NGC 5194). Broadly, these agree with our measurements, with ratios often $\gtrsim 10$ and sometimes $\gtrsim 20$. In detail, [Watanabe et al. \(2014\)](#) measured line ratios in NGC 5194 and found HCN/H¹³CN = 27±18, HCO⁺/H¹³CO⁺ = 34±29, and HNC/HN¹³C > 16, consistent with our results for that system. Using the same data that we employ for NGC 253, [Meier et al. \(2015\)](#) found similar ratios of HCN/H¹³CN, and HCO⁺/H¹³CO⁺ (see [Leroy et al., 2015](#)). Observations of NGC 1068 by [Wang et al. \(2014\)](#) found HCO⁺/H¹³CO⁺ = 20 ± 1, HCN/H¹³CN = 16 ± 1

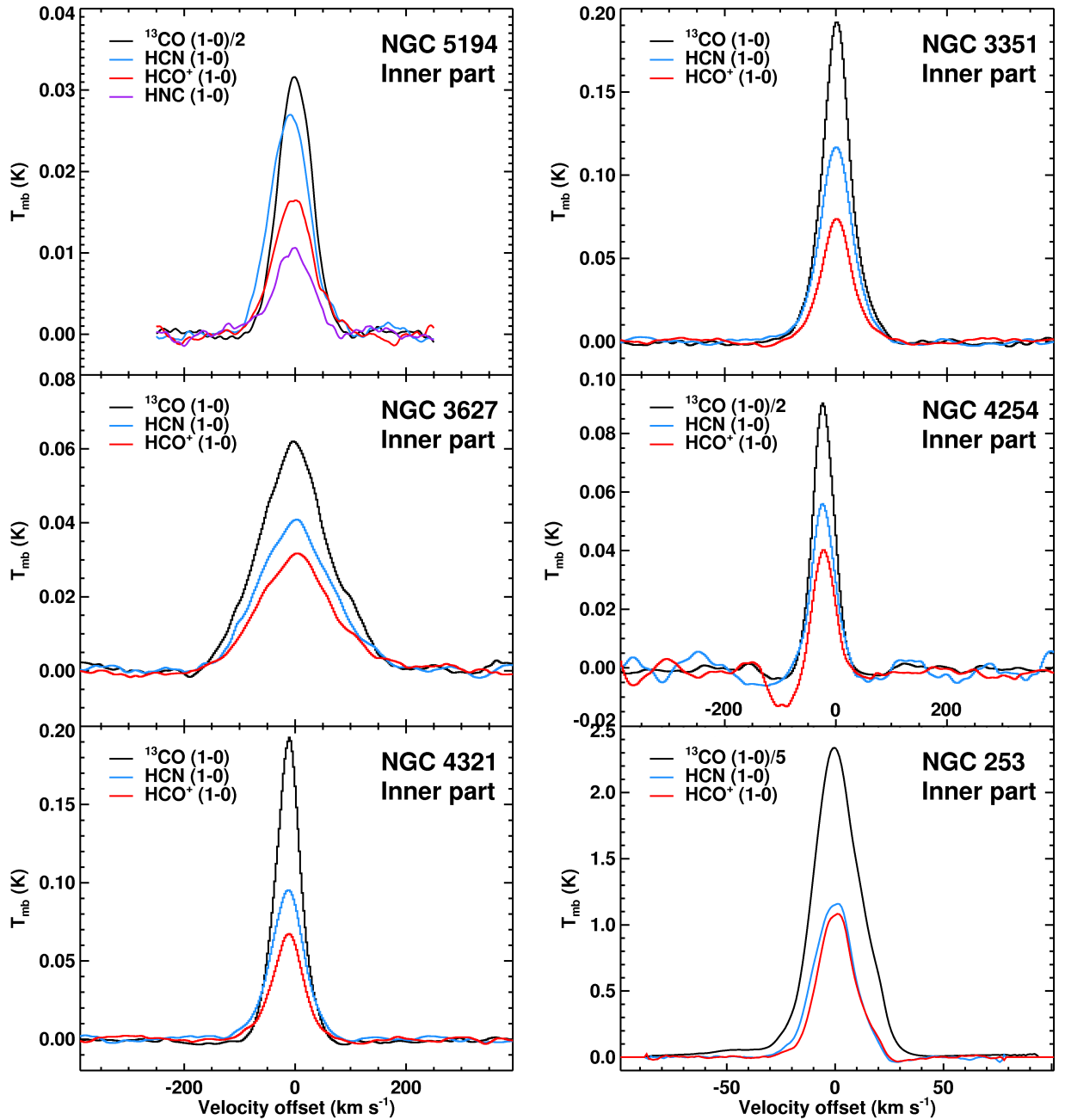


FIGURE 4.2. Stacked ^{13}CO , HCN, and HCO^+ spectra for the bright inner regions (radius $10''$) in our target galaxies. We also include the stacked HNC emission for NGC 5194. ^{13}CO , which serves as our reference for the stacking, is scaled to match the intensity scale of the other lines. The ^{13}CO and dense gas tracers are all detected at very high signal-to-noise. The stacked dense gas tracers show good agreement with the mean ^{13}CO velocity and all lines show similar line widths, indicative of being well mixed on the scale of the beams (\sim few hundred pc to kpc) for our data. Table 4.2 reports Gaussian fits to the lines.

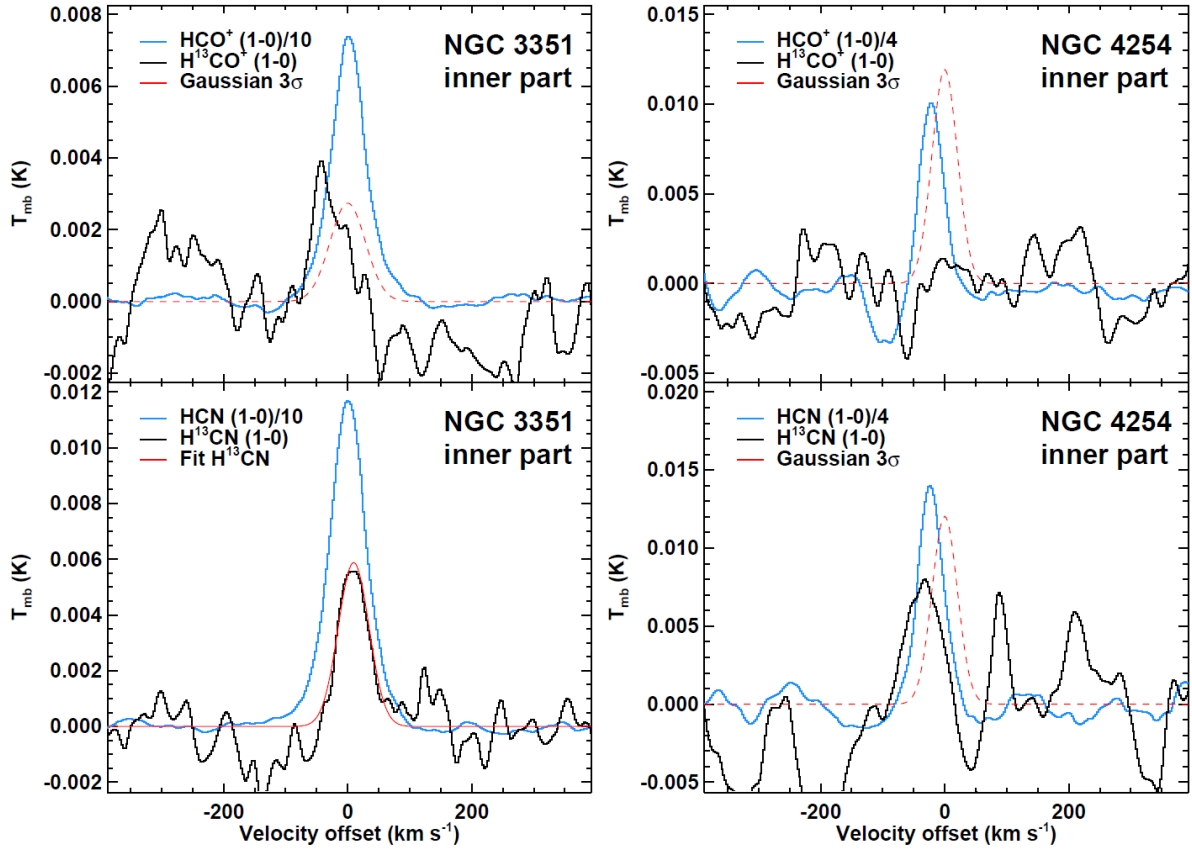


Figure 4.3: Stacked H^{13}CN and H^{13}CO^+ spectra for the bright inner regions of our target galaxies. We show scaled versions of the stacked HCN and HCO^+ spectra from Figure 4.2 for reference. These scaled spectra show the expectation for a ^{12}C -to- ^{13}C line ratios of 1-to-5 to 1-to-10, common values for the ^{12}CO -to- ^{13}CO ratio in galaxy disks. The red line indicates our working upper limit (dashed) or fit (solid) to the isotopologue spectrum. Limits and fit parameters are reported in Table 4.2.

and $\text{HNC}/\text{HN}^{13}\text{C} = 38 \pm 6$. This galaxy is characterized by a strong AGN, which should influence the surrounding chemistry. Two of our targets also host AGN, NGC 5194 and NGC 3627, however we do not see any significant difference in the measured line ratios compared to the rest of the sample. Though we note that at the coarse resolution of our observations such effects may be difficult to isolate.

Studies focused on Milky Way yield a similar picture. [Riquelme et al. \(2010\)](#) carried out a large-scale survey of the Galactic Center region and found $\text{HCO}^+/\text{H}^{13}\text{CO}^+ \sim 15$ in Sgr A, similar to those found here. [Harada et al. \(2015\)](#) observed the Circumnuclear Disk of the Galactic Center and reported ratios of $\text{HCO}^+/\text{H}^{13}\text{CO}^+ \sim 21$ and $\text{HCN}/\text{H}^{13}\text{CN} \sim 11$.

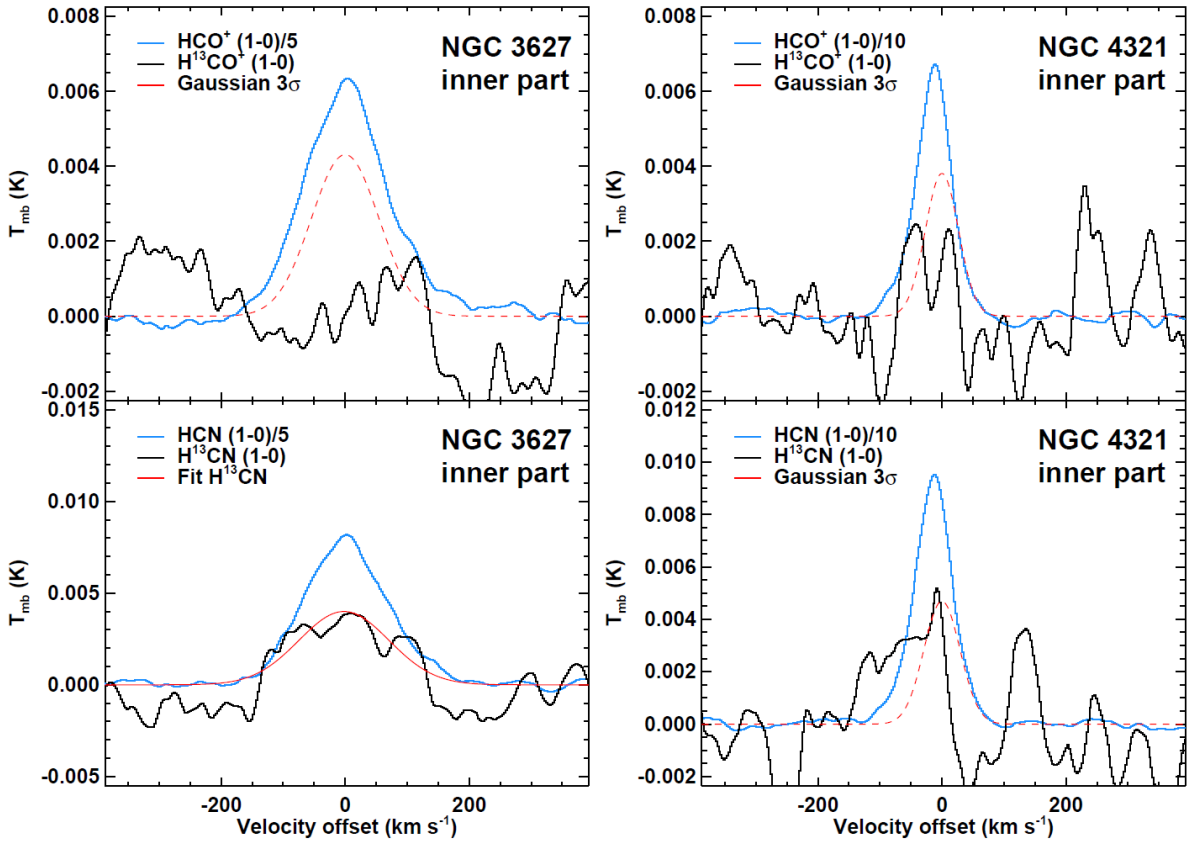


Figure 4.3: continued.

Target	HCN/H ¹³ CN	HCO ⁺ /H ¹³ CO ⁺	Ref.
NGC 1068	~16	~20	1
Orion B	–	~25	2
Sgr A	–	~15	3
Galactic Center	~11	~21	4
NGC 5194	~25	~30	5
NGC 253	~15	~19	6

TABLE 4.4. Integrated intensity ratios from the literature. **Notes** – (1) Wang et al. (2014); (2) J. Pety (priv. comm.); (3) Riquelme et al. (2010); (4) Harada et al. (2015); (5) Watanabe et al. (2014); (6) Meier et al. (2015).

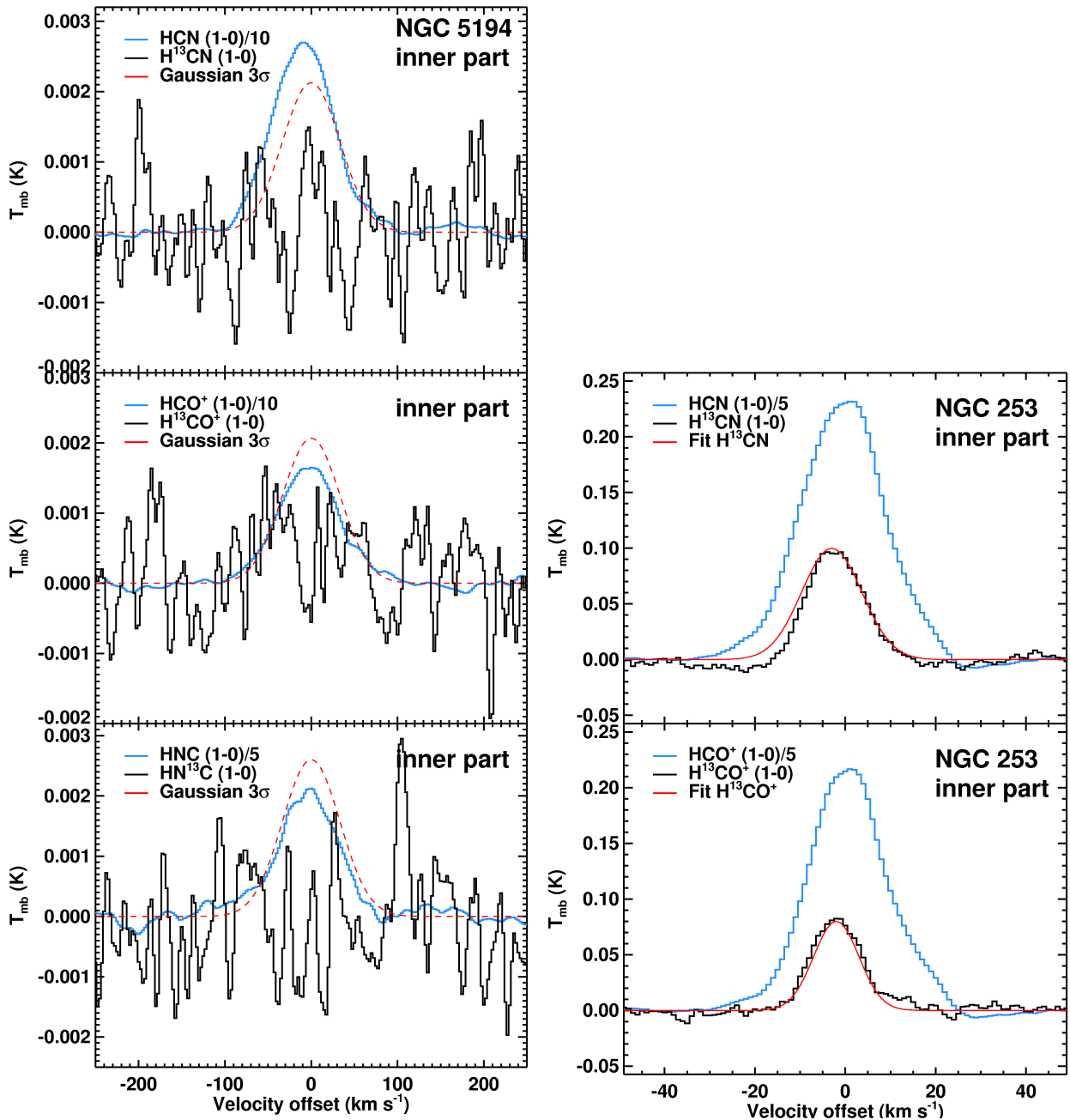


Figure 4.3: continued.

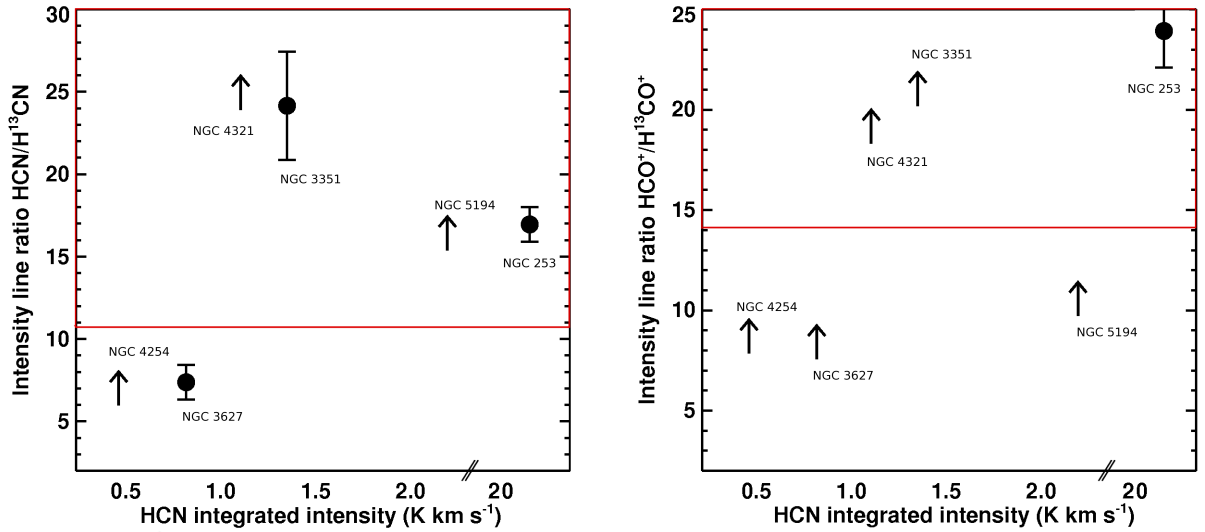


FIGURE 4.4. Comparison between the line ratios measured in our sample of galaxies and the literature values, summarized in Table 4.4. Circles show measurements from the stacked spectra in the inner regions of galaxies, whereas the arrows indicate upper limits. Note the non-continuous x -axis, as the HCN integrated intensity for NGC 253 is much higher than for the other galaxies. The red boxes show the regime of values found for the sources in the literature in Table 4.4, agreeing largely with the values and upper limits we derive.

In the Solar Neighborhood, J. Pety (priv. comm.) found $\text{HCO}^+/\text{H}^{13}\text{CO}^+ \sim 25$ in Orion B.

Figure 4.4 plots our measured ratios along with these literature values. Red boxes highlight an indicative range of values for each ratio: ~ 15 – 25 for $\text{HCN}/\text{H}^{13}\text{CN}$ and ~ 15 – 30 for $\text{HCO}^+/\text{H}^{13}\text{CO}^+$. We discuss the interpretation of these ratios in Section 4.6.

4.5.2 Line Widths

In addition to line ratios, the stacked spectra allow us to compare line widths among the different molecular lines. Potential differences in the line widths may hint at differences in the distribution of such emission along the line of sight.

Table 4.2 and Figure 4.2 show that we do not observe strong differences among the line widths of the dense gas tracers and the ^{13}CO emission tracing lower density gas. Thus, on the scale of our beam, which ranges from a few hundred pc to ≈ 1 kpc (except for the much higher resolution NGC 253), dense gas tracers appear well-mixed with ^{13}CO . Note that at these scales, we expect each beam to encompass many individual

clouds and that we stack beam-by-beam. Therefore the statement here supports the idea that the inter-cloud line width for HCN and HCO⁺ resembles that for ¹³CO. There does not appear to be a large population of clouds emitting only ¹³CO that show different velocities than the clouds emitting dense gas tracers.

We do observe spatial variations in the line width. When exploring stacked emission from disks, which we mostly omit from this chapter, we find line widths as much as a factor of ≈ 2 narrower than in galaxy centers (see Figures 4.2 and 4.5). And in the high spatial resolution data that we use to explore NGC 253, we find narrower line widths than in our other targets despite the high inclination and high degree of turbulence in this galaxy. In NGC 5194 the difference between the disk line width ($\sim 48 \text{ km s}^{-1}$) and the central line width ($\sim 70 \text{ km s}^{-1}$) is almost a factor of two and is present for all lines. The simplest explanation for this difference, and a similar difference shown for NGC 3627, is that the broad line widths in the central region of the galaxy still contain large amounts of unresolved bulk motion. We expect this to mostly be rotation unresolved by our coarse beam (i.e., “beam smearing”) but this may also include streaming motions along the spiral arms and bar or even some contributions from the AGN (e.g., see [Scoville et al., 1998](#); [Meidt et al., 2013](#); [Matsushita et al., 2015](#); [Querejeta et al., 2016b](#)). The narrower line widths in NGC 253 likely reflect the fact that we include less large scale dynamical motion and perhaps that we sample the turbulent cascade at an intermediate scale (e.g. [Caldú-Primo & Schruba, 2016](#)).

4.6 Discussion

Figure 4.4 shows our constraints on isotopologue line ratios for HCN and HCO⁺. The ¹²C-to-¹³C line ratios tend to be higher than those observed for CO molecules, but lower than typical isotopic ratios. How should we interpret these? A main motivation for this study was to constrain the optical depth of the dense gas tracers, and so to understand the importance of line trapping. In the simple case of a fixed ¹²C/¹³C abundance and a cloud with a single density and uniform abundances, these ratios can be translated to an optical depth. The ratios that we observe tend to be lower than commonly inferred ¹²C/¹³C abundances, implying some optical depth in the ¹²C lines. This section steps through key assumptions and results for this simple model. We then discuss how a breakdown in these simple assumptions may drive our observed line ratios. In particular, in the case where the ¹²C lines are optically thick then we would expect the ¹²C and ¹³C lines to emerge from distinct regions of the clouds.

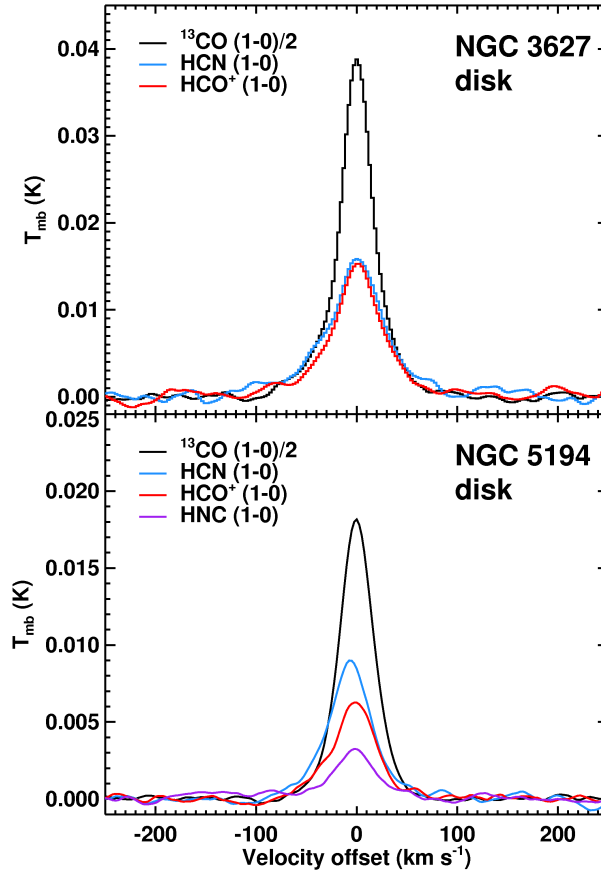


FIGURE 4.5. Stacked spectra across the entire molecular disk for NGC 3627 and NGC 5194 excluding the central aperture (Figures 4.1 and 4.2). We show spectra for the main dense gas tracers and ^{13}CO to trace the bulk, lower-density medium. Line widths are larger by up to a factor of ~ 2 in the inner parts compared to the disks, which we attribute largely to unresolved bulk motions.

4.6.1 Carbon Isotope Abundance Ratio

Table 4.5 lists estimate of the $^{12}\text{C}/^{13}\text{C}$ abundance ratio. A ratio of 89 is thought to characterize the Solar System at its formation (Wilson & Rood, 1994), while local clouds show $\sim 40\text{--}60$, the Milky Way center shows a low ratio of ~ 25 , and starburst galaxies at low and high redshift can reach ratios of ~ 100 . This value varies, at least in part, because ^{12}C and ^{13}C are produced by different phases of stellar evolution. ^{13}C is only created primarily as a result of evolved intermediate-mass stars, whereas very massive stars are the ones that produce ^{12}C at the end of their lives. As a consequence, the $^{12}\text{C}/^{13}\text{C}$ ratio depends on the recent star formation history, tending to be high in regions

Type of Object	Galaxy	$^{12}\text{C}/^{13}\text{C}$	Ref.
Center	Milky Way	~ 25	1
LMC	Magellanic Clouds	~ 50	2
NGC 2024	Milky Way	~ 65	3
Orion A	Milky Way	~ 45	3
Starburst	NGC 253	~ 40	4
		~ 80	5
Starburst	M 82	> 40	4
		> 130	5
Local ULIRGs	Mrk 231/Arp 220	~ 100	4, 6
ULIRG, $z = 2.5$	Cloverleaf	> 100	7

TABLE 4.5. Carbon isotope ratios from the literature in different environments. **Notes** – (1) [Guesten et al. \(1985\)](#); (2) [Wang et al. \(2009\)](#); (3) [Savage et al. \(2002\)](#); (4) [Henkel et al. \(2014\)](#); (5) [Martín et al. \(2010\)](#); (6) [González-Alfonso et al. \(2012\)](#); (7) [Henkel et al. \(2010\)](#).

of recent star formation and then dropping with time.

We measure ratios for the central regions of spiral galaxies. These tend to be actively star-forming regions, but not as extreme as those in ULIRGs. Based on the range of literature values, we adopt 50 as our fiducial $^{12}\text{C}/^{13}\text{C}$ ratio, since its determination is not possible with the present data set, but we note that this is likely uncertain by a factor of ~ 2 . We consider this effect in our EMPIRE and ALMA sample in [Jiménez-Donaire et al. \(2017b\)](#). Several effects can affect this ratio, like selective photo-dissociation or isotopic fractionation. While the strong interstellar radiation field emitted from OB stars, especially in strong starbursts, does not dissociate ^{12}CO in large amounts due to self-shielding (e.g. [van Dishoeck & Black, 1988](#)), ^{13}CO may be more severely affected ([Bally & Langer, 1982](#)) which may increase the $^{12}\text{C}/^{13}\text{C}$ ratio. On the other hand, chemical fractionation in cold regions would lead to preferential formation of ^{13}CO . Qualitatively, fractionation effects would likely marginally increase the H^{13}CO^+ abundance ([Langer & Penzias, 1990](#); [Milam et al., 2005](#)), whereas H^{13}CN and HN^{13}C are expected to decrease (e.g. [Roueff et al., 2015](#)).

4.6.2 Optical Depth in the Simple Case

4.6.2.1 Framework

In the simple case of a cloud with a single density, ^{12}C and ^{13}C lines evenly mixed throughout the cloud, and the ^{12}C line optically thick, then the line ratio implies an

optical depth. To estimate this optical depth, we begin in the following with the simplest case of assuming local thermodynamic equilibrium (LTE) and in particular $T_{\text{ex}}(\text{HCN}) = T_{\text{ex}}(\text{H}^{13}\text{CN})$. Note that we will drop this assumption in Section 4.6.3. We consider the intensity, J_ν , of the ^{12}C and ^{13}C lines in units of brightness temperature, but not necessarily on the Rayleigh-Jeans tail, so that:

$$(4.1) \quad J_\nu = \frac{h\nu/k}{e^{h\nu/kT} - 1}.$$

where ν is the observed frequency, k is Boltzmann's constant, h is Planck's constant, and T is the temperature characterizing the source function. For our cloud, T will be T_{ex} in LTE. Then the equation of radiative transfer gives the observed intensity, T_{obs} , in units of brightness temperature:

$$(4.2) \quad T_{\text{obs}} = \eta_{\text{bf}} [J_\nu(T_{\text{ex}}) - J_\nu(T_{\text{bg}})] (1 - \exp(-\tau)).$$

Here η_{bf} is the beam filling factor, the fraction of the beam area that is filled by the emitting region. T_{bg} is the background radiation field temperature (2.71 K), and τ is the optical depth of the transition in question. Note that η_{obs} , the beam filling factor, is expected to be a very small number, bringing our observed intensities from ~ 10 K down to the observed small fraction of a Kelvin.

If we make the simplifying assumption that the ^{12}C lines, e.g., HCN (1-0), are optically thick, then $1 - \exp(-\tau) \approx 1$ and

$$(4.3) \quad T_{\text{obs}}^{12\text{C}} = \eta_{\text{bf}}^{12\text{C}} [J_{\nu,12\text{C}}(T_{\text{ex}}) - J_{\nu,12\text{C}}(T_{\text{bg}})],$$

where $J_{\nu,12\text{C}}$ refers to Equation evaluated at the frequency of the ^{12}C line. On the other hand, the ^{13}C line has unknown optical depth, so that

$$(4.4) \quad T_{\text{obs}}^{13\text{C}} = \eta_{\text{bf}}^{13\text{C}} [J_{\nu,13\text{C}}(T_{\text{ex}}) - J_{\nu,13\text{C}}(T_{\text{bg}})] (1 - \exp(-\tau^{13\text{C}})).$$

Here we have distinguished the frequency of the ^{13}C line from that of the ^{12}C line above. The equations also allow that the two lines might have different filling factors and so distinguish $\eta_{\text{bf}}^{13\text{C}}$ from $\eta_{\text{bf}}^{12\text{C}}$. The optical depth of the ^{13}C line is unknown. However, our observed ratios are far from ~ 1 , which would be expected for both lines optically thick and matched η_{bf} . Thus, it appears unlikely that both lines are optically thick. Therefore we expect $(1 - \exp(-\tau^{13\text{C}})) \approx \tau^{13\text{C}}$ in most cases.

Then, generally for LTE and an optically thick ^{12}C line we have:

$$(4.5) \quad \frac{T_{\text{obs}}^{13\text{C}}}{T_{\text{obs}}^{12\text{C}}} = \frac{\eta_{\text{bf}}^{13\text{C}}}{\eta_{\text{bf}}^{12\text{C}}} \frac{J_{\nu,13\text{C}}(T_{\text{ex}}) - J_{\nu,13\text{C}}(T_{\text{bg}})}{J_{\nu,12\text{C}}(T_{\text{ex}}) - J_{\nu,12\text{C}}(T_{\text{bg}})} (1 - e^{-\tau^{13\text{C}}}).$$

The differences between the ^{12}C and ^{13}C frequencies are small, so that

$$(4.6) \quad \frac{T_{\text{obs}}^{13\text{C}}}{T_{\text{obs}}^{12\text{C}}} \approx \frac{\eta_{\text{bf}}^{13\text{C}}}{\eta_{\text{bf}}^{12\text{C}}} \left(1 - e^{-\tau^{13\text{C}}}\right)$$

In the simple case, we further assume that the ^{13}C line is optically thin and that the beam filling factors of the two lines match (an assumption we will drop in the next section), so that

$$(4.7) \quad \tau^{13\text{C}} = -\ln\left(1 - \frac{T_{\text{obs}}^{13\text{C}}}{T_{\text{obs}}^{12\text{C}}}\right) \approx \frac{T_{\text{obs}}^{13\text{C}}}{T_{\text{obs}}^{12\text{C}}}$$

This exercise yields the optical depth of the ^{13}C line. Because the opacity is proportional to the column of molecules, we can relate $\tau^{13\text{C}}$ to $\tau^{12\text{C}}$. Again ignoring minor differences between the lines, the ratio of optical depths will simply be the ratio in abundances between the two molecules,

$$(4.8) \quad \tau^{12\text{C}} = \tau^{13\text{C}} \frac{[\text{H}^{12}\text{CN}]}{[\text{H}^{13}\text{CN}]} \approx \tau^{13\text{C}} \frac{[^{12}\text{C}]}{[^{13}\text{C}]} .$$

4.6.2.2 Results

Using the line ratios tabulated in Table 4.3, Equations 4.7 and 4.8, and adopting a Carbon isotope ratio of $^{12}\text{C}/^{13}\text{C} = 50$, we estimate $\tau^{13\text{C}}$ and $\tau^{12\text{C}}$ for each pair of isotopologues. We report these in Table 4.6. Because they use Equation 4.7, these estimates all assume matched beam filling factors and neglect any differences between the frequencies of the two transitions.

In Section 4.4, we place upper limits on the $^{13}\text{C}/^{12}\text{C}$ ratio in a number of cases. These translate into upper limits on $\tau^{12\text{C}}$ and $\tau^{13\text{C}}$. Broadly, the ^{13}C lines are consistent with being optically thin. In this simple case, all of these optical depths are $\lesssim 0.3$. The corresponding optical depths for the ^{12}C lines are all consistent with $\tau^{12\text{C}} \gtrsim 1$, in agreement with our assumption of thick ^{12}C emission. In the case of HCN emission for NGC 3351, NGC 3627, and NGC 253 and HCO^+ for NGC 253, these are all consistent with $\tau^{12\text{C}} \sim 3$ (see also [Meier et al., 2015](#)). However, in the other cases, these results are upper limits. For ^{13}C upper limits, we can mainly conclude that the ratios do not rule out optically thick ^{12}C emission. Thus, in the simple case, the line ratios strongly suggest thin ^{13}C emission. They are consistent with moderate optical depth in the ^{12}C lines.

Galaxy	NGC 3351	NGC 3627	NGC 4254	NGC 4321	NGC 5194	NGC 253
$\tau(\text{H}^{13}\text{CN})$	0.04 ± 0.02	0.15 ± 0.07	< 0.2	< 0.05	< 0.07	0.07 ± 0.01
$\tau(\text{HCN})$	2.4 ± 0.4	4.2 ± 0.5	< 11	< 2.3	< 3.5	2.5 ± 0.6
$\tau(\text{H}^{13}\text{CO}^+)$	< 0.05	< 0.1	< 0.1	< 0.06	< 0.1	0.05 ± 0.02
$\tau(\text{HCO}^+)$	< 2.5	< 5.2	< 6.8	< 2.8	< 6.1	1.8 ± 0.9
$\tau(\text{HN}^{13}\text{C})$	–	–	–	–	< 0.3	–
$\tau(\text{HNC})$	–	–	–	–	< 11	–
$n_{\text{thick}}(\text{HCN})$	$(2.0\pm 0.2)\times 10^6$	$> 8.6\times 10^5$	$> 4.8\times 10^5$	$> 2.0\times 10^6$	$> 1.4\times 10^6$	$(2.0\pm 0.2)\times 10^6$
$n_{\text{thick}}(\text{HCO}^+)$	$> 2.9\times 10^5$	$> 1.5\times 10^5$	$> 1.1\times 10^5$	$> 2.5\times 10^5$	$> 1.2\times 10^5$	$(4.2\pm 0.3)\times 10^5$
$n_{\text{thick}}(\text{HNC})$	–	–	–	–	$> 8.6\times 10^4$	–

TABLE 4.6. Optical depths and derived effective critical densities, assuming matching beam filling factors and a common excitation temperature for the ^{12}C and ^{13}C isotopologues. Critical densities are in units of cm^{-3} .

4.6.3 Non-LTE Effects and Variable Beam Filling Factors

In the previous section, we assumed that $\eta_{\text{bf}}^{12\text{C}} = \eta_{\text{bf}}^{13\text{C}}$, so that both lines emerge from the same region. In fact, the ^{12}C line can be optically thick while the ^{13}C line is optically thin. In this case, line trapping effects will lower the effective density for emission for the ^{12}C line but not the ^{13}C line. Then, lower density gas can emit strongly in the ^{12}C but more weakly in the ^{13}C line. This should yield $\eta_{\text{bf}}^{12\text{C}} > \eta_{\text{bf}}^{13\text{C}}$. That is, the two lines will show distinct distributions within a cloud, with the ^{13}C line (which has no line trapping) confined to the denser parts of the cloud.

The same effect may lead to different excitation temperatures for the two lines. If the ^{12}C line is optically thick, then line trapping will lower its effective critical density. If the collider (H_2) volume density in the galaxy is high compared to the critical density of the ^{12}C line, but low compared to the critical density of the ^{13}C line, then the ^{13}C line may be sub-thermally excited while the ^{12}C line approaches LTE. In this case, $T_{\text{ex}}^{13\text{C}} < T_{\text{ex}}^{12\text{C}}$. The strength of non-LTE effects depends on the exact density distribution within the emitting region (see, [Leroy et al., 2017b](#)). If the region has mostly gas above the critical density of both lines, then the LTE case discussed above will apply. This might often be the case, e.g., for ^{12}CO and ^{13}CO .

On the other hand, if the density of the region is small compared to the effective critical density of the ^{12}C line, then neither line will emit effectively. Most collisional excitations will be balanced by radiative de-excitations and the line ratio will drop. In the extreme limit, the line ratio will reach the abundance ratio. In this chapter, we observe mostly the central, bright areas of galaxies, focusing on regions with bright

HCN emission. We do not expect these central zones to be dominated by extremely low volume density gas. However, if a large amount of $n_{\text{H}_2} \sim 10^{3.5} - 10^4 \text{ cm}^{-3}$ gas contributes to the emission, then these non-LTE effects may still be important. This is the range of densities where n_{H_2} might be above the effective critical density for an optically thick ^{12}C line but not an optically thin ^{13}C line. This range of densities is also well within the range commonly observed inside molecular clouds in nuclear star forming regions.

[Leroy et al. \(2017b\)](#) explore these effects for realistic density distributions. They calculate the amount by which the ^{12}C to ^{13}C line ratio will be suppressed for different lines given some optical depth of the ^{12}C line and an adopted density distribution. The magnitude of the effect depends on the line, the optical depth, and the density distribution. For a lognormal distribution with a powerlaw tail, they found that the $^{12}\text{C}/^{13}\text{C}$ line ratio could be enhanced relative to the LTE expectation by a factor of $\sim 2-3$ for HCN or HCO^+ over a range of plausible densities.

This enhanced line ratio can be captured to first order, by applying different filling factors to the two lines. Thus, to explore the implication of these effects, we revisit our LTE calculations but now assume that $\eta_{\text{bf}}^{12\text{C}}/\eta_{\text{bf}}^{13\text{C}} \approx 2$. To do this, we return to Equation 4.6. We no longer set the beam filling factors equal between the two lines, but still set the temperatures and frequencies equal, and assume LTE with a single common temperature. Then

$$(4.9) \quad \tau_{\text{obs}}^{13\text{C}} \simeq -\ln \left(1 - \frac{\eta_{\text{bf}}^{12\text{C}} T_{\text{obs}}^{13\text{C}}}{\eta_{\text{bf}}^{13\text{C}} T_{\text{obs}}^{12\text{C}}} \right)$$

This is still an approximation, but one that captures some of the effect of differential excitation of the ^{12}C and ^{13}C lines in the non-LTE case. We refer the reader to the non-LTE treatment in [Leroy et al. \(2017b\)](#) for more details and a tabulation of a variety of cases. Equation 4.9 shows that for $\eta_{\text{bf}}^{12\text{C}} > \eta_{\text{bf}}^{13\text{C}}$, our simple estimates of τ in the previous section will be underestimates. We report revised values in Table 4.7. These are higher than the corresponding LTE values in Table 4.6. Even accounting for differential filling factors, we still derive $\tau^{13\text{C}}$ consistent with optically thin ^{13}C emission. These non-LTE effects tend to make the limits on optical depth less stringent because they can push the line ratio towards “optically thin” values even while the ^{12}C line remains thick. Accounting for this effect, our observations may still accommodate substantial thickness in the ^{12}C line, with $\tau^{12\text{C}}$ potentially as high as ~ 10 for our HCN detections.

The exact magnitude of any non-LTE correction will depend on the sub-beam density distribution, the true temperature of the gas, and the optical depth of the lines in

Target	τ_{HCN}	$n_{\text{crit}}^{\text{HCN}}$	τ_{HCO^+}	$n_{\text{crit}}^{\text{HCO}^+}$	τ_{HNC}	$n_{\text{crit}}^{\text{HNC}}$
NGC 3351	5.0 ± 0.4	$(1.0 \pm 0.4) \times 10^6$	< 5.3	$> 1.4 \times 10^5$	–	–
NGC 3627	8.8 ± 0.7	$(5.6 \pm 0.1) \times 10^5$	< 10.6	$> 7.0 \times 10^4$	–	–
NGC 4254	< 25.8	$> 1.2 \times 10^5$	< 16.0	$> 4.5 \times 10^4$	–	–
NGC 4321	< 5.3	$> 9.4 \times 10^5$	< 5.8	$> 1.3 \times 10^5$	–	–
NGC 5194	< 8.0	$> 6.2 \times 10^5$	< 14.3	$> 5.1 \times 10^4$	< 31	$> 1.8 \times 10^4$
NGC 253	6.3 ± 0.5	$(7.9 \pm 0.1) \times 10^5$	4.3 ± 0.6	$(1.7 \pm 0.1) \times 10^5$	–	–

TABLE 4.7. Optical depths and effective critical densities when considering $\eta_{12} \sim 2\eta_{13}$ and under the assumption of a common T_{ex} . Critical densities are in units of cm^{-3} .

question. Our best guess is that a moderate correction does indeed apply, and the factor of ~ 2 correction applied in Table 4.7 may represent a reasonable estimate. In fact, if most of the emission that we see comes from dense clouds, this may be an over-correction, while if no power law tail is present, the correction for non-LTE effects may be even higher. Future multi-line work and isotopologue studies of Galactic Center clouds will help refine these estimates further.

4.6.4 Implications for Dense Gas Tracers

Our simple calculations imply moderate optical depth for the dense gas tracers (the ^{12}C lines) and this depth increases in the case of differential beam filling. Optical thickness in these lines means that radiative trapping will lead to emitted photons being re-absorbed. This lowers the effective critical density and changes the density at which these lines emit most effectively. This correction is likely to be significant for commonly used dense gas tracers. It will affect both the density required for effective emission and the conversion between line brightness and dense gas mass, the dense gas conversion factor.

In a review of this topic, [Shirley \(2015\)](#) note the effective critical density in the presence of line trapping as

$$(4.10) \quad n_{\text{crit}}^{\text{thick}} = \frac{\bar{\beta} A_{jk}}{\sum_{i \neq j} \gamma_{ji}}.$$

Here $\bar{\beta}$ is the solid angle-averaged escape fraction, A_{jk} are the Einstein A coefficients, and γ_{ji} are the collision rates ($\text{cm}^3 \text{s}^{-1}$) out of level j into another level i . The difference with the normal critical density calculation is that $\bar{\beta} \neq 1$, so that not every spontaneous emission escapes the cloud. In the simple case of spherical geometry and large optical depth ($\tau > 1$), the effective spontaneous transition rate becomes $\bar{\beta} A_{jk} \sim A_{jk}/\tau$, so that

the critical density is depressed relative to its nominal (optically thin) value by a factor equal to the optical depth.

Tables 4.6 and 4.7 report the effect of applying corrections based on the estimated optical depths to each line. The effect is to reduce the critical density by a factor of $\sim 2-6$, yielding values that are typically $\sim 7 \times 10^5 \text{ cm}^{-3}$ for HCN, $\sim 1 \times 10^5 \text{ cm}^{-3}$ for HCO^+ and $> 1.8 \times 10^4 \text{ cm}^{-3}$ for HNC. These are, of course, as uncertain as the optical depths, but give some guide as to the density of gas traced by these lines.

4.7 Summary and conclusions

We present observations of the 1-0 transitions of the dense, molecular gas tracers HCN, HCO^+ , HNC and their isotopologues H^{13}CN , H^{13}CO^+ and HC^{13}N across the disks of six nearby galaxies. These include IRAM 30m observations of NGC 5194 (M51), as part of the IRAM large program EMPIRE, ALMA observations of NGC 3351, NGC 3627, NGC 4254, NGC 4321 and NGC 253. Given the faint nature of the ^{13}C isotopologues, we focus our analysis on the inner ($\sim 50''$ for M51 and $\sim 10''$ for the ALMA galaxies), high surface density regions of these galaxies and stack all spectra in this region for each galaxy to improve the significance of our measurements. We use this data set to constrain the optical depth of these lines and study implications for the effective critical densities.

- We detect HCN, HCO^+ , HNC (1-0) with high significance for each galaxy ($> 5\sigma$) in the stacked spectra. Emission from these lines is in fact well detected for individual lines of sight and resolved across the disks of our sample, and in particular, the HCO^+ and HNC emission are distributed very similarly to the HCN emission in NGC 5194. The distribution of these dense gas tracers follows well the bulk molecular medium one as traced by CO emission; it is brightest in the inner parts and follows the spiral structure (where present) in CO.
- The H^{13}CN , H^{13}CO^+ and HN^{13}C (1-0) lines, however, are much fainter; in the stacked spectra from the inner regions of our sample, we detect H^{13}CN (1-0) in NGC 3351, NGC 3627 and NGC 253, and H^{13}CO^+ (1-0) in NGC 253. NGC 4254, NGC 4321 and NGC 5194 show no isotopologue detection in their inner part. Therefore we derive stringent upper limits for those cases, which we use for our analysis.
- We use the optically thin isotopologues to compute or constrain optical depths for each molecular lines in the inner parts of our target galaxies and, where detected,

also in selected CO and HCN bright disk positions. We find that HCN and HCO⁺ have optical depths in the range ~ 2 -11 in the inner parts of the galaxies analyzed (assuming a value of 50 for the ¹²C/¹³C abundance ratio). HN¹³C data is only available for NGC 5194, where we derived an upper limit to the opacity for HCN in its inner region, $\tau < 11$. The optical depth for H¹³CN, H¹³CO⁺ and HN¹³C shows a larger degree of variation, ranging from 0.04 to 0.3 in the inner part of NGC 3351, NGC 3627 and NGC 253. We conclude that HCN, HCO⁺ and HNC (1-0) emission is largely moderately optically thick with optical depths of typically a few, whereas the H¹³CN, H¹³CO⁺ and HN¹³C (1-0) lines are largely optically thin, even in the inner parts of our galaxies on the ~ 0.5 -2 kpc scales we probe.

- Given their non-negligible optical thickness, the critical densities of the HCN, HCO⁺ and HNC are reduced by a factor of 2-6, which implies that these lines are sensitive to molecular gas at lower densities. We also study the non-LTE conditions and the influence of variable beam filling factors for the different isotopologues: given their optical thickness, and thus sensitivity to lower density gas, one may expect larger beam filling factors for the ¹²C molecules. This would further increase optical depths and therefore lead to a further decrease in the effective critical densities for the optically thick dense gas tracers.
- We compare the HCN/H¹³CN, HCO⁺/H¹³CO⁺ and HNC/HN¹³C line ratios measured in our sample to those compiled from the literature. There is good agreement between the values we find for NGC 5194 and NGC 253 with previous studies. The work done in the Galactic Center also shows compatible values with those we find in the inner parts of our sample, within the uncertainties.

THE ^{13}CO -TO- C^{18}O RATIO ACROSS GALAXY DISKS

^{13}CO -to- C^{18}O Gradients across the Disks of Nearby Spiral Galaxies

*M. Jiménez-Donaire, D. Cormier, F. Bigiel, A. Leroy,
M. Gallagher, M. Krumholz, A. Usero, A. Hughes,
C. Kramer, D. Meier, E. Murphy, J. Pety, E. Schinnerer,
A. Schrubba, K. Schuster, K. Sliwa, N. Tomicic,
2017, ApJL, 836, L29.*

High density gas is formed out of the bulk, lower density molecular gas (see Chapter 1). An additional focus of this thesis is to better understand the conditions in the lower density medium too and, ultimately, to understand how both are related. As seen in Chapter 4, the carbon abundance ratio $-\text{[}^{12}\text{C}/^{13}\text{C}\text{]-}$ is a key quantity to determine the optical depth of tracers like HCN, HCO^+ or HNC.

In this chapter, we employ the ^{13}CO and C^{18}O isotopologues of ^{12}CO to trace the variation of isotopic abundances across the disks of galaxies. The content presented in this chapter has been published as: *^{13}CO -to- C^{18}O Gradients across the Disks of Nearby Spiral Galaxies (Jiménez-Donaire et al., 2017, ApJL, 836, L29)*. For clarity and to avoid repetition, we refer the reader to the appropriate sections corresponding to observations and data reduction. The original content, however, can be found in the publication above.

5.1 Abstract

We use the IRAM Large Program EMPIRE and new high-resolution ALMA data to measure $^{13}\text{CO}(1-0)/\text{C}^{18}\text{O}(1-0)$ intensity ratios across nine nearby spiral galaxies. These isotopologues of ^{12}CO are typically optically thin across most of the area in galaxy disks, and this ratio allows us to gauge their relative abundance due to chemistry or stellar nucleosynthesis effects. Resolved $^{13}\text{CO}/\text{C}^{18}\text{O}$ gradients across normal galaxies have been rare due to the faintness of these lines. We find a mean $^{13}\text{CO}/\text{C}^{18}\text{O}$ ratio of 6.0 ± 0.9 for the central regions of our galaxies. This agrees well with results in the Milky Way, but differs from results for starburst galaxies (3.4 ± 0.9) and ultraluminous infrared galaxies (1.1 ± 0.4). In our sample, the $^{13}\text{CO}/\text{C}^{18}\text{O}$ ratio consistently increases with increasing galactocentric radius and decreases with increasing star formation rate surface density. These trends could be explained if the isotopic abundances are altered by fractionation; the sense of the trends also agrees with those expected for carbon and oxygen isotopic abundance variations due to selective enrichment by massive stars.

5.2 Introduction

Rotational transitions of the isotopologues of ^{12}CO are observable as discrete lines, with the strongest being ^{13}CO and C^{18}O . Although these lines are fainter than ^{12}CO , they can be useful diagnostic tools. In contrast to the low- J ^{12}CO lines, ^{13}CO and C^{18}O transitions often remain optically thin over large areas in galaxies. Contrasting them with the thick ^{12}CO lines can constrain the optical depth of both lines and illuminate the underlying molecular gas column and volume densities (e.g. [Young & Scoville, 1982](#); [Pineda et al., 2008](#); [Wilson et al., 2009](#)). Comparing transitions of different optically thin isotopologues, e.g., $^{13}\text{CO}/\text{C}^{18}\text{O}$, offers the chance to trace abundance variations across the disks of galaxies. Such variations may be due to chemistry and/or stellar nucleosynthesis.

The main obstacle to studying the rare CO isotopologues is the faintness of their emission lines, which is driven by their lower abundance. Typically ^{13}CO and C^{18}O are ~ 50 and ~ 500 times less abundant than ^{12}CO . As a consequence, these isotopologues have been mainly studied in bright, actively star forming systems such as (ultra)luminous infrared galaxies (U/LIRGs) and starburst galaxy centers (e.g. [Meier & Turner, 2004](#); [Costagliola et al., 2011](#); [Aladro et al., 2013](#)). Most of our knowledge about the relative variation of the ^{13}CO and C^{18}O lines across the disk of a normal star-forming galaxy comes from the Milky Way ([Langer & Penzias, 1990](#); [Wilson & Rood, 1994](#)). Better

knowledge of this ratio across the disks of normal galaxies will inform our interpretation of ^{12}CO emission, cloud chemistry, and the influence of recent nucleosynthesis.

In this chapter, we report measurements of the ^{13}CO (1-0)-to- C^{18}O (1-0) ratio across wide areas in the disks of nine nearby galaxies. These are targets of the IRAM large program EMPIRE (see Chapter 2) and a related ALMA program (Gallagher et al., *subm.*, [Jiménez-Donaire et al., 2017a](#))

5.3 Observations

EMPIRE is mapping a suite of molecular lines across the whole area of nine nearby galaxy disks using the IRAM 30-m telescope. This includes ^{13}CO (1-0) and C^{18}O (1-0), with respective rest frequencies of 110.20 GHz and 109.78 GHz. Science-ready ^{13}CO and C^{18}O data exist for eight out of the nine galaxies listed in Table 2.1 (NGC 5194 does not have C^{18}O data due to a different observing setup). We refer the reader to Chapter 2 for a detailed description of the data acquisition (see Section 2.2.3) and data reduction (see Section 2.3). We expect the $^{13}\text{CO}/\text{C}^{18}\text{O}$ ratio to be robust because both lines were observed simultaneously and any gain variations will apply to both. Statistical errors and baseline errors induced by receiver instabilities therefore dominate the uncertainties.

We also observed four targets with ALMA (NGC 3351, 3627, 4254 and 4321), using a spectral setup that covered ^{13}CO and C^{18}O . Three of the four ALMA observed systems overlap with the EMPIRE sample (NGC 3627, 4254, 4321). For this chapter, we use versions of these cubes convolved to 8". Those that overlap EMPIRE have been corrected to account for short and zero spacing information using the CASA task feather; for more details, see Section 4.3.2 and Gallagher et al. (*subm.*). The close frequency of the two lines (109.8 and 110.2 GHz), convolution to a common resolution, and simultaneous observation of ^{13}CO and C^{18}O (so that they have nearly matched $u-v$ coverage) should make the internal line ratios from ALMA robust.

Both ^{13}CO and C^{18}O become faint at large galactocentric radii. In order to measure their intensities at large r_{gal} , we employ spectral stacking. To do this, we divide the galaxies into zones of fixed radius or IR surface brightness. Then, we follow a procedure similar to that of [Schrubba et al. \(2011\)](#) and [Caldú-Primo et al. \(2013\)](#): before averaging the spectra, we estimate the local mean velocity of gas from bright ^{12}CO (2-1) emission

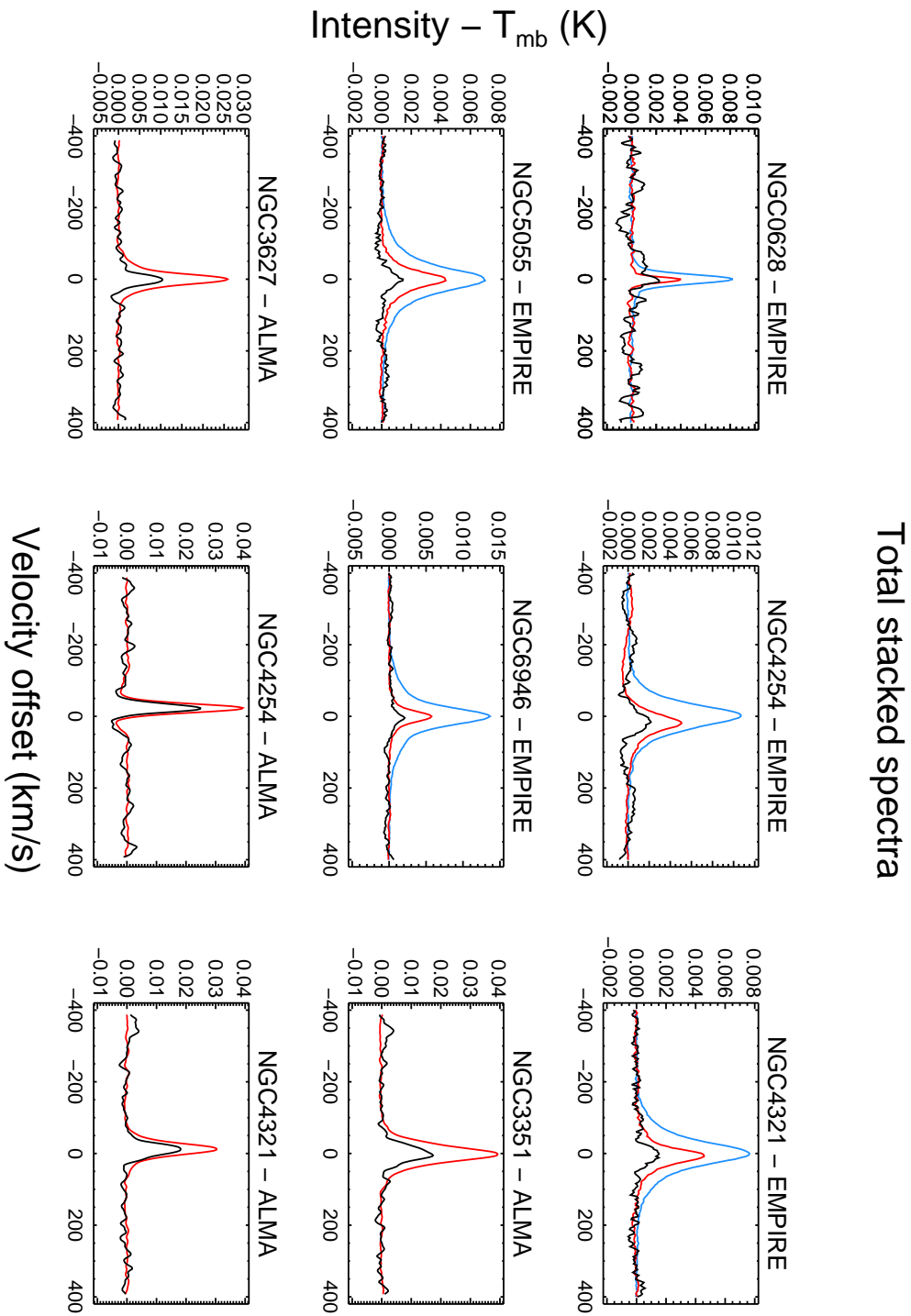


FIGURE 5.1. Stacked spectra for $^{12}\text{CO}(2-1)$ (blue), $^{13}\text{CO}(1-0)$ (red) and $\text{C}^{18}\text{O}(1-0)$ (black) emission summing over the whole IRAM 30-m and ALMA maps. C^{18}O is securely detected across seven targets (NGC 628, NGC 3351, NGC 3627, NGC 4254, NGC 4321, NGC 5055 and NGC 6946). The ^{13}CO spectra are scaled down by a factor of 3 for comparison, while the ^{12}CO spectra are scaled down by a factor of 10.

from HERACLES (Leroy et al., 2009)¹. We recenter the ^{13}CO and C^{18}O spectra about this local mean ^{12}CO velocity. Then, we average all spectra in each zone to construct a single, high signal-to-noise spectrum. After stacking, baseline issues due to receiver and weather instabilities sometimes emerge. When needed, we correct for these with an additional low-order polynomial fit.

This spectrum is then used to measure the integrated intensity of the line, summing over the channels that show bright $^{12}\text{CO}(2-1)$ emission. We apply a similar procedure to the ALMA data, but using the brighter ^{13}CO line to stack the C^{18}O . Thus the ALMA measurements are restricted to the regions of bright ^{13}CO emission. We calculated the uncertainty in the integrated intensity based on the noise estimated from the signal-free part of the stacked spectrum and the width of the integration window (usually $\sim 60 \text{ km s}^{-1}$).

We employ the total infrared (TIR) surface brightness as a proxy for the local surface density of star formation. To estimate this, we use the *Herschel* and *Spitzer* maps (see Section 3.1), and we follow the procedure already described in Section 3.1.1.

5.4 Results

Figure 5.1 shows spectra of both lines averaged over the whole EMPIRE or ALMA area for each target. We observe widespread $^{13}\text{CO}(1-0)$ from each galaxy while $\text{C}^{18}\text{O}(1-0)$ is fainter, requiring substantial averaging to achieve good signal to noise. After averaging, we detect C^{18}O at good significance for six targets in EMPIRE. The other two, NGC 2903 and NGC 3184, show only weak emission and we place lower limits on $^{13}\text{CO}/\text{C}^{18}\text{O}$ in these systems. We recover the C^{18}O line in all four ALMA targets.

Table 5.1 reports our measured $^{13}\text{CO}/\text{C}^{18}\text{O}$ ratios of line-integrated intensities on the T_{mb} scale. For each target, we quote the average ratio over the whole galaxy (from EMPIRE) and the mean ratio within the inner 30" radius from ALMA and EMPIRE combined (except for NGC 3351, see Section 5.3). In cases without clear detections, we report 3σ upper limits. Treating all galaxies equally, but neglecting upper limits, we find a mean ratio of 7.9 ± 0.8 for the whole galaxy disks. Except in NGC 628, this galaxy-averaged ratio does not vary much from galaxy to galaxy. This agrees with results by Davis (2014), who compiled observations of a large set of Seyfert, starburst, and normal

¹The complementary $^{12}\text{CO}(1-0)$ EMPIRE observations were not ready before the publication of this chapter in the original paper.

Source	Total disk (EMPIRE)	Central 30" (ALMA & EMPIRE)
EMPIRE & ALMA		
NGC 628	2.4±0.8	> 2.5
NGC 2903	> 8.0	> 7.0
NGC 3184	> 8.2	> 6.2
NGC 3351*	–	5.4±0.8
NGC 3627	9.0±1.1	> 3.2
NGC 4254	8.5±0.6	6.2±0.7
NGC 4321	9.8±0.5	5.4±0.7
NGC 5055	9.9±0.8	8.7±2.5
NGC 6946	7.6±0.5	3.8±0.3
LITERATURE		
Milky Way ^a	8.27±0.2	7.1±0.2
Solar System ^b	5.5	–
LMC ^c	30±5	–
NGC 5194	2.6±1.7 ^d	3.6±0.3 ^e
NGC 6946 ^f	–	2.3±0.2
M82 ^d – Starburst	–	2.7±0.9
NGC 253 ^g – Starburst	–	3.60±0.04
Maffei2 ^h – Starburst	–	3.8±0.8
NGC 1068 ⁱ – Starburst	–	3.4±0.9
Arp 220 ^j – ULIRG	–	1.0±0.4
Mrk 231 ^g – ULIRG	–	1.3±0.4
SMM J2135 ^k – High- <i>z</i>	–	1.0±0.3

TABLE 5.1. **Notes.** – Measured $^{13}\text{CO}/\text{C}^{18}\text{O}$ line intensity ratios for our sample and literature values. (*) Only observed with ALMA, measurements for NGC 3351 cover the central ~ 1 kpc ($\sim 20''$). **References.** – (a) [Wouterloot et al. \(2008\)](#); (b) [Wilson & Rood \(1994\)](#); (c) [Heikkila et al. \(1998\)](#); (d) [Tan et al. \(2011\)](#); (e) [Vila-Vilaró \(2008\)](#); (f) [Meier & Turner \(2004\)](#); (g) [Henkel et al. \(2014\)](#); (h) [Meier et al. \(2008\)](#); (i) [Aladro et al. \(2013\)](#); (j) [Greve et al. \(2009\)](#); (k) [Danielson et al. \(2013\)](#).

star-forming nuclei and found no clear trend relating the $^{13}\text{CO}/\text{C}^{18}\text{O}$ ratio to galaxy type.

The average $^{13}\text{CO}/\text{C}^{18}\text{O}$ ratio for the inner 30" region of our targets is 6.0 ± 0.9 , slightly lower than the disk-averaged value. Our mean values for both the disk and the nuclear regions of our targets are consistent with early work on the Milky Way, which found a $^{13}\text{CO}/\text{C}^{18}\text{O}$ abundance ratio of 5-10 ([Langer & Penzias, 1990](#)), and more recent results from [Wouterloot et al. \(2008\)](#). Our mean values for local star forming galaxies differ from those found for starburst and ULIRGs. Table 5.1 includes a compilation of literature

measurements targeting the central regions of starburst galaxies and ULIRGs. There the $^{13}\text{CO}/\text{C}^{18}\text{O}$ ratio tends to be lower than what we find, with the lines nearly equal in strength. Our mean value for disk galaxies differs from that found for starburst galaxies by a factor of ~ 2 (e.g. [Tan et al., 2011](#); [Henkel et al., 2014](#)) and from that found for ULIRGs by a factor of ~ 6 (e.g. [Greve et al., 2009](#); [Danielson et al., 2013](#)).

Averaging over whole galaxies may obscure variations in the line ratio by blending together many different physical conditions. In Figure 5.2, we break apart the galaxies where we securely detect C^{18}O at multiple radii (this removes NGC 3627 from the sample, but we show its profile using ALMA data below). We plot $^{13}\text{CO}/\text{C}^{18}\text{O}$ as a function of galactocentric radius and star formation rate surface density. In Figure 5.2 we see $^{13}\text{CO}/\text{C}^{18}\text{O}$ increase with increasing radius for NGC 4254, NGC 4321, NGC 5055 and NGC 6946. Again NGC 628 represents the outlier, with a low ratio and perhaps a dropping rather than rising profile. [Wouterloot et al. \(2008\)](#) showed a similar trend for $^{13}\text{CO}/\text{C}^{18}\text{O}$ to increase with increasing radius in the Milky Way (see their Figure 3a), consistent with the EMPIRE observations of normal-disk galaxies. These rising profiles imply high $^{13}\text{CO}/\text{C}^{18}\text{O}$ at the largest radius where we can still achieve a detection, typically $^{13}\text{CO}/\text{C}^{18}\text{O} \sim 16$ at $\sim 0.4 \times r_{25}$. At this radius, the ISM transitions from H_2 to HI dominate (see [Schruba et al., 2011](#)). To our knowledge, such high ratios have not been reported before for normal star-forming disk galaxies.

Using ALMA, we construct more detailed profiles of the inner part of four of our targets. We show these in Figure 5.4. The inner, molecule-rich parts of these galaxies do not yet show the rising profiles seen at larger radii in Figure 5.2. However, these "zoomed in" profiles show several features not immediately visible at lower resolution. Three of our targets, NGC 3351, NGC 3627, and NGC 4321 host bright inner regions (~ 500 pc, $\sim 0.05 r_{25}$) likely fed by gas flows along the bars in these galaxies. No such features are apparent in NGC 4254, which lacks a strong bar. At least in the barred galaxies we might expect less isotopic abundance variations due to efficient mixing of the gas in their inner parts, similar to what is observed in the Milky Way.

Figure 5.3 shows the ^{13}CO -to- C^{18}O ratio as a function of the surface density of star formation, Σ_{SFR} . Again, NGC 628 appears as an outlier, while the other targets with resolved gradients show decreasing $^{13}\text{CO}/\text{C}^{18}\text{O}$ with increasing Σ_{SFR} . As discussed below, the sense of this trend is what is expected if massive star nucleosynthesis alters the isotopic abundances, but it might also reflect optical depth effects. In either case, as we sort our targets by Σ_{SFR} , we observe a clear trend from "Milky Way" type values in low

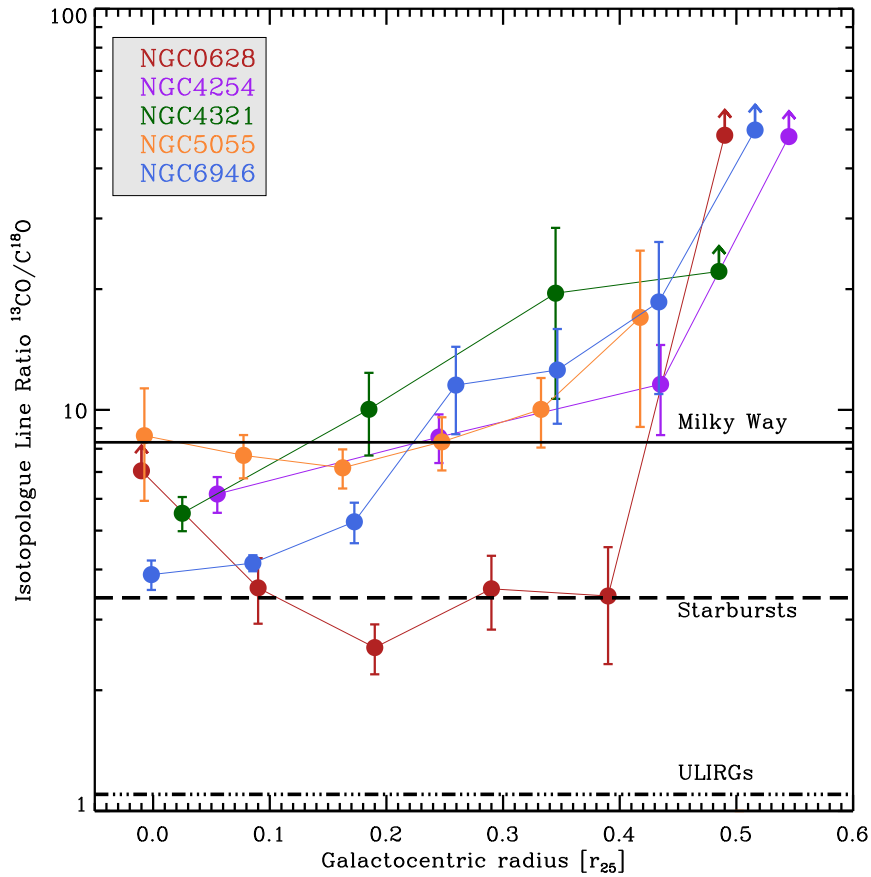


FIGURE 5.2. Stacked isotopologue line ratio $^{13}\text{CO}/\text{C}^{18}\text{O}$ as a function of galactocentric radius (in units of r_{25}). The Figure shows each measurement individually as a colored dot and the error bars show the uncertainty (1σ) from fitting the stacked spectrum. For those radial bins where C^{18}O is not securely detected, we compute upper limits to the C^{18}O emission (plotted as arrows). The radial profiles are derived for $30''$ bins for all galaxies. The black lines show the mean values for Milky Way, starburst galaxies and ULIRGS from Table 5.1.

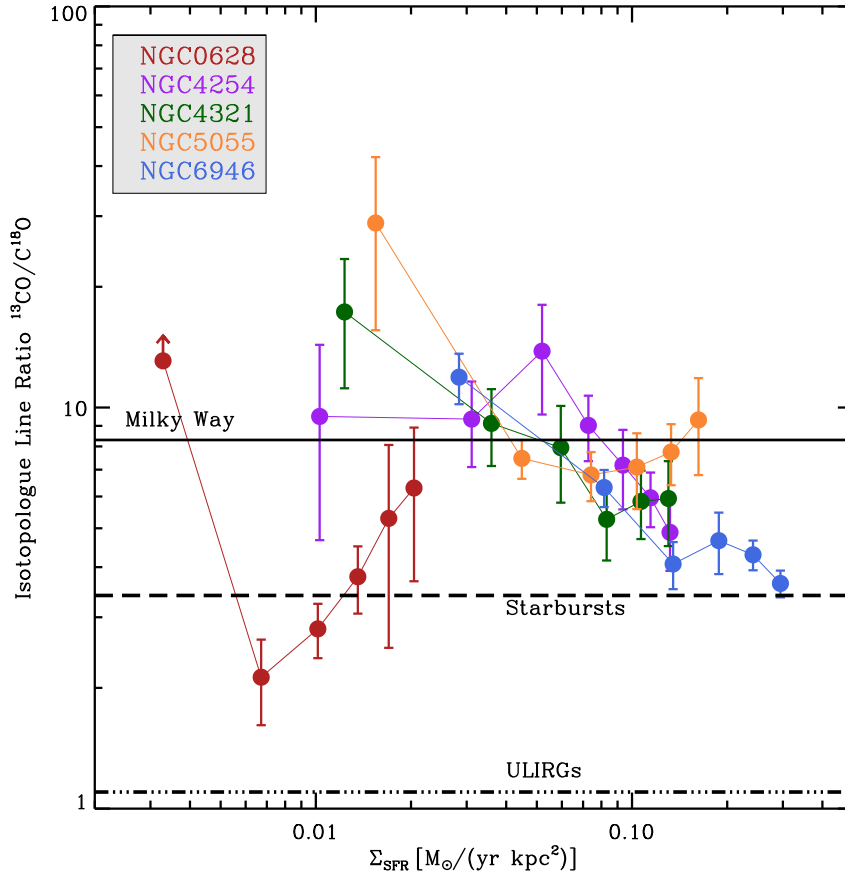


FIGURE 5.3. Stacked isotopologue line ratio $^{13}\text{CO}/\text{C}^{18}\text{O}$ as a function star formation rate surface density. Each measurement individually is represented with a colored dot and the error bars show the uncertainty (1σ) from fitting the stacked spectrum. For those radial bins where C^{18}O is not securely detected, we compute upper limits to the C^{18}O emission (plotted as arrows). The radial profiles are calculated in bins of 0.2 times the maximum Σ_{SFR} value for each galaxy. The black lines show the mean values for Milky Way, starburst galaxies and ULIRGS from Table 5.1.

Σ_{SFR} regions towards "Starburst" type values in high Σ_{SFR} regions, though our targets do not approach the ULIRG regime. We discuss explanations for these trend in the next section.

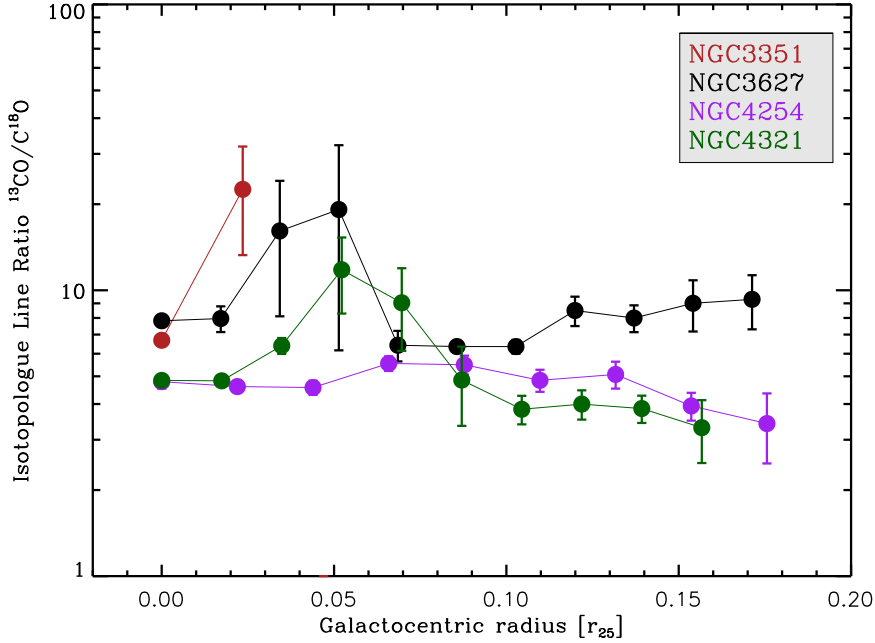


FIGURE 5.4. Stacked $^{13}\text{CO}/\text{C}^{18}\text{O}$ ratios of the inner disk at high-resolution for the four galaxies that have ALMA data vs. radius. The error bars reflect the 1σ uncertainty from the fit to the stacked spectra.

5.5 Discussion

Leaving aside NGC 628, our targets tend to show rising $^{13}\text{CO}/\text{C}^{18}\text{O}$ with increasing galactocentric radius and falling $^{13}\text{CO}/\text{C}^{18}\text{O}$ with increasing Σ_{SFR} . What drives these variations? We consider two scenarios that could explain our observations: (1) changes in the abundances of the observed molecules, and (2) changes in the optical depths of the observed lines.

5.5.1 Variations in the Molecular Abundances

The observed ratio $^{13}\text{CO}/\text{C}^{18}\text{O}$ will vary if the relative abundance of the two species varies. We highlight selective photodissociation, isotope dependent fractionation, and selective enrichment by massive star nucleosynthesis as possible explanations.

Ultraviolet radiation dissociates the molecules in molecular clouds, and preferential dissociation of one species or another could change the $^{13}\text{CO}/\text{C}^{18}\text{O}$ ratio. Selective photodissociation is possible because ^{13}CO is more effective at self-shielding against UV

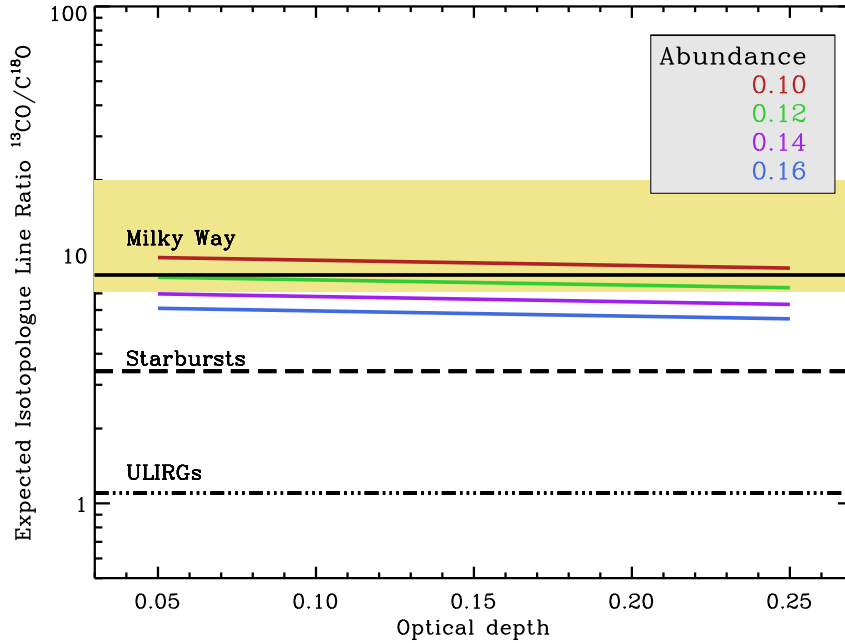
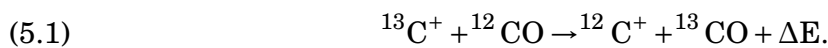


FIGURE 5.5. Expected $^{13}\text{CO}/\text{C}^{18}\text{O}$ line ratio dependence on optical depth for four different abundance ratios over the range of modest $\tau_{^{13}\text{CO}}$ that we find. The effect of changing optical depth in this regime is expected to be negligible. The yellow area represents the region covered by our observations.

photons than C^{18}O due to its higher abundance (Bally & Langer, 1982). However, even for the far more abundant isotopologue ^{12}CO , Safraneck-Shrader et al. (2017) find that self-shielding is only comparable in importance to shielding by dust and cross-shielding by the Lyman-Werner damping wings of H_2 . For the much less abundant ^{13}CO and C^{18}O , self-shielding must therefore be unimportant compared to dust- and H_2 -shielding, which are non-selective. Indeed, using DESPOTIC (Krumholz, 2014), we find that these mechanisms together are sufficient to reduce the dissociation rate for ^{12}CO and its isotopologues to near zero for columns of $N_{\text{H}_2} \sim 10^{22} \text{ cm}^{-2}$, even if there is no self-shielding. We can therefore discard the possibility of selective photodissociation as an explanation for our results.

Alternatively, isotope dependent fractionation may lead to different abundances. In cold regions, where ion-molecule chemistry dominates, there would be preferential formation of ^{13}CO by chemical fractionation:



If, as expected, cloud temperature scales with Σ_{SFR} , and the C^{18}O abundance is not affected by fractionation processes, then the $^{13}\text{CO}/\text{C}^{18}\text{O}$ ratio will decrease with Σ_{SFR} and will increase with the distance to the center of the galaxy. This could explain the increasing radial profiles for the sample if the gas is cold enough further out in their disks, as well as the increasing profiles seen in Figure 5.2 as a function of Σ_{SFR} . It would not explain the decrement in the $^{13}\text{CO}/\text{C}^{18}\text{O}$ ratio of NGC 628 as a function of Σ_{SFR} .

Very massive stars produce ^{12}C at the end of their lives. The ^{18}O is also produced by high-mass stars, but the yield depends on the amount of ^{12}C and ^{16}O that is available (e.g. [Henkel & Mauersberger, 1993](#); [Meier & Turner, 2004](#); [Nomoto et al., 2013](#), and references within). On the other hand, ^{13}C is only produced as a result from the CN cycle of Helium Burning in intermediate-mass stars, or as a secondary product in low and high mass ($>10 M_{\odot}$) stars ([Sage et al., 1991](#)). Thus, one would expect recent star formation to increase the ^{18}O and ^{12}C abundances on a short timescale, as massive stars explode as supernovae and enrich the ISM. Meanwhile, ^{13}C comes primarily from the red giant phase of intermediate-mass stars and requires more time to enrich the ISM. C^{18}O could thus be expected to become overabundant relative to ^{13}CO in regions where enrichment from young stars sets the isotopic abundances. In reality, the abundances in the molecular gas will reflect a complex combination of pre-existing enrichment, enrichment from recent star formation, and removal of gas by feedback. But the basic explanation is that gas preferentially enriched by massive stars should show low $^{13}\text{CO}/\text{C}^{18}\text{O}$.

Abundance variations due to selective nucleosynthesis offer a plausible mechanism that explains the increasing radial profiles of our sample. However, the observed $^{12}\text{C}/^{13}\text{C}$ abundance ratio in the Milky Way shows the opposite trend ([Langer & Penzias, 1990](#); [Milam et al., 2005](#)), implying that the $^{16}\text{O}/^{18}\text{O}$ abundance ratio decreases with galactocentric radius as well. This argues against nucleosynthesis as a general explanation. In NGC 628 where the radial profiles are flat, there could be older populations where the ^{13}C has been created more efficiently and well mixed back into the ISM afterwards. This galaxy could also present strong fractionation effects; however more lines are needed to investigate it in detail.

5.5.2 Changes in the Optical Depth

Our observations could also be explained if the optical depth of ^{13}CO changes across a galaxy. We expect that ^{12}CO remains optically thick over most areas in our targets.

Variations in ^{13}CO optical depth could result from changing line widths or changes in excitation due to temperature or density variations (e.g., see [Meier & Turner, 2004](#)).

We gauge the importance of the optical depth effects on our ^{13}CO measurements by comparing to ^{12}CO measurements (Cormier et al., in prep.). Assuming that the ^{12}CO is optically thick and that both species have a common excitation temperature and beam filling factor (our observations show that ^{13}CO and ^{12}CO have similar large structure, similarly to [Heyer et al. \(2009\)](#)) the ratio allows us to estimate the optical depth of the ^{13}CO transition, $\tau_{^{13}\text{CO}}$. Applying these simple assumptions to our observations, and assuming that the CO (2-1) measured by HERACLES is approximately thermalized with the CO (1-0), we find $0.05 < \tau_{^{13}\text{CO}} < 0.25$. These values imply optically thin ^{13}CO across our sample at the factor of ~ 2 level, even if our simplifying assumptions break down.

In other words, based on the observed $^{13}\text{CO}/^{12}\text{CO}$ line ratios, which are substantially lower than ~ 1 , the ^{13}CO emission that we observe appears mostly optically thin. In order to explain our observed line ratio variations, the ^{13}CO line would need to become optically thick over some regions. Thus, we do not expect that the high $^{13}\text{CO}/\text{C}^{18}\text{O}$ ratios that we observe originate from changes in $\tau_{^{13}\text{CO}}$. To illustrate this, Figure 5.4 shows the expected dependence of the isotopologue ratio on the optical depth of ^{13}CO over the range of modest $\tau_{^{13}\text{CO}}$ that we find. The effect of changing optical depth in this regime is negligible. We therefore prefer fractionation (see above) as a more likely explanation.

5.6 Conclusions

We report observations of the 1-0 transitions of ^{13}CO and C^{18}O across the disks of nine nearby galaxies from the IRAM 30m program EMPIRE and ALMA. Using a spectral stacking approach, we measured the radial variation of this ratio and its dependence on the local surface density of star formation. Because of the faintness of the C^{18}O line, this is the first significant sample of $^{13}\text{CO}/\text{C}^{18}\text{O}$ radial profiles for nearby galaxy disks.

Averaging over whole galaxy disks, we find a mean value of $^{13}\text{CO}/\text{C}^{18}\text{O}$ ratio of 7.9 ± 0.8 with no clear variations from galaxy to galaxy. In NGC 4254, NGC 4321, NGC 5055 and NGC 6946 we do observe systematic internal variations. Here $^{13}\text{CO}/\text{C}^{18}\text{O}$ increases by $\sim 40\%$ with increasing radius. We also find a decreasing $^{13}\text{CO}/\text{C}^{18}\text{O}$ ratio with increasing surface density of star formation. As a result, the central regions of our targets have a mean $^{13}\text{CO}/\text{C}^{18}\text{O}$ of 6.0 ± 0.9 , somewhat lower than the whole disk averages. This central

value resembles that found in the Milky Way (Wouterloot et al., 2008), but differs from values for starburst galaxies (3.4 ± 0.9) and ULIRGs (1.1 ± 0.4).

We argue that ^{13}CO optical depth is unlikely to drive our observed trends. Instead, we suggest that the variations in the observed ratios reflect real changes in the abundance of the two species. In our view, the most likely cause is a decrease in the amount of ^{13}CO due in hotter, higher column density environments as chemical fractionation occurs less. Alternatively, the sense of the trend is that expected if isotopic abundances are altered in active regions by massive star nucleosynthesis. However, this explanation does not appear to apply to the Milky Way.

SUMMARY AND OUTLOOK

In this thesis, we have studied the content and distribution of dense gas and its relation to the star formation process in nearby galaxies. For that, we undertook the first homogeneous large survey -EMPIRE- that systematically maps a suite of dense and molecular gas tracers across the disks of nine star-forming galaxies. The advantage of focusing in the nearby population ($d \sim 10$ Mpc) is that the disks of normal, star-forming galaxies offer a wide range of relevant processes related to star formation to explore, not always accessible from the Milky Way perspective. Our adopted approach in extragalactic sources relies on spectroscopic tracers of gas density: we contrasted high critical density lines such as HCN(1-0) with molecular gas tracers like CO(1-0) and tracers of star formation. In the following, we come back to the main questions raised in the Introduction (Chapter 1) and we outline the main results of this thesis.

6.1 Summary of results

(1) How do dense gas fractions and star formation efficiency of dense gas depend on galactic environment? The first part of this thesis (Chapter 3) was dedicated to explore how the fraction of dense gas (as traced by the HCN-to-CO ratio) and the star formation efficiency of dense gas (as traced by the SFR-to-HCN ratio) depend on local stellar surface density, gas surface density, and dynamical quantities like the mean interstellar pressure. The main results from this project reveal systematic variation in the amount of dense gas and its efficiency to form stars within galaxy disks. While gas

appears denser (larger HCN/CO) in high surface density, high pressure regions; this dense gas appears worse at forming stars (lower SFR/HCN) in high surface density, high pressure regions, regardless the galaxy morphology (Jiménez-Donaire et al. in preparation).

Recent observations in both the Milky Way and external galaxies yield conflicting results regarding the scenario for how star formation is regulated across galaxies. As detailed in Chapter 1, studies led by e.g., [Gao & Solomon \(2004\)](#); [Lada et al. \(2012\)](#); [Evans et al. \(2014\)](#) argue for a picture where molecular gas, once it reaches a particular density, always forms stars with the same efficiency. On the other hand, our results agree more with recent observations of the Milky Way center (e.g., [Longmore et al., 2013](#); [Barnes et al., 2017](#)) and nearby galaxies (e.g., [Usero et al., 2015](#); [Bigiel et al., 2016](#)); which suggest a context-dependent role for gas of a particular density (Jiménez-Donaire et al. in preparation).

(2) In which way do optical depths and abundance variations affect our interpretation of the observed dense gas? The second part of this thesis is focused on better constrain physical and/or chemical processes that can affect the emission coming from the most used dense gas tracers.

Chapter 4 is dedicated to measure the optical depth of the main dense gas tracers used (HCN, HCO⁺ and HNC) and study the effects of line trapping, which can potentially allow these lines to be excited at lower gas densities than their typical critical density. We combined our main dense gas tracers with challenging observations of their optically thin isotopologues (H¹³CN, H¹³CO⁺ and HN¹³C (1-0)) and measured the optical depth of these lines for the first time in the centers of four nearby, normal star-forming galaxies. Our results show a variation of the dense gas optical depths between the galaxy centers and their disks, and lower effective critical densities compared to the optically thin case by a factor of 2-6 ([Jiménez-Donaire et al., 2017a](#)). This basic but key result reflects the fact that dense gas tracers such as HCN do not always trace the same gas densities. Therefore the derived quantities in this project are essential to estimating the masses and density structure of the dense ISM.

In the last chapter of this thesis (Chapter 5) we aimed to bring a deeper insight into the ¹²C/¹³C abundance ratio. This quantity is one of the key parameters that goes into the determination of optical depths and is often naively assumed to have a constant, Solar system value ([Wilson & Rood, 1994](#)). In our Galaxy, an increasing radial gradient in the ¹²C/¹³C isotopic abundance ratio was observed from values of 30 (central 2 kpc) to ≥ 100

(at large radii) and is believed to be tracing the chemical evolution of the Galaxy. Using the simultaneous observations of ^{13}CO and C^{18}O we measured ^{13}CO -to- C^{18}O ratios across galaxy disks to trace the relative abundance¹ of the molecules. Our observations show that the line ratio increases with increasing radii (Figure 5.2), and we mainly attribute it to chemical fractionation, which could also play an important role in the outskirts of galaxies (Jiménez-Donaire et al., 2017b).

As a concluding remark, the key results from the dense gas observations in nearby galaxies presented in this thesis, provide additional support for an environment-dependent role of density in the star formation process (Jiménez-Donaire et al. in prep.). However caution must be taken when interpreting the emission coming from gas tracers and the ratios among them. The work presented in this thesis shows how the optical depth of emission lines coming from dense gas tracers can affect their sensitivity to gas density (Jiménez-Donaire et al., 2017a). In order to better derive dense gas optical depths across galaxy disks, constraining isotopic abundances is key, and can additionally give insight into the physical and chemical processes enriching the disks of nearby galaxies (Jiménez-Donaire et al., 2017b). In that regard, more observations of optically thin isotopologues are crucial to probe the optical depth of mm-wave lines and isotopic abundance.

6.2 Outlook

The EMPIRE survey and the first results presented in this thesis constitute a major step forward into the characterization of the dense ISM in extragalactic sources. Systematic, resolved measurements of a set of dense gas tracers across disks of normal, nearby galaxies was a regime never explored before. Our main findings in this work are the variations in key quantities: dense gas fraction and the efficiency of star formation in dense gas. Understanding how these quantities are linked to the environment is the first step to describe the influence of the galactic context on star formation. Moreover, this is very important to constrain galaxy evolution and star formation in a cosmological context.

Much progress remains to be made in further characterizing the link between molecular gas, dense gas and star formation in galaxies. In particular, better constraining molecular cloud properties in external galaxies is crucial for a better understanding of the interplay between ISM and star formation across a variety of environments. Studying

¹Only true if both isotopologues are optically thin

the nearby galaxy population additionally offers access to a wide range of conditions and an external perspective not available in the Milky Way studies. Observation, analysis and modeling of sets of molecular lines and their correlations are fundamental next steps. The next subsections explore different paths to explore in the future.

Constraining gas volume densities across galaxy disks

The work presented in this thesis highlights the important role of gas density, a key quantity in many star formation theories (e.g., [McKee & Ostriker, 2007](#); [Lada et al., 2012](#); [Krumholz et al., 2012](#)) because it ultimately determines the dynamical time-scales in molecular clouds. In order to test predictions from both analytic models and simulations, an estimation of gas density across galaxies is crucial. However, observations which target external galaxies, like EMPIRE, often integrate emission over a wide range of volume densities within a single telescope beam. In these cases, we can infer molecular gas beam-averaged densities from the mm-wave emission line ratios. Recent studies explored the effect of sub-beam density distributions ([Leroy et al., 2017b](#)) by modeling the emission of a set of extragalactic lines from lognormal and power law density distributions. We find that the result of having a change in density distribution creates a characteristic "flaring" pattern of line ratio variations (such as HCN/CO) when the lines are sorted by effective critical density. Multi-line surveys like EMPIRE, which target lines excited at very different critical densities ($\sim 10^2 - 10^6 \text{ cm}^{-3}$), can be used to investigate and place empirical constraints on the shape of the gas probability density function (PDF) across normal galaxy disks for the first time.

Dense gas excitation across galaxy disks

Understanding line excitation is key to study the physical conditions of the densest molecular gas. One of the main conclusions from the work presented in this thesis is that constraining optical depth variations and effective critical densities is crucial to interpret line ratios and therefore to derive gas volume densities and abundance variations across galaxy disks. Our work on dense gas isotopologues constitutes the first step to derive dense gas optical depths across galaxies, however our current data does not allow to investigate radial variations in dense gas optical depths. Higher resolution and sensitivity observations of the HCN, HNC and HCO⁺ in the (1-0) and (3-2) transitions will allow to constrain changing density distributions in the dense molecular gas using radiative transfer modeling. This will allow to derive optical depths for the main dense

gas tracers, resolved across galaxy disks for the first time. To carry out such challenging observations, the outstanding sensitivity of ALMA at high resolution is key; in addition, the new millimeter array *Argus* at the Green Bank Telescope (GBT) will efficiently map dense gas tracers at a better resolution than EMPIRE (10" instead of 30" with the IRAM-30m telescope) with superb sensitivity.

Extragalactic Molecular Cloud scales

The most direct way to characterize how gas properties, first and foremost density, are related to average cloud properties across galactic disks, is to resolve individual molecular clouds. Single dish telescopes are important to mapping extended, low surface brightness areas in outer galaxy disks. However high-resolution observations at molecular cloud scales (~ 40 pc) can directly probe key dynamical and physical features that are blurred out in lower resolution studies (e.g., [Meidt et al., 2013](#); [Schinnerer et al., 2013, 2017](#)). Mapping nearby galaxies at molecular cloud scales is an expensive but crucial next step to distinguish dynamical features and resolve the inner parts of galaxies. This will further allow to resolve the spiral arms and gas spurs, and to distinguish clouds physically associated with star-formation from quiescent clouds. These kind of high resolution, molecular gas surveys will allow us, for example, to study line profiles for individual molecular clouds, and study extragalactic Larson's relations. Current extragalactic surveys of CO often average the emission from several molecular clouds, and the studied line broadening is mostly due to unresolved motions of the gas, rather than related to velocity dispersion in molecular clouds.

Even though this kind of observations is expensive, current mm-wave facilities like ALMA, NOEMA and the SMA are starting to provide high-sensitivity and resolution CO data which has the prospect to expand our knowledge of cloud-scale ISM structure. These facilities will provide the unique opportunity to map high-resolution CO $J = 1 - 0$, $2 - 1$, and $3 - 2$ in selected regions of galaxies to study average temperature, density, and optical depth of the bulk molecular medium, which can be related to the properties of the dense gas. As an example of what the future science will look like at cloud scales in nearby galaxies, Figure 6.1 shows the new extended coverage of the inner 10×6 kpc of M51 in CO (2-1) with the SMA (PI: K. Sliwa). At ~ 40 pc resolution, this new dataset, in combination with the CO (1-0) dataset from PAWS, will allow to study molecular gas line ratios in the nucleus, spiral arms and the interarm regions of the galaxy.

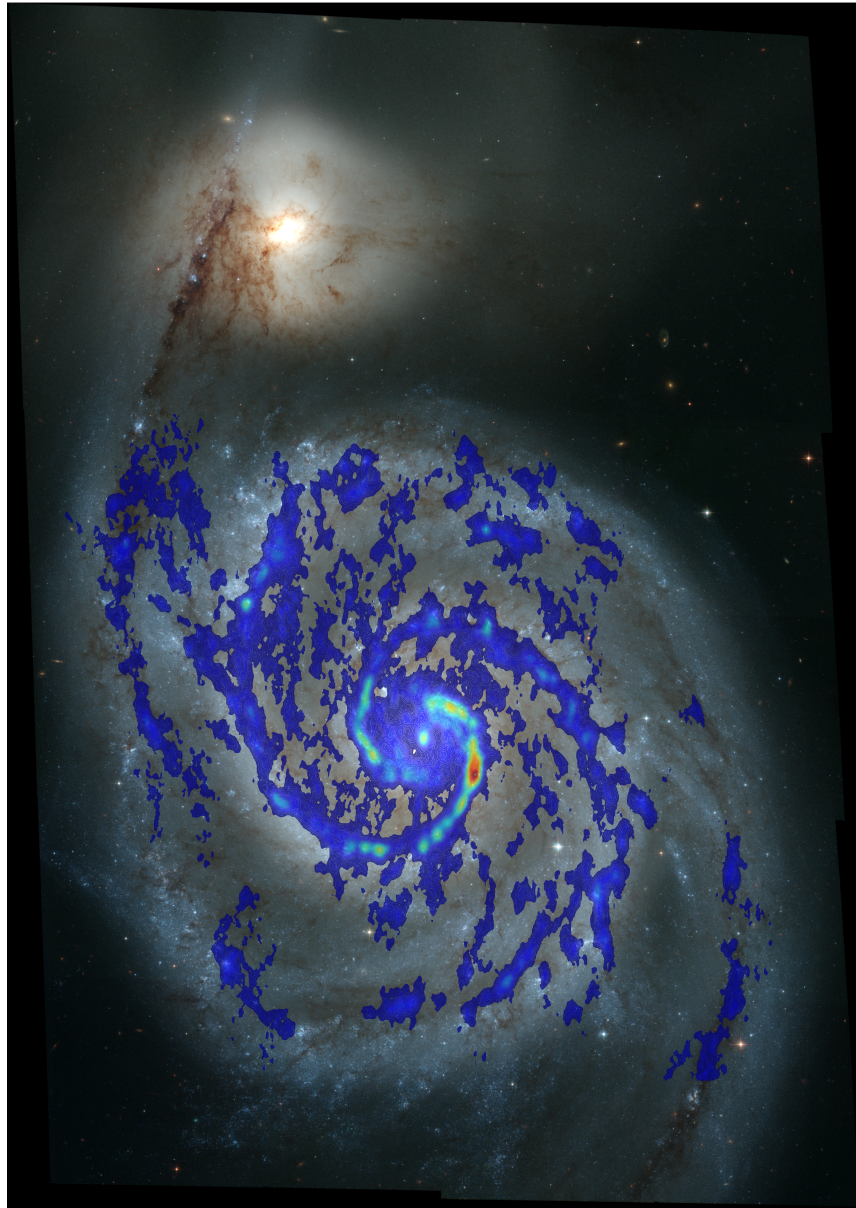
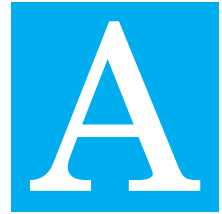


FIGURE 6.1. Integrated intensity CO (2-1) map for NGC 5194 (M51) on a HST map, at a resolution of ~ 40 pc with the SMA. Image credits: K. Sliwa and G. R. Petitpas; HST. Based on observations made with the NASA/ESA Hubble Space Telescope, and obtained from the Hubble Legacy Archive, which is a collaboration between the Space Telescope Science Institute (STScI/NASA), the Space Telescope European Coordinating Facility (ST-ECF/ESA) and the Canadian Astronomy Data Centre (CAD/C/NRC/CSA).

APPENDIX



APPENDIX A

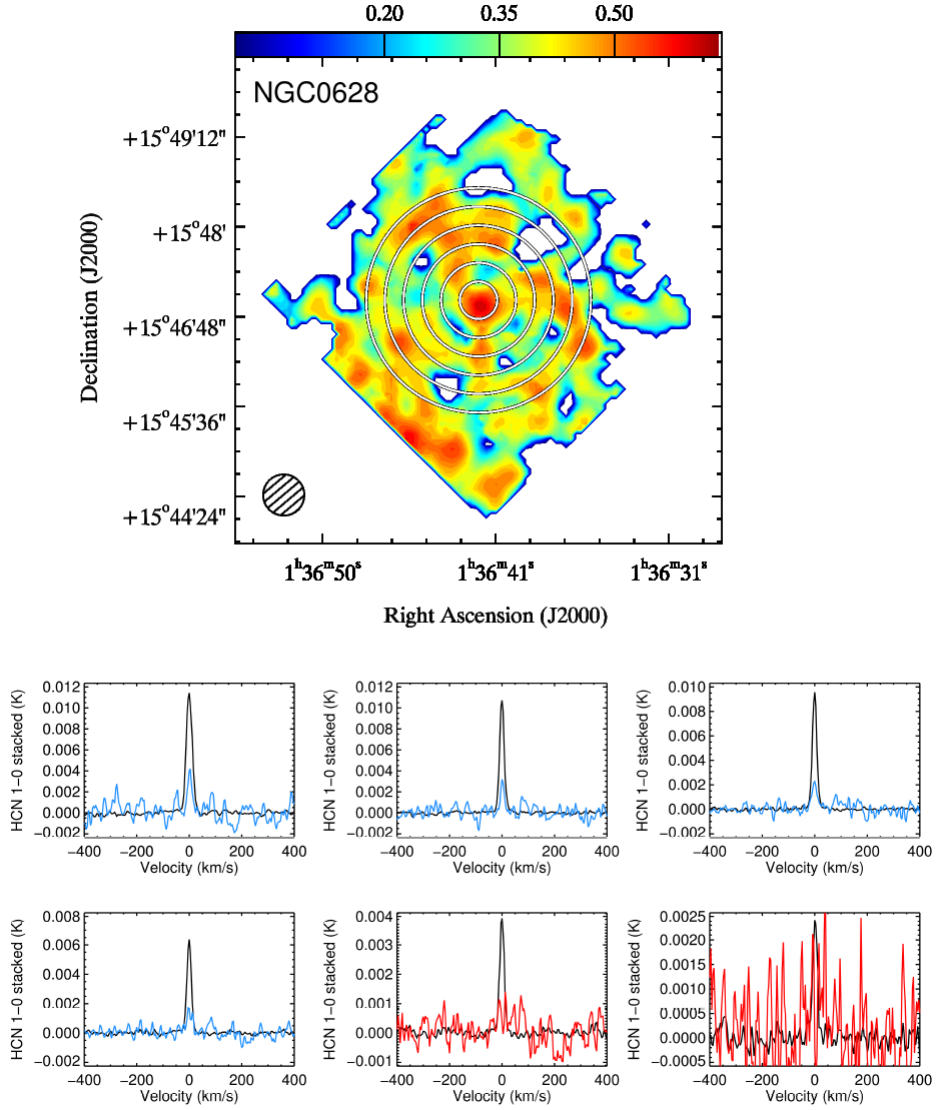


FIGURE A.1. Stacked HCN emission in radial bins of 30'' across the galaxy discs. The black line shows the stacked emission from ^{12}CO (1-0) scaled by a factor of 20 for comparison. The blue line shows the stacked emission coming from HCN (1-0). The red line represents the stacked spectra in regions where HCN (1-0) is no longer detected.

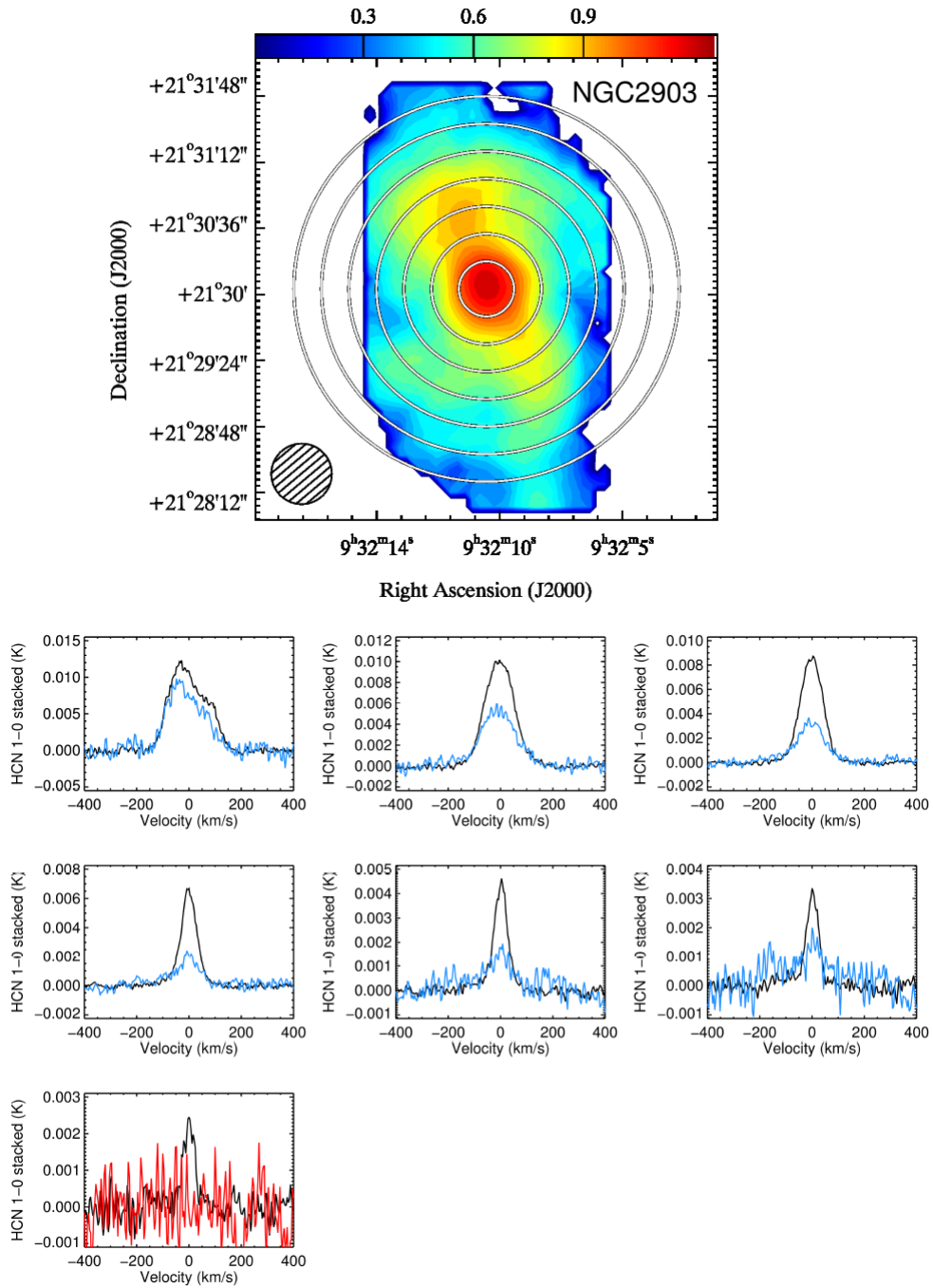


Figure A.1: continued.

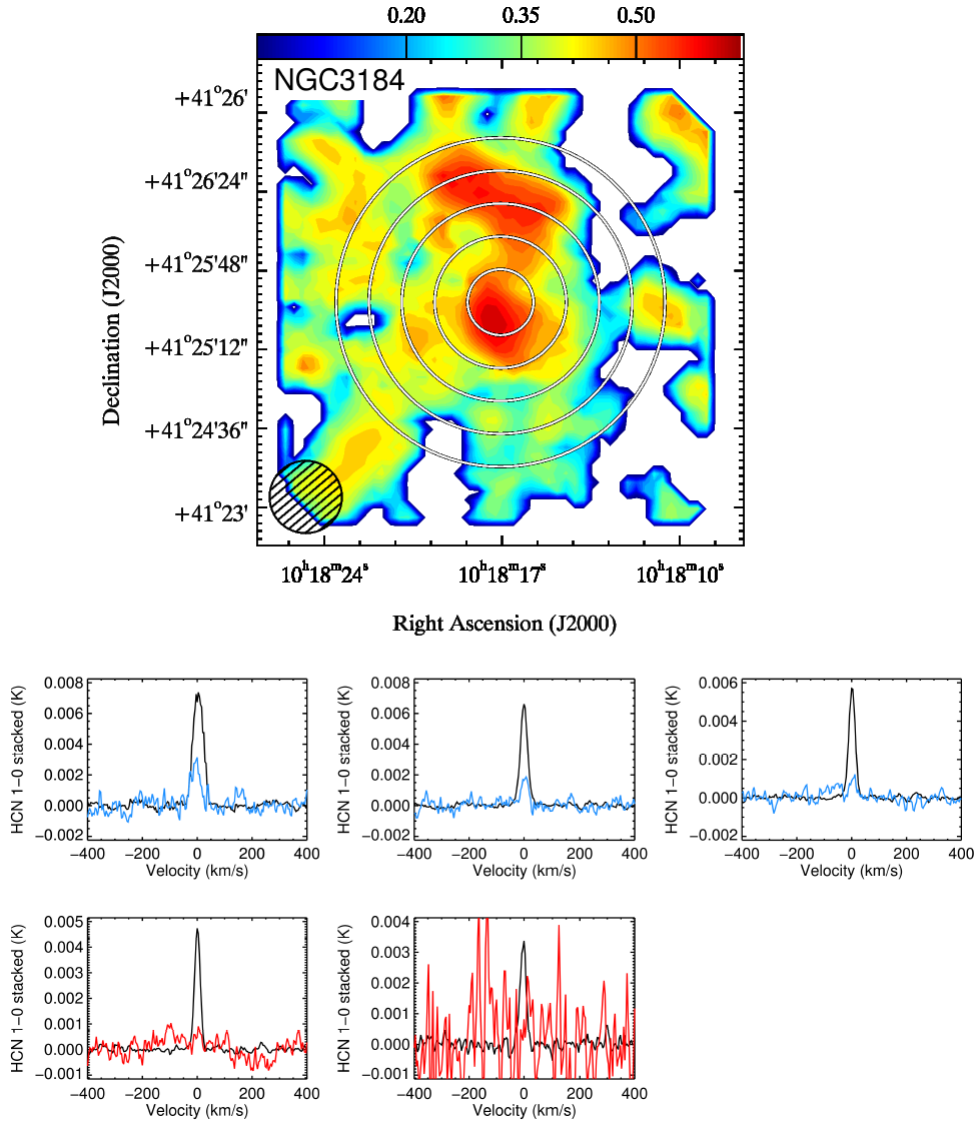


Figure A.1: continued.

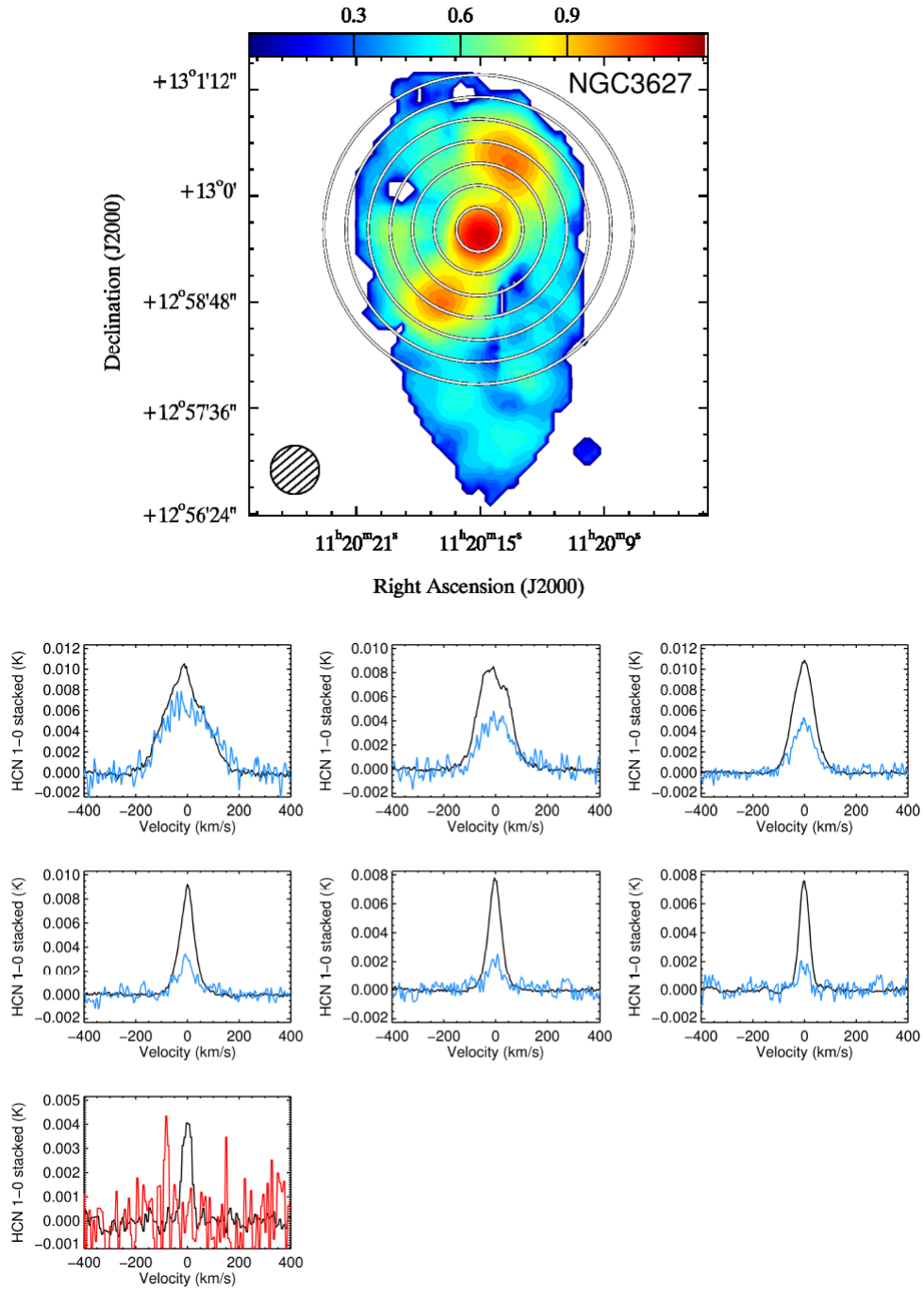


Figure A.1: continued.

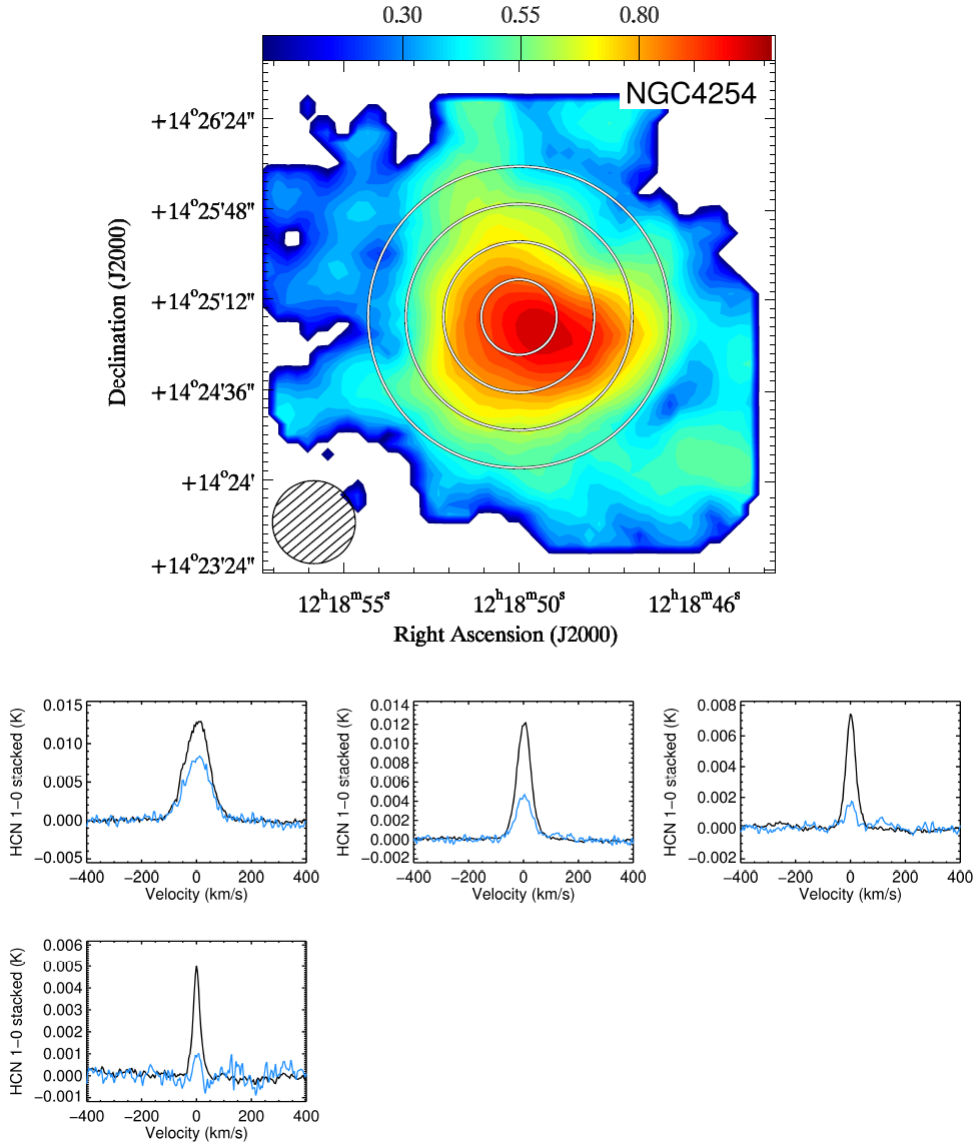


Figure A.1: continued.

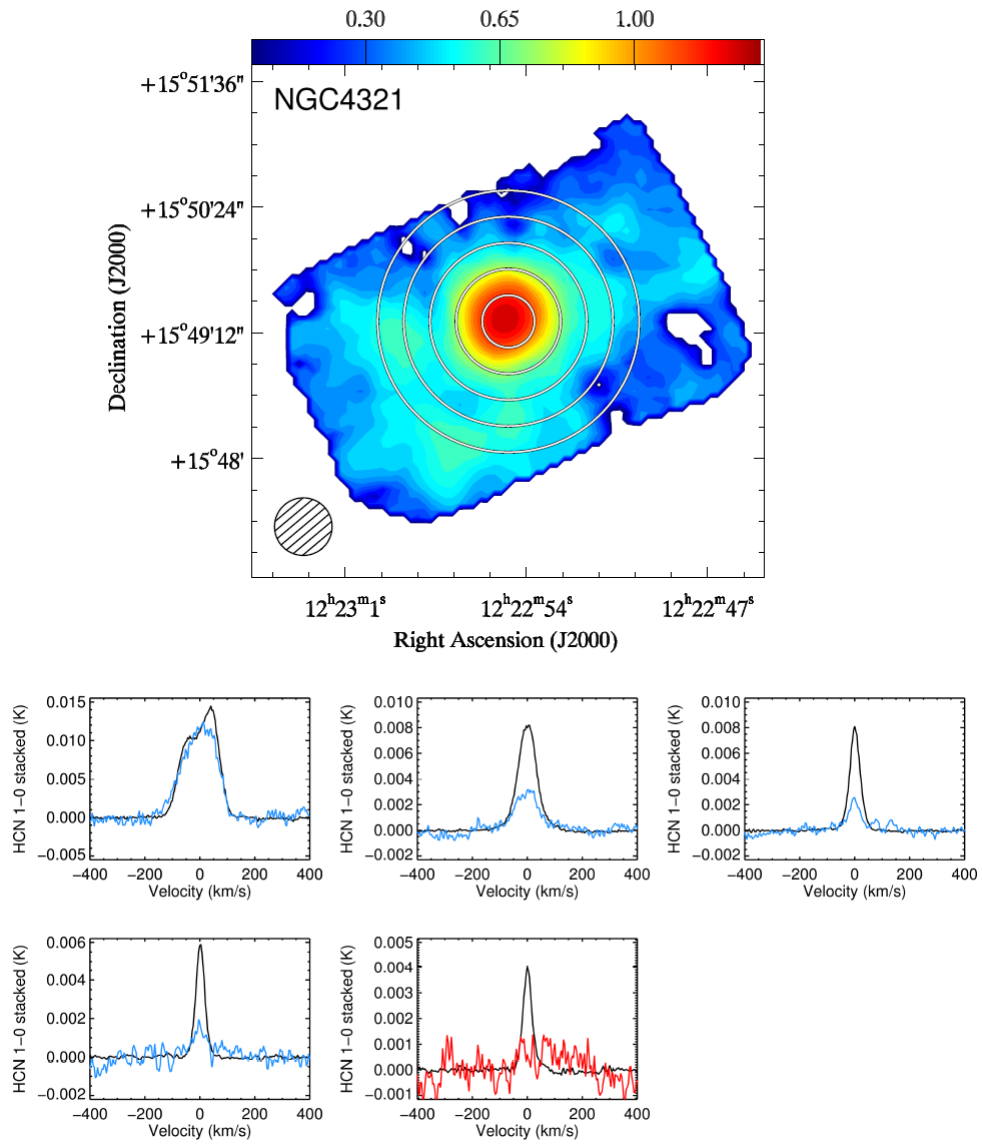


Figure A.1: continued.

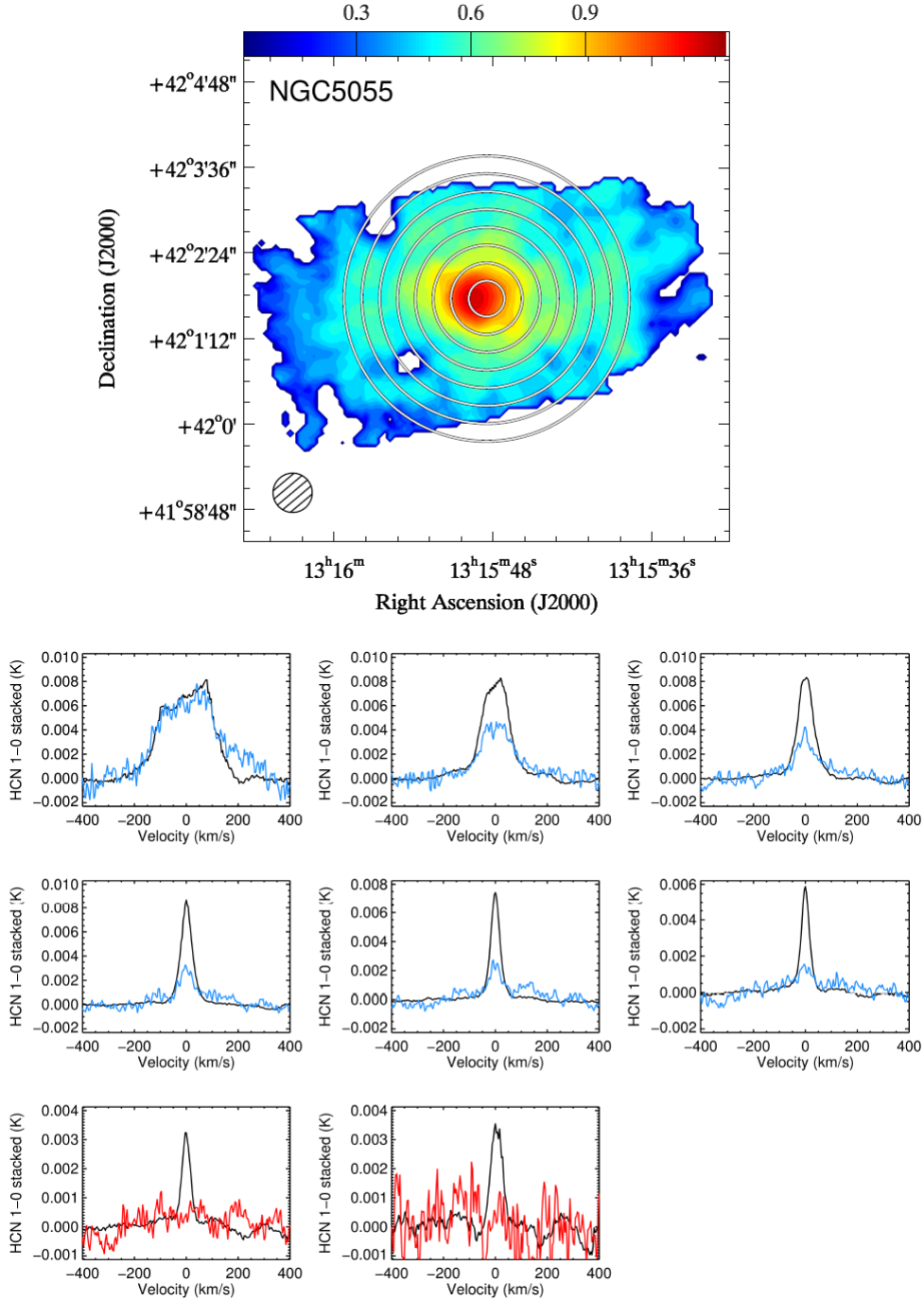


Figure A.1: continued.

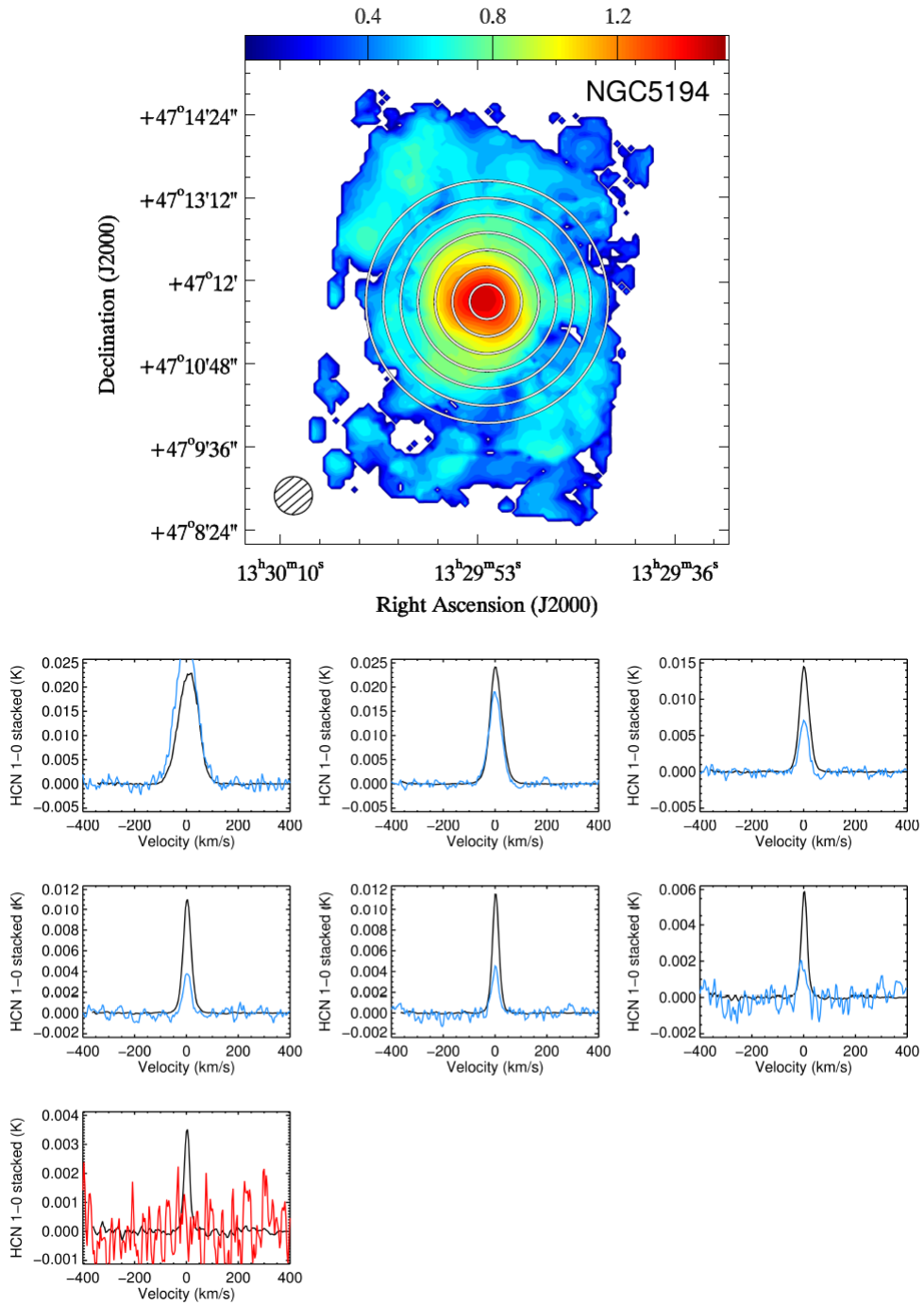


Figure A.1: continued.

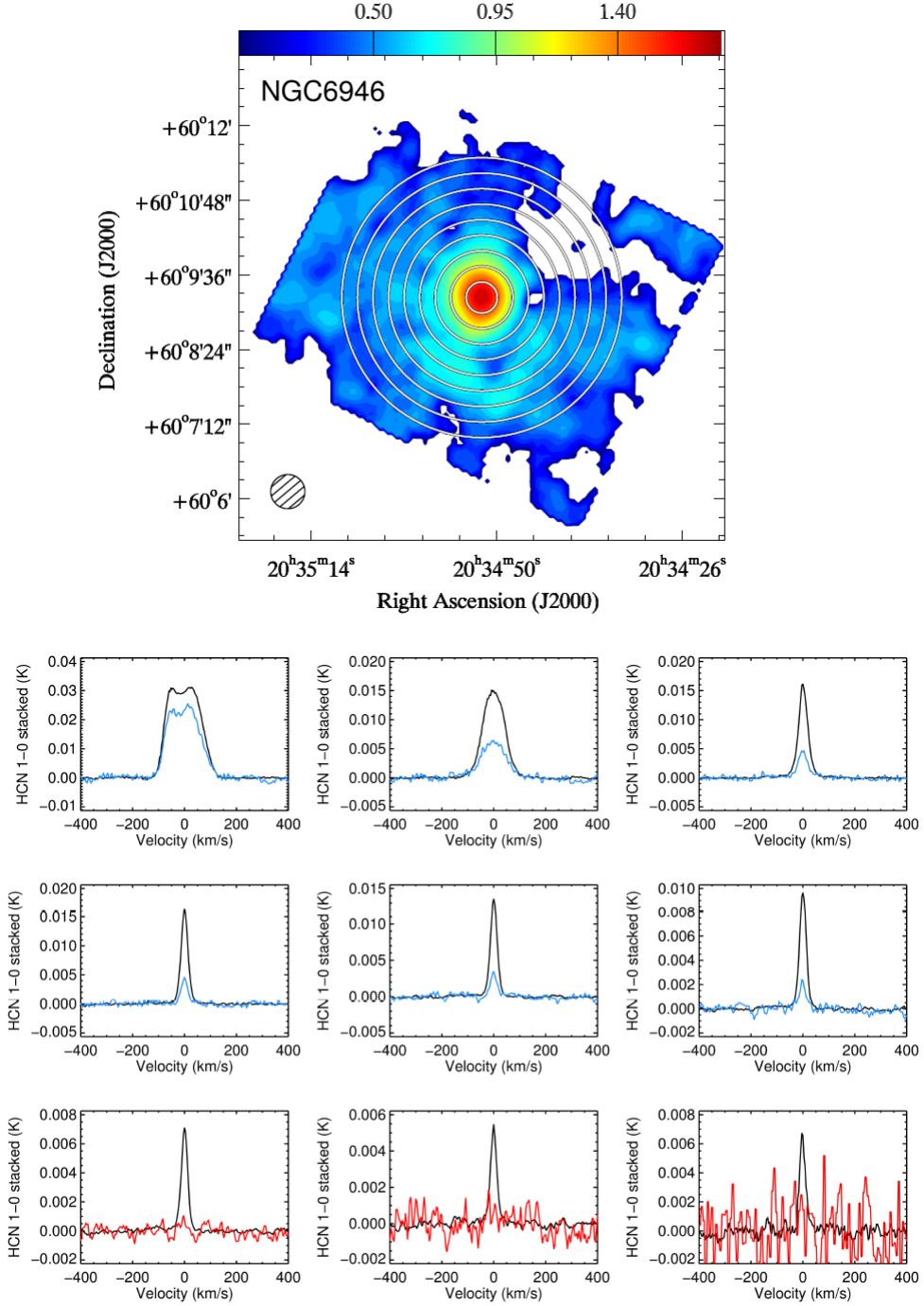
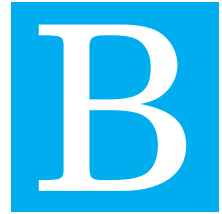


Figure A.1: continued.

APPENDIX



APPENDIX B

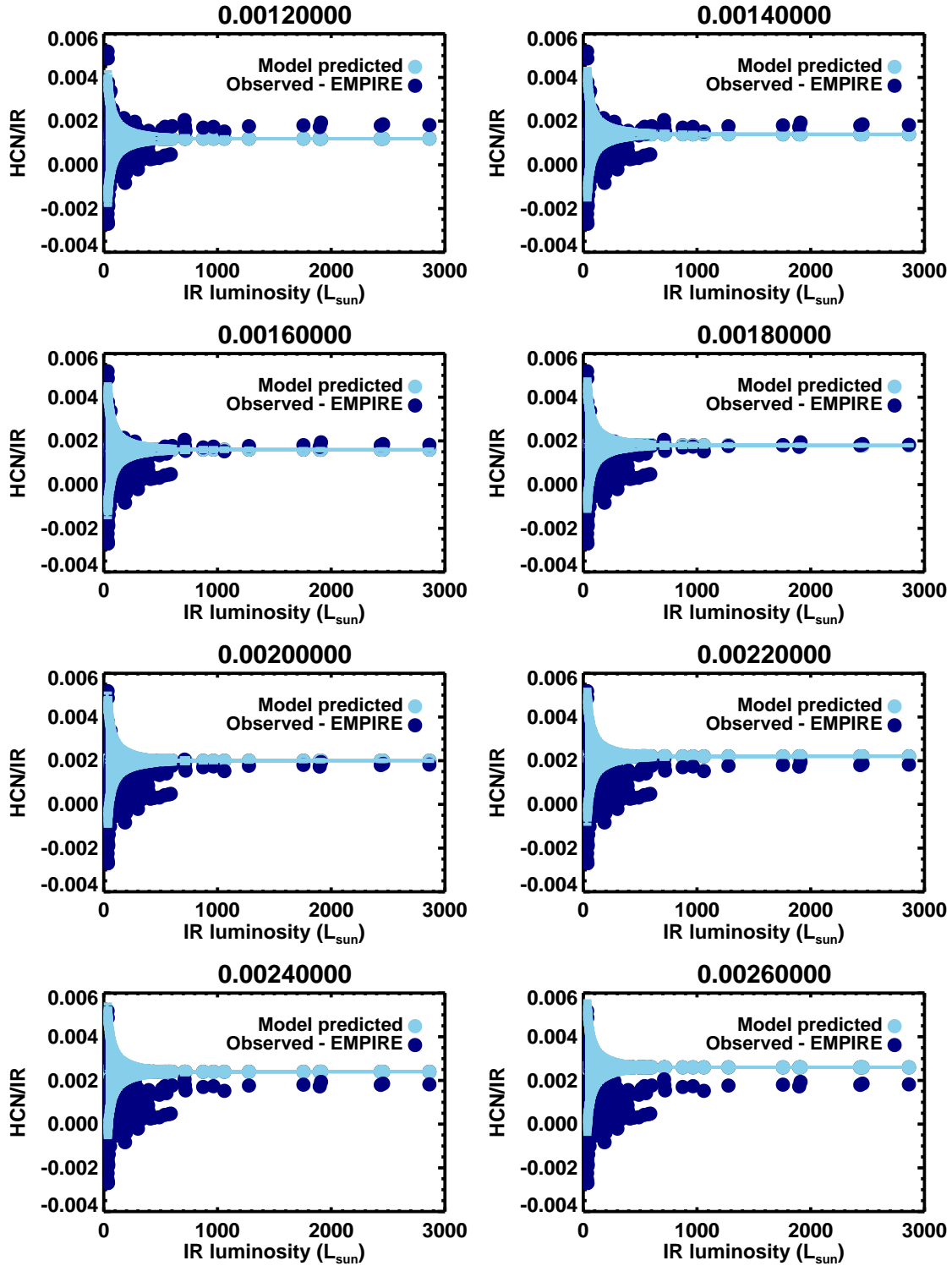


FIGURE B.1. HCN-to-IR as a function of the IR emission for NGC 6946. The EMPIRE observations are shown in dark blue and the constant HCN/IR model including HCN perturbations are shown in light blue. The different panels show the range of values for that constant, initially inferred from our high S/N measurements in the galaxy. The error bars are the (1σ) standard deviations from the modeled points in 100000 realizations.

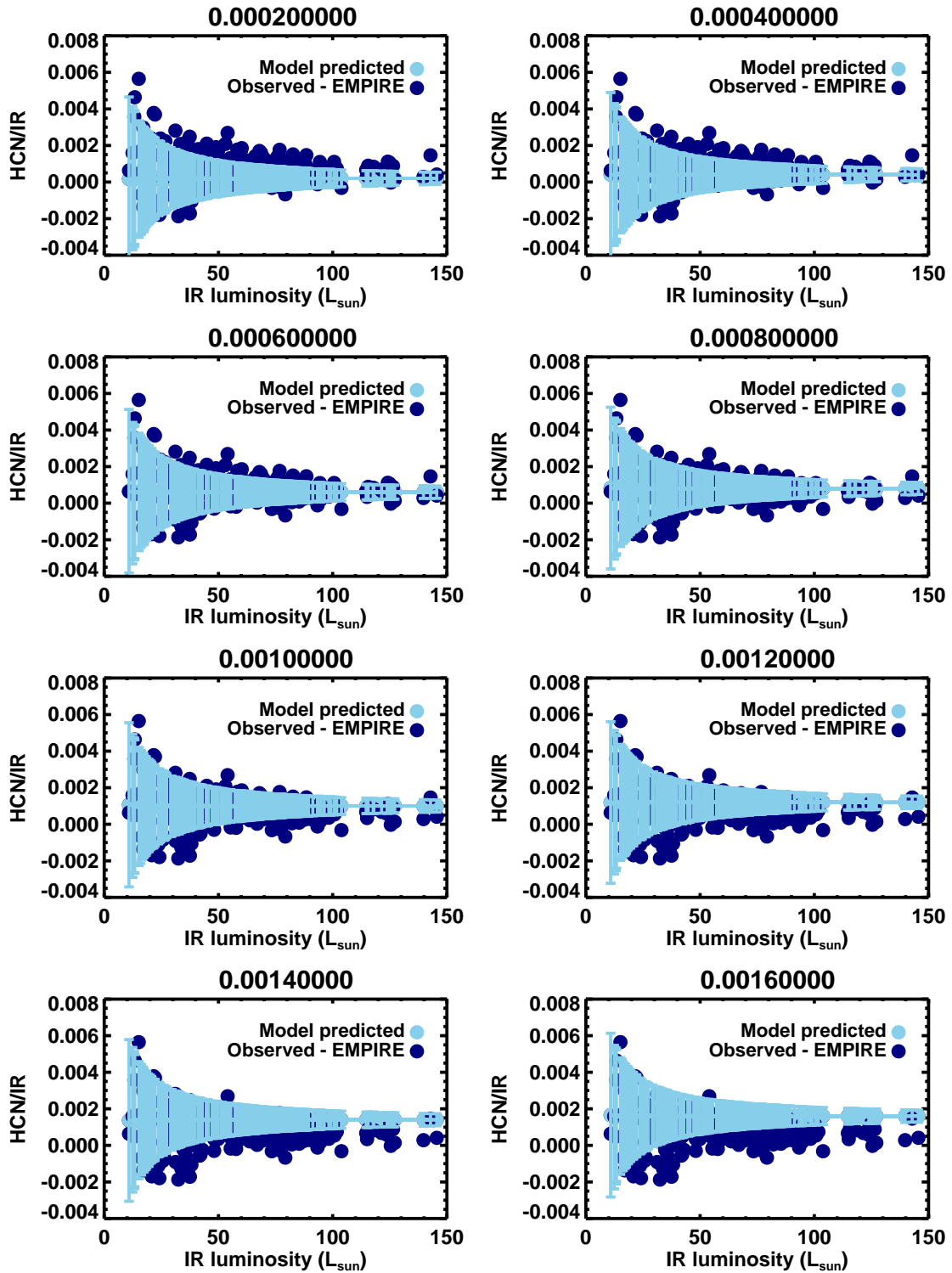


Figure B.1: continued for NGC 628

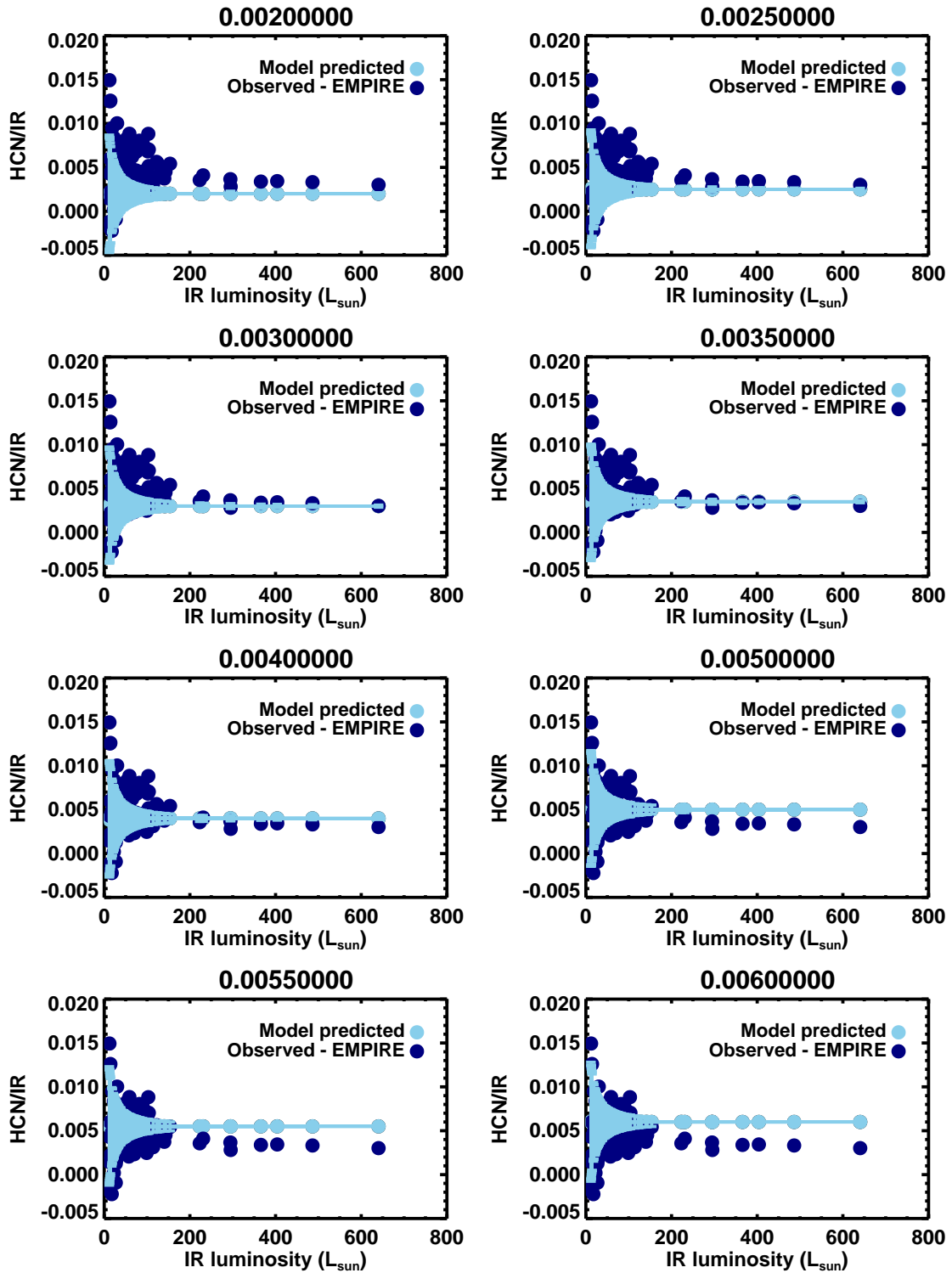


Figure B.1: continued for NGC 2903

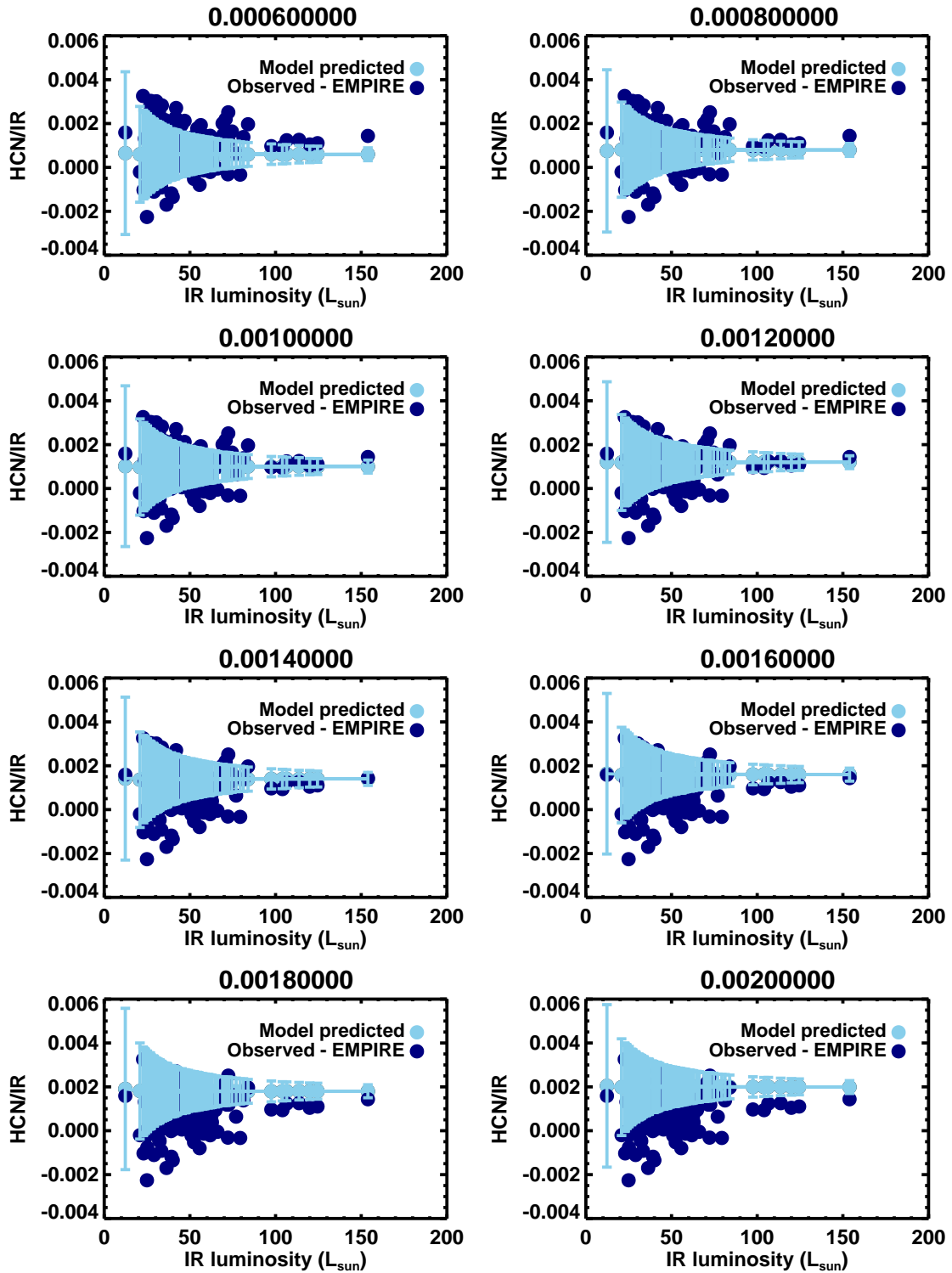


Figure B.1: continued for NGC 3184

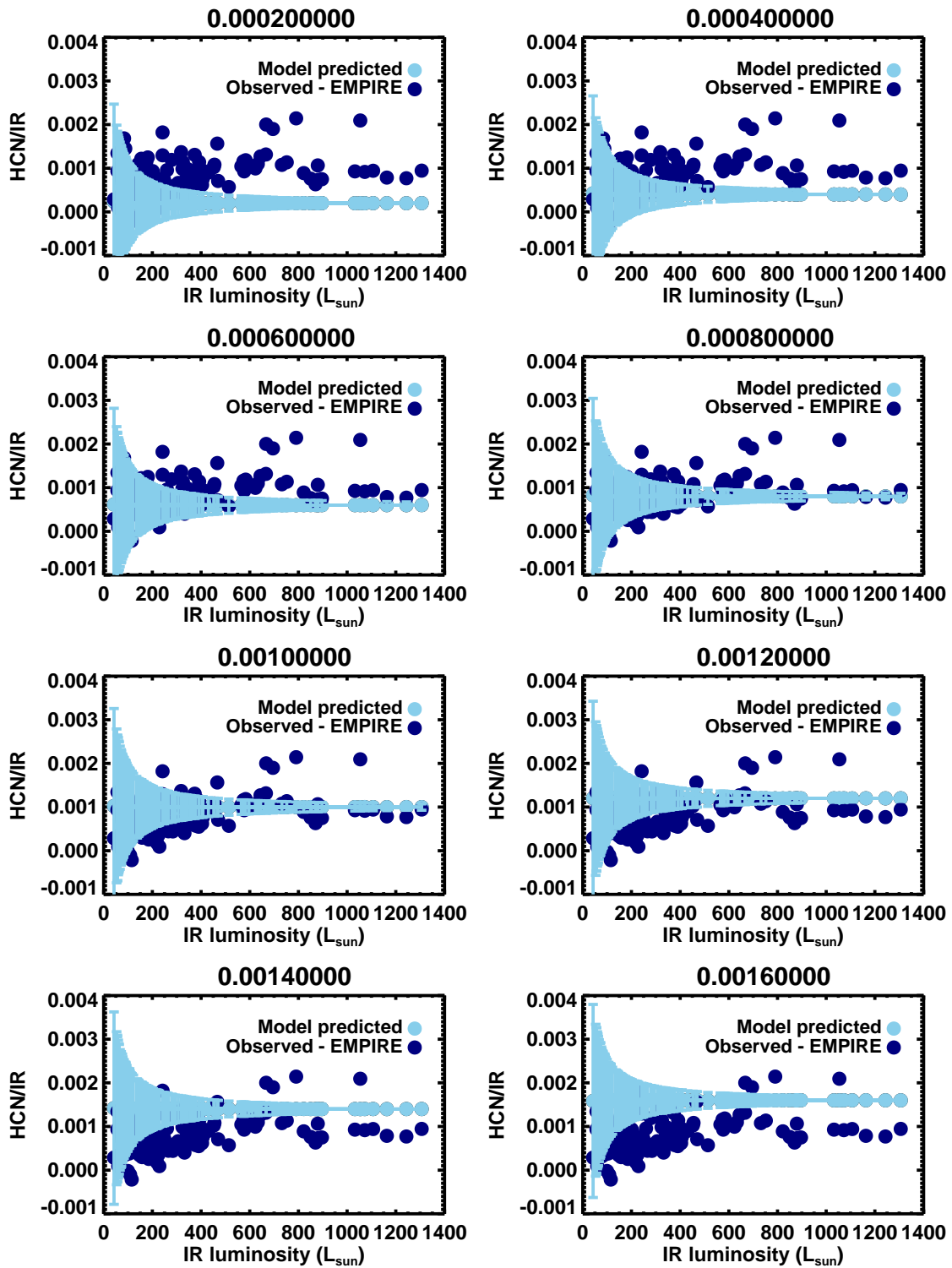


Figure B.1: continued for NGC 3627

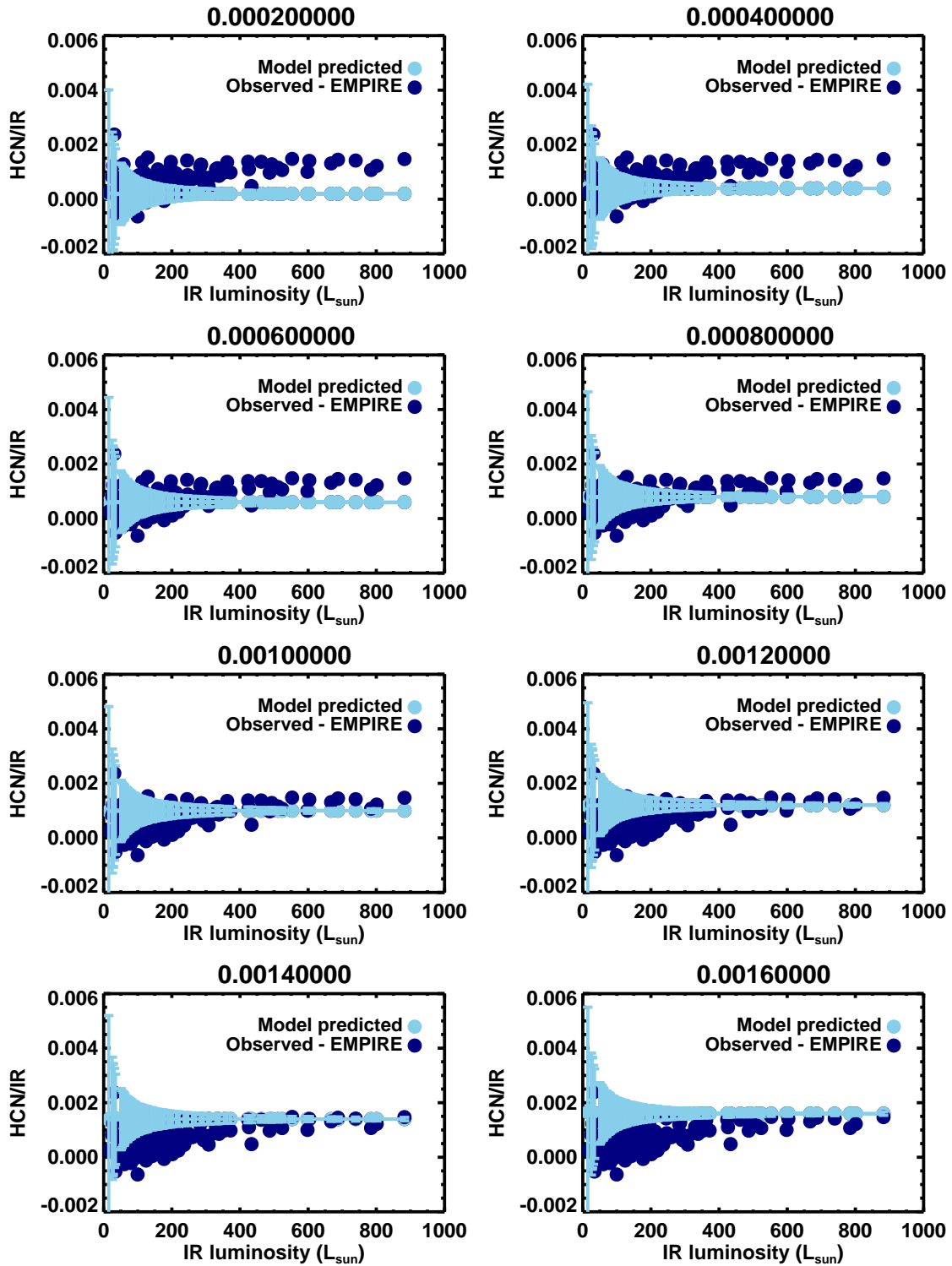


Figure B.1: continued for NGC 4254

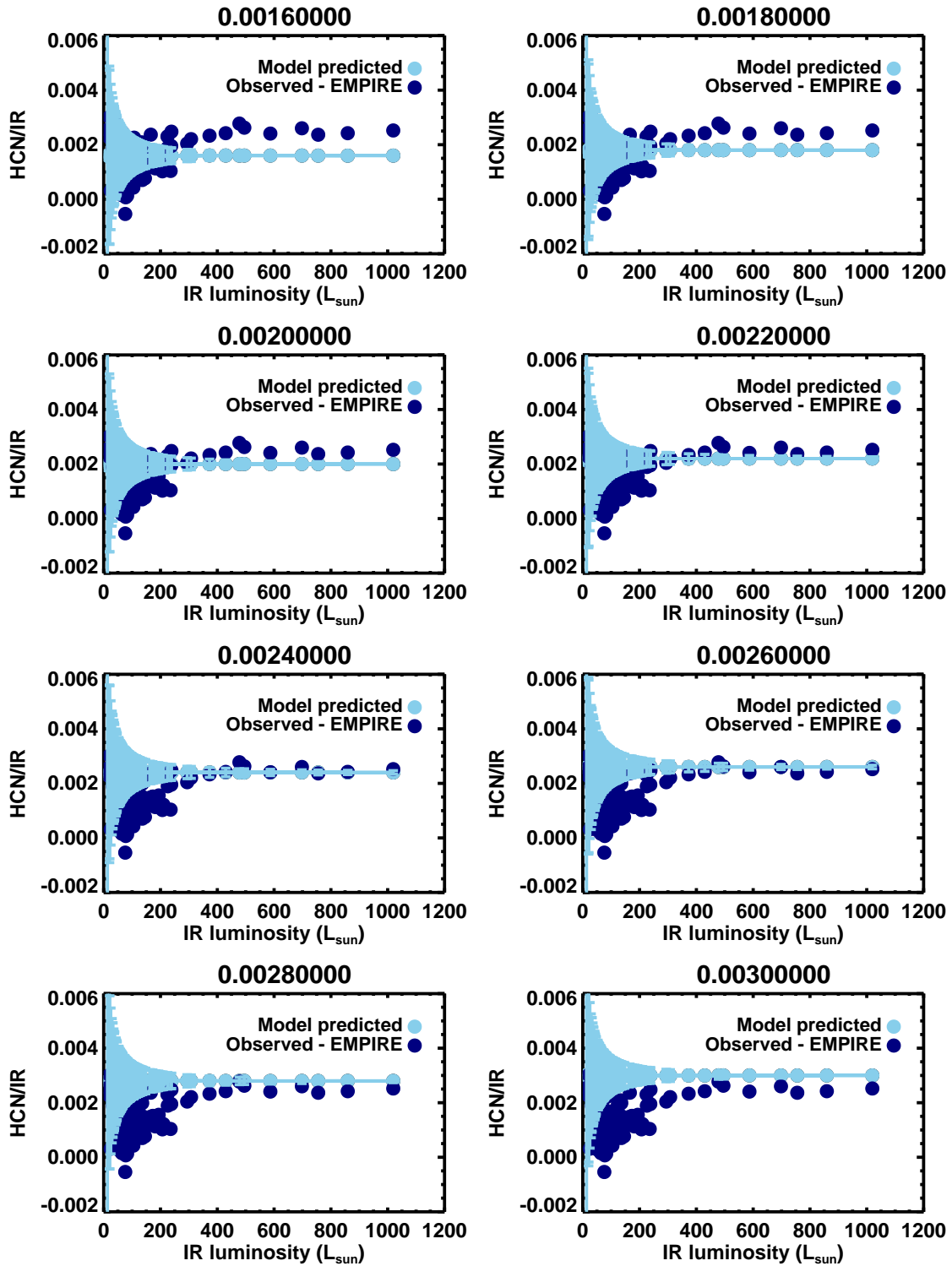


Figure B.1: continued for NGC 4321

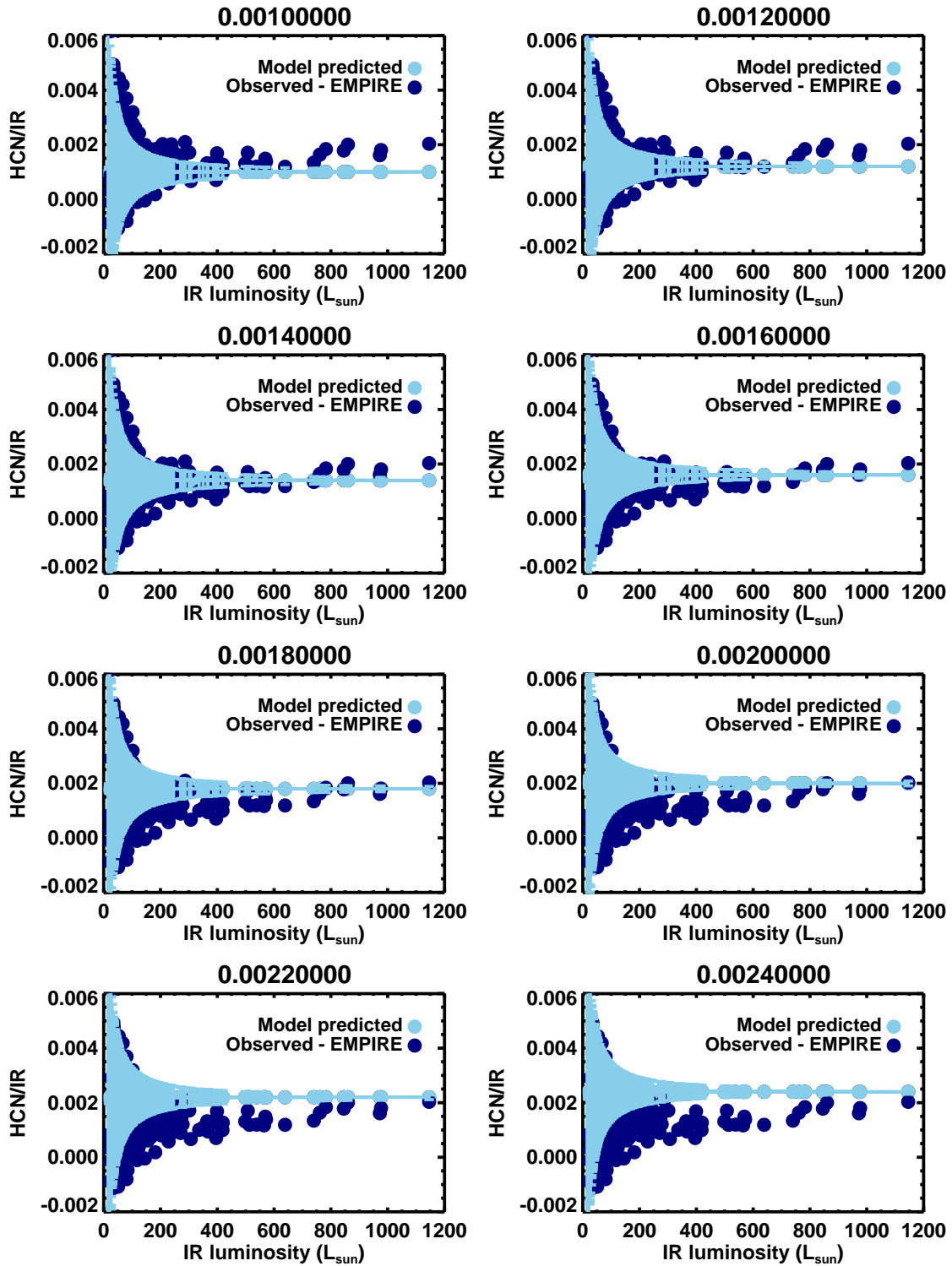


Figure B.1: continued but for NGC 5055

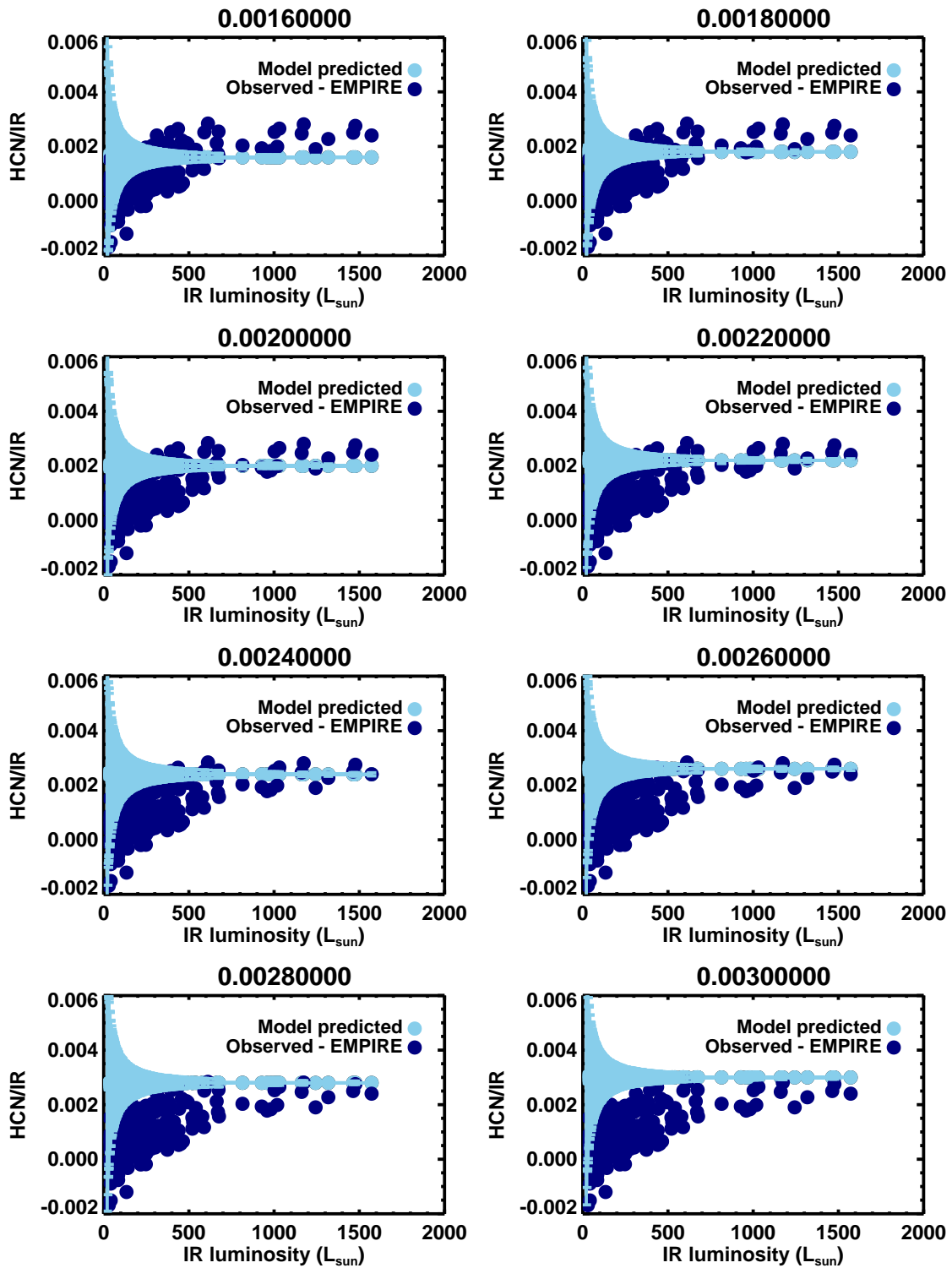


Figure B.1: continued for NGC 5194

LIST OF PUBLICATIONS

The work and results presented in this thesis are contained in papers [1], [2] and [3] from the list below.

- [1] **Jiménez-Donaire, M. J.**, Bigiel, F., Leroy, A. K., Cormier, D., et al., 2017, MNRAS 466, 49-62 ; *Optical Depth Estimates and Effective Critical Densities of Dense Gas Tracers in the Inner Parts of Nearby Galaxy Disks.*
- [2] **Jiménez-Donaire, M. J.**, Cormier, D., Bigiel, F., et al., 2017, ApJL 836, L29; *$^{13}\text{CO}/\text{C}^{18}\text{O}$ Gradients in the Disks of Spiral Galaxies.*
- [3] **Jiménez-Donaire, M. J.**, Bigiel, F., Leroy, A. K., et al., in preparation; *The EMPIRE Dense Gas Survey of Nearby Galaxy Disks.*
- [4] **Jiménez-Donaire, M. J.**, Meeus, G., Karska, A., Montesinos, B., et al., A&A, 605, A62; *Herschel Observations of the Circumstellar Environment of Herbig Be stars.*
- [5] Bigiel, F., Leroy, A. K., **Jiménez-Donaire, M. J.**, et al., 2016, ApJ Letters, 822, L26; *The EMPIRE Survey: Systematic Variations in the Dense Gas Fraction and Star Formation Efficiency from Full-disk Mapping of M51.*
- [6] Roberts-Borsani, G. W., **Jiménez-Donaire, M. J.**, Daprà, M., Alatalo, K., et al., ApJ, 844, 110; *Multiwavelength characterisation of an ACT-selected, lensed dusty star-forming galaxy at $z = 2.64$.*
- [7] Leroy, A. K., et al. incl. **Jiménez-Donaire, M. J.**, ApJ 835; *Millimeter-wave Line Ratios and Sub-beam Volume Density Distributions.*
- [8] Gallagher, M. J., et al. incl. **Jiménez-Donaire, M. J.**, submitted to ApJ; *Dense Gas, Dynamical Equilibrium Pressure, and Star Formation in Four Nearby Star-Forming Galaxies.*
- [9] Cormier, D., Bigiel, F., **Jiménez-Donaire, M. J.**, et al., to be submitted to MNRAS; *$^{13}\text{CO}(1-0)$ emission across nearby disc galaxies in the EMPIRE survey.*
- [10] Kepley, A., et al. incl. **Jiménez-Donaire, M. J.**, submitted to ApJ; *Dense Molecular Gas in the Nearby Low Metallicity Dwarf Starburst Galaxy IC 10.*

BIBLIOGRAPHY

- Aalto S., Polatidis A.G., Hüttemeister S., et al., 2002, *CN and HNC line emission in IR luminous galaxies*, *A&A*, 381, 783
- Aalto S., Spaans M., Wiedner M.C., et al., 2007, *Overluminous HNC line emission in Arp 220, NGC 4418 and Mrk 231. Global IR pumping or XDRs?*, *A&A*, 464, 193
- Aalto S., Garcia-Burillo S., Muller S., et al., 2015, *High resolution observations of HCN and HCO⁺ J = 3-2 in the disk and outflow of Mrk 231. Detection of vibrationally excited HCN in the warped nucleus*, *A&A*, 574, A85
- Aladro R., Martín S., Martín-Pintado J., et al., 2011, *A $\lambda = 1.3$ mm and 2 mm molecular line survey towards M 82*, *A&A*, 535, A84
- Aladro R., Viti S., Bayet E., et al., 2013, *A $\lambda = 3$ mm molecular line survey of NGC 1068. Chemical signatures of an AGN environment*, *A&A*, 549, A39
- Allers K.N., Jaffe D.T., Lacy J.H., et al., 2005, *H₂ Pure Rotational Lines in the Orion Bar*, *ApJ*, 630, 368
- André P., Men'shchikov A., Bontemps S., et al., 2010, *From filamentary clouds to prestellar cores to the stellar IMF: Initial highlights from the Herschel Gould Belt Survey*, *A&A*, 518, L102
- André P., Di Francesco J., Ward-Thompson D., et al., 2014, *From Filamentary Networks to Dense Cores in Molecular Clouds: Toward a New Paradigm for Star Formation*, *Protostars and Planets VI*, 27
- Aniano G., Draine B.T., Gordon K.D., et al., 2011, *Common-Resolution Convolution Kernels for Space- and Ground-Based Telescopes*, *PASP*, 123, 1218
- Aravena M., Hodge J.A., Wagg J., et al., 2014, *CO(1-0) line imaging of massive star-forming disc galaxies at $z=1.5-2.2$* , *MNRAS*, 442, 558
- Baan W.A., Henkel C., Loenen A.F., et al., 2008, *Dense gas in luminous infrared galaxies*, *A&A*, 477, 747
- Ballesteros-Paredes J., Vázquez-Semadeni E., Scalo J., 1999, *Clouds as Turbulent Density Fluctuations: Implications for Pressure Confinement and Spectral Line Data Interpretation*, *ApJ*, 515, 286

BIBLIOGRAPHY

- Bally J., Langer W.D., 1982, *Isotope-selective photodestruction of carbon monoxide*, *ApJ*, 255, 143
- Barnes A.T., Longmore S.N., Battersby C., et al., 2017, *Star formation rates and efficiencies in the Galactic Centre*, *MNRAS*, 469, 2263
- Bayet E., Williams D.A., Hartquist T.W., et al., 2011, *Chemistry in cosmic ray dominated regions*, *MNRAS*, 414, 1583
- Bertoldi F., McKee C.F., 1992, *Pressure-confined clumps in magnetized molecular clouds*, *ApJ*, 395, 140
- Bertram E., Glover S.C.O., Clark P.C., et al., 2015, *Star formation efficiencies of molecular clouds in a galactic centre environment*, *MNRAS*, 451, 3679
- Bigiel F., Leroy A., Walter F., et al., 2008, *The Star Formation Law in Nearby Galaxies on Sub-Kpc Scales*, *AJ*, 136, 2846
- Bigiel F., Leroy A.K., Blitz L., et al., 2015, *Dense Gas Fraction and Star-formation Efficiency Variations in the Antennae Galaxies*, *ApJ*, 815, 103
- Bigiel F., Leroy A.K., Jiménez-Donaire M.J., et al., 2016, *The EMPIRE Survey: Systematic Variations in the Dense Gas Fraction and Star Formation Efficiency from Full-disk Mapping of M51*, *ApJ*, 822, L26
- Blanc G.A., Heiderman A., Gebhardt K., et al., 2009, *The Spatially Resolved Star Formation Law From Integral Field Spectroscopy: VIRUS-P Observations of NGC 5194*, *ApJ*, 704, 842
- Blitz L., 1993, *Giant molecular clouds*, in *Protostars and Planets III*, edited by E.H. Levy, J.I. Lunine, pp. 125–161
- Blitz L., Rosolowsky E., 2004, *The Role of Pressure in Giant Molecular Cloud Formation*, *ApJ*, 612, L29
- Blitz L., Rosolowsky E., 2006, *The Role of Pressure in GMC Formation II: The H₂-Pressure Relation*, *ApJ*, 650, 933
- Boissier S., Prantzos N., Boselli A., et al., 2003, *The star formation rate in disc galaxies: thresholds and dependence on gas amount*, *MNRAS*, 346, 1215
- Bolatto A.D., 2015, *Using CO to Measure Molecular Masses*, in *EAS Publications Series*, vol. 75 of *EAS Publications Series*, pp. 81–86
- Bolatto A.D., Warren S.R., Leroy A.K., et al., 2013a, *Suppression of star formation in the galaxy NGC 253 by a starburst-driven molecular wind*, *Nature*, 499, 450
- Bolatto A.D., Wolfire M., Leroy A.K., 2013b, *The CO-to-H₂ Conversion Factor*, *ARA&A*, 51, 207
- Braine J., Guélin M., Dumke M., et al., 1997, *Gas and dust in the active spiral galaxy*

- NGC 3079., A&A, 326, 963
- Braine J., Shimajiri Y., André P., et al., 2017, *Dense gas in low-metallicity galaxies*, A&A, 597, A44
- Braun R., Thilker D.A., Walterbos R.A.M., et al., 2009, *A Wide-Field High-Resolution H I Mosaic of Messier 31. I. Opaque Atomic Gas and Star Formation Rate Density*, ApJ, 695, 937
- Brouillet N., Muller S., Herpin F., et al., 2005, *HCN and HCO⁺ emission in the disk of <ASTROBJ>M 31</ASTROBJ>*, A&A, 429, 153
- Buat V., 1992, *Global recent star formation in normal galaxies from a multiwavelength study - Comparison with their gas content*, A&A, 264, 444
- Buat V., Deharveng J.M., Donas J., 1989, *Star formation rate and gas surface density in late-type galaxies*, A&A, 223, 42
- Buchbender C., Kramer C., Gonzalez-Garcia M., et al., 2013, *Dense gas in M 33 (HerM33es)*, A&A, 549, A17
- Caldú-Primo A., Schrubba A., 2016, *Molecular Gas Velocity Dispersions in the Andromeda Galaxy*, AJ, 151, 34
- Caldú-Primo A., Schrubba A., Walter F., et al., 2013, *A High-dispersion Molecular Gas Component in Nearby Galaxies*, AJ, 146, 150
- Calzetti D., Kennicutt Jr. R.C., Bianchi L., et al., 2005, *Star Formation in NGC 5194 (M51a): The Panchromatic View from GALEX to Spitzer*, ApJ, 633, 871
- Calzetti D., Kennicutt R.C., Engelbracht C.W., et al., 2007, *The Calibration of Mid-Infrared Star Formation Rate Indicators*, ApJ, 666, 870
- Carter M., Lazareff B., Maier D., et al., 2012, *The EMIR multi-band mm-wave receiver for the IRAM 30-m telescope*, A&A, 538, A89
- Chen H., Gao Y., Braine J., et al., 2015, *Spatially Resolved Dense Molecular Gas and Star Formation Rate in M51*, ApJ, 810, 140
- Chen H., Braine J., Gao Y., et al., 2017, *Dense Gas in the Outer Spiral Arm of M51*, ApJ, 836, 101
- Chin Y.N., Henkel C., Whiteoak J.B., et al., 1997, *Molecular abundances in the Magellanic Clouds. I. A multiline study of five cloud cores.*, A&A, 317, 548
- Chin Y.N., Henkel C., Millar T.J., et al., 1998a, *Molecular abundances in the Magellanic Clouds. III. LIRS36, a star-forming region in the Small Magellanic Cloud*, A&A, 330, 901
- Chin Y.N., Henkel C., Millar T.J., et al., 1998b, *Molecular abundances in the Magellanic Clouds. III. LIRS36, a star-forming region in the Small Magellanic Cloud*, A&A, 330,

901

- Ciardullo R., Feldmeier J.J., Jacoby G.H., et al., 2002, *Planetary Nebulae as Standard Candles. XII. Connecting the Population I and Population II Distance Scales*, ApJ, 577, 31
- Colombo D., Hughes A., Schinnerer E., et al., 2014, *The PdBI Arcsecond Whirlpool Survey (PAWS): Environmental Dependence of Giant Molecular Cloud Properties in M51*, ApJ, 784, 3
- Costagliola F., Aalto S., Rodriguez M.I., et al., 2011, *Molecules as tracers of galaxy evolution: an EMIR survey. I. Presentation of the data and first results*, A&A, 528, A30
- Costagliola F., Sakamoto K., Muller S., et al., 2015, *Exploring the molecular chemistry and excitation in obscured luminous infrared galaxies. An ALMA mm-wave spectral scan of NGC 4418*, A&A, 582, A91
- Crosthwaite L.P., Turner J.L., 2007, *CO(1-0), CO(2-1), and Neutral Gas in NGC 6946: Molecular Gas in a Late-Type, Gas-Rich, Spiral Galaxy*, AJ, 134, 1827
- Curran S.J., Aalto S., Booth R.S., 2000, *Dense molecular gas in Seyfert galaxies*, A&AS, 141, 193
- Daddi E., Elbaz D., Walter F., et al., 2010, *Different Star Formation Laws for Disks Versus Starbursts at Low and High Redshifts*, ApJ, 714, L118
- Dale D.A., Cohen S.A., Johnson L.C., et al., 2009, *The Spitzer Local Volume Legacy: Survey Description and Infrared Photometry*, ApJ, 703, 517
- Danielson A.L.R., Swinbank A.M., Smail I., et al., 2013, *^{13}CO and C^{18}O emission from a dense gas disc at $z = 2.3$: abundance variations, cosmic rays and the initial conditions for star formation*, MNRAS, 436, 2793
- Davis T.A., 2014, *Systematic variation of the $^{12}\text{CO}/^{13}\text{CO}$ ratio as a function of star formation rate surface density*, MNRAS, 445, 2378
- Deharveng J.M., Sasseen T.P., Buat V., et al., 1994, *Ultraviolet observations of galaxies with the FAUST experiment*, A&A, 289, 715
- Diplas A., Savage B.D., 1991, *Neutral hydrogen in the outer Galaxy*, ApJ, 377, 126
- Downes D., Solomon P.M., 1998, *Rotating Nuclear Rings and Extreme Starbursts in Ultraluminous Galaxies*, ApJ, 507, 615
- Draine B.T., 2003, *Interstellar Dust Grains*, ARA&A, 41, 241
- Draine B.T., 2011, *Physics of the Interstellar and Intergalactic Medium*
- Elmegreen B.G., 1989, *Molecular cloud formation by gravitational instabilities in a clumpy interstellar medium*, ApJ, 344, 306
- Elmegreen B.G., 1993, *The H to H₂ transition in galaxies - Totally molecular galaxies*,

- ApJ, 411, 170
- Elmegreen B.G., Parravano A., 1994, *When star formation stops: Galaxy edges and low surface brightness disks*, ApJ, 435, L121
- Emsellem E., Renaud F., Bournaud F., et al., 2015, *The interplay between a galactic bar and a supermassive black hole: nuclear fuelling in a subparsec resolution galaxy simulation*, MNRAS, 446, 2468
- Engelbracht C.W., Rieke G.H., Gordon K.D., et al., 2008, *Metallicity Effects on Dust Properties in Starbursting Galaxies*, ApJ, 678, 804
- Evans II N.J., Allen L.E., Blake G.A., et al., 2003, *From Molecular Cores to Planet-forming Disks: An SIRTf Legacy Program*, PASP, 115, 965
- Evans II N.J., Dunham M.M., Jørgensen J.K., et al., 2009, *The Spitzer c2d Legacy Results: Star-Formation Rates and Efficiencies; Evolution and Lifetimes*, ApJS, 181, 321
- Evans II N.J., Heiderman A., Vutisalchavakul N., 2014, *Star Formation Relations in Nearby Molecular Clouds*, ApJ, 782, 114
- Ewen H.I., Purcell E.M., 1951, *Observation of a Line in the Galactic Radio Spectrum: Radiation from Galactic Hydrogen at 1,420 Mc./sec.*, Nature, 168, 356
- Federrath C., 2015, *Inefficient star formation through turbulence, magnetic fields and feedback*, MNRAS, 450, 4035
- Federrath C., Roman-Duval J., Klessen R.S., et al., 2010, *Comparing the statistics of interstellar turbulence in simulations and observations. Solenoidal versus compressive turbulence forcing*, A&A, 512, A81
- Fukui Y., Kawamura A., Minamidani T., et al., 2008, *The Second Survey of the Molecular Clouds in the Large Magellanic Cloud by NANTEN. I. Catalog of Molecular Clouds*, ApJS, 178, 56
- Galametz M., Kennicutt R.C., Calzetti D., et al., 2013, *Calibration of the total infrared luminosity of nearby galaxies from Spitzer and Herschel bands*, MNRAS, 431, 1956
- Gao Y., Solomon P.M., 2004, *The Star Formation Rate and Dense Molecular Gas in Galaxies*, ApJ, 606, 271
- Gao Y., Carilli C.L., Solomon P.M., et al., 2007, *HCN Observations of Dense Star-forming Gas in High-Redshift Galaxies*, ApJ, 660, L93
- García-Burillo S., Usero A., Alonso-Herrero A., et al., 2012, *Star-formation laws in luminous infrared galaxies. New observational constraints on models*, A&A, 539, A8
- Genzel R., Tacconi L.J., Gracia-Carpio J., et al., 2010, *A study of the gas-star formation relation over cosmic time*, MNRAS, 407, 2091
- Gil de Paz A., Boissier S., Madore B.F., et al., 2007, *The GALEX Ultraviolet Atlas of*

BIBLIOGRAPHY

- Nearby Galaxies*, ApJS, 173, 185
- Goldsmith P.F., Heyer M., Narayanan G., et al., 2008, *Large-Scale Structure of the Molecular Gas in Taurus Revealed by High Linear Dynamic Range Spectral Line Mapping*, ApJ, 680, 428
- González-Alfonso E., Fischer J., Graciá-Carpio J., et al., 2012, *Herschel/PACS spectroscopy of NGC 4418 and Arp 220: H₂O, H₂¹⁸O, OH, ¹⁸OH, O I, HCN, and NH₃*, A&A, 541, A4
- Graciá-Carpio J., García-Burillo S., Planesas P., et al., 2006, *Is HCN a True Tracer of Dense Molecular Gas in Luminous and Ultraluminous Infrared Galaxies?*, ApJ, 640, L135
- Graciá-Carpio J., García-Burillo S., Planesas P., et al., 2008, *Evidence of enhanced star formation efficiency in luminous and ultraluminous infrared galaxies*, A&A, 479, 703
- Grenier I.A., Casandjian J.M., Terrier R., 2005, *Unveiling Extensive Clouds of Dark Gas in the Solar Neighborhood*, Science, 307, 1292
- Greve T.R., Papadopoulos P.P., Gao Y., et al., 2009, *Molecular Gas in Extreme Star-Forming Environments: The Starbursts Arp 220 and NGC 6240 as Case Studies*, ApJ, 692, 1432
- Guesten R., Henkel C., Batrla W., 1985, *(H₂/C-12/O)/(H₂/C-13/O) ratios from molecular clouds near the galactic center*, A&A, 149, 195
- Harada N., Riquelme D., Viti S., et al., 2015, *Chemical features in the circumnuclear disk of the Galactic center*, A&A, 584, A102
- Hartwick F.D.A., 1971, *On the Rate of Star Formation in M31*, ApJ, 163, 431
- Heiderman A., Evans II N.J., Allen L.E., et al., 2010, *The Star Formation Rate and Gas Surface Density Relation in the Milky Way: Implications for Extragalactic Studies*, ApJ, 723, 1019
- Heikkilä A., Johansson L.E.B., Olofsson H., 1998, *The C¹⁸O/C¹⁷O ratio in the Large Magellanic Cloud*, A&A, 332, 493
- Heitsch F., Mac Low M.M., Klessen R.S., 2001, *Gravitational Collapse in Turbulent Molecular Clouds. II. Magnetohydrodynamical Turbulence*, ApJ, 547, 280
- Helfer T.T., Blitz L., 1997, *Dense Gas in the Milky Way*, ApJ, 478, 233
- Helfer T.T., Thornley M.D., Regan M.W., et al., 2003, *The BIMA Survey of Nearby Galaxies (BIMA SONG). II. The CO Data*, ApJS, 145, 259
- Henkel C., Mauersberger R., 1993, *C and O Nucleosynthesis in Starbursts - the Connection Between Distant Mergers the Galaxy and the Solar System*, A&A, 274, 730
- Henkel C., Baan W.A., Mauersberger R., 1991, *Dense molecular gas in galactic nuclei*,

- A&ARv, 3, 47
- Henkel C., Chin Y.N., Mauersberger R., et al., 1998, *Dense gas in nearby galaxies. XI. Interstellar $^{12}\text{C}/^{13}\text{C}$ ratios in the central regions of M82 and IC342*, A&A, 329, 443
- Henkel C., Downes D., Weiß A., et al., 2010, *Weak ^{13}CO in the Cloverleaf quasar: evidence for a young, early generation starburst*, A&A, 516, A111
- Henkel C., Asiri H., Ao Y., et al., 2014, *Carbon and oxygen isotope ratios in starburst galaxies: New data from NGC 253 and Mrk 231 and their implications*, A&A, 565, A3
- Heyer M., Krawczyk C., Duval J., et al., 2009, *Re-Examining Larson's Scaling Relationships in Galactic Molecular Clouds*, ApJ, 699, 1092
- Heyer M.H., Corbelli E., Schneider S.E., et al., 2004, *The Molecular Gas Distribution and Schmidt Law in M33*, ApJ, 602, 723
- Hollenbach D.J., Tielens A.G.G.M., 1997, *Dense Photodissociation Regions (PDRs)*, ARA&A, 35, 179
- Hughes A., Meidt S.E., Colombo D., et al., 2013, *A Comparative Study of Giant Molecular Clouds in M51, M33, and the Large Magellanic Cloud*, ApJ, 779, 46
- Imanishi M., Nakanishi K., Izumi T., 2016, *ALMA Investigation of Vibrationally Excited HCN/HCO⁺/HNC Emission Lines in the AGN-Hosting Ultraluminous Infrared Galaxy IRAS 20551-4250*, ApJ, 825, 44
- Jackson J.M., Heyer M.H., Paglione T.A.D., et al., 1996, *HCN and CO in the Central 630 Parsecs of the Galaxy*, ApJ, 456, L91
- Jenkins E.B., Meloy D.A., 1974, *A survey with Copernicus of interstellar O VI absorption*, ApJ, 193, L121
- Jiménez-Donaire M.J., Bigiel F., Leroy A.K., et al., 2017a, *Optical depth estimates and effective critical densities of dense gas tracers in the inner parts of nearby galaxy discs*, MNRAS, 466, 49
- Jiménez-Donaire M.J., Cormier D., Bigiel F., et al., 2017b, *$^{13}\text{CO}/\text{C}^{18}\text{O}$ Gradients across the Disks of Nearby Spiral Galaxies*, ApJ, 836, L29
- Jones P.A., Burton M.G., Cunningham M.R., et al., 2012, *Spectral imaging of the Central Molecular Zone in multiple 3-mm molecular lines*, MNRAS, 419, 2961
- Juneau S., Narayanan D.T., Moustakas J., et al., 2009, *Enhanced Dense Gas Fraction in Ultraluminous Infrared Galaxies*, ApJ, 707, 1217
- Kainulainen J., Beuther H., Henning T., et al., 2009, *Probing the evolution of molecular cloud structure. From quiescence to birth*, A&A, 508, L35
- Kennicutt R.C., Evans N.J., 2012, *Star Formation in the Milky Way and Nearby Galaxies*, ARA&A, 50, 531

BIBLIOGRAPHY

- Kennicutt R.C., Calzetti D., Aniano G., et al., 2011, *KINGFISH - Key Insights on Nearby Galaxies: A Far-Infrared Survey with Herschel: Survey Description and Image Atlas*, PASP, 123, 1347
- Kennicutt Jr. R.C., 1989, *The star formation law in galactic disks*, ApJ, 344, 685
- Kennicutt Jr. R.C., 1998, *The Global Schmidt Law in Star-forming Galaxies*, ApJ, 498, 541
- Kennicutt Jr. R.C., Armus L., Bendo G., et al., 2003, *SINGS: The SIRTf Nearby Galaxies Survey*, PASP, 115, 928
- Kennicutt Jr. R.C., Calzetti D., Walter F., et al., 2007, *Star Formation in NGC 5194 (M51a). II. The Spatially Resolved Star Formation Law*, ApJ, 671, 333
- Kennicutt Jr. R.C., Lee J.C., Funes J.G., et al., 2008, *An H α Imaging Survey of Galaxies in the Local 11 Mpc Volume*, ApJS, 178, 247
- Kepley A.A., Leroy A.K., Frayer D., et al., 2014, *The Green Bank Telescope Maps the Dense, Star-forming Gas in the Nearby Starburst Galaxy M82*, ApJ, 780, L13
- Klessen R.S., Heitsch F., Mac Low M.M., 2000, *Gravitational Collapse in Turbulent Molecular Clouds. I. Gasdynamical Turbulence*, ApJ, 535, 887
- Knudsen K.K., Walter F., Weiss A., et al., 2007, *New Insights on the Dense Molecular Gas in NGC 253 as Traced by HCN and HCO⁺*, ApJ, 666, 156
- Kohno K., Kawabe R., Tosaki T., et al., 1996, *Aperture Synthesis CO and HCN Observations of M51: Dense Molecular Disk around a Low-Luminosity Active Galactic Nucleus*, ApJ, 461, L29
- Kohno K., Matsushita S., Vila-Vilaró B., et al., 2001, *Dense Molecular Gas and Star Formation in Nearby Seyfert Galaxies*, in *The Central Kiloparsec of Starbursts and AGN: The La Palma Connection*, edited by J.H. Knapen, J.E. Beckman, I. Shlosman, T.J. Mahoney, vol. 249 of *Astronomical Society of the Pacific Conference Series*, p. 672
- Kregel M., van der Kruit P.C., de Grijs R., 2002, *Flattening and truncation of stellar discs in edge-on spiral galaxies*, MNRAS, 334, 646
- Krips M., Neri R., García-Burillo S., et al., 2008, *A Multi-transition HCN and HCO⁺ Study of 12 Nearby Active Galaxies: Active Galactic Nucleus versus Starburst Environments*, ApJ, 677, 262
- Kruijssen J.M.D., Longmore S.N., 2013, *Comparing molecular gas across cosmic time-scales: the Milky Way as both a typical spiral galaxy and a high-redshift galaxy analogue*, MNRAS, 435, 2598
- Kruijssen J.M.D., Longmore S.N., Elmegreen B.G., et al., 2014, *What controls star formation in the central 500 pc of the Galaxy?*, MNRAS, 440, 3370

- Krumholz M.R., 2014, *DESPOTIC - a new software library to Derive the Energetics and Spectra of Optically Thick Interstellar Clouds*, MNRAS, 437, 1662
- Krumholz M.R., Kruijssen J.M.D., 2015, *A dynamical model for the formation of gas rings and episodic starbursts near galactic centres*, MNRAS, 453, 739
- Krumholz M.R., McKee C.F., Tumlinson J., 2009, *The Star Formation Law in Atomic and Molecular Gas*, ApJ, 699, 850
- Krumholz M.R., Dekel A., McKee C.F., 2012, *A Universal, Local Star Formation Law in Galactic Clouds, nearby Galaxies, High-redshift Disks, and Starbursts*, ApJ, 745, 69
- Kulkarni S.R., Heiles C., 1988, *Neutral hydrogen and the diffuse interstellar medium*, pp. 95–153
- Kuno N., Nakai N., Handa T., et al., 1995, *Distribution and Dynamics of Molecular Gas in the Galaxy M51. II. Formation of Giant Molecular Associations and Massive Stars*, PASJ, 47, 745
- Kuno N., Sato N., Nakanishi H., et al., 2007, *Nobeyama CO Atlas of Nearby Spiral Galaxies: Distribution of Molecular Gas in Barred and Nonbarred Spiral Galaxies*, PASJ, 59, 117
- Lada C.J., Lada E.A., 2003, *Embedded Clusters in Molecular Clouds*, ARA&A, 41, 57
- Lada C.J., Lombardi M., Alves J.F., 2010, *On the Star Formation Rates in Molecular Clouds*, ApJ, 724, 687
- Lada C.J., Forbrich J., Lombardi M., et al., 2012, *Star Formation Rates in Molecular Clouds and the Nature of the Extragalactic Scaling Relations*, ApJ, 745, 190
- Langer W.D., Penzias A.A., 1990, *C-12/C-13 isotope ratio across the Galaxy from observations of C-13/O-18 in molecular clouds*, ApJ, 357, 477
- Larson R.B., 1981, *Turbulence and star formation in molecular clouds*, MNRAS, 194, 809
- Leroy A.K., Walter F., Brinks E., et al., 2008, *The Star Formation Efficiency in Nearby Galaxies: Measuring Where Gas Forms Stars Effectively*, AJ, 136, 2782
- Leroy A.K., Walter F., Bigiel F., et al., 2009, *Heracles: The HERA CO Line Extragalactic Survey*, AJ, 137, 4670
- Leroy A.K., Bigiel F., de Blok W.J.G., et al., 2012, *Estimating the Star Formation Rate at 1 kpc Scales in nearby Galaxies*, AJ, 144, 3
- Leroy A.K., Walter F., Sandstrom K., et al., 2013, *Molecular Gas and Star Formation in nearby Disk Galaxies*, AJ, 146, 19
- Leroy A.K., Bolatto A.D., Ostriker E.C., et al., 2015, *ALMA Reveals the Molecular Medium Fueling the Nearest Nuclear Starburst*, ApJ, 801, 25
- Leroy A.K., Schinnerer E., Hughes A., et al., 2017a, *Cloud Scale ISM Structure and Star*

BIBLIOGRAPHY

- Formation in M51*, ArXiv e-prints
- Leroy A.K., Usero A., Schrubba A., et al., 2017b, *Millimeter-wave Line Ratios and Sub-beam Volume Density Distributions*, ApJ, 835, 217
- Loenen A.F., Spaans M., Baan W.A., et al., 2008, *Mechanical feedback in the molecular ISM of luminous IR galaxies*, A&A, 488, L5
- Longmore S.N., Bally J., Testi L., et al., 2013, *Variations in the Galactic star formation rate and density thresholds for star formation*, MNRAS, 429, 987
- Mac Low M.M., Klessen R.S., 2004, *Control of star formation by supersonic turbulence*, Reviews of Modern Physics, 76, 125
- Martin C.L., Kennicutt Jr. R.C., 2001, *Star Formation Thresholds in Galactic Disks*, ApJ, 555, 301
- Martín S., Aladro R., Martín-Pintado J., et al., 2010, *A large $^{12}\text{C}/^{13}\text{C}$ isotopic ratio in M 82 and NGC 253*, A&A, 522, A62
- Martín-Pintado J., de Vicente P., Fuente A., et al., 1997, *SiO Emission from the Galactic Center Molecular Clouds*, ApJ, 482, L45
- Matsushita S., Trung D.V., Boone F., et al., 2015, *Molecular Gas and Radio Jet Interaction: a Case Study of the Seyfert 2 AGN M51*, Publication of Korean Astronomical Society, 30, 439
- McKee C.F., Ostriker E.C., 2007, *Theory of Star Formation*, ARA&A, 45, 565
- McMullin J.P., Waters B., Schiebel D., et al., 2007, *CASA Architecture and Applications*, in *Astronomical Data Analysis Software and Systems XVI*, edited by R.A. Shaw, F. Hill, D.J. Bell, vol. 376 of *Astronomical Society of the Pacific Conference Series*, p. 127
- McQuinn K.B.W., Simon R., Law C.J., et al., 2002, *A Comparison of ^{13}CO and CS Emission in the Inner Galaxy*, ApJ, 576, 274
- Meidt S.E., 2016, *How Galactic Environment Regulates Star Formation*, ApJ, 818, 69
- Meidt S.E., Schinnerer E., García-Burillo S., et al., 2013, *Gas Kinematics on Giant Molecular Cloud Scales in M51 with PAWS: Cloud Stabilization through Dynamical Pressure*, ApJ, 779, 45
- Meidt S.E., Schinnerer E., van de Ven G., et al., 2014, *Reconstructing the Stellar Mass Distributions of Galaxies Using S^4G IRAC 3.6 and 4.5 μm Images. II. The Conversion from Light to Mass*, ApJ, 788, 144
- Meier D.S., Turner J.L., 2004, *Dynamically Influenced Molecular Clouds in the Nucleus of NGC 6946: Variations in the CO Isotopic Line Ratios*, AJ, 127, 2069
- Meier D.S., Turner J.L., 2012, *Spatially Resolved Chemistry in nearby Galaxies. II. The Nuclear Bar in Maffei 2*, ApJ, 755, 104

- Meier D.S., Turner J.L., Hurt R.L., 2008, *Nuclear Bar Catalyzed Star Formation: ^{13}CO , C^{18}O , and Molecular Gas Properties in the Nucleus of Maffei 2*, ApJ, 675, 281
- Meier D.S., Turner J.L., Beck S.C., 2014, *Spatially Resolved Chemistry in Nearby Galaxies. III. Dense Molecular Gas in the Inner Disk of the LIRG IRAS 04296+2923*, ApJ, 795, 107
- Meier D.S., Walter F., Bolatto A.D., et al., 2015, *ALMA Multi-line Imaging of the Nearby Starburst NGC 253*, ApJ, 801, 63
- Meijerink R., Spaans M., Israel F.P., 2007, *Diagnostics of irradiated dense gas in galaxy nuclei. II. A grid of XDR and PDR models*, A&A, 461, 793
- Mihalas D., Binney J., 1981, *Galactic astronomy: Structure and kinematics /2nd edition/*
- Milam S.N., Savage C., Brewster M.A., et al., 2005, *The $^{12}\text{C}/^{13}\text{C}$ Isotope Gradient Derived from Millimeter Transitions of CN: The Case for Galactic Chemical Evolution*, ApJ, 634, 1126
- Mizuno A., Yamaguchi R., Tachihara K., et al., 2001, *A Large Scale ^{12}CO ($J = 1 - 0$) Survey toward the Chamaeleon Region with NANTEN*, PASJ, 53, 1071
- Mogotsi K.M., de Blok W.J.G., Caldú-Primo A., et al., 2016, *HI and CO Velocity Dispersions in Nearby Galaxies*, AJ, 151, 15
- Molinari S., Swinyard B., Bally J., et al., 2010, *Clouds, filaments, and protostars: The Herschel Hi-GAL Milky Way*, A&A, 518, L100
- Morris M., Serabyn E., 1996, *The Galactic Center Environment*, ARA&A, 34, 645
- Moustakas J., Kennicutt Jr. R.C., Tremonti C.A., et al., 2010, *Optical Spectroscopy and Nebular Oxygen Abundances of the Spitzer/SINGS Galaxies*, ApJS, 190, 233
- Murphy E.J., Condon J.J., Schinnerer E., et al., 2011, *Calibrating Extinction-free Star Formation Rate Diagnostics with 33 GHz Free-free Emission in NGC 6946*, ApJ, 737, 67
- Narayanan D., Krumholz M.R., Ostriker E.C., et al., 2012, *A general model for the CO- H_2 conversion factor in galaxies with applications to the star formation law*, MNRAS, 421, 3127
- Nguyen Q.R., Jackson J.M., Henkel C., et al., 1992, *A survey for extragalactic HCN and HCO(+)*, ApJ, 399, 521
- Nishimura Y., Shimonishi T., Watanabe Y., et al., 2015, *Spectral Line Survey toward Molecular Clouds in the Large Magellanic Cloud*, The Astrophysical Journal, Volume 818, Issue 2, article id. 161, 17 pp. (2016)., 818, URL <http://arxiv.org/abs/1512.02327><http://dx.doi.org/10.3847/0004-637X/818/2/161>
- Nishimura Y., Shimonishi T., Watanabe Y., et al., 2016, *Spectral Line Survey toward a*

BIBLIOGRAPHY

- Molecular Cloud in IC10*, URL <http://arxiv.org/abs/1608.01099>
- Nomoto K., Kobayashi C., Tominaga N., 2013, *Nucleosynthesis in Stars and the Chemical Enrichment of Galaxies*, ARA&A, 51, 457
- Onishi T., Mizuno A., Kawamura A., et al., 1998, *A C¹⁸O Survey of Dense Cloud Cores in Taurus: Star Formation*, ApJ, 502, 296
- Padoan P., Scalo J., 2005, *Confinement-driven Spatial Variations in the Cosmic-Ray Flux*, ApJ, 624, L97
- Papadopoulos P.P., Greve T.R., van der Werf P., et al., 2007, *A large CO and HCN line survey of Luminous Infrared Galaxies*, ArXiv Astrophysics e-prints
- Papadopoulos P.P., van der Werf P., Xilouris E., et al., 2012, *The Molecular Gas in Luminous Infrared Galaxies. II. Extreme Physical Conditions and Their Effects on the X_{co} Factor*, ApJ, 751, 10
- Pellegrini E.W., Baldwin J.A., Brogan C.L., et al., 2007, *A Magnetically Supported Photodissociation Region in M17*, ApJ, 658, 1119
- Pellegrini E.W., Baldwin J.A., Ferland G.J., et al., 2009, *Orion's Bar: Physical Conditions Across the Definitive H⁺/H⁰/H₂ Interface*, ApJ, 693, 285
- Peterson D.E., Caratti o Garatti A., Bourke T.L., et al., 2011, *The Spitzer Survey of Interstellar Clouds in the Gould Belt. III. A Multi-wavelength View of Corona Australis*, ApJS, 194, 43
- Pety J., Schinnerer E., Leroy A.K., et al., 2013, *The Plateau de Bure + 30 m Arcsecond Whirlpool Survey Reveals a Thick Disk of Diffuse Molecular Gas in the M51 Galaxy*, ApJ, 779, 43
- Pety J., Guzmán V.V., Orkisz J.H., et al., 2017, *The anatomy of the Orion B giant molecular cloud: A local template for studies of nearby galaxies*, A&A, 599, A98
- Pillai T., Kauffmann J., Tan J.C., et al., 2015, *Magnetic Fields in High-mass Infrared Dark Clouds*, ApJ, 799, 74
- Pineda J.E., Caselli P., Goodman A.A., 2008, *CO Isotopologues in the Perseus Molecular Cloud Complex: the X-factor and Regional Variations*, ApJ, 679, 481
- Privon G.C., Herrero-Illana R., Evans A.S., et al., 2015, *Excitation Mechanisms for HCN (1-0) and HCO⁺ (1-0) in Galaxies from the Great Observatories All-sky LIRG Survey*, ApJ, 814, 39
- Querejeta M., Meidt S.E., Schinnerer E., et al., 2016a, *Gravitational torques imply molecular gas inflow towards the nucleus of M 51*, A&A, 588, A33
- Querejeta M., Schinnerer E., García-Burillo S., et al., 2016b, *AGN feedback in the nucleus of M51*, ArXiv e-prints

- Rahman N., Bolatto A.D., Wong T., et al., 2011, *CARMA Survey Toward Infrared-bright Nearby Galaxies (STING): Molecular Gas Star Formation Law in NGC 4254*, ApJ, 730, 72
- Requena-Torres M.A., Martín-Pintado J., Martín S., et al., 2008, *The Galactic Center: The Largest Oxygen-bearing Organic Molecule Repository*, ApJ, 672, 352
- Riquelme D., Bronfman L., Mauersberger R., et al., 2010, *A survey of the Galactic center region in HCO⁺, H¹³CO⁺, and SiO*, A&A, 523, A45
- Rosolowsky E., Pineda J.E., Gao Y., 2011, *Minimal HCN emission from molecular clouds in M33*, MNRAS, 415, 1977
- Roueff E., Loison J.C., Hickson K.M., 2015, *Isotopic fractionation of carbon, deuterium, and nitrogen: a full chemical study*, A&A, 576, A99
- Safraneck-Shrader C., Krumholz M.R., Kim C.G., et al., 2017, *Chemistry and radiative shielding in star-forming galactic discs*, MNRAS, 465, 885
- Sage L.J., Henkel C., Mauersberger R., 1991, *Extragalactic O-18/O-17 ratios and star formation - High-mass stars preferred in starburst systems?*, A&A, 249, 31
- Sakamoto K., Aalto S., Evans A.S., et al., 2010, *Vibrationally Excited HCN in the Luminous Infrared Galaxy NGC 4418*, ApJ, 725, L228
- Sanders D.B., Scoville N.Z., Solomon P.M., 1985, *Giant molecular clouds in the Galaxy. II - Characteristics of discrete features*, ApJ, 289, 373
- Sandstrom K.M., Leroy A.K., Walter F., et al., 2013, *The CO-to-H₂ Conversion Factor and Dust-to-gas Ratio on Kiloparsec Scales in Nearby Galaxies*, ApJ, 777, 5
- Sanduleak N., 1969, *Correlation of the Distributions of Young Stars and Neutral Hydrogen in the Small Magellanic Cloud*, AJ, 74, 47
- Savage C., Apponi A.J., Ziurys L.M., et al., 2002, *Galactic ¹²C/¹³C Ratios from Millimeter-Wave Observations of Interstellar CN*, ApJ, 578, 211
- Schilke P., Walmsley C.M., Pineau Des Forets G., et al., 1992, *A study of HCN, HNC and their isotopomers in OMC-1. I - Abundances and chemistry*, A&A, 256, 595
- Schinnerer E., Meidt S.E., Pety J., et al., 2013, *The PdBI Arcsecond Whirlpool Survey (PAWS). I. A Cloud-scale/Multi-wavelength View of the Interstellar Medium in a Grand-design Spiral Galaxy*, ApJ, 779, 42
- Schinnerer E., Meidt S.E., Colombo D., et al., 2017, *The PdBI Arcsecond Whirlpool Survey (PAWS): The Role of Spiral Arms in Cloud and Star Formation*, ApJ, 836, 62
- Schmidt M., 1959, *The Rate of Star Formation.*, ApJ, 129, 243
- Schruba A., Leroy A.K., Walter F., et al., 2010, *The Scale Dependence of the Molecular Gas Depletion Time in M33*, ApJ, 722, 1699

BIBLIOGRAPHY

- Schruba A., Leroy A.K., Walter F., et al., 2011, *A Molecular Star Formation Law in the Atomic-gas-dominated Regime in Nearby Galaxies*, *AJ*, 142, 37
- Schuster K.F., Kramer C., Hitschfeld M., et al., 2007, *A complete ^{12}CO 2-1 map of M 51 with HERA. I. Radial averages of CO, HI, and radio continuum*, *A&A*, 461, 143
- Scoville N.Z., Yun M.S., Armus L., et al., 1998, *Molecular Gas in the Inner 100 Parsecs of M51*, *ApJ*, 493, L63
- Seab C.G., 1987, *Grain destruction, formation, and evolution*, in *Interstellar Processes*, edited by D.J. Hollenbach, H.A. Thronson Jr., vol. 134 of *Astrophysics and Space Science Library*, pp. 491–512
- Sembach K.R., Savage B.D., 1992, *Observations of highly ionized gas in the Galactic halo*, *ApJS*, 83, 147
- Shapiro K.L., Gerssen J., van der Marel R.P., 2003, *Observational Constraints on Disk Heating as a Function of Hubble Type*, *AJ*, 126, 2707
- Shetty R., Glover S.C., Dullemond C.P., et al., 2011, *Modelling CO emission - I. CO as a column density tracer and the X factor in molecular clouds*, *MNRAS*, 412, 1686
- Shimajiri Y., André P., Braine J., et al., 2017, *Testing the universality of the star formation efficiency in dense molecular gas*, *ArXiv e-prints*
- Shirley Y.L., 2015, *The Critical Density and the Effective Excitation Density of Commonly Observed Molecular Dense Gas Tracers*, *Publications of the Astronomical Society of the Pacific*, 127(949), 299, URL <http://www.jstor.org/stable/10.1086/680342>
- Solomon P.M., Rivolo A.R., Barrett J., et al., 1987, *Mass, luminosity, and line width relations of Galactic molecular clouds*, *ApJ*, 319, 730
- Spergel D.N., Blitz L., 1992, *Extreme gas pressures in the Galactic bulge*, *Nature*, 357, 665
- Spezzi L., Vernazza P., Merín B., et al., 2011, *The Spitzer Survey of Interstellar Clouds in the Gould Belt. IV. Lupus V and VI Observed with IRAC and MIPS*, *ApJ*, 730, 65
- Stephens I.W., Jackson J.M., Whitaker J.S., et al., 2016, *Linking Dense Gas from the Milky Way to External Galaxies*, *ApJ*, 824, 29
- Strong A.W., Mattox J.R., 1996, *Gradient model analysis of EGRET diffuse Galactic γ -ray emission.*, *A&A*, 308, L21
- Suzuki T.K., Fukui Y., Torii K., et al., 2015, *Stochastic non-circular motion and outflows driven by magnetic activity in the Galactic bulge region*, *MNRAS*, 454, 3049
- Tamburro D., Rix H.W., Leroy A.K., et al., 2009, *What is Driving the H I Velocity Dispersion?*, *AJ*, 137, 4424
- Tan Q.H., Gao Y., Zhang Z.Y., et al., 2011, *^{12}CO , ^{13}CO and C^{18}O observations along the*

- major axes of nearby bright infrared galaxies*, *Research in Astronomy and Astrophysics*, 11, 787
- Taylor G.B., Morris M., Schulman E., 1993, *Water masers in the direction of the galactic center. 1: Results from initial observations*, *AJ*, 106, 1978
- Thilker D.A., Boissier S., Bianchi L., et al., 2007, *Ultraviolet and Infrared Diagnostics of Star Formation and Dust in NGC 7331*, *ApJS*, 173, 572
- Tielens A.G.G.M., 2005, *The Physics and Chemistry of the Interstellar Medium*
- Tielens A.G.G.M., 2010, *The Physics and Chemistry of the Interstellar Medium*
- Tielens A.G.G.M., McKee C.F., Seab C.G., et al., 1994, *The physics of grain-grain collisions and gas-grain sputtering in interstellar shocks*, *ApJ*, 431, 321
- Torrey P., Hopkins P.F., Faucher-Giguère C.A., et al., 2017, *An instability of feedback-regulated star formation in galactic nuclei*, *MNRAS*, 467, 2301
- Usero A., Leroy A.K., Walter F., et al., 2015, *Variations in the Star Formation Efficiency of the Dense Molecular Gas across the Disks of Star-forming Galaxies*, *AJ*, 150, 115
- van der Kruit P.C., 1988, *The three-dimensional distribution of light and mass in disks of spiral galaxies*, *A&A*, 192, 117
- van der Tak F.F.S., Black J.H., Schöier F.L., et al., 2007, *A computer program for fast non-LTE analysis of interstellar line spectra. With diagnostic plots to interpret observed line intensity ratios*, *A&A*, 468, 627
- van Dishoeck E.F., Black J.H., 1988, *The photodissociation and chemistry of interstellar CO*, *ApJ*, 334, 771
- van Dishoeck E.F., Blake G.A., 1998, *Chemical Evolution of Star-Forming Regions*, *ARA&A*, 36, 317
- Vázquez-Semadeni E., Kim J., Ballesteros-Paredes J., 2005, *Star Formation Efficiency in Driven, Supercritical, Turbulent Clouds*, *ApJ*, 630, L49
- Verley S., Corbelli E., Giovanardi C., et al., 2010, *Star formation in M 33: the radial and local relations with the gas*, *A&A*, 510, A64
- Vila-Vilaró B., 2008, *Rare CO Isotope Observations of M51a (NGC5194)*, *PASJ*, 60, 1231
- Vincenzo F., Belfiore F., Maiolino R., et al., 2016, *Nitrogen and oxygen abundances in the Local Universe*, *MNRAS*, 3477, 3466
- Wada K., Tomisaka K., 2005, *Molecular Gas Structure around an Active Galactic Nucleus with Nuclear Starburst: Three-dimensional Non-LTE Calculations of CO Lines*, *ApJ*, 619, 93
- Walter F., Brinks E., de Blok W.J.G., et al., 2008, *THINGS: The H I Nearby Galaxy Survey*, *AJ*, 136, 2563

BIBLIOGRAPHY

- Wang J., Qiu J., Shi Y., et al., 2014, *ISOTOPOLOGUES OF DENSE GAS TRACERS IN NGC 1068*, *Astrophysical Journal*, 796(1)
- Wang M., Henkel C., Chin Y.N., et al., 2004, *Dense gas in nearby galaxies. XVI. The nuclear starburst environment in NGC 4945*, *A&A*, 422, 883
- Wang M., Chin Y.N., Henkel C., et al., 2009, *Abundances and Isotope Ratios in the Magellanic Clouds: The Star-Forming Environment of N 113*, *ApJ*, 690, 580
- Watanabe Y., Sakai N., Sorai K., et al., 2014, *Spectral Line Survey toward the Spiral Arm of M51 in the 3 and 2 mm Bands*, *ApJ*, 788, 4
- Webber W.R., Yushak S.M., 1983, *A measurement of the energy spectra and relative abundance of the cosmic-ray H and He isotopes over a broad energy range*, *ApJ*, 275, 391
- Wilson C.D., Warren B.E., Israel F.P., et al., 2012a, *The JCMT Nearby Galaxies Legacy Survey - VIII. CO data and the $L_{CO(3-2)}$ - L_{FIR} correlation in the SINGS sample*, *MNRAS*, 424, 3050
- Wilson T.L., Rood R., 1994, *Abundances in the Interstellar Medium*, *ARA&A*, 32, 191
- Wilson T.L., Rohlfs K., Hüttemeister S., 2009, *Tools of Radio Astronomy*, Springer-Verlag
- Wilson T.L., Rohlfs K., Hüttemeister S., 2012b, *Tools of Radio Astronomy, 5th edition*
- Wolfire M.G., Hollenbach D., McKee C.F., 2010, *The Dark Molecular Gas*, *ApJ*, 716, 1191
- Wong T., Blitz L., 2002, *The Relationship between Gas Content and Star Formation in Molecule-rich Spiral Galaxies*, *ApJ*, 569, 157
- Wouterloot J.G.A., Henkel C., Brand J., et al., 2008, *Galactic interstellar $^{18}\text{O}/^{17}\text{O}$ ratios - a radial gradient?*, *A&A*, 487, 237
- Wu J., Evans II N.J., Gao Y., et al., 2005, *Connecting Dense Gas Tracers of Star Formation in our Galaxy to High-z Star Formation*, *ApJ*, 635, L173
- Wu J., Evans II N.J., Shirley Y.L., et al., 2010, *The Properties of Massive, Dense Clumps: Mapping Surveys of HCN and CS*, *ApJS*, 188, 313
- Wyder T.K., Martin D.C., Barlow T.A., et al., 2009, *The Star Formation Law at Low Surface Density*, *ApJ*, 696, 1834
- Young J.S., Scoville N., 1982, *Extragalactic CO - Gas distributions which follow the light in IC 342 and NGC 6946*, *ApJ*, 258, 467
- Young J.S., Scoville N.Z., 1991, *Molecular gas in galaxies*, *ARA&A*, 29, 581
- Yusef-Zadeh F., Hewitt J.W., Arendt R.G., et al., 2009, *Star Formation in the Central 400 pc of the Milky Way: Evidence for a Population of Massive Young Stellar Objects*, *ApJ*, 702, 178
- Zhang Q., Fall S.M., Whitmore B.C., 2001, *A Multiwavelength Study of the Young Star*

- Clusters and Interstellar Medium in the Antennae Galaxies*, ApJ, 561, 727
- Zibetti S., Charlot S., Rix H.W., 2009, *Resolved stellar mass maps of galaxies - I. Method and implications for global mass estimates*, MNRAS, 400, 1181

ACKNOWLEDGEMENTS

I would like to use this small section of the thesis to acknowledge the people who have accompanied me for the past three years. It was definitely a short, but intense time, full of new experiences and thoughts, which eventually led to the end of this PhD. First of all, I would like to thank Frank Bigiel, my supervisor. Thank you for offering me this position and the opportunity to work in this fantastic project, EMPIRE. Thank you, Frank, for the support during my talks in conferences, for your help writing down proposals (especially with the last minute ones!) and for always trying to make me see what is important.

There are two special people I would like to thank infinitely, Diane Cormier and Sacha Hony. I don't even know where to begin or end. Thank you, both of you, for always supporting me scientifically and personally. For helping me with the terrible IDL with unlimited patience and for your useful comments on this thesis. But also thank you for our amazing joint birthday parties, the dinners, and all the fun. I cannot ever bring enough Jamón to compensate all that. Thank you very much.

Moreover, I need to say that this work would have not been possible without my collaborators, most of them abroad. I would like to sincerely thank Adam Leroy and Antonio Usero for their constant support during these three years, and their fantastic academic advice. I want to thank the two additional members of my thesis committee, Ralf Klessen and Fabian Walter, for their great scientific feedback which helped carrying out this work.

Regarding this thesis, I would also like extend my gratitude to Hans-Walter Rix for kindly agreeing on refereeing this thesis, as well as Henrik Beuther and Luca Amendola for accepting to be part of my examination committee.

On the personal side, these wonderful three years in Heidelberg would not have been the same without the amazing friends I got to make since the beginning.

Merci Sara va Rezaye golam, ke too in se saal dar Heidelberg baram mesle khanevad-eye khodam boodin. Sara, azat mamnoonam ke behtarin hamkhooneyi boodi ke mitoonestam dashte basham, baraye tamaame khandeha va shabhayi ke ba ham Modern Family didim, baraye poshtibaanit ba postdoce morede alagheam, baraye talaashhat ke ba ham varzesh konim, va ashpazihaye 4 sa'ate vase pokhtane ghazahaye Irani. Reza, chico, to dar Alman baram behtarin doosti boodi ke mitoonestam tasavvore dashtanesho konam. Behtarin tinto va sharik baraye raghs va party va tamame naharha va ghahveh haayi

BIBLIOGRAPHY

ke be sokhanchini vaght gozaroondim. Fekr nemikonam ke betoonam hich joor behtari behetoon neshoon bedam ke cheghadr doostetoon daram, begheir az inke chand kalame be Farsi benevisam: Golam! Pesaram! Khoobi?

Thank you Anna, for being my first and best friend in Heidelberg. It all started with a trip to Ikea, and continued with fiesta nights, the coffee chats... Thanks for always making me nice dinners, for always filling my glass with a bit more of Prosecco, and for trying to teach me how to bake cookies! Since I know you, I even bought a German backpack! To sum up: thank you for making me feel that Germany can also be a nice place to live (but I will never do the hiking sticks. Never). Peter, thank you for your awesome parties where La Gasolina or Danza Kuduro are always playing, and for the amazing weisswurst breakfasts! Chiara, thanks for all our moments of "fashion depression" and your "I hate/love it so much"s. Please never stop driving the way you do.

Thank you Pedro, for always reminding me how exciting Astronomy is and the reasons why I wanted to be a physicist in the first place. Thank you for listening, and for your advice. Thank you for being by my side, this period of time has changed all aspects of my life.

Daniel, even though I know I will regret writing this, thank you for being my office mate during most of my PhD. I actually learned things from you (like RADEX). I did miss hearing you screaming "God damn it", "Cazzo" and "Mierda" when your code does not work. And the window/heating fights. Thank you for everything, including the comments.

And also thanks to all my ITA friends! Juanito, Onix, Eric, Sebastian, The Daniels, Robin, Christian, Lionel, Akimasa, Sam, Utte, Mattia, Katharina, Mattis, Stephan, Carla, Ondrej, Kiwan, Dimitros... And my fantastic friends from MPIA: Christina, Richard, Jorge, Aida, Adriana... I hope I'm not forgetting anyone!

Finally, none of my adventures here would have been possible without the ones I once left, especially without the support of my family. Por eso me gustaría dedicar esta tesis a mi padre, a mi madre y a mi hermano Fernando, por todos los sacrificios que han hecho y su paciencia cuando me "traspongo". Y también por prepararme siempre paquetitos de jamón, lomo y mantequilla de Portugal para mis viajes. Aunque no lo diga nunca, os quiero mucho. También a mis abuelos, en especial a Nani que, aunque a veces diga que le gustaría que fuese más tonta para quedarme cerca de ella, luego sé que le gusta presumir de nieta por ahí.

To my best friend in the world, Nani, thank you for all these ~ 22 years of friendship. I miss you, and I know we will probably live far away from each other, but I know that will not be an issue for always watching Gilmore Girls together or eating butter toasts in the brasero. Te quiero y siempre estaremos pegadas con superglue. And also thanks to all my school, college, and CERN friends: Maria, Paula, Pablo, Mario, Santi, Arancha, Stella, Bruno, Sandesh, Ana, Maria Brigida...

Thank you all for sharing these exciting years with me.